Analysis and Design of Linear-to-Circular Polarising Reflector Antennas Exploiting Periodic Metallodielectric Arrays

Salvador Mercader Pellicer

Submitted for the degree of Doctor of Philosophy

School of Energy, Geoscience, Infrastructure and Society
School of Engineering & Physical Sciences
Heriot-Watt University

April 2018

Abstract

This thesis presents an efficient way to analyse and design linear-to-circular polarising reflector antennas comprising doubly periodic metallodielectric arrays. These type of structures, used in conjunction with subreflectors, has risen as a promising solution to reduce the number of reflectors in multi-beam antennas in single-feed-per-beam architectures while providing circular polarisation for the downlink/uplink. The first part of the thesis is concerned with the analysis of single reflector antennas, focusing on their depolarisation properties. MATLAB® codes are developed to obtain the far-field from the reflector and are successfully compared against the preferred tool in the market for the analysis and design of reflector antennas, i.e., TICRA's GRASP.

This analysis tool is used in conjunction with a Floquet analysis of periodic structures to obtain the far-field from doubly periodic metallodielectric arrays. An efficient way to extract the fundamental modes from the near-field of the feed is introduced for cases where the the reflector is placed at the near-field of the feed. A design procedure to reduce the cross-polarisation of the polarising reflector far-field is included. This procedure is based on physical insight rather than brute-force optimisation, leading to computational efficiencies. Design examples are shown are compared against the original uniform unit-cell array design. Improvements up to 16 dB in the cross-polarisation levels across a wide bandwidth are achieved. The procedure is validated experimentally. The design procedure is also applied to a multi-beam case where three ideal sources are used to feed the reflector. Compared with the uniform unit-cell array, improvements up to 10 dB are obtained in the cross-polarisation performance for the whole bandwidth and the three feeds at the same time.

Dedication

To my parents and brother,

To Natalia, the best life companion I could ever ask for,

A mis padres y mi hermano,

A Natalia por su incensante e incondicional apoyo desde el inicio, a pesar de sus propios desafíos,

Acknowledgements

I would like to thank my supervisors Dr. Gabriela M. Medero and Prof. George Goussetis for believing I was up to this challenging task and supporting me during this enriching adventure. I would also like to thank my Master's dissertation supervisor Dr. José Luis Gómez Tornero for considering me as a good candidate for this PhD: José, you started all this!

A PhD is a long and difficult process during which you receive help from too many people to be named here. However, I would like to thank to Dr. María Llorente Crespo and Dr. Carolina Mateo Segura for their help specially in the first stages of the PhD. Also to my collaborators Adrián Ayastuy Rodríguez, Dr. Wenxing Tang and Francesco Rigobello. I have received a lot of help and support from all the colleagues and friends in the PhD office: Dr. José Antonio García Pérez, María Jesús Cañavate Sánchez, Victoria Gómez-Guillamón Buendía, Pascual Hilario Re, Dr. Daniel Rodríguez Prado, Dr. Francisco Cervera, Dr. Ross Aitken and Dr. David Watson, among others (you know who you are guys).

I have to express a lot gratitude to Daniele Bresciani and Dr. Hervé Legay from the Research and Technology Department of Thales Alenia Space for their continuous help and material exchange. I would also like to thank Dr. Nelson J. G. Fonseca from the Antenna and Sub-Millimetre Wave Section of the European Space Agency for fruitful contributions and help with the papers.

Finally I have to thank Natalia Rodríguez Vicente for her continuous support, patience, help and trust. She made the whole process much easier.

ACADEMIC REGISTRY

Research Thesis Submission

Name*:*	Salvador Mercader Pellicer		
School:	Energy, Geoscience, Infrastructure and Society		
Version: *(i.e. First, Resubmission, Final)*	Final	Degree Sought:	PhD

Declaration

In accordance with the appropriate regulations I hereby submit my thesis and I declare that:

1) the thesis embodies the results of my own work and has been composed by myself
2) where appropriate, I have made acknowledgement of the work of others and have made reference to work carried out in collaboration with other persons
3) the thesis is the correct version of the thesis for submission and is the same version as any electronic versions submitted*.
4) my thesis for the award referred to, deposited in the Heriot-Watt University Library, should be made available for loan or photocopying and be available via the Institutional Repository, subject to such conditions as the Librarian may require
5) I understand that as a student of the University I am required to abide by the Regulations of the University and to conform to its discipline.
6) I confirm that the thesis has been verified against plagiarism via an approved plagiarism detection application e.g. Turnitin.

* *Please note that it is the responsibility of the candidate to ensure that the correct version of the thesis is submitted.*

Signature of Candidate*:*		Date:	18/04/2018

Submission

Submitted By *(name in capitals):*	Salvador Mercader Pellicer
Signature of Individual Submitting:	
Date Submitted:	

For Completion in the Student Service Centre (SSC)

Received in the SSC by *(name in capitals):*			
Method of Submission *(Handed in to SSC; posted through internal/external mail):*			
*E-thesis Submitted (**mandatory for final theses)***			
Signature:		Date:	

Please note this form should be bound into the submitted thesis.

Contents

List of Figures

List of Tables

Glossary

AR	Axial ratio
AUT	Antenna under test
BFN	Beam forming networks
CP	Circular polarisation
CPSS	Circular polarisation selective surface
CS	Coordinate system
EFIE	Electric field integral equation
FFT	Fast Fourier transform
FSS	Frequency selective surface
FT	Fourier transform
GO	Geometrical optics
GTD	Geometrical theory of diffraction
HLP	Horizontal linear polarisation
LHCP	Left-handed circular polarisation
LP	Linear polarisation
MBA	Multi-beam antenna
MFB	Multi feed per beam
MoM	Method of moments
PEC	Perfect electric conductor
PO	Physical optics
PTD	Physical theory of diffraction
RF	Radio-frequency
RHCP	Right-handed circular polarisation
RWG	Rao-Wilson-Glisson
SFB	Single feed per beam
TE	Transverse electric

TEM	Transverse electromagnetic
TM	Transverse magnetic
UTD	Unified theory of diffraction
VLP	Vertical linear polarisation

List of Symbols

Mathematical operators

∇	Del operator to calculate the gradient, divergence or curl
$\frac{\partial}{\partial i}$	Partial derivative with respect to i
$\times$	Cross product
$\cdot$	Dot product
*	Conjugate
$\mathscr{R}e\{\}$	Real part
j	Complex number $\sqrt{-1}$
$< A, B >_C$	Inner product of A and B over an area C
δ_{pq}	Kronecker delta

Constant, functions and vectors

t	time (s)
$\vec{H}$	magnetic field intensity vector (A/m)
$\vec{E}$	electric field intensity vector (V/m)
$\vec{A}$	magnetic vector potential
$\vec{F}$	electric vector potential
$\vec{J}$	electric current density vector (A/m^2)
$\vec{M}$	magnetic current density vector (imaginary entity, V/m^2)
$\vec{J}_s$	electric surface current vector (A/m)
$\vec{M}_s$	magnetic surface current vector (imaginary entity, V/m)
$\vec{I}_e$	electric current vector (A)
$\vec{I}_m$	magnetic current vector (imaginary entity, V)
ρ_e	electric charge density (C/m^3)
ϵ	permittivity of the material (F/m)
μ	permeability of the material (H/m)
ϵ_0	permittivity of free space (F/m)
μ_0	permeability of free space (H/m)
n	Refractive index
f_0	frequency (Hz)
ω	Angular frequency $(rad \cdot Hz)$
λ	Wavelength (m)
k	Wave number (rad/m)
ψ	Eikonal function (m)
c	Speed of light (m/s)
W_{rad}	Radiation density (W/m^2)
η	Intrinsic impedance of the medium (Ω)
η_0	Intrinsic impedance of free space (Ω)
k_c	Cut-off wave number (rad/m)
β_{pq}	Propagation constant of mode pq (rad/m)
Ξ_{pq}	Field solution of the wave equation for mode pq
ψ_{pq}	Floquet's phasor for mode pq
$\vec{\kappa}_{mpq}$	Unit vector of tangential TM $(m = 1)$ or TE $(m = 2)$ for mode pq

Y_{mpq}	Tangential TM ($m = 1$) or TE ($m = 2$) admittance for mode pq (S)
T^n_{mpq}	Tangential TM ($m = 1$) or TE ($m = 2$) amplitude for region n and mode pq (V/m)
R^n_{mpq}	Tangential TM ($m = 1$) or TE ($m = 2$) reflection coefficient for region n and mode pq (V/m)
ϵ_r	Relative permittivity
$tan\,\delta$	Loss tangent
s_{ij}	S-parameters where i and j stand for 1 (TE) or/and 2 (TM)
$\Delta\phi$	Function to describe the unit-cell's element rotation (rad)

Geometrical symbols

$\vec{n}$	Unit vector locally normal to the surface
f	Distance between feed and reflector (m)
D	Reflector diameter for front-fed configuration (m)
d	Reflector diameter for offset configuration (m)
h	Reflector offset (m)
x_c	Distance along the x-axis to the centre of the projected circle
θ_c	Aperture angle (rad)
θ_i	Angle of incidence (rad)
θ_r	Angle of reflection (rad)
θ_0	Offset angle (rad)
θ_f	Angle subtended to the projected aperture centre (rad)
(ϑ, φ)	Orientation angles for the ideal feeds (rad)
φ_0	Polarisation angle for the electric dipole in the Huygens source (rad)
β_0	Polarisation angle for the Gaussian beam (rad)
(θ_l, ϕ_l)	Angles of incidence over the unit-cell (rad)
(D_x, D_y)	Unit-cell dimensions (m)
(l, w)	Length and width of the unit-cell's element (m)

List of publications

Journal papers

1. W. Tang **S. Mercader-Pellicer**, G. Goussetis, H. Legay and N.J.G. Fonseca, "Low-profile compact dual-band unit cell for polarising surfaces operating in orthogonal polarizations," *IEEE Trans. Antennas Propag. Comm.*, vol. 65, no. 3, pp. 1472-1477, March 2017.

2. **S. Mercader-Pellicer**, G. Goussetis, A. Ayastuy Rodríguez, G.M. Medero, D. Bresciani, H. Legay, N.J.G. Fonseca, "Cross-polarisation reduction of linear-to-circular polarising offset reflectors," *IEEE Trans. Antennas Propag.*, (in preparation).

Conferences

1. **S. Mercader-Pellicer**, G.M. Medero and G. Goussetis, "Comparison of geometrical and physical optics for cross-polarisation prediction in reflector antennas," *Active and Passive RF Devices IET Conf.*, London, UK, 2017.

2. **S. Mercader-Pellicer**, G. Goussetis, G.M. Medero, D. Bresciani, H. Legay and N.J.G. Fonseca, "Optimisation of linear-to-circular reflection polarisers for non-plane wave incidence," *38th ESA Antenna Workshop*, Noordwijk, The Netherlands, Oct 2017.

3. **S. Mercader-Pellicer**, G. Goussetis, G.M. Medero, D. Bresciani, H. Legay and N.J.G. Fonseca, "Optimisation by unit-cell rotation of linear-to-circular polarising reflectors for multiple primary feeds," *12th Eur. Conf. Antennas Propag. (EuCAP'18)*, London, UK, Apr 2018.

4. **S. Mercader-Pellicer**, G. Goussetis, G.M. Medero, D. Bresciani, H. Legay and N.J.G. Fonseca, "Optimisation by unit-cell rotation of linear-to-circular polarising reflectors for practical primary feeds," *12th Eur. Conf. Antennas Propag. (EuCAP'18)*, London, UK, Apr 2018.

Chapter 1

Introduction

1.1 Motivation

The requirements of telecommunication systems for satellite communications have exponentially grown in the last decades due to the introduction of new and diverse services such as direct broadcast, mobile communications, and high-capacity personal communications [1]. Some of them are summarized in Fig. 1.1, extracted from [2]. Reflector antennas have been traditionally one of the preferred ways to provide such services since they provide high gain and wide bandwidth, and low cross-polarisation and sidelobe levels [3].

Frequency and polarisation reuse has become a basic feature for many of these high demanding applications in order to improve their efficiency and reduce their weight and cost [1]. Therefore, the complete knowledge of the depolarisation properties of reflector antennas is a keystone. For this reason, the study of the depolarisation properties of font-fed and offset reflector antennas received a lot of attention specially during the 1970s and 1980s [4–8]. Since then, the basic theory related to reflector antennas and their depolarisation properties has been assumed to be known for many other authors. The differences in the way of explaining and in the terminology have been the motivation to present a unified and self-contained explanation of depolarisation properties of single reflector antennas, along with new information to give more physical insight.

Figure 1.1: Different services provided by satellite communications. (From [2] © 2015 IEEE.)

A common trend in modern applications for satellite communications is to provide high-capacity personal communications services [1]. These broadband services demand higher capacities for the antenna system, which in turn imposes high requirements for the antenna spectral efficiency. These high requirements can be met with multi-beam antennas (MBA), where several reflectors fed by an array of feeds are used to provide a large number of spot beams to cover a specific geographic area [1]. In order to cope with these new services, other tecnologies as well as the use of circular polarisation for uplink/downlink have been included in MBAs [9]. Some of these technologies are gridded subreflectors (strips of metal to filter out the polarisation orthogonal to the strips) [10], frequency selective surfaces (arrays of uniform unit-cells to perform some change to the incoming field within a specific frequency band) [11] and reflectarrays (flat arrays of unit-cells to mimic the high gains of parabolic reflectors within a specific frequency band) [12].

Linear-to-circular polarising composite main reflectors have been identified as a promising way in MBAs to provide circular polarisation while maintaining the configuration subsystem (feeds and subreflectors) in linear polarisation [9]. The optics in these structures are performed in linear polarisation (for which the technologies are more mature) up to the main reflector surface, where the conversion to circular polarisation takes place. The cross-polarisation performance of such large surfaces can be identified as their main drawback. Therefore, optimisation procedures to

improve the cross-polarisation performance of linear-to-circular polarising surfaces have been the second motivation for the present thesis.

To perform the design/analysis/synthesis of reflector antennas it is common to use the software GRASP from TICRA [13]. This software is mainly based on quasi-optical approaches to obtain the far-field from the reflector, but it also includes an integral equation solver based on the method of moments (MoM) [14]. However, to get the complete knowledge around the depolarisation properties of reflectors, it was chosen to develop in-house tools programmed in MATLAB® [15] to compute the fields at any stage (feed, reflector aperture, surface currents, far-field).

For the analysis of FSSs it is possible to use any software based on MoM for the analysis of periodic surfaces. It is also possible to use in-house tools. This analysis will give as output the value of S-parameters for a specific angle of incidence. Therefore, a reflector antenna analysis tool is needed to obtain the far-field from the FSS (or reflectarray) where the S-parameters of the periodic surface for each unit-cell are used to obtain the local reflected field. Since this tool is not available in the market (only in possession of other research groups), it has been developed for this thesis, where the S-parameters from the unit-cells will be obtained using CST Microwave Studio® [16].

1.2 Background

Reflector antennas have been used for decades in almost any telecommunication application where high gain is a priority, such as satellite communications, Earth observation, remote sensing or astronomy [3]. They also provide wide bandwidth and reasonable levels of sidelobes and cross-polarisation at relatively low cost [17]. A reflector antenna consists on a feed (usually a circular horn) or array of feeds radiating over a reflector (usually parabolic) or a sub-reflector. The field radiated from the feed to the reflector is denoted as primary field, whereas the field radiated from the reflector is denoted as secondary field. Reflector antennas can be classified by their geometry (following the different conic sections: plane, hyperbola, parabola, ellipse and sphere), the number of reflectors, the planes of curvature (single or double curved) or the feeding strategy (front-fed or offset). The frequency range of operation

imposes the size range of the aperture. For example, Fig. 1.2 shows the largest radio telescope in the world (China), which consists on a main dish of 500 m of diameter for frequencies between 70 MHz and 3 GHz. However, the aperture size also depends on the desired gain: the bigger the aperture, the higher the gain. Typical sizes can vary between 20λ and 1000λ [17].

Figure 1.2: Largest reflector in the world (China): Five hundred meter Aperture Spherical Telescope (FAST). Image credit & Copyright: Jeff Dai (TWAN).

A brief background of the different aspects of reflector antennas is provided in this section. First, a brief history of reflectors and their early applications for space communications will be held in Section 1.2.1. For these stringent applications, the complete knowledge of the depolarisation properties of reflector antennas and their correct estimation is of utter importance. Therefore, a brief review of the depolarisation properties for single reflector antennas will be held in Section 1.2.2. More recently, there has been an important growth in the use of multi-beam reflector antennas to provide cell-type coverages. The state of the art of this technology will be briefly reviewed in Section 1.2.3.

1.2.1 Brief history of reflector antennas and early applications for space communications

The focusing properties of reflector antennas have been known for centuries. If the legend is true, Archimedes would have been the first person in history to use a parabolic reflector (in offset configuration) to focus the Sun's heat on the enemy's ships to set them on fire [18]. Nevertheless, their official practical introduction would

occur during the Renaissance, with the renewed interest in visible-light optics for astronomic applications. It would be in the XVII century when a Scotsman named James Gregory, a Frenchman named Sieur Cassegrain and an Englishman named Isaac Newton presented their famous double reflector designs known as Gregorian, Cassegrain and Newtonian configurations, respectively. With the rapid expansion of missiles and microwave technologies after the Second World War, reflector antennas experienced their final consolidation [19].

Since NASA's Project Echo first introduced reflector antennas for space communications in the 1960s [20], new and smart ways to improve reflector antennas performance and expand their applications have appeared. For example, in order to achieve frequency reuse capabilities while not increasing the size of the whole structure, dual-gridded reflectors working with orthogonal linear polarisations were introduced in the 1970s [21]. Shaped or contoured beam reflector antennas to provide specific shaped coverages were introduced in the 1970s [22], and consolidated in the 80s [23]. On the mechanical side, mesh reflectors were introduced in the late 1980s to allow their folding during launch, saving a lot of storage space on board of the spacecraft [24].

The development of low-profile printed antennas in the late 1980s made possible the introduction of reflectarrays [12]. Reflectarrays combine advantages of reflector antennas and phased arrays since they provide collimated beams in a specific direction by the individual tuning of the unit-cells printed on a planar surface [25]. They have also demonstrated their capabilities to produce contoured beams [26]. Their main disadvantage lays in their narrow-bandwidth behaviour. This limitation can be overcome with multilayer unit-cells [12], at the expense of extra manufacturing complexities.

Frequency selective surfaces (FSS) have also found some applications in reflector antennas. The general principle of FSS has been known since the early XX century, but it was in the 1960s when they started to be used for military applications [11,27]. They consist on periodic surfaces comprising a uniform distribution of unit-cells. Since they originally do not posses any focusing properties, they started to be used in the 1980s as subreflectors. The FSS could be carefully designed so that it was totally reflecting for the operating frequency band of one feed, while nearly transparent for the band of another feed. This allowed the reduction in the complexity of the

configuration since two feeds would share the same subreflector [28].

1.2.2 Depolarisation properties of single parabolic reflector antennas

The eccentricity of the conic sections shown in Fig. 1.3 determines their focusing properties. For the parabola, a ray emanating from one focus, will be reflected on the surface and directed towards the second focus, which is placed at infinity. This simple property is the key feature that allows parabolic reflectors to achieve high gains, since it allows the parabola to convert a spherical wave emanating from the feed (placed at the focus) into a plane wave. Moreover, due to this simple geometrical principle to achieve high gains, parabolic reflector antennas also maintain reasonable sidelobe and cross-polarisation levels [29].

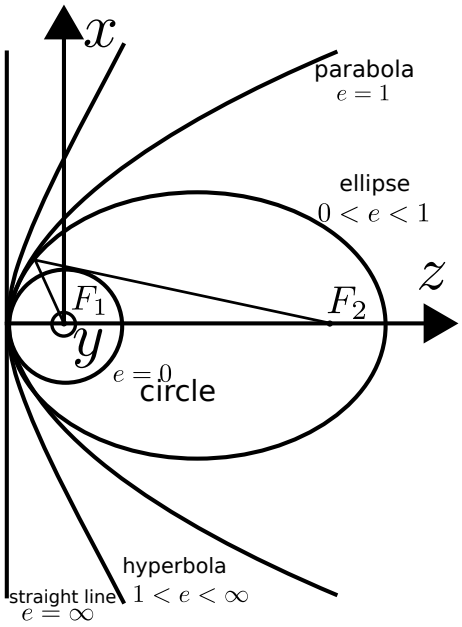

Figure 1.3: Conic sections and their eccentricities.

The simplest parabolic reflector is the single front-fed reflector, shown in Fig. 1.4a. Cutler [30], Silver [4], Jones [5] and Koffman [6] introduced in the 1940s, 1950s and 1960s the first studies that can be found in the literature about the depolarisation properties of this configuration. They used quasi-optical approximations [31] to follow the rays from the ideal point source to the reflector surface and the field upon reflection. Initially they used electric and magnetic dipoles to feed the reflector, which created cross-polarised reflected field and surface currents. By exploiting the

symmetries of the cross-polarised components, they introduced a combination of orthogonal electric and magnetic dipoles (with the proper ratio) to suppress the cross-polarised field. The source that generate such fields is known as Huygens source and it follows the Ludwig-III definition of polarisation [32]. The analysis was focused on the aperture plane of the reflector probably due to the computation limitations to perform the far-field integrals. Only approximations for specific cases were provided for the far-fields.

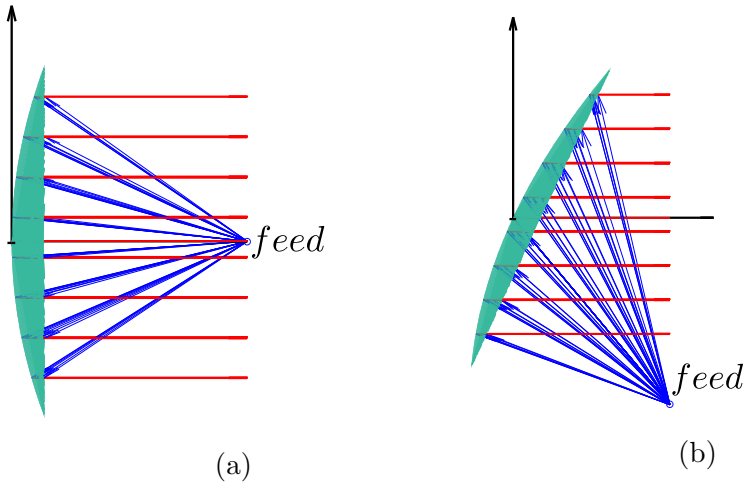

Figure 1.4: Parabolic reflector antenna: (a) front-fed and (b) offset configurations.

Following these analyses, it can be asserted that the front-fed configuration does not give rise to cross-polarised reflected field if a source free of cross-polarisation is used as feed. However, the feed and its supporting struts interfere with the energy path. This aperture blocking leads to scattering radiation which results in a degradation of the antenna performance [33]. This degradation comes in the form of cross-polarisation, higher sidelobes or gain loss. Dual reflector configurations, such as Cassegrain or Gregorian, can be introduced to increase the focal distance, and to allow the possibility to keep the feed electronics behind the dish [17].

In order to avoid the aperture blocking of front-fed configurations, offset configurations were introduced [7]. A basic example can be seen in Fig. 1.4b. They can be understood as the offset illuminated portion of a imaginary reflector with the feed placed at the focus. Therefore, the collimation properties are still maintained but the blocking is avoided.

However, the offset configuration gives rise to cross-polarised reflected field due to the introduced asymmetry. Consecuently, the study and accurate estimation of

this cross-polarisation is of high importance. A simple method to estimate the cross-polarised components in the aperture fields (reflected field) by stereographic mapping of the feed polarisation was presented in [34]. By using geometrical optics (GO), more detailed analysis to estimate the aperture fields and its transformation to far-field was presented in subsequent years [7,33,35,36]. The calculation of the far-field was performed by the integration of the aperture fields, a method usually known as aperture distribution or GO. This method has been known to give an incorrect description of the sidelobe levels and null positions [8]. Another method based on surface currents integration, usually known as current distribution or Physical Optics (PO), has demonstrated to give more accurate results [37]. In the case of circularly polarised feeds, offset reflector antennas are known to produce a beam squint in the far-field [7]. Closed and simple equations to predict it can be easily found [38, 39].

It has been demonstrated that the cross-polarisation in offset configurations can be reduced with large f/d ratios, where f represents the focal distance and d the reflector diameter [33]. Moreover, the more flexible designs that can be achieved by dual offset configurations can even suppress the cross-polarisation [33]. Matched feeds were also shown to be able to compensate the cross-polarisation of single offset reflectors [40].

1.2.3 Multi-beam reflector antennas

Even though some studies around reflectors fed by several feeds can be found in the literature from the 1970s [41, 42], the emergence in the 1990s of mobile and personal communication applications, Internet and direct-broadcast satellites produced a huge growth in the use of multi-beam reflector antennas [43]. Their high gain per beam and frequency re-use capabilities made them very convenient solutions to satisfy the demands on data-rate and capacity [24]. Multi-beam reflector antennas can be classified into two groups, depending on the feeding strategy: single-feed-per-beam (SFB) and multi-feed-per-beam (MFB) [1]. SFB advantages include the simplicity of the feeding system and improved performance [9]. However, several reflectors are needed to provide typical beam coverages since adjacent beams must be generated by different reflectors [24]. For example, four reflectors would be needed

to provide a four-colour frequency and polarisation reuse scheme [43]. MFB architectures are used to reduce the number of reflectors while providing the same beam coverage [1]. However, this reduction in the number of reflectors comes with the price of increased complexity in the feeding system due to the necessity of complex beam forming networks (BFN) to generate adjacent beams by a single reflector [44]. This complexity in the BFN and some radio-frequency (RF) performance degradation present serious disadvantages for MFB architectures [45–47].

The reduction in the number of reflectors while maintaining simplicity and good performance still remains a desired improvement for satellites communications [9]. The dual-gridded concept firstly introduced in the 1970s has received some attention to enable reflector reuse in SFB architectures, e.g. [10,48]. However, the polarisation selective properties of this technology are limited to operate in linear polarisation (LP). This presents a serious limitation as the current trend in satellite communications is to operate in circular polarisation (CP) [49]. Consequently, recent studies have focused on the development of FSSs in CP [50,51] or circular polarisation selective surfaces (CPSS) [52–55]. Nevertheless, these structures are still not sufficiently mature and are still limited in terms of RF performance as well as some mechanical complexities.

Recently a concept that hybridises optics in LP with reflection LP to CP polarisers has been proposed [9, 49, 56, 57]. Simulated and experimental results of antennas exploiting these polarisers have demonstrated promising performances [58]. However, the cross-polarised signal remains too high for practical applications, even if a unit-cell with good angular stability is used [58]. This is attributed to the use of uniform (fully periodic) array geometries, which do not account for the broad range of angles of incidence experienced by each unit-cell locally. Brute-force optimisation routines extensively used in reflectarray designs could be used to reduce the cross-polarisation [59, 60]. Nevertheless, these methods are computationally costly and may not provide the best results due to the large number of unknowns. Consequently, a reflection polariser optimised for cross-polarisation performance in a specific antenna architecture has yet to appear in the literature.

1.3 Scope of the thesis and survey of its contents

This thesis can be summarized in two scopes:

- Understanding the depolarisation properties of single reflector antennas.
- Methods for cross-polarisation reduction in linear-to-circular polarising offset reflectors with applications in multi-beam reflector antennas.

A brief literature review of the first scope can be found in Section 1.2.2. Some extra comments about depolarisation properties of reflector antennas can be found in very good books (or sections of them) [3,61–66]. However, as it was mentioned in Section 1.1, different authors used different notations and different ways of explaining the same concepts. Furthermore, not all the needed theory to have the complete grasp is available in each reference, since depending on the focus, each author preferred to review or not different parts of the theory. For this reason, Chapter 2 reviews the basic theory needed for the proper analysis of reflector antennas, starting with a review of the quasi-optical approximations to analyse the reflection properties of such large structures. These set of quasi-optical approximations are known as Geometrical Optics. The radiation characteristics of point sources (ideal feeds) and non-point sources (reflector) will be reviewed as well. Finally, the needed theory to analyse periodic structures (FSS and reflectarrays) using Floquet's Theorem will also be reviewed. Then, the depolarisation properties of single reflector antennas will be reviewed in Chapter 3, starting with the geometrical properties of parabolic reflectors, and the ideal sources commonly used to feed them. The depolarisation properties of single front-fed and offset reflectors will be studied for linearly and circularly polarised feeds both in terms of the aperture field and the far-field. These two chapters together have the aim of presenting the needed theory to understand and analyse the radiation and depolarisation properties of single reflector antennas, in a self-contained way.

Linear-to-circular polarising main reflectors were identified in Section 1.2.3 as a promising approach to maintain simple linearly polarised subsystems, i.e. single-feed-per-beam architectures and gridded subreflectors, in multi-beam antennas. Their main drawback lies in their cross-polarisation performance. Therefore, Chapter 4 presents an optimisation procedure to reduce the cross-polarisation of single offset

polarising reflectors fed by ideal (point) and practical (non-point) primary feeds. Similar optimisation procedures are applied to reflectarrays based on brute-force optimisation routines. However, the high number of unknowns in the optimisation process may not guaranty the best solution. Therefore, the optimisation procedure presented here is based on the theoretical insights gained by the previous chapters and exploits geometrical unit-cell optimisation and unit-cell rotation. Then, as a follow up, Chapter 5 presents an optimisation procedure based on unit-cell rotation to reduce the cross-polarisation of the same type of surface for multiple ideal feeds.

Finally, in Chapter 6 some conclusions of the work presented in this thesis will be summarised, as well as the possible future work that arises from it.

References

[1] S. K. Rao, "Advanced antenna technologies for satellite communications payloads," *IEEE Trans. Antennas Propag.*, vol. 63, no. 4, pp. 1205–1217, April 2015.

[2] Y. Rahmat-Samii and A. C. Densmore, "Technology trends and challenges of antennas for satellite communication systems," *IEEE Trans. Antennas Propag.*, vol. 63, no. 4, pp. 1191–1204, April 2015.

[3] Y. Rahmat-Samii, "Chapter 15 - Reflector Antennas," in *Antenna Engineering Handbook*, 4th ed. McGraw-Hill, 2007.

[4] S. Silver, *Microwave Antenna Theory and Design.* McGraw-Hill, 1949.

[5] E. M. T. Jones, "Parabolic reflector and hyperboloid lens antennas," *Trans. of the IRE Prof. Group on Antennas and Propag.*, vol. 2, no. 3, pp. 119–127, July 1954.

[6] I. Koffman, "Feed polarization for parallel currents in reflectors generated by conic sections," *IEEE Trans. Antennas Propag.*, vol. 20, no. 1, pp. 37–40, Jan 1966.

[7] T. S. Chu and R. H. Turrin, "Depolarization properties of offset reflector antennas," *IEEE Transactions on Antennas and Propagion*, vol. 21, no. 3, pp. 339–345, May 1973.

[8] Y. Rahmat-Samii, "A comparison between GO/aperture field and Physical-Optics methods for offset reflectors," *IEEE Trans. Antennas Propag.*, vol. 32, no. 53, pp. 301–306, Mar 1984.

[9] N. J. G. Fonseca and C. Mangenot, "High-performance electrically thin dual-band polarizing reflective surface for broadband satellite applications," *IEEE*

Trans. Antennas Propag., vol. 64, no. 2, pp. 640–649, Feb 2015.

[10] M. Baunge, H. Ekstrom, P. Ingvarson, and M. Peterson, "A new concept for dual gridded reflectors," *Proc. 4th Eur. Conf. Antennas Propag. (EuCAP'10)*, 2010.

[11] B. A. Munk, *Frequency Selective Surfaces: Theory and Design.* Wiley & Sons, 2000.

[12] J. Huang and J. A. Encinar, *Reflectarray Antennas.* Wiley & Sons, 2008.

[13] TICRA staff, *GRASP Technical Description, TICRA, Copenhagen, 2005-2008.*

[14] R. F. Harrington, *Field Computation by Moment of Methods.* IEEE Press, 1993.

[15] MATLAB® Toolbox [Online]. Available: https://uk.mathworks.com/products/matlab.html.

[16] CST Microwave Studio® [Online]. Available: https://www.cst.com/products/cstmws/.

[17] S. T. Sharma, S. Rao, and L. Shafai, *Handbook of Reflector Antennas and Feed Systems, vol. I: Theory and Design of Reflectors.* Artech House, 2013.

[18] Y. Rahmat-Samii and R. Haupt, "Reflector antenna developments: A perspective on the past, present, and future," *IEEE Antennas and Propag. Mag.*, vol. 57, no. 2, pp. 85–95, April 2015.

[19] G. Maral and M. Bousquet, *Satellite Communications Systems: Systems, Techniques and Technologies*, 5th ed. Wiley & Sons, 2009.

[20] A. B. Crawford, D. C. Hogg, and L. E. Hunt, "Project Echo - Horn-reflector antenna for space communication," NASA Technical Note D-1131, Tech. Rep., 1961.

[21] R. W. Gruner and W. J. English, "Antenna design studies for a U.S. domestic satellite," Comsat Tech. Rev., vol. 4, 2, pp. 413-447, Tech. Rep., 1974.

[22] P. Wood *et al.*, "Elliptical beam antenna for satellite applications," *Proc. Inst. Elec. Eng. Int. Conf. on Antennas for Aircraft and Spacecraft, London (UK)*, pp. 83–94, June 1975.

[23] B. S. Westcott, *Shaped Reflector Antenna Design.* Research Study Press, UK, 1983.

[24] S. T. Sharma, S. Rao, and L. Shafai, *Handbook of Reflector Antennas and Feed Systems, vol. III: Applications of Reflectors.* Artech House, 2013.

[25] J. Huang, "Microstrip reflectarray," *IEEE AP-S/URSI symposium*, pp. 612–615, June 1991.

[26] D. M. Pozar, S. D. Targonski, and R. Pokuls, "A shaped-beam microstrip patch reflectarray," *IEEE Trans. Antennas Propag.*, vol. 47, pp. 1167–1173, July 1999.

[27] J. C. Vardaxoglou, *Frequency Selective Surfaces: Analysis and Design.* Wiley & Sons, 1997.

[28] R. Mittra, C. H. Chan, and T. Cwik, "Techniques for analyzing frequency selective surfaces - a review," *Proceedings of the IEEE*, vol. 76, no. 12, pp. 1593–1615, Dec 1988.

[29] C. A. Balanis, *Antenna Theory: Analysis and Design*, 3rd ed. Wiley & Sons, 2015.

[30] C. C. Cutler, "Parabolic-antenna design for microwaves," vol. 35, no. 11, pp. 1284–1294, Nov 1947.

[31] M. Born and E. Wolf, *Principles of Optics*, 6th ed. Cambridge Uni. Press, 1998.

[32] A. C. Ludwig, "The definition of cross polarization," *IEEE Trans. Antennas Propag.*, vol. 21, no. 1, pp. 116–119, Jan 1973.

[33] A. W. Rudge and N. A. Adatia, "Offset-parabolic-reflector antennas: A review," *Proceedings of the IEEE*, vol. 66, no. 12, pp. 1592–1618, Dec 1978.

[34] J. D. Hanfling, "Aperture fields of paraboloidal reflectors by stereographic mapping of feed polarization," *IEEE Trans. Antennas Propag.*, vol. 18, no. 3, pp. 392–396, Sept 1969.

[35] J. Dijk, C. T. W. van Diepenbeek, E. J. Maanders, and L. F. G. Thurlings, "The polarization losses of offset paraboloid antennas," *IEEE Trans. Antennas Propag.*, vol. 22, no. 4, pp. 513–520, July 1974.

[36] J. Jacobsen, "On the cross polarization of asymmetric reflector antennas for satellite applications," *IEEE Trans. Antennas Propag.*, vol. 25, no. 2, pp. 276–283, Mar 1977.

[37] N. A. Adatia, "Cross-polarisation of reflector antennas," Ph.D. dissertation, Surrey University, England, UK, Dec 1974.

[38] N. A. Adatia and A. W. Rudge, "Beam-squint in circularly polarised offset reflector antennas," *Electr. Lett.*, vol. 11, no. 21, pp. 513–515, Oct 1975.

[39] D. W. Duan and Y. Rahmat-Samii, "Beam squint determination in conic-section reflector antennas with circularly polarized feeds," *IEEE Trans. Antennas Propag.*, vol. 39, no. 5, pp. 612–619, May 1991.

[40] A. W. Rudge and N. A. Adatia, "New class of primary-feed antennas for use with offset parabolic-reflector antennas," *Electronics Lett.*, vol. 11, no. 24, pp. 597–599, Nov 1975.

[41] A. W. Rudge, "Multiple-beam antennas: Offset reflectors with offset feeds," *IEEE Transactions on Antennas and Propagion*, vol. 23, no. 3, pp. 317–322, Nov 1975.

[42] A. W. Rudge and P. R. Foster, "Study of the performance and limitations of multiple-beam antennas," ERA, Rep. ESA Con. 2277/74HP, Tech. Rep., 1975.

[43] S. K. Rao, "Parametric design and analysis of multiple-beam reflector antennas for satellite communications," *IEEE Antennas Propag. Mag.*, vol. 45, no. 4, p. 2634, Aug 2003.

[44] B. Palacin *et al.*, "Multibeam antennas for very high throughput satellites in europe: technologies and trends," *Proc. 11th Eur. Conf. Antennas Propag. (EuCAP'17)*, p. 24132417, 2017.

[45] P. Bosshard *et al.*, "Thales alenia space hts/v-hts multiple beam antennas subsystems on the right track," *Proc. 10th Eur. Conf. Antennas Propag. (EuCAP'16)*, 2016.

[46] Y. Demers *et al.*, "Ka-band user antennas for vhts geo applications," *Proc. 11th Eur. Conf. Antennas Propag. (EuCAP'17)*, 2017.

[47] J. M. Montero, A. M. Ocampo, and N. J. G. Fonseca, "C-band multiple beam antennas for communication satellites," *IEEE Trans. Antennas Propag.*, vol. 63, no. 4, pp. 1263–1275, April 2015.

[48] E. K. Pfeiffer *et al.*, "Compact and stable earth deck multi-beam ka-band antenna structure and dual gridded reflector," *Proc. 5th Eur. Conf. Antennas Propag. (EuCAP'11)*, 2011.

[49] N. J. G. Fonseca and C. Mangenot, "Low-profile polarizing surface with dual-band operation in orthogonal polarizations for broadband satellite applications," *Proc. 8th Eur. Conf. Antennas Propag. (EuCAP'14)*, 2014.

[50] R. Orr *et al.*, "Circular polarization frequency selective surface operating in ku and ka band," *IEEE Trans. Antennas Propag.*, vol. 63, no. 11, pp. 5194–5197, Nov 2015.

[51] R. Orr, G. Goussetis, V. Fusco, and E. Sáenz, "Linear-to-circular polarization reflector with transmission band," *IEEE Trans. Antennas Propag.*, vol. 63, no. 5, pp. 1949–1956, May 2015.

[52] J. Sanz-Fernández, E. Sáenz, and P. de Maagt, "A circular polarization selective surface for space applications," *IEEE Trans. Antennas Propag.*, vol. 63, no. 6, pp. 2460–2470, June 2015.

[53] W. Tang *et al.*, "Coupled split-ring resonator circular polarization selective surface," *IEEE Trans. Antennas Propag.*, vol. 65, no. 9, pp. 4664–4675, Sept 2017.

[54] A. Ericsson and D. Sjoberg, "Design and analysis of a multilayer meander line circular polarization selective surface structure," *IEEE Trans. Antennas Propag.*, vol. 65, no. 8, pp. 4089–4101, Aug 2017.

[55] A. Ericsson, J. Lundgren, and D. Sjoberg, "Experimental characterization of circular polarization selective surface structures using linearly-polarized antennas," *IEEE Trans. Antennas Propag.*, vol. 65, no. 8, pp. 4239–4249, Aug 2017.

[56] M. Albani *et al.*, "Concepts for polarising sheets & "dual-gridded" reflectors for circular polarisation," *Proc. ICEComp*, 2010.

[57] W. Tang, S. Mercader-Pellicer, G. Goussetis, H. Legay, and N. J. G. Fonseca, "Low-profile compact dual-band unit cell for polarising surfaces operating in orthogonal polarizations," *IEEE Trans. Antennas Propag.*, vol. 65, no. 3, pp. 1472–1477, March 2017.

[58] W. Tang, D. Bresciani, H. Legay, G. Goussetis, and N. J. G. Fonseca, "Circularly polarised multiple beam antenna for satellite applications," *Proc. 11th Eur. Conf. Antennas Propag. (EuCAP'17)*, 2017.

[59] M. Zhou *et al.*, "The generalized direct optimization technique for printed reflectarrays," *IEEE Trans. Antennas Propag.*, vol. 62, no. 4, pp. 1690–1700, April 2014.

[60] D. R. Prado, D. Arrebola, M. R. Pino, and F. Las-Heras, "Efficient crosspolar optimization of shaped-beam dual-polarized reflectarrays using full-wave analysis for the antenna element characterization," *IEEE Trans. Antennas Propag.*, vol. 65, no. 2, pp. 623–635, Feb 2017.

[61] A. W. Rudge, A. W. Love, and A. D. Olver, *The Handbook of Antenna Design, Volume I.* Peter Peregrinus Ltd., 1982.

[62] R. S. Elliot, "Chapter 10 - Reflector and lenses," in *Antenna Theory and Design.* Wiley & Sons, 2003.

[63] Y. Rahmat-Samii, "Chapter 15 - Reflector Antennas," in *Antenna Handbook.* Van Nostrand Reinhold, 1993.

[64] P. J. Wood, *Reflector Antenna Analysis and Design.* Peter Peregrinus Ltd, 1980.

[65] C. J. Sletten, "Chapter 17 - Reflector Antennas," in *Antenna Theory.* McGraw-Hill, 1969.

[66] W. V. T. Rusch and P. D. Potter, *Analysis of Reflector Antennas.* Academic Press, Inc., 1970.

Chapter 2

Electromagnetic theory

2.1 Introduction

Analysing reflector antennas is a complex task that encompasses several sub-fields of applied electrodynamics. As it was mentioned in Chapter 1, a source whose fields are known is placed at the focus of the reflector. The most basic type of sources to feed reflectors are point sources, where far-field approximations are usually taken into account. Therefore, common antenna theory is needed for the modelling of these sources [1, 2].

Since the dimensions of common reflectors are far greater than the wavelength, optical approximations, known as Geometrical Optics, can be applied to analyse how the reflector affects the incident field [3, 4]. This method discretises the field emanating from the feed and, by ray tracing techniques, follows it up to the reflector surface where the reflected field or the surface currents can be easily computed. Diffraction effects can also be included at the rims of the reflector or at the struts [5–7]. The reflector itself can be seen as a non-point (distributed) source. Therefore, common antenna theory can be used to obtain the far-field of the whole reflector antenna.

Furthermore, the performance of the reflector can be engineered by replacing the metallic reflector by a Frequency Selective Surface (FSS) [8]. The curvature of the reflector can also be suppressed while maintaining the gain by the proper design of each unit-cell of a planar FSS, giving rise to a reflectarray [9]. Floquet's Theorem

is the most common way to analyse the unit-cells of these structures. Also, local or global optimisation routines are needed for the proper design and tuning of each unit-cell [10, 11].

In this chapter the aforementioned electromagnetic theory will be reviewed to provide the background needed for the analysis and design of reflector antennas and FSSs. Maxwell's Equations and the wave equation are the starting point, reviewed in Section 2.2. Following on from these, the three theoretical pillars of this thesis will be reviewed: Geometrical Optics in Section 2.3, radiation characteristics of antennas using vector potential functions in Section 2.4, and analysis of 2D periodic structures using Floquet's Theorem in Section 2.5.

2.2 Maxwell's equations and the wave equation

Maxwell's equations are a set of four equations describing the relations and variations of electric and magnetic fields, given a set of known sources (charges and currents). These relations can be known over a region of space (integral form) or at a specific point in space at any time (differential form). Throughout this thesis only the fields at a specific point are of interest. Therefore only the differential form will be used, supposing that the field vectors are continuous functions and their derivatives are also continuous.

2.2.1 Time-varying electromagnetic fields

Maxwell's equations may be written in their differential form as[1]

$$\nabla \times \vec{\mathscr{H}} = \vec{\mathscr{J}} + \frac{\partial \vec{\mathscr{D}}}{\partial t} \qquad Ampère's\ Law \qquad (2.2.1a)$$

$$\nabla \times \vec{\mathscr{E}} = -\frac{\partial \vec{\mathscr{B}}}{\partial t} \qquad Faraday's\ Law \qquad (2.2.1b)$$

$$\nabla \cdot \vec{\mathscr{B}} = 0 \qquad Gauss'\ Law\ for\ magnetic\ fields \qquad (2.2.1c)$$

[1]The Ampère's Law presented here is the one with Maxwell's correction, the original being $\nabla \times \vec{\mathscr{H}} = \vec{\mathscr{J}}$

$$\nabla \cdot \vec{\mathscr{D}} = \rho_e \qquad Gauss' \, Law \, for \, electric \, fields \qquad (2.2.1d)$$

where $\vec{\mathscr{D}} = \epsilon\vec{\mathscr{E}}$ and $\vec{\mathscr{B}} = \mu\vec{\mathscr{H}}$, and where the different vectors and scalars are

- $\vec{\mathscr{H}}$: magnetic field intensity vector (A/m)
- $\vec{\mathscr{E}}$: electric field intensity vector (V/m)
- $\vec{\mathscr{J}}$: electric current density vector (A/m^2)
- $\vec{\mathscr{D}}$: electric flux density vector (C/m^2)
- $\vec{\mathscr{B}}$: magnetic flux density vector (Wb/m^2)
- ρ_e: electric charge density (C/m^3)
- ϵ: permittivity of the material (F/m)
- μ: permeability of the material (H/m)

In the absence of currents and charges, $\vec{\mathscr{J}} = 0$ and $\rho_e = 0$. The parameters ϵ and μ are scalar functions since an isotropic inhomogeneous medium is initially considered. With these assumptions, the curl of Eq.2.2.1b and the time derivative of Eq.2.2.1a can be taken

$$\nabla \times \left(\frac{1}{\mu}\nabla \times \vec{\mathscr{E}}\right) = -\nabla \times \frac{\partial \vec{\mathscr{H}}}{\partial t} \qquad (2.2.2a)$$

$$\frac{\partial}{\partial t}(\nabla \times \vec{\mathscr{H}}) = \epsilon\frac{\partial^2 \vec{\mathscr{E}}}{\partial t^2} \qquad (2.2.2b)$$

Combining Eq.2.2.2a and 2.2.2b yields

$$\nabla \times \left(\frac{1}{\mu}\nabla \times \vec{\mathscr{E}}\right) + \epsilon\frac{\partial^2 \vec{\mathscr{E}}}{\partial t^2} = 0 \qquad (2.2.3)$$

It is possible to expand the curl using the relations A.0.4 and A.0.3 described in Appendix A [2]

$$\nabla^2\vec{\mathscr{E}} - \nabla(\nabla \cdot \vec{\mathscr{E}}) + \nabla \ln\mu \times (\nabla \times \vec{\mathscr{E}}) - \epsilon\mu\frac{\partial^2 \vec{\mathscr{E}}}{\partial t^2} = 0 \qquad (2.2.4)$$

[2]The next relation has been used: $-f\nabla\frac{1}{f} = \frac{\nabla f}{f} = \nabla \ln f$

Relation A.0.5 can be applied to Eq.2.2.1d (with $\rho_e = 0$) as

$$\epsilon \nabla \vec{\mathscr{E}} = -\vec{\mathscr{E}} \cdot \nabla \epsilon \tag{2.2.5}$$

If this Eq.2.2.5 is substituted into Eq.2.2.4 and the same analysis is applied to the magnetic field, one reaches

$$\nabla^2 \vec{\mathscr{E}} - \epsilon\mu \frac{\partial^2 \vec{\mathscr{E}}}{\partial t^2} + \nabla \ln \mu \times (\nabla \times \vec{\mathscr{E}}) + \nabla(\vec{\mathscr{E}} \cdot \nabla \ln \epsilon) = 0 \tag{2.2.6a}$$

$$\nabla^2 \vec{\mathscr{H}} - \epsilon\mu \frac{\partial^2 \vec{\mathscr{H}}}{\partial t^2} + \nabla \ln \epsilon \times (\nabla \times \vec{\mathscr{H}}) + \nabla(\vec{\mathscr{H}} \cdot \nabla \ln \mu) = 0 \tag{2.2.6b}$$

Eq.2.2.6a and Eq.2.2.6b are known as the *wave equation* for electric and magnetic fields in inhomogeneous media for the electric and magnetic fields, respectively. They are differential equations which both electric and magnetic field intensity vectors must fulfil. If the medium is homogeneous, ϵ and μ are constants, and Eq.2.2.6a and Eq.2.2.6b are reduced to

$$\nabla^2 \vec{\mathscr{E}} - \epsilon\mu \frac{\partial^2 \vec{\mathscr{E}}}{\partial t^2} = 0 \tag{2.2.7a}$$

$$\nabla^2 \vec{\mathscr{H}} - \epsilon\mu \frac{\partial^2 \vec{\mathscr{H}}}{\partial t^2} = 0 \tag{2.2.7b}$$

Eq.2.2.7a and Eq.2.2.7b are thus known as the *wave equation* for the electric or the magnetic fields in homogeneous media.

2.2.2 Time-harmonic electromagnetic fields

In many electromagnetic applications is common to assume a harmonic time dependence of the electric and magnetic field intensities $\vec{\mathscr{E}}$ and $\vec{\mathscr{H}}$, in the form

$$\vec{\mathscr{E}}(\vec{r}, t) = \mathscr{R}e\{\vec{E}(\vec{r}) e^{\pm j\omega t}\} \tag{2.2.8a}$$

$$\vec{\mathscr{H}}(\vec{r}, t) = \mathscr{R}e\{\vec{H}(\vec{r}) e^{\pm j\omega t}\} \tag{2.2.8b}$$

where $\vec{E}$ is a complex vector function of the position vector $\vec{r}$ and $\omega = 2\pi f_0$ is the angular frequency. These time-harmonic relations can be introduced into Maxwell's equations, assuming a region free of currents and charges, yielding

$$\nabla \times \vec{H} = j\omega\epsilon\vec{E} \tag{2.2.9a}$$

$$\nabla \times \vec{E} = -j\omega\mu\vec{H} \tag{2.2.9b}$$

$$\nabla \cdot \epsilon\vec{E} = 0 \tag{2.2.9c}$$

$$\nabla \cdot \mu\vec{H} = 0 \tag{2.2.9d}$$

which are known as Maxwell's equations for time-harmonic fields. The term $e^{j\omega t}$ was used instead of $e^{-j\omega t}$, and it has been omitted for clarity. Eq.2.2.8a and Eq.2.2.8b can be also introduced into the wave equation for inhomogeneous media (Eq.2.2.6a and Eq.2.2.6b), yielding

$$\nabla^2\vec{E} + k^2n^2\vec{E} + \nabla \ln\mu \times (\nabla \times \vec{E}) + \nabla(\vec{E} \cdot \nabla \ln\epsilon) = 0 \tag{2.2.10a}$$

$$\nabla^2\vec{H} + k^2n^2\vec{H} + \nabla \ln\epsilon \times (\nabla \times \vec{H}) + \nabla(\vec{H} \cdot \nabla \ln\mu) = 0 \tag{2.2.10b}$$

where the following relation has been used

$$\omega^2\mu\epsilon = k^2n^2$$

and where $k = \omega/c = 2\pi/\lambda_0$ is the wavenumber, λ_0 is the vacuum wavelength and

$$n(\vec{r}) = \sqrt{\frac{\mu(\vec{r})\epsilon(\vec{r})}{\mu_0\epsilon_0}} \tag{2.2.11}$$

In Eq.2.2.11 n represents the *refractive index*, and μ_0 and ϵ_0 represent the vacuum permeability and vacuum permittivity, respectively.

As before, if the medium is supposed homogeneous Eq.2.2.10a and Eq.2.2.10b can be simplified to

$$\nabla^2 \vec{E} + k^2 n^2 \vec{E} = 0 \tag{2.2.12a}$$

$$\nabla^2 \vec{H} + k^2 n^2 \vec{H} = 0 \tag{2.2.12b}$$

If waves propagate through vacuum, where $n = 1$, then

$$\nabla^2 \vec{E} + k^2 \vec{E} = 0 \tag{2.2.13a}$$

$$\nabla^2 \vec{H} + k^2 \vec{H} = 0 \tag{2.2.13b}$$

2.3 Geometrical Optics

As mentioned in the introduction to the chapter, it is common to use optical approximation techniques such as *Geometrical Optics* or *GO* for the analysis of reflector antennas. The dimensions of common reflectors are far greater than the wavelength [4], which makes possible to neglect the wavelength in the equations. With this approximation, waves can be viewed as rays and optical geometry can be applied [3].

In order to obtain a more precise analysis it is also possible to add diffraction analysis (geometrical and physical theories of diffraction) for the rims of the reflectors and other possible edges or corners from the mounting struts of the feed [6, 12]. However it is noted that the truncation of the radiation integrals at the rims of the reflector often leads to reasonably accurate results even without considering the edge diffraction. It is further noted that, particularly for antenna architectures where blockage from the feed and the struts is low, these effects can be neglected in the first design and only considered in the final tuning simulations. This applies e.g. for offset antenna architectures, both in single or double configurations.

GO was fully detailed in 1959 by Max Born and Emil Wolf in their book "*Principles of Optics*" [3]. In it, they start the analysis with Maxwell's equations in

inhomogeneous media for optic frequencies by neglecting the wavelength. From this assumption they obtain the *Eikonal equation*, a partial differential equation that provides information about the medium and how the energy propagates. It follows from this analysis that energy propagation can be approximated by rays, whose direction of propagation is orthogonal to the electric and magnetic fields since they are transverse electromagnetic (TEM) waves [13]. Following Fermat's principle [14], it is deduced that a ray's trajectory is the shortest among other possible trajectories. For a homogeneous medium, the ray's trajectory will therefore be a straight line.

In the analysis of reflector antennas, GO is commonly used to trace the rays from the feed to the reflector surface. It also predicts how the rays are reflected onto the surface, and follows their trajectories to the *aperture plane*. The aperture plane is an imaginary plane usually placed at the same distance from the reflector as the feed. This aperture is assumed to be an aperture antenna with associated electric and magnetic currents following Love's Principle of equivalence [2]. By performing an inverse Fourier transform of the fields at this aperture, the fields at the far-field of the reflector antenna are obtained. This way to obtain the far-field of a reflector antenna is known as the *aperture distribution method*.

GO is suitable when the wavelength is small compared with the interacting structure's size, but it does not takes into account diffraction effects or interference. Diffraction was introduced as a complement of GO in 1962 by Joseph B. Keller in his paper "*Geometrical Theory of Diffraction*" [6] or GTD. GTD describes more accurately the electromagnetic phenomena associated with a ray hitting a surface edge, corner or vertice of boundary surfaces. The complete fields can then be obtained considering interference of waves associated with edge diffraction and surface reflection according to the Huygens-Fresnel principle. GTD was extend in 1974 by Robert G. Kouyoumjian and Prabhakar H. Pathak in "*A Uniform Geometrical Theory of Diffraction for an Edge in a Perfectly Conducting Surface*" [7], also known as UTD. GTD mainly affects the secondary lobes of the secondary radiation pattern and its effects become less important with the increase of the electrical dimensions of the reflector.

Since the reflector is supposed a perfect electric conductor, the electric surface currents can be easily obtained from the magnetic field incident to or reflected from the surface [15]. These surface currents can be integrated over the reflector surface

to obtain the far-field of the reflector antenna. This way of obtaining the far-field is known as the *current distribution method* [16]. Diffraction effects were also included to the current distribution method in the *Physical Theory of Diffraction* or PTD [12].

The aperture distribution method performs a surface integral over the reflector 2D aperture, while the current distribution method performs a surface integral over the reflector 3D surface. Therefore, it can be deduced that the latter is more accurate but more computationally expensive than the former since it performs a 3D integral, or, as Victor Galindo-Israel and Raj Mittra proved in [17], a summation of Fourier transforms.

In this section, a review of Geometrical Optics is provided, starting with the derivation of its most important equation: the Eikonal equation. The properties of the field under this approximation will then be stated, along with the relations for amplitude, phase and polarisation.

2.3.1 The Eikonal Equation

For large distances with respect to the wavelength, it is common to introduce a constant-phase surface to the field intensities [3]

$$\vec{E}(\vec{r}) = \vec{E}_0(\vec{r})e^{-jk\psi(\vec{r})} \tag{2.3.1a}$$

$$\vec{H}(\vec{r}) = \vec{H}_0(\vec{r})e^{-jk\psi(\vec{r})} \tag{2.3.1b}$$

where $\vec{E}_0$ and $\vec{H}_0$ are vectors function of the position vector. They can be complex if the field is circularly polarised. The real scalar ψ function of the position vector represents the optical path or phase. This scalar defines the equiphase surfaces [4], which depending on the coordinate system can represent the planes, spheres or cylinders with the same phase. It is expressed in units of distance.

If Eq.2.3.1a and Eq.2.3.1b are introduced into Eq.2.2.9a-2.2.9d, after some algebraic operations and assuming $1/k \simeq 0$ (only if the multiplicand is not very large [4]) it

is possible to yield to

$$\nabla\psi \times \vec{H}_0 + \frac{\omega\epsilon}{k}\vec{E}_0 = 0 \tag{2.3.2a}$$

$$\nabla\psi \times \vec{E}_0 - \frac{\omega\mu}{k}\vec{H}_0 = 0 \tag{2.3.2b}$$

$$\vec{H}_0 \cdot \nabla\psi = 0 \tag{2.3.2c}$$

$$\vec{E}_0 \cdot \nabla\psi = 0 \tag{2.3.2d}$$

Substituting Eq.2.3.2b into Eq.2.3.2a or vice versa gives

$$\nabla\psi \times (\nabla\psi \times \vec{E}_0) + n^2\vec{E}_0 = 0 \tag{2.3.3a}$$

$$\nabla\psi \times (\nabla\psi \times \vec{H}_0) + n^2\vec{H}_0 = 0 \tag{2.3.3b}$$

Expanding (using relation A.0.6 from Appendix A) either Eq.2.3.3a or Eq.2.3.3b and substituting Eq.2.3.2c and Eq.2.3.2d yields

$$-|\nabla\psi|^2\vec{E}_0 + n^2\vec{E}_0 = 0 \tag{2.3.4}$$

From this last equation, it follows

$$|\nabla\psi|^2 = \left(\frac{\partial\psi}{\partial x}\right)^2 + \left(\frac{\partial\psi}{\partial y}\right)^2 + \left(\frac{\partial\psi}{\partial z}\right)^2 = n^2(x,y,z) \tag{2.3.5}$$

if a Cartesian coordinate system is chosen. This is the basic equation of GO and is known as the *eikonal equation*, where ψ is usually referred as the *eikonal function*. For a homogeneous medium with a constant n, the right hand side of the eikonal equation is constant and therefore at a fixed distance from the origin r_0 all rays share the same wavefront surface ψ_0, as Fig.2.1 shows.

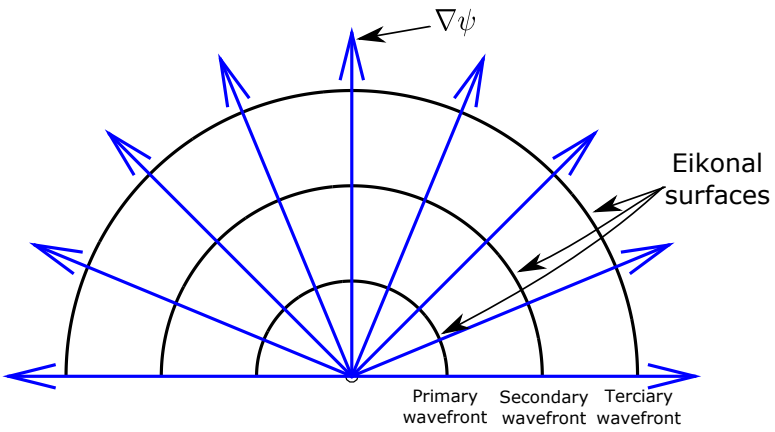

Figure 2.1: Eikonal surfaces.

Considering the definition of the gradient, it can be asserted that $\nabla\psi$ expresses the increment with respect to the space coordinates experienced by the ray (in a vector form), i.e., $\nabla\psi$ points to the direction of propagation of the ray, with unit vector

$$\hat{s} = \frac{\nabla\psi}{|\nabla\psi|} = \frac{\nabla\psi}{n} \tag{2.3.6}$$

The eikonal function therefore defines an equiphase surface and is also known as *eikonal surface* or geometrical wavefront, which is always normal to the direction of propagation regardless of the wave definition, whether it be a plane, cylindrical or spherical wave. The eikonal equation can also be derived from the wave equation for inhomogeneous media. Substituting Eq.2.3.1a or Eq.2.3.1b into Eq.2.2.10a or Eq.2.2.10b respectively, yields

$$\vec{K}(\vec{E}_0, \psi, n) + \frac{1}{jk}\vec{L}(\vec{E}_0, \psi, n, \mu) + \frac{1}{(jk)^2}\vec{M}(\vec{E}_0, \epsilon, \mu) = 0 \tag{2.3.7a}$$

$$\vec{K}(\vec{H}_0, \psi, n) + \frac{1}{jk}\vec{L}(\vec{H}_0, \psi, n, \epsilon) + \frac{1}{(jk)^2}\vec{M}(\vec{H}_0, \mu, \epsilon) = 0 \tag{2.3.7b}$$

where for the electric field

$$\vec{K}(\vec{E}_0, \psi, n) = (|\nabla\psi|^2 - n^2)\vec{E}_0 \tag{2.3.8a}$$

$$\vec{L}(\vec{E}_0,\psi,n,\mu) =(\nabla\psi\cdot\nabla\ln\mu-\nabla^2\psi)\vec{E}_0-2(\vec{E}_0\cdot\nabla\ln n)\nabla\psi - 2(\nabla\psi\cdot\nabla)\vec{E}_0 \tag{2.3.8b}$$

$$\vec{M}(\vec{E}_0,\epsilon,\mu) = -(\nabla\times\vec{E}_0)\times\nabla\ln\mu+\nabla^2\vec{E}_0+\nabla(\vec{E}_0\cdot\nabla\ln\epsilon) \tag{2.3.8c}$$

and for the magnetic field

$$\vec{K}(\vec{H}_0,\psi,n) = (|\nabla\psi|^2-n^2)\vec{H}_0 \tag{2.3.9a}$$

$$\vec{L}(\vec{H}_0,\psi,n,\epsilon) =(\nabla\psi\cdot\nabla\ln\epsilon-\nabla^2\psi)\vec{H}_0-2(\vec{H}_0\cdot\nabla\ln n)\nabla\psi - 2(\nabla\psi\cdot\nabla)\vec{H}_0 \tag{2.3.9b}$$

$$\vec{M}(\vec{H}_0,\mu,\epsilon) = -(\nabla\times\vec{H}_0)\times\nabla\ln\epsilon+\nabla^2\vec{H}_0+\nabla(\vec{H}_0\cdot\nabla\ln\mu) \tag{2.3.9c}$$

For large k, as it is supposed in the geometrical optics analysis, $\vec{L}$ and $\vec{M}$ can be neglected and the eikonal equation is obtained from the remaining $\vec{K}=0$.

2.3.2 Properties of the geometric field

From the eikonal equation and the relations described by Eq.2.3.2a, Eq.2.3.2b, Eq.2.3.2c and Eq.2.3.2d, it is possible to deduce some important properties [3, 4]:

1) The electric and magnetic fields lie in the same plane that the eikonal surface. The electric and magnetic fields are therefore transversal to the direction of propagation (TEM).

The gradient of the eikonal function $\nabla\psi$ is perpendicular to $\vec{E}_0$ and $\vec{H}_0$, as shown in Eq. 2.3.2c and 2.3.2d, and they are also perpendicular to each other. Therefore, $\vec{E}_0$ and $\vec{H}_0$ lie on the equiphase surface plane, with the eikonal surface ψ being a constant, as Fig. 2.1 shows.

2) The time-average electric and magnetic energy densities are equal.

Using the scalar triple product identity A.0.7 from Appendix A,

$$W_e = \frac{\epsilon}{4}\vec{E}_0 \cdot \vec{E}_0^* = \frac{1}{4c}\vec{E}_0 \cdot (-\nabla\psi \times \vec{H}_0^*) = \frac{1}{4c}\vec{E}_0 \cdot (\vec{H}_0^* \times \nabla\psi) \tag{2.3.10a}$$

$$W_m = \frac{\mu}{4}\vec{H}_0 \cdot \vec{H}_0^* = \frac{1}{4c}\vec{H}_0^* \cdot (\nabla\psi \times \vec{E}_0) = \frac{1}{4c}(\vec{H}_0^* \times \nabla\psi) \cdot \vec{E}_0 \tag{2.3.10b}$$

where $c = 1/\sqrt{\mu_0\epsilon_0}$ represents the speed of light in the vacuum, and where Eq. 2.3.2a and 2.3.2b have been applied. Therefore they are equal and $W_t = 2W_e = 2W_m$, since $W_t = W_e + W_m$.

3) The time-average Poynting vector is normal to the wavefront, and its magnitude is equal to the product of the time-average energy density with the propagation velocity.

Using the vector triple product identity A.0.6 from Appendix A and Eq.2.3.10a or Eq.2.3.10b it is possible to yield

$$\begin{aligned}\mathscr{P} &= \frac{1}{2}\mathscr{R}e\{\vec{E}_0 \times \vec{H}_0^*\} = \frac{1}{2c\mu}\mathscr{R}e\{\vec{E}_0 \times (\nabla\psi \times \vec{E}_0^*)\} = \frac{1}{2c\mu}(\vec{E}_0 \cdot \vec{E}_0^*)\nabla\psi \\ &= \frac{1}{2c^2\mu\epsilon}\vec{E}_0 \cdot (\vec{H}_0^* \times \nabla\psi)\nabla\psi = \frac{2c}{n^2}W_e\nabla\psi = \frac{c}{n^2}W_t\nabla\psi\end{aligned} \tag{2.3.11}$$

Introducing the unit vector from Eq.2.3.6 into Eq.2.3.11 yields

$$\mathscr{P} = \frac{c}{n}W_t\hat{s} = v_p W_t\hat{s} \tag{2.3.12}$$

where $v_p = c/n$ is the propagation velocity of the wave. An interpretation of this equation is that the time-average energy of the GO field is transported with velocity $v_p = c/n$ in the direction of $\hat{s}$ (direction of propagation), perpendicular to the wave fronts [18].

4) The geometrical rays are the family of curves perpendicular to the wavefronts $\psi = constants$**. If** $n = constant$ **(homogeneous medium), the**

rays are straight lines.

The position vector of a point P on a ray is given by $\vec{r}(s)$, with s being the distance along the ray. Therefore, $d\vec{r}(s)/ds = \hat{s}$ and using Eq.2.3.6, the equation of a ray can be expressed as

$$n(s)\frac{d\vec{r}(s)}{ds} = \nabla\psi(s) \tag{2.3.13}$$

Taking the derivative with respect to s at both sides, knowing that $\frac{d}{ds} = \frac{d\vec{r}(s)}{ds} \cdot \nabla$ [3] yields

$$\begin{aligned}\frac{d}{ds}n(s)\left(\frac{d\vec{r}(s)}{ds}\right) &= \frac{d}{ds}\nabla\psi(s) = \left(\frac{d\vec{r}(s)}{ds}\cdot\nabla\right)\nabla\psi(s) \\ &= \frac{1}{n}(\nabla\psi(s)\cdot\nabla)\nabla\psi(s) = \frac{1}{2n}\nabla|\nabla\psi(s)|^2 = \frac{1}{2n}\nabla n^2(s)\end{aligned} \tag{2.3.14}$$

Knowing that $\nabla n^2 = 2n\nabla n$, the last equation reduces to

$$\frac{d}{ds}\left(n(s)\frac{d\vec{r}(s)}{ds}\right) = \nabla(n(s)) \tag{2.3.15}$$

Eq.2.3.15 is particularly useful since it presents the differential equation that defines a ray involving only the refractive index. If the medium is homogeneous, $\nabla(n(s)) = 0$. To fulfil this condition the term $\frac{d\vec{r}(s)}{ds}$ in the left side must be a constant. Therefore the second derivative of $\vec{r}(s)$ is 0. In conclusion, for a homogeneous medium $\vec{r}(s)$ is a straight line, i.e., for a homogeneous medium all rays are straight lines.

An increase in the wavefront with respect to the distance along the ray can be viewed as an increase in the position along the ray multiplied by the gradient of the wavefront, which must be equal to the refractive index on that point

$$\frac{d\psi(s)}{ds} = \frac{d\vec{r}(s)}{ds}\cdot\nabla\psi(s) = n(s) \tag{2.3.16}$$

It can be seen from Eq.2.3.16 that the infinitesimal displacement ds is inversely proportional to n, and therefore directly proportional to the propagation velocity v_p.

[3] For $\nabla(\vec{A}\cdot\vec{B})$, a special case arises when $\vec{A} = \vec{B} \rightarrow \nabla(\vec{A}\cdot\vec{A}) = 2(\vec{A}\cdot\nabla)\vec{A} + 2\vec{A}\times(\nabla\times\vec{A})$. If $\vec{A} = \nabla\psi$ the second term at the right is 0 so $(\vec{A}\cdot\nabla)\vec{A} = \frac{1}{2}\nabla(\vec{A}\cdot\vec{A})$.

5) The optical length of a ray τ that joins two points P_1 and P_2 is equal to the product of c and the time required for light to travel from P_1 to P_2, fulfilling Fermat's principle of least time.

The *Fermat's principle* or *principle of least time* states that the path taken for the energy to travel between two points P_1 and P_2, termed the optical length, is the one that can be traversed in the least time, i.e., the one that gives the minimum value for the integral [4]

$$\tau = \int_{P_1}^{P_2} n(s)ds = \int_{P_1}^{P_2} \frac{d\psi(s)}{ds} ds = \psi(P_2) - \psi(P_1) \tag{2.3.18}$$

with τ being the optical length. Since the time-average energy densities travel at the propagation velocity $v_p(s) = c/n(s)$ it is possible to relate v_p with the infinitesimal displacements ds and the infinitesimal time to travel it, dt, as $v_p(s) = ds/dt$.Therefore

$$n(s)ds = \frac{c}{v_p(s)} ds = cdt$$

And finally

$$\tau = c \int_{P_1}^{P_2} dt \tag{2.3.19}$$

Another consequence of Fermat's principle is Snell's law of reflection (also refraction), illustrated in Fig.2.2, where two possible paths to go from P to Q are drawn. The first one has already been discussed for a homogeneous medium: the straight line. The second includes a reflection in a perfect electric conductor (PEC) wall. By Fermat's principle, the correct path would be the shorter one. This is obtained by

[4]This statement is not general. In modern physics, the principle states that "*light takes a path such that there are many other paths nearby which take almost exactly the same time*" [14]. The energy (light) will take the path that fulfil

$$\delta \int_{P_1}^{P_2} n(s)ds = 0 \tag{2.3.17}$$

which means that the time to travel from one point to the other is stationary with respect to small deformations in the path, implying a minimum. Hence, the shortest path.

equating the derivative of the total path (after and before reflection) to 0, yielding $\sin\theta_i = \sin\theta_r$, i.e., $\theta_i = \theta_r$.

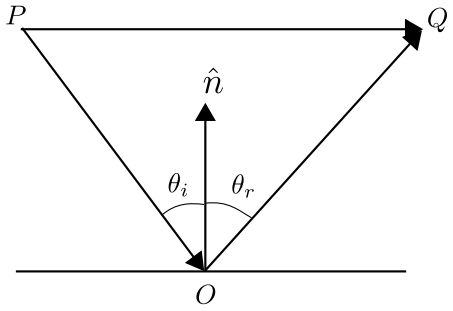

Figure 2.2: Fermat's principle for a homogeneous medium.

Since the wavelength tends to 0 in accordance with the GO approximation, for the incoming wave, the radii of curvature is close to infinite. Thus, even if the reflector is curved, it can be supposed to be locally planar and Snell's law is again valid.

6) The phase delay along a ray from a point P_1 to a point P_2 can be expressed as the optical length multiplied by the wavenumber.

By definition, the phase delay is

$$\Phi = \omega T \tag{2.3.20}$$

where $\omega = kc$. Expanding T as

$$T = \int dt = \int_{P_1}^{P_2} \frac{ds}{v_p(s)} = \int_{P_1}^{P_2} \frac{n(s)ds}{c} = \frac{\tau}{c} \tag{2.3.21}$$

where τ represents the optical length and was defined in Eq. 2.3.19. Finally, substituting Eq.2.3.21 into Eq.2.3.20 yields

$$\Phi = k\tau \tag{2.3.22}$$

7) The *intensity law of Geometrical Optics* states that in a lossless media, the radiation density at the different transverse cross-sectional areas associated with the same solid angle along a tube of rays must remain constant.

The radiation density at the transverse cross-sectional area of a specific point along the tube of rays has to be the same as the radiation density at the transverse cross-sectional area of another point, as Fig. 2.3 from [5] shows, fulfilling the conservation of energy

$$W_{rad}^{0} dA_0 = W_{rad} dA \tag{2.3.23}$$

where W_{rad}^{i} is the radiation density and dA_i the differential surface area at a specific point i.

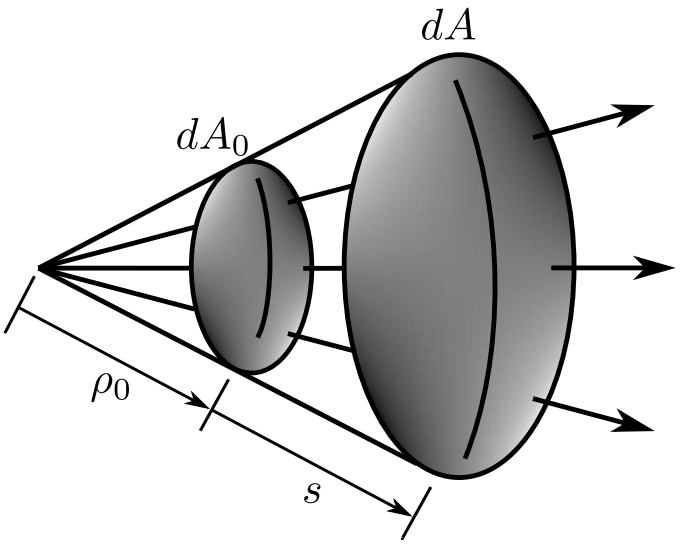

Figure 2.3: Tube of rays for a spherical wave [5].

Amplitude relation

From property 7) of Section 2.3.2 it is possible to obtain information about the amplitude of the wave [5]. The radiation density is related with the far-field electric field by [1]

$$W_{rad} = \frac{1}{2\eta}|\vec{E}(\rho,\theta,\phi)|^2 = \frac{1}{2\eta}(|E_\theta(\theta,\phi)|^2 + |E_\phi(\theta,\phi)|^2) \tag{2.3.24}$$

where $\eta = \sqrt{\mu/\epsilon}$ is the intrinsic impedance of the medium. Another way to express Eq.2.3.23 with respect to Fig. 2.3 is

$$\frac{W_{rad}(s)}{W_{rad}^{0}(0)} = \frac{dA_0}{dA} \tag{2.3.25}$$

It is possible to write the differential surface areas dA_0 and dA in terms of their radii using the area of the sphere and Fig. 2.3

$$dA_0 = 4\pi \frac{R_0^2}{C_0} = \frac{4\pi}{C_0}\rho_0^2 \tag{2.3.26a}$$

$$dA = 4\pi \frac{R_1^2}{C_0} = \frac{4\pi}{C_0}(\rho_0 + s)^2 \tag{2.3.26b}$$

where C_0 is a proportionality constant to include only the portion of interest. If Eq.2.3.24 as function of the radii is introduced into Eq.2.3.25 then the relation between the amplitudes and the radii is obtained

$$\frac{|\vec{E}(s)|}{|\vec{E}(0)|} = \frac{R_0}{R_1} = \frac{\rho_0}{\rho_0 + s} \tag{2.3.27}$$

being $\vec{E}(s)$ the electric field at s and $\vec{E}(0)$ the electric field at $s = 0$. This relation was obtained for spherical waves. However, a more general expression can be obtained from Fig.2.4.

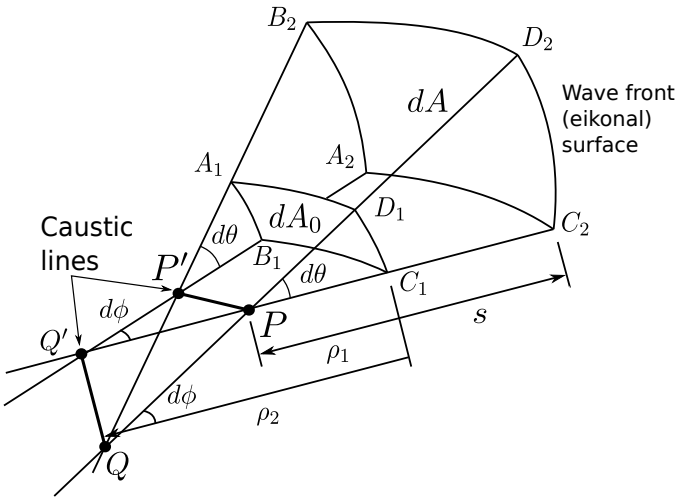

Figure 2.4: Astigmatic tube of rays: eikonal surfaces and caustic lines.

The lines QQ' and PP' in Fig.2.4 are caustic lines [5]. The following relation can be established between the segments that define the eikonal surface and the radii of

[5] Where the definition of caustic was taken from [5]: "*point, line or surface through which all the rays of a wave pass*". *Astigmatic* lines are lines which do not meet in a single point.

curvature

$$A_1B_1 = \rho_1 d\theta$$

$$B_1C_1 = \rho_2 d\phi$$

From these relations, the differential surface areas can be expressed as

$$dA_0 = A_1B_1 \cdot B_1C_1 = \rho_1\rho_2 d\theta d\phi \tag{2.3.29a}$$

$$dA = A_2B_2 \cdot B_2C_2 = (\rho_1 + s)(\rho_2 + s)d\theta d\phi \tag{2.3.29b}$$

Entering Eq.2.3.29a and Eq.2.3.29b into Eq.2.3.25 function of the electric field amplitudes yields

$$\frac{|\vec{E}(s)|}{|\vec{E}_0|} = \sqrt{\frac{dA_0}{dA}} = \sqrt{\frac{\rho_1\rho_2}{(\rho_1 + s)(\rho_2 + s)}} \tag{2.3.30}$$

The general relation Eq.2.3.30 relates the electric field magnitudes of two wavefront surfaces, and from it, different relations can be obtained for different wavefront-types:

- Spherical wavefront: $\rho_1 = \rho_2 = \rho_0$ (Eq.2.3.27)

$$\frac{|\vec{E}(s)|}{|\vec{E}_0|} = \frac{\rho_0}{\rho_0 + s}$$

- Cylindrical wavefront: $\rho_1 = \infty$,$\rho_2 = \rho_0$ or $\rho_2 = \infty$,$\rho_1 = \rho_0$

$$\frac{|\vec{E}|(s)}{|\vec{E}_0|} = \sqrt{\frac{\rho_0}{\rho_0 + s}}$$

- Planar wavefront: $\rho_1 = \rho_2 = \infty$

$$\frac{|\vec{E}(s)|}{|\vec{E}_0|} = 1$$

These expressions are only sufficiently accurate for large frequencies and they are only referred to the amplitude information. It is desirable to introduce polarization and phase information as well.

Polarization and phase information

Eq.2.3.30 only gives information about the amplitude relation between the electric fields at two wavefronts. The modulus can be removed, moving $\vec{E}_0$ to the other side of the equality (polarization information), and introducing the exponential for the phase information

$$\vec{E}(s) \simeq \vec{E}_0 e^{-jk\psi(s)} \sqrt{\frac{\rho_1 \rho_2}{(\rho_1 + s)(\rho_2 + s)}} \tag{2.3.31}$$

From the integration of Eq.2.3.16, $\int d\psi(s) = n \int ds$, it is possible to obtain the following relation

$$\psi(s) = \psi(0) + ns \tag{2.3.32}$$

Entering Eq.2.3.32 into Eq.2.3.31 yields

$$\vec{E}(s) \simeq \vec{E}_0 e^{-jk\psi(0)} \sqrt{\frac{\rho_1 \rho_2}{(\rho_1 + s)(\rho_2 + s)}} e^{-jkns} \tag{2.3.33}$$

where the the field at the reference point is $\vec{E}_0 e^{-jk\psi(0)}$; the third term is the spatial attenuation; and the term e^{-jkns} is the phase factor. A more rigorous way to obtain Eq.2.3.33 is to integrate the *transport equation* along s, as shown in [5] or [19].

2.3.3 Reflection from surfaces

Polarization relation

As it was stated in property 5) of Section 2.3.2, the reflectors can be considered locally planar. Therefore, evaluating how a perfect planar conductor affects the polarization of the wave is straightforward [20,21]. If a point on the reflector surface defines the origin of a local coordinate system, the direction of a ray incident to this

coordinate system defines the plane of incidence. Taking this plane of incidence as reference, it is possible to define two states of polarization:

- TE (Transverse-Electric): polarization in which the electric field is always transversal to the plane of incidence.
- TM (Transverse-Magnetic): polarization in which the magnetic field is always transversal to the plane of incidence.

Fig. 2.5, shows TE and TM polarizations, respectively, where Snell's law of reflection is fulfilled. The magnetic field is orthogonal to the electric field and to the direction of propagation, so it can be defined as

$$\vec{H} = \frac{1}{\eta}(\hat{k} \times \vec{E}) \tag{2.3.34}$$

where η is the intrinsic impedance of the medium. The incident field is the field at reference point Q_R, $\vec{E}_i(Q_R)$. For a TE incidence (Fig. 2.5 a)), the electric vector is always parallel to the surface, i.e., orthogonal to the unit vector normal to the surface, $\hat{n} = -\hat{z}$. Therefore, the reflected electric vector is $\vec{E}_r = -\vec{E}_i$.

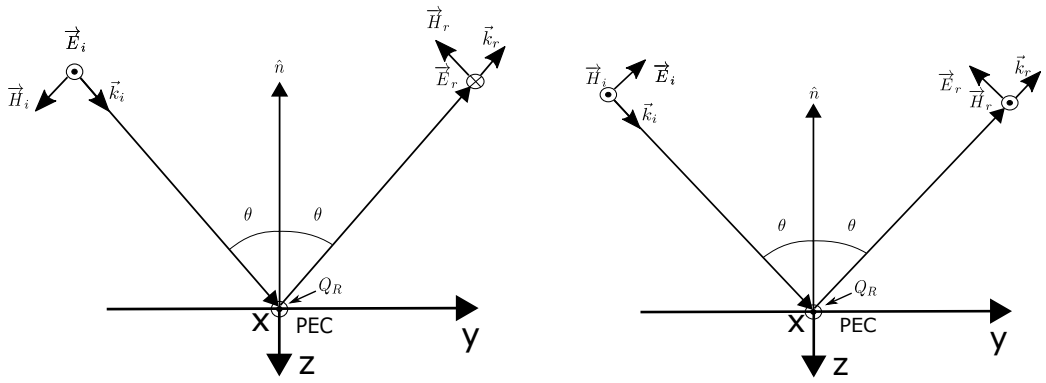

(a) TE polarization

(b) TM polarization

Figure 2.5: Reflection on a PEC planar surface for an incident wave with: a) TE polarization and b) TM polarization

For a TM incidence (Fig. 2.5 b)), the electric vector is not transverse to the direction of propagation, therefore the incidence and reflected electric vectors can be expressed

respectively as

$$\vec{E}_i = -E_z^i \hat{z} + E_y^i \hat{y} \tag{2.3.35a}$$

$$\vec{E}_r = -E_z^i \hat{z} - E_y^i \hat{y} \tag{2.3.35b}$$

After some basic operations the equation that gives the reflected electric vector function of the incidence electric vector is obtained:

$$\begin{aligned} \vec{E}_r &= -E_z^i \hat{z} - E_y^i \hat{y} = E_z^i \hat{z} - E_y^i \hat{y} - 2E_z^i \hat{z} \\ &= -\vec{E}_i - 2\hat{z}(-\vec{E}_i \hat{z}) = -2\hat{z}(-\vec{E}_i \hat{z}) - \vec{E}_i \end{aligned} \tag{2.3.36}$$

Knowing that the unit vector normal to the surface is in this case $\hat{n} = -\hat{z}$, Eq. 2.3.36 can be rewritten as

$$\vec{E}_r = 2\hat{n}(\hat{n} \cdot \vec{E}_i) - \vec{E}_i \tag{2.3.37}$$

The same analysis applies to the magnetic field, yielding

$$\vec{H}_r = \vec{H}_i - 2\hat{n}(\hat{n} \cdot \vec{H}_i) \tag{2.3.38}$$

And also to the propagation vectors $\vec{k}_i$ and $\vec{k}_r$

$$\vec{k}_r = \vec{k}_i - 2\hat{n}(\hat{n} \cdot \vec{k}_i) \tag{2.3.39}$$

Phase relation

For the reflected field, a different astigmatic tube of rays for the wavefronts must be considered. The reflecting surface can be curved along two principal and orthogonal planes. Therefore it has two focal distances, f_1 and f_2. The expression of the reflected field is then very similar to Eq.2.3.33 but with the parameters of the reflected astigmatic tube of rays

$$\vec{E}_r(s) = (2\hat{n}(\hat{n}\cdot\vec{E}_i(Q_R)) - \vec{E}_i(Q_R))\sqrt{\frac{\rho_1^r\rho_2^r}{(\rho_1^r+s)(\rho_2^r+s)}}e^{-jkns} \tag{2.3.40}$$

where ρ_1^r and ρ_2^r are the principal radii of curvature of the reflected wavefront at the reflection point. It is possible to obtain the next two relations [5] [22] (Appendix II) between ρ_1^r and ρ_2^r and the principal radii of curvature of the of the incident wavefront, ρ_1^i and ρ_2^i

$$\frac{1}{\rho_1^r} = \frac{1}{2}\left(\frac{1}{\rho_1^i} + \frac{1}{\rho_2^i}\right) + \frac{1}{f_1} \tag{2.3.41a}$$

$$\frac{1}{\rho_2^r} = \frac{1}{2}\left(\frac{1}{\rho_1^i} + \frac{1}{\rho_2^i}\right) + \frac{1}{f_2} \tag{2.3.41b}$$

Since only reflection at the reflector surface is considered here, the supposition of planar surface is valid, and therefore $f_1 = f_2 = \infty$. Eq.2.3.41a and Eq.2.3.41b are equal since $\rho_1^r = \rho_2^r = \rho_r$. This reduces both expressions to

$$\frac{1}{\rho_0^r} = \frac{1}{2}\left(\frac{1}{\rho_1^i} + \frac{1}{\rho_2^i}\right) \tag{2.3.42}$$

If the incident wavefronts are spherical, $\rho_0^r = \rho_i$. If $s = \rho_r$, the case of Fig.2.6 is considered, where the image of the incident wave is shown using the method of images [21]. Therefore, the path travelled by the reflected wave at a distance from the reflector is the sum of the path travelled by the incoming wave and the path travelled by the reflected wave, i.e., $\rho_i + \rho_r$.

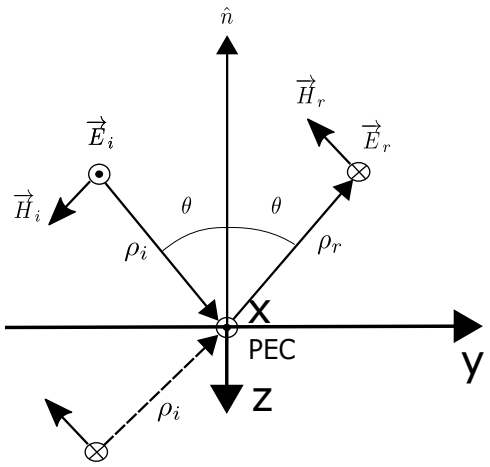

Figure 2.6: Paths taken for the incoming and reflected waves.

The field at the reference point Q_R for spherical waves, with polarization $\vec{E}_0$, amplitude and phase information can be expressed as

$$\vec{E}_i(Q_R) = \vec{E}_0 \frac{e^{-jkn\rho_i}}{\rho_i} \tag{2.3.43}$$

If the suppositions made in Fig.2.6 and Eq.2.3.43 are introduced into Eq.2.3.40, this yields

$$\vec{E}_r(\rho_r) = \frac{\rho_i}{\rho_i + \rho_r}(2\hat{n}(\hat{n} \cdot \vec{E}_0) - \vec{E}_0)\frac{e^{-jkn\rho_i}}{\rho_i} e^{-jkn\rho_r} \tag{2.3.44}$$

Therefore, the reflected wave from the reflector for an incoming spherical wave is

$$\vec{E}_r(\rho_r) = (2\hat{n}(\hat{n} \cdot \vec{E}_0) - \vec{E}_0)\frac{e^{-jkn\rho}}{\rho} \tag{2.3.45}$$

where $\rho = \rho_i + \rho_r$.

2.4 Radiation characteristics using vector potential functions

To simplify the calculus of the fields from Maxwell's equations it is common to use some auxiliary functions known as *vector potentials* [1]. Since in general the curl of the electric and magnetic fields is non-zero (see Eq. 2.2.1a and 2.2.1b), it is not possible to uniquely obtain these fields from scalar potentials. However, as it will be shown, it is possible to uniquely associate the electric and magnetic fields with vector potentials. This method will be used to obtain the far-field expressions of point sources (reflector's feed) and distributed sources (reflector itself).

First, the electric and magnetic field intensities $\vec{E}$ and $\vec{H}$ will be obtained as functions of the magnetic vector potential $\vec{A}$ and the electric vector potential $\vec{F}$. Then, these two vector potentials $\vec{A}$ and $\vec{F}$ will be obtained from the electric and magnetic currents of a generic source $\vec{J}$ and $\vec{M}$, respectively. It should be noted that magnetic currents, which are formed by fictitious moving magnetic monopoles, have not been found in nature and are only mathematical entities.

The starting point is rewriting Maxwell's equations in their complex vector form (Eq.2.2.9a-2.2.9d), supposing a region with currents and charges,

$$\nabla \times \vec{H} = \vec{J} + j\omega\epsilon\vec{E} \tag{2.4.1a}$$

$$\nabla \times \vec{E} = -j\omega\mu\vec{H} \tag{2.4.1b}$$

$$\nabla \cdot \vec{E} = \frac{\rho_e}{\epsilon} \tag{2.4.1c}$$

$$\nabla \cdot \vec{H} = 0 \tag{2.4.1d}$$

The electric and magnetic fields can be expressed as their contributions from the vector potentials

$$\vec{E} = \vec{E}_A + \vec{E}_F \tag{2.4.2a}$$

$$\vec{H} = \vec{H}_A + \vec{H}_F \tag{2.4.2b}$$

In the following subsections, these contributions will be obtained as function of the electric and magnetic currents.

2.4.1 E and H as functions of A

Since the divergence of the curl of any vector field is always zero (see A.0.1 in Appendix A), i.e. the flux of a curl of any vector is zero, $\vec{B}$ in Eq. 2.2.1c can be substituted by the curl of the magnetic vector potential: $\vec{B} = \nabla \times \vec{A}$, or in terms of the magnetic field as

$$\vec{H}_A = \frac{1}{\mu}\nabla \times \vec{A} \tag{2.4.3}$$

Eq. 2.4.3 can be then introduced into Eq. 2.4.1b. If $\vec{A}$ is moved to the other side of the equation, and knowing that the curl of the gradient of any scalar field is always

0 (see A.0.2 in Appendix A), $\vec{E}_A + j\omega\vec{A} = -\nabla\phi_J$ can be defined. Therefore $\vec{E}_A$ can be express as

$$\vec{E}_A = -\nabla\phi_J - j\omega\vec{A} \tag{2.4.4}$$

where ϕ_J is an arbitrary electric scalar potential. Using relation A.0.3 from Appendix A and Eq. 2.4.1a yields

$$\mu\vec{J} - \nabla(j\omega\mu\epsilon\phi_J) + k^2\vec{A} = \nabla(\nabla\cdot\vec{A}) - \nabla^2\vec{A} \tag{2.4.5}$$

where $k = \omega\sqrt{\mu\epsilon}$ is the wave-number. Since the divergence is a linear operator, the two divergences of Eq. 2.4.5 can be expressed as $\nabla(j\omega\mu\epsilon\phi_J + \nabla\cdot\vec{A})$. In order to simplify Eq. 2.4.5, the term $\nabla(j\omega\mu\epsilon\phi_J + \nabla\cdot\vec{A})$ can be made zero by

$$\phi_J = \frac{j}{\omega\mu\epsilon}\nabla\cdot\vec{A} \tag{2.4.6}$$

Eq. 2.4.6 is known as the *Lorentz condition*. Applying this condition to Eq. 2.4.5 and Eq. 2.4.4 reduces them to

$$\nabla^2\vec{A} + k^2\vec{A} = -\mu\vec{J} \tag{2.4.7}$$

$$\vec{E}_A = -j\omega\vec{A} - j\frac{1}{\omega\mu\epsilon}\nabla(\nabla\cdot\vec{A}) \tag{2.4.8}$$

It is now possible to obtain the contributions $\vec{E}_A$ (Eq. 2.4.8) and $\vec{H}_A$ (Eq. 2.4.3) from the magnetic vector potential $\vec{A}$.

2.4.2 E and H as functions of F

A harmonic current in a homogeneous medium should generate fields with $\vec{J} = 0$ and $\vec{M} \neq 0$ and satisfy $\nabla\cdot\vec{D} = 0$. Hence, taking again the divergence of the curl for an electric vector potential $\nabla\cdot(-\nabla\times\vec{F}) = 0$ and using $\vec{D} = \epsilon\vec{E}_F$

$$\vec{E}_F = -\frac{1}{\epsilon}\nabla\times\vec{F} \tag{2.4.9}$$

Eq. 2.4.9 can be substituted into Eq. 2.4.1a with $\vec{J} = 0$. Moving $\vec{F}$ to the left hand side of the equation, and taking $\vec{H}_F + j\omega\vec{F} = -\nabla\phi_M$, leads to

$$\vec{H}_F = -\nabla\phi_M - j\omega\vec{F} \tag{2.4.10}$$

where ϕ_M is an arbitrary magnetic scalar potential. Following the same steps that in Section 2.4.1 it is possible to obtain the next three equations

$$\phi_M = \frac{j}{\omega\mu\epsilon}\nabla\cdot\vec{F} \tag{2.4.11}$$

$$\nabla^2\vec{F} + k^2\vec{F} = -\epsilon\vec{M} \tag{2.4.12}$$

$$\vec{H} = -j\omega\vec{F} - j\frac{1}{\omega\mu\epsilon}\nabla(\nabla\cdot\vec{F}) \tag{2.4.13}$$

As in the previous subsection, it is possible to obtain the contributions $\vec{E}_F$ (Eq. 2.4.26c) and $\vec{H}_F$ (Eq. 2.4.13) from the electric vector potential $\vec{F}$.

2.4.3 A and F as functions of J and M

With $\vec{E}$ and $\vec{H}$ expressed as functions of $\vec{A}$ and $\vec{F}$, the final step is to obtain $\vec{A}$ and $\vec{F}$ as functions of the electric and magnetic currents densities $\vec{J}$ and $\vec{M}$, respectively. To do so, Eq. 2.4.7 and Eq. 2.4.12 must be solved. The next general equation can be defined

$$\nabla^2 Q_i + k^2 Q_i = -qS_i \tag{2.4.14}$$

Eq. 2.4.14 is a general Helmholtz equation where $\vec{Q}$ is either $\vec{A}$ or $\vec{F}$, $\vec{S}$ is either $\vec{J}$ or $\vec{M}$ and i is one of the three Cartesian coordinates (x, y, z). For instance, J_z would represent an infinitesimal source with electric current density directed along the z-axis. q represents the permeability of the medium μ for $\vec{A}$, and the permittivity of the medium ϵ for $\vec{F}$. The source of electric or magnetic currents is placed at the origin $(0, 0, 0)$. Outside that source, there is no current, hence

$$\nabla^2 Q_i + k^2 Q_i = 0 \tag{2.4.15}$$

Assuming a spherical coordinate system, there is no dependence with θ and ϕ since the source is considered a point source. Therefore $Q_i = Q_i(\rho)$. Using the Laplacian operator (see Appendix B), Eq. 2.4.15 reduces to

$$\frac{d^2 Q_i(\rho)}{d\rho^2} + \frac{2}{\rho}\frac{dQ_i(\rho)}{d\rho} + k^2 Q_i = 0 \tag{2.4.16}$$

This differential equation has two possible solutions. These two solutions represent two travelling waves, one being an outward wave and the other an inward wave. Since a source placed at the origin with waves travelling away from it is presumed, the first solution is chosen. Therefore the solution for the general function Q_i is

$$Q_i(\rho) = C_1 \frac{e^{-jk\rho}}{\rho} \tag{2.4.17}$$

On the other hand, for the static case, in which $k = 0$, Eq. 2.4.14 reduces to $\nabla^2 Q_i = -qS_i$, which in electrostatics is known as the Poisson's equation

$$\nabla^2 \phi_p = -\frac{\rho_e}{\epsilon} \tag{2.4.18a}$$

$$\phi_p = \frac{1}{4\pi\epsilon} \iiint \frac{\rho_e}{\rho} dv \tag{2.4.18b}$$

where Eq. 2.4.18b is the solution for Eq. 2.4.18a, i.e., the Poisson's equation that relates the scalar electric potential ϕ_p with the electric charge density ρ_e, being ρ the distance from any point on the charge density to the observation point. Taking Eq. 2.4.18b, it is possible to express Eq. 2.4.17 as

$$Q_i = \frac{q}{4\pi} \iiint \frac{S_i}{\rho} dv \tag{2.4.19}$$

Taking into account the general case (electrodynamics), with the form of Eq. 2.4.17, and substituting for every axis and for both vector potentials yields

$$\vec{A}(x, y, z) = \frac{\mu}{4\pi} \iiint \vec{J}(x', y', z') \frac{e^{-jkr}}{r} dv \tag{2.4.20}$$

$$\vec{F}(x,y,z) = \frac{\epsilon}{4\pi}\iiint \vec{M}(x',y',z')\frac{e^{-jkr}}{r}dv \tag{2.4.21}$$

where the source has been placed at a position (x',y',z') from the origin, and $r = \sqrt{(x-x')^2+(y-y')^2+(z-z')^2}$. For given electric and magnetic surface currents $\vec{J}_s$ and $\vec{M}_s$

$$\vec{A}(x,y,z) = \frac{\mu}{4\pi}\iint \vec{J}_s(x',y',z')\frac{e^{-jkr}}{r}ds \tag{2.4.22}$$

$$\vec{F}(x,y,z) = \frac{\epsilon}{4\pi}\iint \vec{M}_s(x',y',z')\frac{e^{-jkr}}{r}ds \tag{2.4.23}$$

Finally, for given electric and magnetic currents $\vec{I}_e$ and $\vec{I}_m$

$$\vec{A}(x,y,z) = \frac{\mu}{4\pi}\int \vec{I}_e(x',y',z')\frac{e^{-jkr}}{r}dl \tag{2.4.24}$$

$$\vec{F}(x,y,z) = \frac{\epsilon}{4\pi}\int \vec{I}_m(x',y',z')\frac{e^{-jkr}}{r}dl \tag{2.4.25}$$

Eq. 2.4.20 and Eq. 2.4.21 make it possible to obtain the magnetic and electric vector potentials $\vec{A}$ and $\vec{F}$ as functions of the electric and magnetic currents densities $\vec{J}$ and $\vec{M}$, respectively. On the other hand, Eq. 2.4.22 and Eq. 2.4.23 make it possible to obtain the magnetic and electric vector potentials $\vec{A}$ and $\vec{F}$ as functions of the electric and magnetic surface currents $\vec{J}_s$ and $\vec{M}_s$, respectively. Finally, Eq. 2.4.24 and Eq. 2.4.25 can be used to define $\vec{A}$ and $\vec{F}$ as functions of the electric and magnetic currents $\vec{I}_e$ and $\vec{I}_m$, respectively. Also, using Eq. 2.4.3 and Eq. 2.4.8, or Eq. 2.4.9 and Eq. 2.4.13 it is possible to obtain the electric and magnetic field intensities $\vec{E}$ and $\vec{H}$ as function of these vector potentials.

The final relations between $\vec{E}$ and $\vec{H}$, and $\vec{A}$ and $\vec{F}$ as obtain above are summarised

below:

$$\vec{E}_A = -j\omega\vec{A} - j\frac{1}{\omega\mu\epsilon}\nabla(\nabla\cdot\vec{A}) \tag{2.4.26a}$$

$$\vec{H}_A = \frac{1}{\mu}\nabla\times\vec{A} \tag{2.4.26b}$$

$$\vec{E}_F = -\frac{1}{\epsilon}\nabla\times\vec{F} \tag{2.4.26c}$$

$$\vec{H}_F = -j\omega\vec{F} - j\frac{1}{\omega\mu\epsilon}\nabla(\nabla\cdot\vec{F}) \tag{2.4.26d}$$

Throughout this thesis, two types of antennas are used: point sources and distributed sources. The first type refers to the ideal sources that will be used to feed the reflector, and the second refers to the radiative aperture of the reflector.

Vector potentials for point sources

For point sources, where $x' = y' = z' = 0$, the distance r is simplified to $r = \sqrt{x^2+y^2+z^2} = P$. The term e^{-jkr}/r in Eq.2.4.24 and Eq.2.4.25 can therefore be moved outside the integral. Point sources antennas will be examined in Section 3.4.

Vector potentials for distributed sources

For distributed sources, even if they are placed at the origin, contributions from outside the origin can arise. A typical example would be a circular aperture as the one shown in Fig. 2.7. The theory reviewed here is applied to aperture antennas [1].

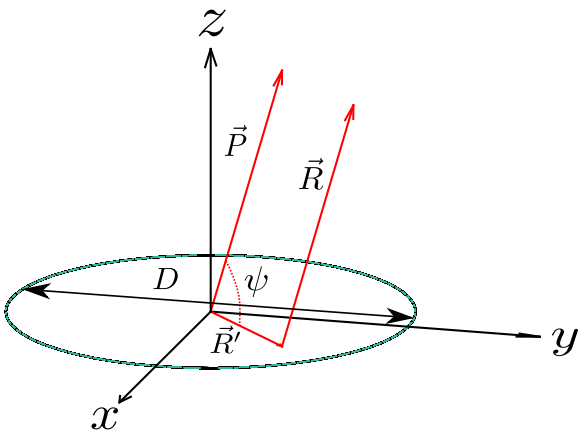

Figure 2.7: Circular aperture.

The *far-field* (also known as the *Fraunhoffer region*) is the region of the space where $k\rho \gg 1$ for point sources and $2D^2/\lambda$ for distributed sources [1]. In this region, it is common to simplify the amplitude variations by $R \simeq P$, and by simple trigonometry, the phase variations by $R \simeq P - R' \cos\psi$. The potentials $\vec{A}$ and $\vec{F}$ can therefore be expressed as

$$\vec{A} = \frac{\mu e^{-jkP}}{4\pi P}\vec{N} \tag{2.4.27a}$$

$$\vec{F} = \frac{\epsilon e^{-jkP}}{4\pi P}\vec{L} \tag{2.4.27b}$$

where the spherical coordinate system (P,Θ,Φ) refers to the radiating field, and (ρ,θ,ϕ) to the source. From Eq.2.4.20-2.4.21, the radiation integrals are

$$\vec{N} = \iint \vec{J}_s e^{jkR'\cos\psi} ds \tag{2.4.28a}$$

$$\vec{L} = \iint \vec{M}_s e^{jkR'\cos\psi} ds \tag{2.4.28b}$$

where the electric surface current can be obtained from the magnetic field across the aperture using Eq.C.0.6 from Appendix C. These radiation integrals can be seen as 3D Fourier Transforms. The magnetic surface current can be obtained from the electric field across the aperture if boundary conditions for a magnetic surface are applied

$$\vec{M}_s = \vec{E} \times \hat{n} \tag{2.4.29}$$

The spherical components of $\vec{N}$ and $\vec{L}$ can be written as

$$N_P = \iint (J_x^s \sin\Theta\cos\Phi + J_y^s \sin\Theta\sin\Phi + J_z^s \cos\Theta) e^{jkR'\cos\psi} ds \tag{2.4.30a}$$

$$N_\Theta = \iint (J_x^s \cos\Theta\cos\Phi + J_y^s \cos\Theta\sin\Phi - J_z^s \sin\Theta) e^{jkR'\cos\psi} ds \tag{2.4.30b}$$

$$N_\Phi = \iint (-J_x^s \sin\Phi + J_y^s \cos\Phi) e^{jkR'\cos\psi} ds \tag{2.4.30c}$$

$$L_P = \iint (M_x^s \sin\Theta\cos\Phi + M_y^s \sin\Theta\sin\Phi + M_z^s \cos\Theta) e^{jkR'\cos\psi} ds \tag{2.4.30d}$$

$$L_\Theta = \iint (M_x^s \cos\Theta\cos\Phi + M_y^s \cos\Theta\sin\Phi - M_z^s \sin\Theta) e^{jkR'\cos\psi} ds \tag{2.4.30e}$$

$$L_\Phi = \iint (-M_x^s \sin\Phi + M_y^s \cos\Phi) e^{jkR'\cos\psi} ds \tag{2.4.30f}$$

In order to reduce Eq.2.4.26a-2.4.26d, it can be supposed that in the far-field $1/\rho^n = 0$ for $n = 2, 3, ...$ [1]. $\nabla \cdot \vec{A}$ and $\nabla \cdot \vec{F}$ can therefore be reduced to

$$\nabla \cdot \vec{A} \simeq \frac{\partial(A_P)}{\partial P} \tag{2.4.31a}$$

$$\nabla \cdot \vec{F} \simeq \frac{\partial(F_P)}{\partial P} \tag{2.4.31b}$$

The same procedure for $\nabla(\nabla \cdot \vec{A})$ and $\nabla(\nabla \cdot \vec{F})$ yields

$$\nabla(\nabla \cdot \vec{A}) \simeq \hat{\rho}\frac{\partial^2 A_P}{\partial P^2} \tag{2.4.32a}$$

$$\nabla(\nabla \cdot \vec{F}) \simeq \hat{\rho}\frac{\partial^2 F_P}{\partial P^2} \tag{2.4.32b}$$

The curls of Eq. 2.4.26a-2.4.26d can also be reduced to

$$\nabla \times \vec{A} \simeq -\hat{\theta}\frac{\partial A_\Phi}{\partial P} + \hat{\phi}\frac{\partial A_\Theta}{\partial P} \tag{2.4.33a}$$

$$\nabla \times \vec{F} \simeq -\hat{\theta}\frac{\partial F_\Phi}{\partial P} + \hat{\phi}\frac{\partial F_\Theta}{\partial P} \tag{2.4.33b}$$

On the other hand, the derivatives and second derivatives of the different spherical components of $\vec{A}$ and $\vec{F}$ with respect to P (Eq. 2.4.31a-2.4.33b) only affect the terms outside the integral G_A and G_F

$$G_A = \frac{\mu e^{-jkP}}{4\pi P} \tag{2.4.34a}$$

$$G_F = \frac{\epsilon e^{-jkP}}{4\pi P} \tag{2.4.34b}$$

Therefore,

$$\frac{\partial G_A}{\partial P} = -\frac{\mu}{4\pi}\frac{(-jkP+1)e^{-jkP}}{P^2} = -jkG_A - \frac{G_A}{P} \tag{2.4.35a}$$

$$\frac{\partial G_F}{\partial P} = -\frac{\epsilon}{4\pi}\frac{(-jkP+1)e^{-jkP}}{P^2} = -jkG_F - \frac{G_F}{P} \tag{2.4.35b}$$

$$\frac{\partial^2 G_A}{\partial P^2} = \frac{\mu}{4\pi}\frac{(2jkP+2-k^2P^2)e^{-jkP}}{P^3} = 2jk\frac{G_A}{P} + 2\frac{G_A}{P^2} - k^2G_A \tag{2.4.36a}$$

$$\frac{\partial^2 G_F}{\partial P^2} = \frac{\epsilon}{4\pi}\frac{(2jkP+2-k^2P^2)e^{-jkP}}{P^3} = 2jk\frac{G_F}{P} + 2\frac{G_F}{P^2} - k^2G_F \tag{2.4.36b}$$

By applying the far-field approximation, Eq. 2.4.35a-2.4.36b become

$$\frac{\partial G_A}{\partial P} \simeq -jk\mu\frac{e^{-jkP}}{4\pi P} \tag{2.4.37a}$$

$$\frac{\partial G_F}{\partial P} \simeq -jk\epsilon\frac{e^{-jkP}}{4\pi P} \tag{2.4.37b}$$

$$\frac{\partial^2 G_A}{\partial P^2} \simeq -k^2 \mu \frac{e^{-jkP}}{4\pi P} \tag{2.4.37c}$$

$$\frac{\partial^2 G_F}{\partial P^2} \simeq -k^2 \epsilon \frac{e^{-jkP}}{4\pi P} \tag{2.4.37d}$$

With the inclusion of these approximations for G_A and G_F, Eq.2.4.32a and Eq.2.4.32b, and Eq.2.4.33a and Eq.2.4.33b can be expressed as

$$\nabla(\nabla \cdot \vec{A}) \simeq -k^2(\hat{\rho} \cdot \vec{A})\hat{\rho} \tag{2.4.38a}$$

$$\nabla(\nabla \cdot \vec{F}) \simeq -k^2(\hat{\rho} \cdot \vec{F})\hat{\rho} \tag{2.4.38b}$$

$$\nabla \times \vec{A} \simeq -jk(\hat{\rho} \times \vec{A}) \tag{2.4.38c}$$

$$\nabla \times \vec{F} \simeq -jk(\hat{\rho} \times \vec{F}) \tag{2.4.38d}$$

The electric and magnetic far-field due to the potentials can be approximately obtained using the previous approximations as

$$\vec{E}_A \simeq j\omega\hat{\rho} \times (\hat{\rho} \times \vec{A}) \tag{2.4.39a}$$

$$\vec{H}_A \simeq -j\frac{k}{\mu}(\hat{\rho} \times \vec{A}) \tag{2.4.39b}$$

$$\vec{E}_F \simeq j\frac{k}{\epsilon}(\hat{\rho} \times \vec{F}) \tag{2.4.39c}$$

$$\vec{H}_F \simeq j\omega\hat{\rho} \times (\hat{\rho} \times \vec{F}) \tag{2.4.39d}$$

Finally, using Eq.2.4.2a and Eq.2.4.2b, the spherical components of the electric and magnetic far-field can be approximately expressed as

$$E_P \simeq 0 \tag{2.4.40a}$$

$$E_\Theta \simeq -(\eta N_\Theta + L_\Phi)\frac{jke^{-jkP}}{4\pi P} \tag{2.4.40b}$$

$$E_\Phi \simeq (-\eta N_\Phi + L_\Theta)\frac{jke^{-jkP}}{4\pi P} \tag{2.4.40c}$$

$$H_P \simeq 0 \tag{2.4.40d}$$

$$H_\Theta \simeq (N_\Phi - \frac{L_\Theta}{\eta})\frac{jke^{-jkP}}{4\pi P} \tag{2.4.40e}$$

$$H_\Phi \simeq -(N_\Theta + \frac{L_\Phi}{\eta})\frac{jke^{-jkP}}{4\pi P} \tag{2.4.40f}$$

This section has aimed to describe the methodology to obtain the far-field components radiated from point (ideal) and distributed (reflector) sources using the vector potentials. The vector potentials, summarised in Eq. 2.4.27a, 2.4.27b and Eq. 2.4.30a-2.4.30f are obtained from the surface currents. Therefore, knowing the source surface currents, the far-field components can be easily obtained using Eq. 2.4.40a-2.4.40f.

2.5 Analysis of 2D periodic structures using Floquet's Theorem

As discussed in the introduction to the present chapter, both FSSs and reflectarrays consist of doubly periodic arrays of passive unit-cells that perform a specific change to the incident wave. One of the most common examples of FSS is a reflection/transmission FSS that works as a metallic reflector for one frequency band and as an invisible surface for another frequency band. Another example is a reflection/transmission polariser where the FSS transforms the incident LP wave into reflected/transmitted orthogonal LP or CP wave. On the other hand, the basic principle of reflectarrays is to tune the magnitude and phases of each unit-cell of the flat array to mimic the focusing properties of a parabolic reflector. Theoretically, the reflected focused beam can point to any desired direction.

Every unit-cell's geometry is assumed to be equal to the next. In order to simplify the analysis, this assumption is still maintained for non-uniform FSS or reflectarrays, where the changes between adjacent unit-cells are smooth. As mentioned in Section 2.3.2, reflectors are large enough compared to the wavelength to be supposed as

infinite. Taking into account these suppositions, the most common way to analyse the unit-cells in such structures is Floquet's Theorem.

In this section, an illustration of the Floquet spectral domain analysis for the case of a single periodic array consisting of isolated metal elements at a certain distance from an infinite and fully conducting ground plane is held. Next, in the following subsections the incident and reflected field from a generic unit-cell of this type will be presented.

2.5.1 General solutions for transversal TE/TM waves

As in the canonical PEC reflection problem (see Section 2.3.3), with FSSs it is common to decompose the incoming field into TE and TM components. However, only the transversal components are taken into account in the formulation, since they are the ones supported by the 2D periodic structure. The direction of propagation for these fields is supposed to be $\mp z$. As in the methodology used by Pozar [13], the starting point is to substitute Eq.2.2.9a into Eq.2.2.9b to obtain the Cartesian components of $\vec{H}$ and vice versa to obtain the Cartesian components of $\vec{E}$. Since $\pm z$ is the direction of propagation, the partial derivative of $\vec{E}$ or $\vec{H}$ with respect to z is given by:

$$\frac{\partial Q_i}{\partial z} = \pm j\beta Q_i \tag{2.5.1}$$

where β is the propagation constant, Q stands for E or H and i for x or y. After some algebra the Cartesian components of the tangential field can be expressed as

$$E_x = -\frac{j}{k_c^2}\left(\mp\beta\frac{\partial E_z}{\partial x} + \omega\mu\frac{\partial H_z}{\partial y}\right) \tag{2.5.2a}$$

$$E_y = \frac{j}{k_c^2}\left(\pm\beta\frac{\partial E_z}{\partial y} + \omega\mu\frac{\partial H_z}{\partial x}\right) \tag{2.5.2b}$$

$$H_x = \frac{j}{k_c^2}\left(\omega\epsilon\frac{\partial E_z}{\partial y} \pm \beta\frac{\partial H_z}{\partial x}\right) \tag{2.5.2c}$$

$$H_y = -\frac{j}{k_c^2}\left(\omega\epsilon\frac{\partial E_z}{\partial x} \mp \beta\frac{\partial H_z}{\partial y}\right) \tag{2.5.2d}$$

where $k_c = \omega^2\mu\epsilon - \beta^2$ is the cut-off wave number.

Transversal TM components

As defined in Section 2.3.3, TM waves have their magnetic field transversal to the plane of incidence, which makes $H_z = 0$. Using this simplification in Eq.2.5.2a-2.5.2d, and expressing the field in vector form yields

$$\vec{E}_t = \pm j\frac{\beta}{k_c^2}\nabla_t E_z \tag{2.5.3a}$$

$$\vec{H}_t = -j\frac{\omega\epsilon}{k_c^2}\hat{z} \times \nabla_t E_z \tag{2.5.3b}$$

Transversal TE components

As also discussed in Section 2.3.3, TE waves have their electric field transversal to the plane of incidence, which makes $E_z = 0$. And once again, using this simplification in Eq.2.5.2a-2.5.2d, and expressing the field in vector form yields

$$\vec{E}_t = j\frac{\omega\mu}{k_c^2}\hat{z} \times \nabla_t H_z \tag{2.5.4a}$$

$$\vec{H}_t = \pm j\frac{\beta}{k_c^2}\nabla_t H_z \tag{2.5.4b}$$

2.5.2 Floquet modes

Floquet's Theorem states that in a periodic structure, the field at any point of a unit-cell is the same at a similar point of any other unit-cell except from a propagation factor multiplying the field, known as Floquet's phasor [23]. This field is then expressed as a periodic function. As with any periodic function, it can be expanded as an infinite Fourier series, where the terms are known as space harmonics. Each space harmonic has a different wavenumber and phase velocity. The terms of the series, or modes, are usually denoted as p, q, which can take values from 0 to ± 1, ± 2, ... Since the field is supposed to be constant accross the unit-cell, the modal

field solution Ξ_{pq} of the wave equation (see Eq. 2.2.13a) can be easily obtained from the phase component by applying separation of variables [23]:

$$\Xi_{pq}(\vec{r}, z) = e^{-j(k_{xpq}x + k_{ypq}y)} e^{\pm j\beta_{pq}z} = \psi_{pq}(\vec{r}) e^{\pm j\beta_{pq}z} \tag{2.5.5}$$

where ψ_{pq} is Floquet's phasor and $\vec{r} = x\hat{x} + y\hat{y}$.

TM case

One possible solution for the z component of the electric field is [23]

$$E_{zpq}(\vec{r}) = \frac{k_{tpq}}{\beta_{pq}} \psi_{pq}(\vec{r}) \tag{2.5.6}$$

Now Eq.2.5.6 can be introduced into the transversal TM components in Eq.2.5.3a and Eq.2.5.3b. Performing the partial derivatives and arranging components yields

$$\vec{E}^t_{pq} = \vec{\kappa}_{1pq} \psi_{pq}(\vec{r}) \tag{2.5.7a}$$

$$\vec{H}^t_{pq} = \mp Y_{1pq} \hat{z} \times \vec{\kappa}_{1pq} \psi_{pq}(\vec{r}) \tag{2.5.7b}$$

where $\vec{\kappa}_{1pq} = \pm(\hat{x}k_{xpq} + \hat{y}k_{ypq})/k_{tpq}$ is the unit vector of the tangential TM components and $Y_{1pq} = \omega\epsilon/\beta_{pq}$ is the tangential TM modal admittance associated with the pq Floquet space harmonic.

TE case

One possible solution for the z component of the magnetic field is [23]

$$H_{zpq}(\vec{r}) = Y \frac{k_{tpq}}{k} \psi_{pq}(\vec{r}) \tag{2.5.8}$$

Now Eq.2.5.8 can be introduced into the tangential TE components in Eq.2.5.4a

and Eq.2.5.4b. Performing the partial derivatives and arranging components yields

$$\vec{E}^t_{pq} = \vec{\kappa}_{2pq}\psi_{pq}(\vec{r}) \tag{2.5.9a}$$

$$\vec{H}^t_{pq} = \mp Y_{2pq}\hat{z} \times \vec{\kappa}_{2pq}\psi_{pq}(\vec{r}) \tag{2.5.9b}$$

where $\vec{\kappa}_{2pq} = (-\hat{x}k_{ypq} + \hat{y}k_{xpq})/k_{tpq}$ is the unit vector of tangential TE components and $Y_{2pq} = \eta\beta_{pq}/k$ is the tangential TE modal admittance.

2.5.3 Incident tangential field and wavenumber

The total tangential field for each mode will be the direct summation of the tangential TE and TM components, i.e., adding Eq.2.5.7a and Eq.2.5.9a for the electric field, and Eq.2.5.7b and Eq.2.5.9b for the magnetic field:

$$\vec{E}^t_{pq}(\vec{r}) = \left(\vec{\kappa}_{1pq} + \vec{\kappa}_{2pq}\right)\psi_{pq}(\vec{r}) \tag{2.5.10a}$$

$$\vec{H}^t_{pq}(\vec{r}) = \mp\left(Y_{1pq}\hat{z} \times \vec{\kappa}_{1pq} + Y_{2pq}\hat{z} \times \vec{\kappa}_{2pq}\right)\psi_{pq}(\vec{r}) \tag{2.5.10b}$$

The tangential field incident to the FSS, based on the tangential TM/TE modes decomposition, can be expressed as

$$\vec{E}^t_i = \sum_{m=1}^{2} T^1_{m00}\psi_{00}(\vec{r})\vec{\kappa}_{m00}e^{\pm j\beta^1_{00}z} \tag{2.5.11a}$$

$$\vec{H}^t_i = \mp \sum_{m=1}^{2} Y^1_{m00}T^1_{m00}\psi_{00}(\vec{r})\hat{z} \times \vec{\kappa}_{m00}e^{\pm j\beta^1_{00}z} \tag{2.5.11b}$$

where $m = 1$ stands for the tangential TM components and $m = 2$ for the tangential TE components, $p = 0, q = 0$ represents the fundamental Floquet mode, T^1_{m00} is the amplitude of the incident field, and β^1_{00} is the propagation constant of the fundamental mode. The unitary vectors of the tangential fundamental TM/TE

mode are reduced to

$$\vec{\kappa}_{100} = \pm\hat{x}\cos\phi_i \pm \hat{y}\sin\phi_i \tag{2.5.12a}$$

$$\vec{\kappa}_{200} = -\hat{x}\sin\phi_i + \hat{y}\cos\phi_i \tag{2.5.12b}$$

From now on, only incidence in $-z$ will be considered, which corresponds to the upper sign in the previous equations. In order to generalise the directions in which the periodic cells are repeated, it is common to express the lattice in a set of two general axes denoted as (l, w) [23], as shown in Fig. 2.8.

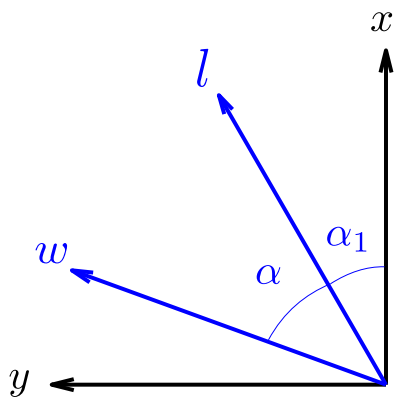

Figure 2.8: Arbitrary lw lattice.

The relation of these vectors with (x, y) is

$$\vec{D}_l = D_l\hat{l} = D_l\left(\hat{x}\cos\alpha_1 + \hat{y}\sin\alpha_1\right) \tag{2.5.13a}$$

$$\vec{D}_w = D_w\hat{w} = D_w\left(\hat{x}\cos\alpha_2 + \hat{y}\sin\alpha_2\right) \tag{2.5.13b}$$

where $\alpha_2 = \alpha + \alpha_1$, and $A = |\vec{D}_l \times \vec{D}_w| = D_l D_w \sin\alpha$. Therefore, the phase displacement along the lattice directions lw in Cartesian is

$$\vec{k}_1 = -\frac{2\pi}{A}\hat{z} \times \vec{D}_w = \frac{2\pi}{A}D_w\left(\hat{x}\sin\alpha_2 - \hat{y}\cos\alpha_2\right) \tag{2.5.14a}$$

$$\vec{k}_2 = \frac{2\pi}{A}\hat{z} \times \vec{D}_l = \frac{2\pi}{A}D_l\left(-\hat{x}\sin\alpha_1 + \hat{y}\cos\alpha_1\right) \tag{2.5.14b}$$

The tangential wavenumber for each harmonic has contributions from the fundamental mode and from the periodicity, i.e., $\vec{k}^t_{pq} = \vec{k}^t_{00} + p\vec{k}_1 + q\vec{k}_2$. Therefore, using Eq.2.5.14a and Eq.2.5.14b, they can be expanded as

$$k_{xpq} = k_0 \sin\theta_i \cos\phi_i + \frac{2\pi}{A}\left(pD_w \sin\alpha_2 - qD_l \sin\alpha_1\right) \tag{2.5.15a}$$

$$k_{ypq} = k_0 \sin\theta_i \sin\phi_i + \frac{2\pi}{A}\left(-pD_w \cos\alpha_2 + qD_l \cos\alpha_1\right) \tag{2.5.15b}$$

2.5.4 Boundary conditions for a grounded one layer FSS

A general representation of the problem is shown in Fig.2.9. As it was mentioned in the introduction, the periodic arrays treated in this thesis consist of isolated metal elements. This problem is usually treated by expressing all unknowns in terms of the electric currents on the metallic elements, which can be obtained by applying the Method of Moments (MoM). The dual problem of an inductive array can be solved in a similar fashion expressing all unknowns in terms of magnetic currents in the apertures. For the case under consideration, the FSS space is split in three regions:

- Region 1: incident field on the FSS. A portion of the field will be reflected by the FSS and a portion will be transmitted into region 2. The medium in this region is supposed to be vacuum.
- Region 2: substrate of the FSS. All the field in this region will be reflected by the ground plane. The medium will be described by a relative permittivity ϵ_r and a loss tangent $\tan\delta$.
- Region 3: due to the ground plane, no field will be transmitted to this region.

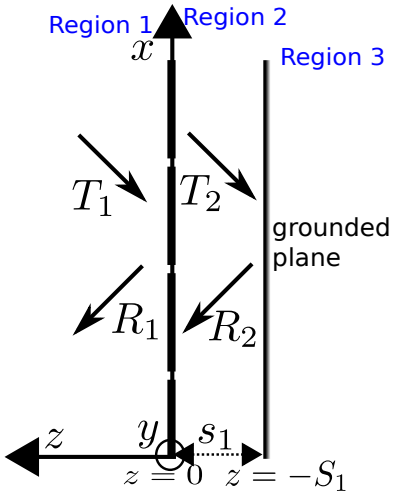

Figure 2.9: Plane of incidence on the FSS.

The tangential field in region 1 can be expressed as

$$\vec{E}_1^t = \vec{E}_i^t + \sum_{mpq} R^1_{mpq}\psi_{pq}(\vec{r})\vec{\kappa}_{mpq}e^{-j\beta^1_{pq}z} \tag{2.5.16a}$$

$$\vec{H}_1^t = \vec{H}_i^t + \sum_{mpq} Y^1_{mpq}R^1_{mpq}\psi_{pq}(\vec{r})\hat{z}\times\vec{\kappa}_{mpq}e^{-j\beta^1_{pq}z} \tag{2.5.16b}$$

And in region 2 as

$$\vec{E}_2^t = \sum_{mpq}\left(T^2_{mpq}e^{j\beta^1_{pq}z} + R^2_{mpq}e^{-j\beta^2_{pq}z}\right)\psi_{pq}(\vec{r})\vec{\kappa}_{mpq} \tag{2.5.17a}$$

$$\vec{H}_2^t = \sum_{mpq} Y^2_{mpq}\left(-T^2_{mpq}e^{j\beta^2_{pq}z} + R^2_{mpq}e^{-j\beta^2_{pq}z}\right)\psi_{pq}(\vec{r})\hat{z}\times\vec{\kappa}_{mpq} \tag{2.5.17b}$$

At the boundary between region 2 and 3 a PEC is placed ($z = -S_1$). Therefore, the boundary conditions from Appendix C apply, i.e., $\vec{E}_2^t(\vec{r}, -S_1) = 0$. Eq. 2.5.17a can be multiplied by $\psi^*_{ln}\vec{\kappa}_{mln}$ and integrated over the unit-cell

$$\iint\sum_{mpq}\left(T^2_{mpq}e^{j\beta^2_{pq}z} + R^2_{mpq}e^{-j\beta^2_{pq}z}\right)\psi_{pq}\psi^*_{ln}\vec{\kappa}_{mpq}\vec{\kappa}_{mln}dxdy \tag{2.5.18}$$

The orthogonality between modes can be expressed in an inner product notation as [24]

$$< \psi_{pq}, \psi^*_{ln} >_A = \iint \psi_{pq}\psi^*_{ln} dxdy = A\delta_{pl}\delta_{qn} \begin{cases} A, & p = l \ q = n \\ 0, & \text{otherwise} \end{cases} \tag{2.5.19}$$

which reduces Eq.2.5.18 to

$$T^2_{mpq} e^{j\beta^2_{pq} z} + R^2_{mpq} e^{-j\beta^2_{pq} z} = 0 \tag{2.5.20}$$

From this the reflection coefficient at the interface between region 2 and 3 can be expressed as

$$\rho^2_{mpq} = -e^{-2j\beta^2_{pq} S_1} \tag{2.5.21}$$

At the boundary between regions 1 and 2 ($z = 0$), $\vec{E}^t_1(\vec{r}, 0) = \vec{E}^t_2(\vec{r}, 0)$. Also, an electric current is created on that surface $\vec{J}(\vec{r}, 0) = \hat{n} \times (\vec{H}^t_1(\vec{r}, 0) - \vec{H}^t_2(\vec{r}, 0))$. $\vec{H}^t_1(\vec{r}, 0)$ can therefore be expressed as

$$\vec{H}^t_1(\vec{r}, 0) = \vec{H}^t_2(\vec{r}, 0) - \hat{z} \times \vec{J}(\vec{r}, 0) \tag{2.5.22}$$

Eq.2.5.22 can be expanded using Eq.2.5.11b, Eq.2.5.16b and Eq.2.5.17b. Rearraigning the components, it is possible to arrive at

$$\begin{aligned} -\hat{z} \times \left(\sum_{m=1}^{2} Y^1_{m00} T^1_{m00} \psi_{pq}(\vec{r}) \vec{\kappa}_{m00} - \sum_{mpq} Y^1_{mpq} R^1_{mpq} \psi_{pq}(\vec{r}) \vec{\kappa}_{mpq} \right) = \\ -\hat{z} \times \left(\sum_{mpq} Y^2_{mpq} (T^2_{mpq} - R^2_{mpq}) \psi_{pq}(\vec{r}) \vec{\kappa}_{mpq} + \vec{J}(\vec{r}, 0) \right) \end{aligned} \tag{2.5.23}$$

Since the components in Eq.2.5.23 refer to the tangential field, it is correct to assume that the equality also holds for what is within the parenthesis on both sides. Therefore, it is possible to multiply both sides again by $\psi^*_{ln} \vec{\kappa}_{mln}$ and integrate over the unit-cell. However, since the surface currents also depend on the unit-cell position, some comments should be made before continuing. The surface currents can be expanded as a sum of basis functions as

$$\vec{J}(\vec{r}, 0) = \hat{x} \sum_{s=1}^{\infty} c_s h^s_x(\vec{r}) + \hat{y} \sum_{t=1}^{\infty} c_t h^t_y(\vec{r}) \tag{2.5.24}$$

Therefore the integration over the unit-cell of the currents multiplied by $\psi^*_{ln}\vec{\kappa}_{mln}$ leads to

$$\tilde{J}_{mpq} = \tilde{J}_{xpq}\kappa_{xmpq} + \tilde{J}_{ypq}\kappa_{ympq} = \sum_s^\infty c_s \iint h^s_x(\vec{r})\psi^*_{ln}(\vec{r})dxdy\kappa_{xmln} + \sum_t^\infty c_t \iint h^t_y(\vec{r})\psi^*_{ln}(\vec{r})dxdy\kappa_{ymln} \tag{2.5.25}$$

Applying inner products and considering the orthogonality of Floquet phasors as in Eq. 2.5.25, Eq.2.5.23 can be reduced to

$$Y^1_{m00}T^1_{m00}\delta_{p0}\delta_{q0} - Y^1_{mpq}R^1_{mpq} = Y^2_{mpq}T^2_{mpq}(1-\rho^2_{mpq}) + \frac{\tilde{J}_{mpq}}{A} \tag{2.5.26}$$

Applying a similar procedure to the condition at the boundary for the electric field $\vec{E}^t_1(\vec{r},0) - \vec{E}^t_2(\vec{r},0) = 0$ yields

$$T^1_{m00}\delta_{p0}\delta_{q0} + R^1_{mpq} = T^2_{mpq}(1+\rho^2_{mpq}) \tag{2.5.27}$$

Then, dividing Eq.2.5.26 (with the currents at the left hand side of the equation) over Eq.2.5.27 yields the coefficient ζ^2_{mpq}

$$\zeta^2_{mpq} = \frac{1-\rho^2_{mpq}}{1+\rho^2_{mpq}} \tag{2.5.28}$$

The same procedure also yields to the reflected field amplitude relationship R^1_{mpq}

$$R^1_{mpq} = \rho^1_{m00}T^1_{m00}\delta_{p0}\delta_{q0} - \frac{\tilde{J}_{mpq}}{A(Y^1_{mpq} + Y^2_{mpq}\zeta^1_{mpq})} \tag{2.5.29}$$

where

$$\rho^1_{m00} = \frac{Y^1_{m00} - Y^2_{m00}\zeta^2_{m00}}{Y^1_{m00} + Y^2_{m00}\zeta^2_{m00}} \tag{2.5.30}$$

Finally, it can be observed that the electric field is zero on the metallic elements of the FSS (boundary between region 1 and 2). From this condition applied to Eq.2.5.16a, and using Eq.2.5.28-2.5.30, it is possible to derive the electric field integral equation (EFIE)

$$\sum_{m=1}^{2}(1+\rho_{m00}^{1})T_{m00}^{1}\psi_{00}(\vec{r})\vec{\kappa}_{m00}=\sum_{mpq}\frac{\tilde{J}_{mpq}}{A(Y_{mpq}^{1}+Y_{mpq}^{2}\zeta_{mpq}^{1})}\psi_{pq}(\vec{r})\vec{\kappa}_{mpq} \tag{2.5.31}$$

The next step would be to apply the Method of Moments (MoM) [24] to obtain the coefficients of the currents. For example, Galerkin MoM expresses the Electric Field Integral Equation (EFIE) in matrix form as $[Z_{in}][c_n] = [\tilde{E}_i^t]$. However, some basis functions should be chosen to solve the problem. The efficiency in applying the method and its accuracy will depend on the chosen basis functions. Sub-domain basis functions involve discretising the element and expressing the current in each fragment of the cell with a function [25]. Some examples of sub-domain basis functions are the roof-top [26] and the Rao-Wilton-Glisson (RWG) [27]. However, for simple element geometries, where the current closely resembles zero-ended sinusoidal and cosinusoidal terms, it is computationally more efficient to use entire-domain basis functions [25]. These functions allow a manageable matrix size, but they limit the element shape that can be simulated [25].

More recently, non-singular higher-order hierarchical Legendre basis functions have been presented [28] to be applied to any arbitrary shape while attempting to minimize the increase in the number of basis functions and Floquet harmonics. These types of basis functions have been applied to the design and optimisation of reflectarrays [29], where each unit-cell has to be locally optimised to meet certain specific phase and amplitude requirements.

At it was mentioned in Chapter 1, there are already several software packages to analyse a general unit-cell under periodic conditions where an integral equation solver (or similar) is used to accurately compute the currents. For the present work, the preferred software has been CST Studio Suite [30]. Therefore, the remaining task is to use the scattering parameters provided by CST to obtain the field reflected from the FSS.

2.5.5 Scattering parameters

The scattering parameters (S-parameters) are the most usual way to describe the relationship between incident and reflected fields. Since the incident (and reflected)

wave is decomposed into TM and TE components, the scattering matrix will have four entries, as can be seen in Eq.2.5.32 [31].

$$\mathbf{S} = \begin{bmatrix} \frac{TE_r}{TE_i}|_{TM_i=0} & \frac{TE_r}{TM_i}|_{TE_i=0} \\ \frac{TM_r}{TE_i}|_{TM_i=0} & \frac{TM_r}{TM_i}|_{TE_i=0} \end{bmatrix} \tag{2.5.32}$$

The component $\frac{TE_r}{TE_i}|_{TM_i=0}$ in Eq. 2.5.32 refers to the reflected TE component when only TE incidence is supposed. The component $\frac{TE_r}{TM_i}|_{TE_i=0}$ refers to the reflected TE component when only TM incidence is supposed and so on. In order to simplify the notation, the components will be renamed as $\frac{TE_r}{TE_i}|_{TM_i=0} = s_{11}$, $\frac{TE_r}{TM_i}|_{TE_i=0} = s_{12}$, $\frac{TM_r}{TE_i}|_{TM_i=0} = s_{21}$ and $\frac{TM_r}{TM_i}|_{TE_i=0} = s_{22}$.

Eq. 2.5.32 refers only to propagating modes, i.e., fundamental incident and reflected TM/TE modes. Other non-propagating modes could appear, but they are excluded in the present work.

In order to represent physically realizable elements, the scattering matrix has to fulfil the energy conservation rule as presented in [31]. The relationship between incident and reflected field using the S-parameters can be expressed as

$$\begin{bmatrix} E^r_{TE} \\ E^r_{TM} \end{bmatrix} = \begin{bmatrix} s_{11} & s_{12} \\ s_{21} & s_{22} \end{bmatrix} \begin{bmatrix} E^i_{TE} \\ E^i_{TM} \end{bmatrix} \tag{2.5.33}$$

The TM/TE components of the electric field are defined with respect to the plane of incidence, as previously stated in Section 2.3.3, and since they are TEM waves, there is orthogonality between them and to the direction of propagation. These orthogonality properties must apply as well to the TM/TE components of the magnetic field and between the electric and magnetic fields. Taking all of this into consideration, the most suitable definition for the TM and TE components is

$$E_{TM} = E_\theta \tag{2.5.34a}$$

$$E_{TE} = E_\phi \tag{2.5.34b}$$

$$H_{TM} = H_\phi = \pm\frac{E_\theta}{\eta_0} = \pm\frac{E_{TM}}{\eta_0} \tag{2.5.34c}$$

$$H_{TE} = H_\theta = \mp\frac{E_\phi}{\eta_0} = \mp\frac{E_{TE}}{\eta_0} \tag{2.5.34d}$$

where $\eta_0 = 120\pi$ is the impedance of free space, and where the signs in Eq.2.5.34c and Eq.2.5.34d depend on the direction of propagation, choosing the upper sign for propagation in ρ (reflected field) and the lower sign for propagation in $-\rho$ (incident field). If the TM/TE components of the magnetic field from Eq.2.5.34c and Eq.2.5.34d are introduced into Eq.2.5.33 (using the proper sign for reflected and incident fields), the relation between incident and reflected magnetic fields using the S-parameters is obtained:

$$\begin{bmatrix} H^r_{TE} \\ H^r_{TM} \end{bmatrix} = \begin{bmatrix} -s_{11} & s_{12} \\ s_{21} & -s_{22} \end{bmatrix} \begin{bmatrix} H^i_{TE} \\ H^i_{TM} \end{bmatrix} \tag{2.5.35}$$

These scattering matrices are referred to the total incident/reflected field. However, in FSS analysis, it is common to work only with the field tangential to the surface. Therefore, a new 2D (u, v) coordinate system is presented in Fig. 2.10. This coordinate system is based on a very similar one provided by Daniele Bresciani from the Research and Technology Department of Thales Alenia Space. They are defined by the incidence angles, where $\hat{u} = \hat{\phi}$ and $\hat{v} = \hat{u} \times \hat{z} = \hat{x}\cos\phi_i + \hat{y}\sin\phi_i$. Therefore, the rotation matrix from xy to uv is

$$\begin{bmatrix} \hat{v} \\ \hat{u} \end{bmatrix} = \begin{bmatrix} \cos\phi_i & \sin\phi_i \\ -\sin\phi_i & \cos\phi_i \end{bmatrix} \begin{bmatrix} \hat{x} \\ \hat{y} \end{bmatrix} \tag{2.5.36}$$

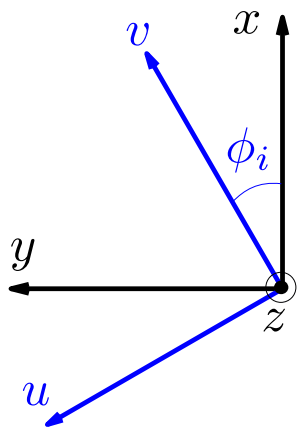

Figure 2.10: Relation between uv and xy coordinate systems.

The relation between the electric field components is therefore

$$E_v = E_{TM} \cos\theta_i \tag{2.5.37a}$$

$$E_u = E_{TE} \tag{2.5.37b}$$

And for the magnetic field:

$$H_v = H_{TE} \cos\theta_i \tag{2.5.38a}$$

$$H_u = H_{TM} \tag{2.5.38b}$$

2.6 Summary

This chapter has aimed to describe the basic theory of the three pillars of this thesis: reflection on surfaces much bigger than the wavelength using optical approaches, the analysis of electromagnetic sources using vector potentials and the analysis of 2D periodic structures using Floquet's Theorem.

Since these three pillars have Maxwell's Equations as a common source, their review in Section 2.2 has been the starting point. Then in Section 2.3 Geometrical Optics has been reviewed in order to describe how rays propagate in a medium and how they reflect on a surface whose dimensions are much larger than the wavelength. Section 2.4 has reviewed the needed theory to model the ideal sources that will be used as feeds for the reflectors, and how to obtain the far-field from the reflector's aperture and surface. Finally, Section 2.5 has focused on the analysis of periodic 2D structures by Floquet's theorem and how the S-parameters can be used to obtain the reflected field from these surfaces.

References

[1] C. A. Balanis, *Antenna Theory: Analysis and Design*, 3rd ed. Wiley & Sons, 2015.

[2] K. Barkeshli, *Advanced Electromagnetic and Scattering Theory.* Springer, 2015.

[3] M. Born and E. Wolf, *Principles of Optics*, 6th ed. Cambridge Uni. Press, 1998.

[4] R. S. Elliot, "Chapter 10 - Reflector and lenses," in *Antenna Theory and Design.* Wiley & Sons, 2003.

[5] C. A. Balanis, *Advanced Engineering Electromagnetics*, 2nd ed. Wiley & Sons, 2012.

[6] G. B. Keller, "Geometrical theory of diffraction," *J. Opt. Soc. Amer.*, vol. 52, no. 2, pp. 116–130, Feb 1962.

[7] R. G. Kouyoumjian and P. H. Pathak, "A uniform geometrical theory of diffraction for an edge in a perfectly conducting surface," *Proceedings of the IEEE*, vol. 62, no. 11, pp. 1448–1461, Nov 1974.

[8] B. A. Munk, *Frequency Selective Surfaces: Theory and Design.* Wiley & Sons, 2000.

[9] J. Huang and J. A. Encinar, *Reflectarray Antennas.* Wiley & Sons, 2008.

[10] D. Rodriguez-Prado, "Advanced techniques for the analysis and synthesis of reflectarray antennas with applications in near and far fields," Ph.D. dissertation, Universidad de Oviedo, Spain, June 2016.

[11] M. Zhou *et al.*, "The generalized direct optimization technique for printed reflectarrays," *IEEE Trans. Antennas Propag.*, vol. 62, no. 4, pp. 1690–1700, April 2014.

[12] P. Y. Ufimtsev, *Fundamentals of the Physical Theory of Diffraction.* Wiley & Sons, 2007.

[13] D. M. Pozar, *Microwave Engineering*, 4th ed. Wiley & Sons, 2012.

[14] R. Feynman, R. B. Leighton, and M. Sands, *The Feynman Lectures on Physics, Vol. 1.* Basic Books, 2011.

[15] J. D. Jackson, *Classical Electrodynamics*, 3rd ed. Wiley & Sons, 1999.

[16] S. T. Sharma, S. Rao, and L. Shafai, *Handbook of Reflector Antennas and Feed Systems, vol. I: Theory and Design of Reflectors.* Artech House, 2013.

[17] V. Galindo-Israel and R. Mittra, "A new series representation for the radiation integral with application to reflector antennas," *IEEE Trans. Antennas Propag.*, vol. 25, no. 4, pp. 631–641, Sept 1977.

[18] W. V. T. Rusch and P. D. Potter, *Analysis of Reflector Antennas.* Academic Press, Inc., 1970.

[19] R. G. Kouyoumjian, "Asymptotic high-frequency methods," *Proceedings of the IEEE*, vol. 53, no. 8, pp. 864–876, Aug 1965.

[20] S. Ramo, J. R. Whinnery, and T. van Duzer, *Fields and Waves in Communication Electronics.* Wiley & Sons, 1965.

[21] S. Silver, *Microwave Antenna Theory and Design.* McGraw-Hill, 1949.

[22] R. G. Kouyoumjian and P. H. Pathak, "The dyadic diffraction coefficient for a curved edge," ElectroScience Lab, Dep. Elec. Eng., Ohio State Uni, Columbus, Rep. 3001-3, prepared under Grant NGR 36-008-144 for NASA, Langley Research Centre, Hampton, Va, Tech. Rep., Aug 1973.

[23] J. C. Vardaxoglou, *Frequency Selective Surfaces: Analysis and Design.* Wiley & Sons, 1997.

[24] R. F. Harrington, *Field Computation by Moment of Methods.* IEEE Press, 1993.

[25] R. Mittra, C. H. Chan, and T. Cwik, "Techniques for analyzing frequency selective surfaces - a review," *Proceedings of the IEEE*, vol. 76, no. 12, pp. 1593–1615, Dec 1988.

[26] A. W. Glisson and D. R. Wilton, "Simple and efficient numerical methods for problems of electromagnetic radiation and scattering from surfaces," *IEEE Trans. Antennas Propag.*, vol. 28, no. 5, pp. 593–603, Sept 1980.

[27] S. M. Rao, D. R. Wilton, and A. W. Glisson, "Electromagnetic scattering by surface of arbitrary shape," *IEEE Trans. Antennas Propag.*, vol. 30, no. 3, pp. 409–411, May 1982.

[28] E. Jorgensen, J. L. Volakis, P. Meincke, and O. Breinbjerg, "Higher order hierarchical legendre basis functions for electromagnetic modeling," *IEEE Trans. Antennas Propag.*, vol. 52, no. 11, pp. 2985–2995, Nov 2004.

[29] M. Zhou *et al.*, "Accurate and efficient analysis of printed reflectarrays with arbitrary elements using higher-order hierarchical legendre basis functions," *IEEE Antennas and Wireless Propag. Lett.*, vol. 11, pp. 814–817, July 2012.

[30] CST Microwave Studio® [Online]. Available: https://www.cst.com/products/cstmws/.

[31] X. Artiga, D. Bresciani, H. Legay, and J. Perruisseau-Carrier, "Polarimetric control of reflective metasurfaces," *IEEE Antennas and Wireless Propag. Lett.*, vol. 11, pp. 1489–1492, Dec 2012.

Chapter 3

Depolarisation properties of single reflector antennas

3.1 Introduction

In order to study the depolarisation properties of single reflector antennas, the following information is required:

- Geometry of the reflector and reflection properties at its surface.
- Position of the feed and its fields at the reflector surface.
- Clear definition of polarisation used both by the feed and by the reflector.
- Numerical tools to obtain the far-field as an inverse Fourier Transform of the aperture fields or surface currents.

This chapter will start with the definition of the different coordinate systems used throught the whole thesis and how to change from one to another. Then a review of the two main configurations: single front-fed and single offset reflectors. In the literature, several kinds of geometries have been used for the reflector surface, following the different conic sections [1]: planar, spherical, ellipsoidal, hyperboloidal or paraboloidal. The focus will be on the paraboloidal reflectors, due to their high gain capabilities, being the most prevalent in space communications [2].

The different types of ideal feeds and their polarisation definition will also be reviewed: electric and magnetic dipoles, Huygens source, Gaussian beam and cir-

cularly polarised source. As it will be demonstrated, the electric and magnetic dipoles give rise to cross-polarised field after reflection on the surface of a front-fed parabolic reflector [3]. Due to symmetries between the cross-polarised components of the electric and magnetic dipoles, they can be combined (with the proper ratio between them) to suppress the cross-polarisation [4]. This combination is known as Huygens source. The Gaussian beam source is a special type of Huygens source with some additional control on its directivity [5]. The circularly polarised source introduced here is a combination of two Gaussian beams with the proper phase and magnitude relations. The depolarisation properties of these sources when feeding a front-fed reflector will be analysed at the reflector aperture. General equations will be provided.

The aperture blocking of the struts and feed in front-fed configurations introduce losses and scattering effects that deteriorate the directivity and sidelobe levels, and ultimately depolarisation of the signal [6]. Offset configurations can be employed to reduce the interference from the struts and the feed itself. However, as it will be described, offset configurations introduce cross-polarisation even when fed by the Huygens source. The origin and properties of this cross-polarisation will be discussed with the aid of closed equations and graphs.

Two methods to obtain the far-field of reflector antennas by quasi-optical approaches can be found in the literature: the aperture distribution method (commonly known as GO) and the current distribution method (commonly known as PO) [7]. The accuracy of these methods to obtain the far-field will be discussed and compared by simulations and closed equations. The far-field beam squint [6] in offset reflectors fed by circularly polarised sources will be reviewed. An explanation on its origin will be provided. Finally, a comparison between two numerical methods to implement the integrals to obtain the far-field will be held.

To validate all this theory, a tool written in MATLAB [8] has been developed. As it will be shown, the tool matches with the results obtained by the preferred tool in the market for reflector antenna analysis and design (also based on quasi-optical approaches), GRASP from TICRA [5].

3.2 Coordinate System defitions and transformations

In order to analyse the depolarisation properties and far-field characteristics of reflector antennas, different coordinate systems are needed. Fig. 3.1 shows the four different coordinate systems used in this thesis. The first coordinate system (CS) is the one defined by the feed position, known as *feed CS* and shown in Fig. 3.1a. As it will be shown in Section 3.5, a second coordinate system known as *non-tilted CS* is very useful to study the depolarisation properties of offset reflector antennas at the reflector aperture. This coordinate system, shown in Fig. 3.1b, shares the same origin that the feed CS but with no offset. Therefore, for front-fed configurations, feed CS and non-tilted CS are the same. These two coordinate systems will be the only ones used in Sections 3.3-3.5. A third coordinate system known as *local CS* is defined by the unit vector locally normal to the surface, as seen in Fig. 3.1c. This coordinate system will be used in the following chapters to define the local coordinate systems of the unit-cells that form a frequency selective surface (see Section 2.5). Finally, the fourth coordinate system is defined by the reflector antenna far-field origin, and shown in Fig. 3.1d. For the front-fed configuration, the z-axis of the far-field CS and the broadside direction of the feed are aligned, but for the offset configuration they are not. This coordinate system will be used in Section 3.6 to obtain the reflector antenna far-field.

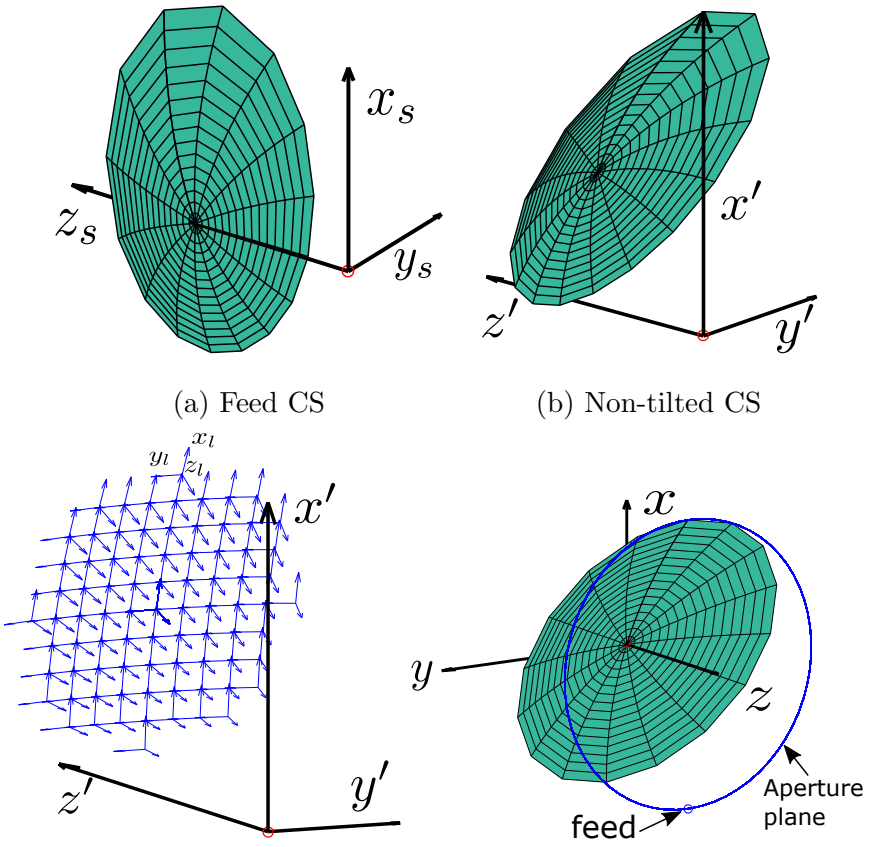

(a) Feed CS (b) Non-tilted CS

(c) Local CS (d) Far-field CS

Figure 3.1: 3D Reflector using: a) the feed CS, b) the non-tilted CS, c) the local CS and d) the far-field CS

Therefore, the four coordinate systems to be employed can be defined as:

- *Feed CS*: defined by the feed radiation pattern, where the z-axis matches the feed broadside direction

$$\{\hat{c}_s\} = \begin{Bmatrix} \hat{x}_s \\ \hat{y}_s \\ \hat{z}_s \end{Bmatrix} \qquad \{\hat{s}_s\} = \begin{Bmatrix} \hat{\rho}_s \\ \hat{\theta}_s \\ \hat{\phi}_s \end{Bmatrix} \tag{3.2.1}$$

- *Non-tilted CS*: same origin as the feed CS but with no offset

$$\{\hat{c}'\} = \begin{Bmatrix} \hat{x}' \\ \hat{y}' \\ \hat{z}' \end{Bmatrix} \qquad \{\hat{s}'\} = \begin{Bmatrix} \hat{\rho}' \\ \hat{\theta}' \\ \hat{\phi}' \end{Bmatrix} \tag{3.2.2}$$

- *Local CS*: defined by a given point in the reflector surface, where the z-axis matches the local normal unit vector

$$\{\hat{c}_l\} = \begin{Bmatrix} \hat{x}_l \\ \hat{y}_l \\ \hat{z}_l \end{Bmatrix} \qquad \{\hat{s}_l\} = \begin{Bmatrix} \hat{\rho}_l \\ \hat{\theta}_l \\ \hat{\phi}_l \end{Bmatrix} \tag{3.2.3}$$

- *Far-field CS*: defined by the far-field pattern where the z direction matches the secondary pattern broadside direction

$$\{\hat{c}\} = \begin{Bmatrix} \hat{x} \\ \hat{y} \\ \hat{z} \end{Bmatrix} \qquad \{\hat{s}\} = \begin{Bmatrix} \hat{\rho} \\ \hat{\theta} \\ \hat{\phi} \end{Bmatrix} \tag{3.2.4}$$

If the feed CS, shown in Fig. 3.1a is used as reference, the non-tilted CS, shown in Fig. 3.1b, is obtained by rotating the feed CS around its y_s-axis a specific quantity. This quantity is equal to the offset angle but with opposite sign. Consequently, both feed and non-tilted CS share the origin. The local CS in Fig. 3.1c is obtained from the non-tilted CS if a special transformation is applied (see Appendix D). Finally, the far-field CS, shown in Fig. 3.1d is obtained by rotating 180° the non-tilted CS around the x'-axis (so that its z direction matches the reflector antenna broadside direction) and by displacing the origin an specific amount. This amount is the one that place the origin at the reflector centre, as shown in Fig. 3.1d. If the far-field CS is used as the reference, the inverse procedure should be followed.

To perform these changes using a general procedure, the Eulerian angles will be used. Rahmat-Samii dedicated a paper to coordinate system changes with antenna applications [9]. The same procedure will be used here. The Eulerian angles are represented in Fig.3.2. Following Euler's rotation theorem, *any rotation may be described using three angles*. These angles, known as Eulerian or Euler angles are α, β and γ.

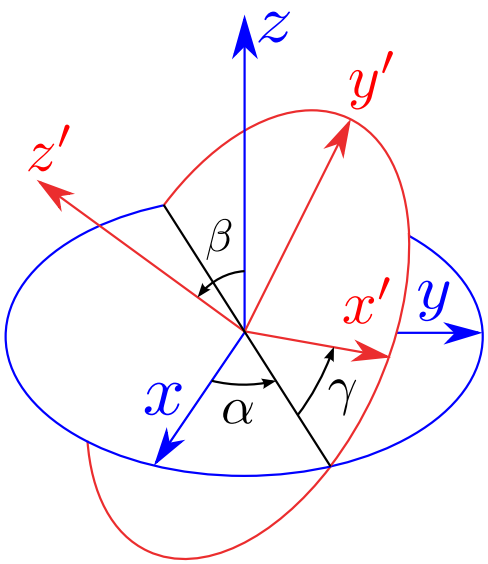

Figure 3.2: Eulerian angles.

where α describes a rotation of the x-axis along the z-axis. β describes a rotation of the z-axis along the x-axis. And γ describes a second rotation of the x-axis along the z-axis. Therefore, the general rotation matrix can be expressed as a multiplication of the three Euler rotation matrices

$$\mathbf{A} = \mathbf{BCD} = \begin{bmatrix} A_{11} & A_{12} & A_{13} \\ A_{21} & A_{22} & A_{23} \\ A_{31} & A_{32} & A_{33} \end{bmatrix} \tag{3.2.5}$$

where,

$$\mathbf{B} = \begin{bmatrix} \cos\gamma & \sin\gamma & 0 \\ -\sin\gamma & \cos\gamma & 0 \\ 0 & 0 & 1 \end{bmatrix} \tag{3.2.6a}$$

$$\mathbf{C} = \begin{bmatrix} 1 & 0 & 0 \\ 0 & \cos\beta & \sin\beta \\ 0 & -\sin\beta & \cos\beta \end{bmatrix} \tag{3.2.6b}$$

$$\mathbf{D} = \begin{bmatrix} \cos\alpha & \sin\alpha & 0 \\ -\sin\alpha & \cos\alpha & 0 \\ 0 & 0 & 1 \end{bmatrix} \tag{3.2.6c}$$

and

$$A_{11} = \cos\gamma\cos\alpha - \sin\gamma\cos\beta\sin\alpha \tag{3.2.7a}$$

$$A_{12} = \cos\gamma\sin\alpha + \sin\gamma\cos\beta\cos\alpha \tag{3.2.7b}$$

$$A_{13} = \sin\gamma\sin\beta \tag{3.2.7c}$$

$$A_{21} = -\sin\gamma\cos\alpha - \cos\gamma\cos\beta\sin\alpha \tag{3.2.7d}$$

$$A_{22} = -\sin\gamma\sin\alpha + \cos\gamma\cos\beta\cos\alpha \tag{3.2.7e}$$

$$A_{23} = \cos\gamma\sin\beta \tag{3.2.7f}$$

$$A_{31} = \sin\beta\sin\alpha \tag{3.2.7g}$$

$$A_{32} = -\sin\beta\cos\alpha \tag{3.2.7h}$$

$$A_{31} = \cos\beta \tag{3.2.7i}$$

Using Eq.3.2.5 it is possible to move between a coordinate system $\{\hat{c}_1\}$ defined by $\vec{r}_1 = \hat{x}_1 x_1 + \hat{y}_1 y_1 + \hat{z}_1 z_1$ to another coordinate system $\{\hat{c}_2\}$ defined by $\vec{r}_2 = \hat{x}_2 x_2 + \hat{y}_2 y_2 + \hat{z}_2 z_2$ and displaced by a quantity$\vec{f} = \hat{x} f_x + \hat{y} f_y + \hat{z} f_z$, as

$$\vec{r}_2 = \mathbf{A}\left(\vec{r}_1 - \vec{f}\right) \tag{3.2.8a}$$

$$\vec{r}_1 = \mathbf{A}^t \vec{r}_2 + \vec{f} \tag{3.2.8b}$$

and for fields defined in these coordinate systems as

$$\vec{S}_2 = \mathbf{A}\vec{S}_1 \tag{3.2.9a}$$

$$\vec{S}_1 = \mathbf{A}^t \vec{S}_2 \tag{3.2.9b}$$

where $\vec{S}$ stands both for electric or magnetic field. The Eulerian angles for the difference CS changes can be summarized in table 3.1.

CS change	$\boldsymbol{\alpha}$	$\boldsymbol{\beta}$	$\boldsymbol{\gamma}$
Far-field $\Leftrightarrow$ feed	$90°$	$180° - \theta_f$	$90°$
Far-field $\Leftrightarrow$ non-tilted	$90°$	$180°$	$90°$
feed $\Leftrightarrow$ non-tilted	$-90°$	$-\theta_f$	$90°$

Table 3.1: Eulerian angles for the different CS changes

3.3 Reflectors

A parabolic reflector can be curved in one or in both of its two axes. The ones that are single curved are usually referred to as *parabolic cylinder reflectors*, and the ones which are double curved as *paraboloidal reflectors*. In this chapter only the second case is taken into account. Firstly, the single front-fed configuration will be reviewed, followed by the single offset configuration.

3.3.1 Front-fed configuration

Geometry of the front-fed reflector

If a parabola is rotated around its axis, a paraboloid of revolution is formed. The reflectors discussed here follow the geometry of these surfaces. The paraboloids used for these reflectors are usually circular paraboloids, which are a special case of elliptic paraboloids. The equation for these circular paraboloids can be derived from the 2D case of Eq.E.0.4 in Appendix E

$$-\frac{x^2}{4f} - \frac{y^2}{4f} + f = z \tag{3.3.1}$$

where $a = -\frac{1}{4f}$, $b = 0$ and $c = f$. One of the principal properties of these reflectors is to convert a spherical wave into a planar wave [10]. This is due to the fact that the rays emanating from one focus of the conic section are reflected on its surface and directed to the second focus, placed at infinity. From Section 2.3, GO can be

applied so that optical rays and optical laws of reflection can be used to describe the paths followed by the wave. Fig. 3.3 shows the two-dimensional configuration of a paraboloidal reflector:

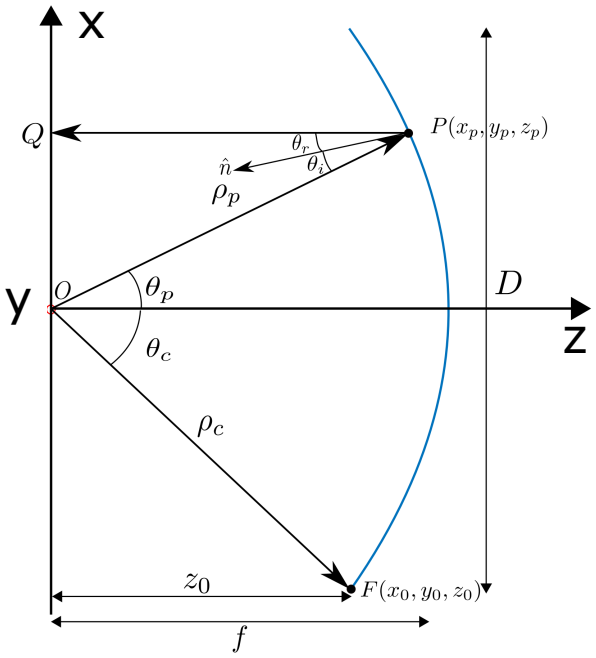

Figure 3.3: 2-D geometry of the reflector.

The origin of the coordinate system is placed at the focus. In order to benefit from the advantages of the parabola, the feed (ideal point source) is also placed at the focus. The parameters of interest are:

- D: length of the reflector.
- f: focal distance to the reflector.
- θ_c: aperture angle.
- $\hat{n}$: unit vector locally normal to the surface.
- θ_i: angle of incidence.
- θ_r: angle of reflection.

The paths OP and PQ are, respectively

$$OP = \rho_p \tag{3.3.2a}$$

$$PQ = \rho_p \cos\theta_p \tag{3.3.2b}$$

By the definition of the parabola (see Appendix E), the summation of the total path from O to any P_n on the reflector surface and from any P_n to its correspondent Q_n is equal for any pair P_n-Q_n

$$OP + PQ = constant = 2f \tag{3.3.3}$$

Substituting Eq. 3.3.2a and 3.3.2b into Eq. 3.3.3 yields

$$\rho_p + \rho_p \cos\theta_p = \rho_p(1 + \cos\theta_p) = 2f \tag{3.3.4}$$

It is noted that $\theta_p \leq \theta_c$. From Eq.3.3.4, the parabola equation in spherical coordinates can be obtained

$$\rho_p = \frac{2f}{1 + \cos\theta_p} = \frac{f}{\cos^2\frac{\theta_p}{2}} = f\sec^2\frac{\theta_p}{2} \tag{3.3.5}$$

It can be observed from Eq.3.3.5 that the surface geometry (ρ_p) is independent of ϕ due to the rotational symmetry. Eq.3.3.1 can be verified if Eq.3.3.5 is converted to Cartesian using Appendix F.

Normal unit vector, angle of incidence and angle of reflection

In this subsection three important parameters are obtained: the unit vector normal to the surface $\hat{n}$, the angle of incidence θ_i and the angle of reflection θ_r.

In property 5) of Section 2.3.2 it was stated that by Snell's law of reflection, a ray incident to a perfectly conducting planar surface is reflected from that surface by an angle equal to the incident angle. It was also stated that the conformal surface of the paraboloid is locally seen as a planar surface for a ray since the wavelength is very small compared to the reflector dimensions. Therefore, the angle formed by the incident ray with the normal to the surface has to be the same as the angle formed by the normal to the surface with the reflected ray, as shown in Fig. 3.3.

To obtain the normal to the surface, the gradient of Eq.3.3.4 is taken

$$\vec{N} = \nabla\left(f - \rho_p \cos^2\frac{\theta_p}{2}\right) = -\hat{\rho}_p \cos^2\frac{\theta_p}{2} + \hat{\theta}_p \cos\frac{\theta_p}{2}\sin\frac{\theta_p}{2} \tag{3.3.6}$$

To form the unit vector, the magnitude $|N|$ is needed

$$|N| = \sqrt{\cos^4\frac{\theta_p}{2} + \cos^2\frac{\theta_p}{2}\sin^2\frac{\theta_p}{2}} = \cos\frac{\theta_p}{2} \tag{3.3.7}$$

Finally, the normal unit vector in spherical coordinates can be obtained as

$$\hat{n} = \frac{\vec{N}}{|N|} = -\hat{\rho}_p \cos\frac{\theta_p}{2} + \hat{\theta}_p \sin\frac{\theta_p}{2} \tag{3.3.8}$$

It is also useful to express the normal unit vector in rectangular coordinates. Applying the coordinates transformation (see Appendix F) leads to

$$\hat{n} = -\hat{x}_p \sin\frac{\theta_p}{2}\cos\phi_p - \hat{y}_p \sin\frac{\theta_p}{2}\sin\phi_p - \hat{z}_p \cos\frac{\theta_p}{2} \tag{3.3.9}$$

Balanis [11] used this method for obtaining the normal unit vector. However, other authors obtained it or expressed it in a different way, such as Jones [3], Rudge, Love and Olver [12], or Hanfling [13]. There is also a third way for defining it very convenient for the future transformation to the tilted axes of the offset reflector:

$$\hat{n} = -\hat{x}\frac{\sin\theta_p\cos\phi_p}{\sqrt{2(1+\cos\theta_p)}} - \hat{y}\frac{\sin\theta_p\sin\phi_p}{\sqrt{2(1+\cos\theta_p)}} - \hat{z}\frac{1+\cos\theta_p}{\sqrt{2(1+\cos\theta_p)}} \tag{3.3.10}$$

Knowing the normal unit vector, both angles θ_i and θ_r can be obtained

$$\cos\theta_i = -\hat{\rho}_p\hat{n} = -\hat{\rho}_p\left(-\hat{\rho}_p\cos\frac{\theta_p}{2} + \hat{\theta}_p\sin\frac{\theta_p}{2}\right) = \cos\frac{\theta_p}{2} \tag{3.3.11a}$$

$$\cos\theta_r = -\hat{z}_p\hat{n} = -\left(\hat{\rho}_p\cos\theta_p - \hat{\theta}_p\sin\theta_p\right)\left(-\hat{\rho}_p\cos\frac{\theta_p}{2} + \hat{\theta}_p\sin\frac{\theta_p}{2}\right) = \cos\frac{\theta_p}{2} \tag{3.3.11b}$$

These relations confirm the split of θ_p into two equal angles by the normal unit vector: $\theta_i = \theta_r = \theta_p/2$, in agreement with Snell's law (see property 5) of Section 2.3.2) and with Fig. 3.3.

Angular aperture

Here the relationship between the ratio of focal length f (see Fig. 3.3) to diameter D is obtained. This ratio specifies the shape of the reflector. Another way to specify this is by the angular aperture θ_c, that is, the angle subtended at the focus by the radius of aperture [10]. From the geometry of Fig. 3.3

$$\theta_c = \tan^{-1} \frac{D/2}{z_0} \tag{3.3.12}$$

where z_0 is the distance along the axis of the reflector from the focal point to the edge of the rim. From Eq. 3.3.1

$$z_0 = f - \frac{x_0^2 + y_0^2}{4f} = f - \frac{(D/2)^2}{4f} = f - \frac{D^2}{16f} \tag{3.3.13}$$

Substituting Eq. 3.3.13 into Eq. 3.3.12 yields

$$\theta_c = \tan^{-1} \frac{D/2}{f - \dfrac{D^2}{16f}} = \tan^{-1} \frac{\dfrac{f}{2D}}{(\dfrac{f}{D})^2 - \dfrac{1}{16}} \tag{3.3.14}$$

There are also other ways of expressing this equation [10, 11]:

$$\sin\theta_c = \frac{D/2}{\rho_0} = \frac{D/2}{\sqrt{4f(f - z_0) + z_0^2}} = \frac{D/2}{2f - z_0} = \frac{1}{2} \frac{\dfrac{D}{f}}{1 + \dfrac{D^2}{16f^2}} \tag{3.3.15}$$

$$\tan\theta_c = \frac{1}{2} \frac{\dfrac{D}{f}}{1 - \dfrac{D^2}{16f^2}} \tag{3.3.16}$$

Finally, it can be observed that a cone can be traced with the feed in the apex, and sides $\rho_c = 2f/(1 + \cos\theta_c)$. These sides are formed by the lines from the feed to the rims of the reflector. The circle formed by the base of this cone would be what is called aperture plane, with centre $(0, 0)$ and diameter D.

3.3.2 Offset configuration

As previously stated in Chapter 1, the aperture blocking in the front-fed configuration leads to some scattered radiation causing, amongst other things, losses in the radiation pattern, degradation in the sidelobes and even giving rise to a degree of cross-polarisation.

An offset parabolic reflector can be regarded as the illuminated offset section of a bigger imaginary paraboloid. Therefore, the feed is still placed at the focus of the paraboloid, but its broadside direction no longer matches the vertex of the paraboloid anymore, as shown in Fig. 3.4. Nevertheless, this configuration brings its own problems, since the loss of symmetry between the feed and the reflector causes new cross-polarisation radiation. This configuration has been well studied by various authors [10, 12, 14].

The analysis of this configuration will be reviewed in the following subsections, following the same structure as in the front-fed case.

Geometry of the offset reflector

The geometry of the offset configuration is shown in Fig. 3.4. The basic parameters and axes are (see Section 3.2 for the coordinate system definitions):

- f: focal length.
- D: diameter of the parent imaginary front-fed reflector.
- d: diameter of the offset reflector, or diameter of the projected circle.
- h: reflector offset.
- x_c: distance along the x-axis to the centre of the projected circle.
- θ_0: offset angle.
- θ_c: aperture angle, or, half angle subtended by the reflector at the focus.
- (x', y', z'): Cartesian coordinates for the non-tilted coordinate system (CS).
- (x_s, y_s, z_s): Cartesian coordinates for the feed CS.
- (ρ', θ', ϕ'): spherical coordinates for the non-tilted CS.

- $(\rho_s, \theta_s, \phi_s)$: spherical coordinates for the feed CS.

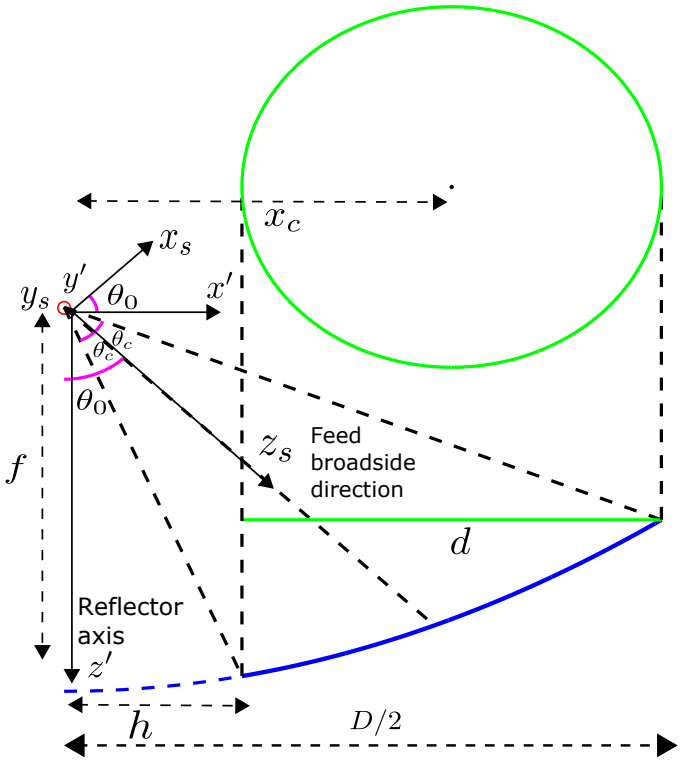

Figure 3.4: Geometry of the offset configuration.

If a cone is traced with the feed in the apex and the lines that join the apex with the rims of the offset reflector as sides, an ellipse in the $x_s y'$ plane would be formed if observed from above. If this ellipse is projected onto the $x'y'$ plane, a circle with centre at x_c and diameter d is obtained. The aperture plane would be this circle.

A coordinate transformation is needed from the feed spherical CS to the non-tilted Cartesian CS: $(\rho_s, \theta_s, \phi_s) \rightarrow (\rho', \theta', \phi') \rightarrow (x', y', z')$. This change is important since the polarisation characteristics of the antenna will be studied at the aperture plane, defined by the non-tilted CS. First, the Cartesian to spherical transformation for the tilted system is (see Appendix F)

$$\hat{\rho}_s = \hat{x}_s \sin\theta_s \cos\phi_s + \hat{y}_s \sin\theta_s \sin\phi_s + \hat{z}_s \cos\theta_s \tag{3.3.17a}$$

$$\hat{\theta}_s = \hat{x}_s \cos\theta_s \cos\phi_s + \hat{y}_s \cos\theta_s \sin\phi_s - \hat{z}_s \sin\theta_s \tag{3.3.17b}$$

$$\hat{\phi}_s = -\hat{x}_s \sin\phi_s + \hat{y}_s \cos\phi_s \tag{3.3.17c}$$

From the geometry of Fig. 3.4

$$\hat{x}_s = \hat{x}' \cos\theta_0 - \hat{z}' \sin\theta_0 \tag{3.3.18a}$$

$$\hat{y}_s = \hat{y}' \tag{3.3.18b}$$

$$\hat{z}_s = \hat{x}' \sin\theta_0 + \hat{z}' \cos\theta_0 \tag{3.3.18c}$$

The position vector in both Cartesian systems is identical, i.e., $\rho' \equiv \rho_s$ and $\hat{\rho}' \equiv \hat{\rho}_s$. This simplifies the relations between both coordinate systems. The relation in spherical coordinates can be obtained if Eq. 3.3.18a, 3.3.18b and 3.3.18c are introduced in Eq. 3.3.17a, and then Eq. 3.3.17a is equated to the vector transformation $\hat{\rho}$ from rectangular to spherical for the non-tilted CS. Equating both sides of the last equation in terms of $\hat{x}'$, $\hat{y}'$ and $\hat{z}'$ yields

$$\sin\theta' \cos\phi' = \sin\theta_s \cos\phi_s \cos\theta_0 + \cos\theta_s \sin\theta_0 \tag{3.3.19a}$$

$$\sin\theta' \sin\phi' = \sin\theta_s \sin\phi_s \tag{3.3.19b}$$

$$\cos\theta' = -\sin\theta_s \cos\phi_s \sin\theta_0 + \cos\theta_s \cos\theta_0 \tag{3.3.19c}$$

It is also useful to express $(\rho_s, \theta_s, \phi_s)$ as a function of (x', y', z'), introducing Eq. 3.3.18a, 3.3.18b and 3.3.18c into Eq. 3.3.17a, 3.3.17b and 3.3.17c

$$\begin{aligned}\hat{\rho}_s = {} & \hat{x}'(\sin\theta_s \cos\phi_s \cos\theta_0 + \cos\theta_s \sin\theta_0) + \hat{y}' \sin\theta_s \sin\phi_s \\ & + \hat{z}'(\cos\theta_s \cos\theta_0 - \sin\theta_s \cos\phi_s \sin\theta_0)\end{aligned} \tag{3.3.20a}$$

$$\begin{aligned}\hat{\theta}_s = {} & \hat{x}'(\cos\theta_s \cos\phi_s \cos\theta_0 - \sin\theta_s \sin\theta_0) + \hat{y}' \cos\theta_s \sin\phi_s \\ & - \hat{z}'(\cos\theta_s \cos\phi_s \sin\theta_0 \sin\theta_s \cos\theta_0)\end{aligned} \tag{3.3.20b}$$

$$\hat{\phi}_s = -\hat{x}' \sin\phi_s \cos\theta_0 + \hat{y}'(\cos\phi_s + \sin\phi_s \sin\theta_0) \tag{3.3.20c}$$

From Eq. 3.3.5 and the vector transformation from Appendix F, the distance from the reflector focus to a point on the parabolic surface, ρ_s, is given by

$$\rho' = \frac{2f}{1+\cos\theta'} = \frac{2f}{1+\cos\theta_s\cos\theta_0 - \sin\theta_s\cos\phi_s\sin\theta_0} \tag{3.3.21}$$

To obtain the distance to the centre x_c of the projected circle and its diameter d, several authors, such as Chu and Turrin [6], make use of the widely referenced report by Cook, Elam and Zucker [15]. These authors used the equation of the ellipse to obtain the projected circle. However, these two parameters can also be obtained from simple trigonometry extracted from Fig. 3.4.

It should be noted that the distance to the parabola $\rho_0 = 2f/(1+\cos\theta_0)$, even when splitting the cone aperture in two equal angles θ_c, does not divide the parabola surface or the aperture plane into two equal parts. Therefore, to obtain the diameter d, a quantity has to be subtracted from $D/2$. This quantity is obtained using the right triangle of angle $\theta_0 - \theta_c$, and can be found in Fig. 3.4 as the parameter h. The right triangle formed with $D/2$ as side is the one with angle $\theta_0 + \theta_c$. The diameter d can be then obtained as

$$d = \frac{2f\sin(\theta_0+\theta_c)}{1+\cos(\theta_0+\theta_c)} - \frac{2f\sin(\theta_0-\theta_c)}{1+\cos(\theta_0-\theta_c)} = \frac{4f\sin\theta_c}{\cos\theta_c+\cos\theta_0} \tag{3.3.22}$$

On the other hand, to obtain the distance to the centre of the circle the quantity previously extracted should be added to $d/2$

$$x_c = \frac{2f\sin(\theta_0-\theta_c)}{1+\cos(\theta_0-\theta_c)} + \frac{d}{2} = \frac{2f\sin\theta_0}{\cos\theta_c+\cos\theta_0} \tag{3.3.23}$$

The only important parameter left is the normal unit vector of the offset reflector.

Normal unit vector

The normal unit vector $\hat{n}'$ for the offset configuration can be obtained from the normal unit vector of the front-fed configuration, with the pertinent coordinate transformation. If the coordinate transformation to spherical coordinates (see Appendix F) is applied to Eq. 3.3.10, and relation 3.3.19c is applied to the dividend, one obtains

$$\hat{n} = -\frac{\hat{\rho}' + \hat{z}'}{\sqrt{2t}} \tag{3.3.24}$$

where

$$t = 1 + \cos\theta_s \cos\theta_0 - \sin\theta_s \sin\theta_0 \cos\phi_s \tag{3.3.25}$$

For the calculation of the reflected fields in the offset configuration, it is also useful to express the normal unit vector in the non-tilted Cartesian coordinates, first applying the coordinates change for $\hat{\rho}'$ and then the relations from Eq. 3.3.19a, Eq. 3.3.19b and Eq. 3.3.19c

$$\hat{n} = n'_x \hat{x}' + n'_y \hat{y}' + n'_z \hat{z}' \tag{3.3.26}$$

where

$$n'_x = \frac{-(\sin\theta_s \cos\phi_s \cos\theta_0 + \cos\theta_s \sin\theta_0)}{\sqrt{2t}} \tag{3.3.27a}$$

$$n'_y = \frac{-(\sin\theta_s \sin\phi_s)}{\sqrt{2t}} \tag{3.3.27b}$$

$$n'_z = \frac{-t}{\sqrt{2t}} \tag{3.3.27c}$$

3.4 Feeds

Given the importance in the selection of the feed for the depolarisation properties of the reflector antenna, this section will review the different types of linear polarisations and ideal feeds used in the literature, i.e., electric dipole, magnetic dipole, Huygens source, Gaussian beam and circularly polarised source.

In order to obtain the different orientations for a given source, two methodologies can be employed. In the first one, an initial source is defined along a known orientation, and coordinate system transformations are applied to obtain any other orientation. This methodology will be employed in Section 3.6 to move between the different

coordinate systems. The second methodology consists on defining general equations for the sources for a general orientation (ϑ, φ). Then the desired orientation angles are introduced to obtain the source fields for the selected orientation. This second methodology is employed in the present section.

3.4.1 Linear polarisation definitions

The *IEEE Standard* [16] defines the cross-polarisation as "*the polarisation orthogonal to a specified reference polarisation*". As Ludwig stated in [17], this definition is not enough when linear polarisation is used because the direction of the reference polarisation has to be defined first. It follows in [17] three definitions for the principal (co) and cross polarisation components, shown in in Fig. 3.5 (extracted from [17]). This definitions are:

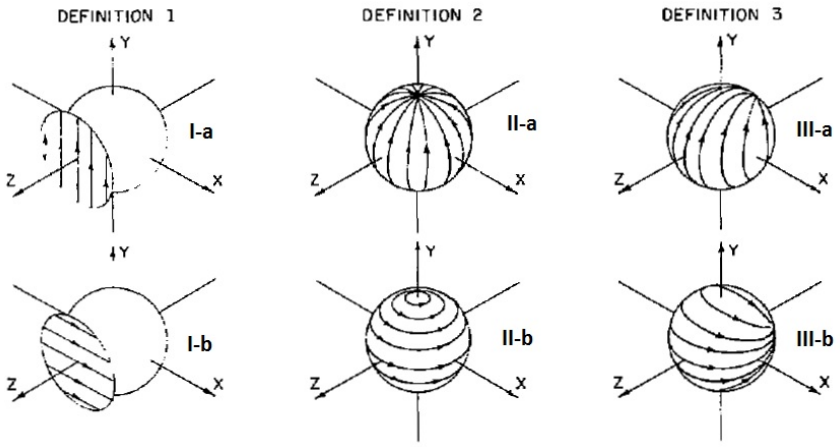

Figure 3.5: Polarisation definitions. (From [17] © 1972 IEEE.)

- Ludwig-I: using a Cartesian coordinate system, and for a propagation along the z-axis, the co-polarisation ($\hat{e}_{co}$) component would be the unit vector in one axis orthogonal to z, and the cross-polarisation ($\hat{e}_{xp}$) component the unit vector in the other axis orthogonal to z. This definition is suitable for plane waves, but unsuitable for spherical waves and can be expressed as:

$$\hat{e}_{co} = \hat{y} = \hat{\rho}\sin\theta\sin\phi + \hat{\theta}\cos\theta\sin\phi + \hat{\phi}\cos\phi \tag{3.4.1a}$$

$$\hat{e}_{xp} = \hat{x} = \hat{\rho}\sin\theta\cos\phi + \hat{\theta}\cos\theta\cos\phi - \hat{\phi}\sin\phi \tag{3.4.1b}$$

- Ludwig-II: using a spherical coordinate system, the co-polarisation would be the unit vector tangent to the spherical surface along one Cartesian axis, and the cross-polarisation the unit vector tangent to the surface along the other axis. This definition is suitable for electric and magnetic dipoles, as Fig. 3.6a shows. The definition can be expressed as:

$$\hat{e}_{co} \propto \hat{\theta}\cos\theta\sin\phi + \hat{\phi}\cos\phi \tag{3.4.2a}$$

$$\hat{e}_{xp} \propto \hat{\theta}\cos\phi - \hat{\phi}\cos\theta\sin\phi \tag{3.4.2b}$$

- Ludwig-III: the co-polarisation and the cross-polarisation components are the ones measured when the antenna pattern is used in the usual matter, as described by Silver [10]. This definition is suitable for the Huygens source, as Fig. 3.6b shows. The definition can be expressed as:

$$\hat{e}_{co} = \hat{\theta}\sin\phi + \hat{\phi}\cos\phi \tag{3.4.3a}$$

$$\hat{e}_{xp} = \hat{\theta}\cos\phi - \hat{\phi}\sin\phi \tag{3.4.3b}$$

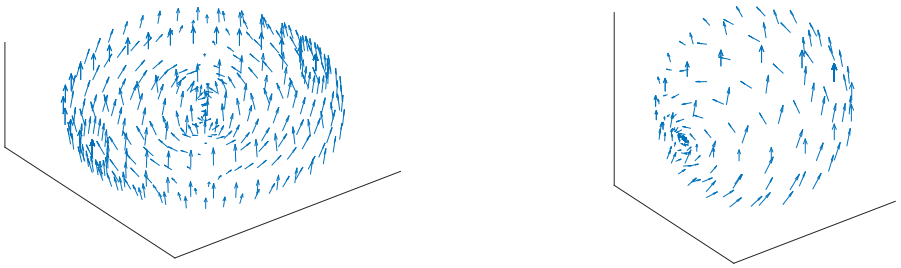

(a) Electric dipole (b) Huygens source

Figure 3.6: Polarisation lines for: (a) electric dipole and (b) Huygens source

In the three cases the y-axis has been used to describe the co-polarisation component. If the polarisation in x-axis is desired, an interchange in the subscripts is needed.

In the literature it can be found that the most adequate definition for real case antennas is Ludwig-III, since "*it closely corresponds to what it is measured by an usual antenna radiation pattern*" [12]. This is true when the antenna pattern procedure is as the one described by Silver [10], i.e., performing the measurement along a sphere in the far-field and assuming spherical waves. Nevertheless, after reflection on a parabolic reflector, when planar waves are assumed locally, the most suitable definition for the polarisation is Ludwig-I. This last statement will be only true for the near-fields, when the study of the fields at the aperture plane is of interest. The definition used for the polarisation in the far-field of a reflector antenna is Ludwig-III [5].

3.4.2 Electric dipole

The basic theory of the electric dipole will be reviewed here, obtaining its fields for a generic orientation.

An electric dipole [10] is formed by two charges of the opposite sign and the same magnitude $|q|$ with a specific separation l between them. Fig. 3.7 shows a conventional electric dipole oriented along the z-axis, i.e., with its current flowing along the z-axis and its electric field flowing from the positive to the negative charge.

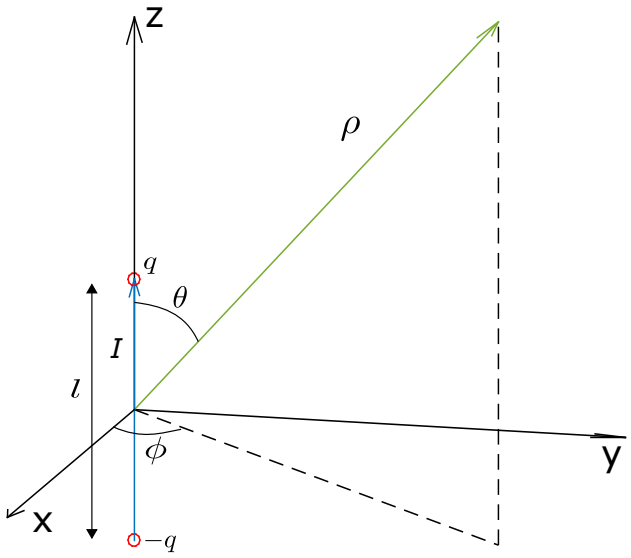

Figure 3.7: Electric dipole.

There are two important assumptions:

- The electric dipole has an infinitesimal size: $l \ll \lambda_0$.
- Far-field conditions apply: $k\rho \gg 1$.

Fig. 3.8 shows the orientation angles φ and ϑ. To obtain the fields, the magnetic vector potential will be used (see Section 2.4). Because the dipole is oriented at a random direction in the space, $\vec{A}$ has components in the three Cartesian axes. Its electric current density $\vec{J}$ also has components in the three axes: $\hat{x}l/2 \sin\vartheta \cos\varphi$, $\hat{y}l/2 \sin\vartheta \sin\varphi$ and $\hat{z}l/2 \cos\vartheta$.

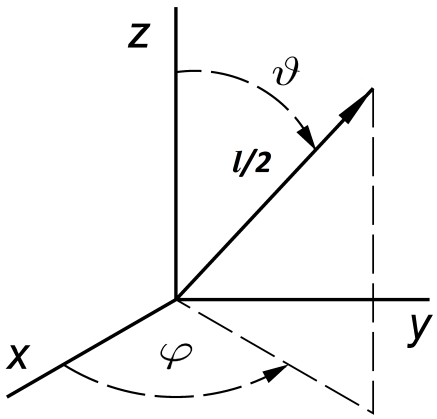

Figure 3.8: Dipole orientation angles.

Using the integration limits ($\vartheta \in [0, \pi]$ and $\varphi \in [0, 2\pi]$) into Eq. 2.4.24 yields

$$\vec{A}(x,y,z) = \frac{\mu I_0}{4\pi\rho} e^{-jk\rho} \left(\hat{x} \int_{-\frac{l}{2}\sin\vartheta\cos\varphi}^{\frac{l}{2}\sin\vartheta\cos\varphi} dx + \hat{y} \int_{-\frac{l}{2}\sin\vartheta\sin\varphi}^{\frac{l}{2}\sin\vartheta\sin\varphi} dy + \hat{z} \int_{-\frac{l}{2}\cos\vartheta}^{\frac{l}{2}\cos\vartheta} dz \right)$$

$$= \frac{\mu I_0 l}{4\pi\rho} e^{-jk\rho} \left(\hat{x}\sin\vartheta\cos\varphi + \hat{y}\sin\vartheta\sin\varphi + \hat{z}\cos\vartheta \right) \tag{3.4.4}$$

where I_0 is the constant value of the electric current. As it is derived from Eq. 3.4.4, a dipole with an orientation that involves the three Cartesian coordinates can be seen as the combination of three dipoles, one on each axis, with a contribution of each dipole given by the orientation angles. To obtain the spherical components of

$\vec{E}$ and $\vec{H}$ it is necessary to express $\vec{A}$ in spherical components (see Appendix F)

$$A_\theta = \frac{\mu I_0 l}{4\pi\rho} e^{-jk\rho} \left(\sin\vartheta\cos\theta(\cos\varphi\cos\phi + \sin\varphi\sin\phi) - \cos\vartheta\sin\theta\right) \tag{3.4.5a}$$

$$A_\phi = \frac{\mu I_0 l}{4\pi\rho} e^{-jk\rho} \sin\vartheta(\sin\varphi\cos\phi - \cos\varphi\sin\phi) \tag{3.4.5b}$$

where A_ρ was omitted since $E_\rho = H_\rho \simeq 0$. Substituting Eq. 3.4.5a and Eq. 3.4.5b into Eq. 2.4.26a and Eq. 2.4.26b gives the spherical components of the electric and magnetic field intensities for the generic electric dipole

$$E_\theta = -j\eta\frac{kI_0 l}{4\pi\rho} e^{-jk\rho} \left(\sin\vartheta\cos\theta(\cos\varphi\cos\phi + \sin\varphi\sin\phi) - \cos\vartheta\sin\theta\right) \tag{3.4.6a}$$

$$E_\phi = -j\eta\frac{kI_0 l}{4\pi\rho} e^{-jk\rho} \sin\vartheta(\sin\varphi\cos\phi - \cos\varphi\sin\phi) \tag{3.4.6b}$$

$$H_\theta = j\frac{kI_0 l}{4\pi\rho} e^{-jk\rho} \sin\vartheta(\sin\varphi\cos\phi - \cos\varphi\sin\phi) \tag{3.4.7a}$$

$$H_\phi = -j\frac{kI_0 l}{4\pi\rho} e^{-jk\rho} \left(\sin\vartheta\cos\theta(\cos\varphi\cos\phi + \sin\varphi\sin\phi) - \cos\vartheta\sin\theta\right) \tag{3.4.7b}$$

For a desired orientation, the values of the angles ϑ and φ have to be introduced into Eq. 3.4.6a and Eq. 3.4.6b for the electric field intensity $\vec{E}$ and into Eq. 3.4.7a and Eq. 3.4.7b for the magnetic field intensity $\vec{H}$.

3.4.3 Magnetic dipole

The magnetic dipole is analogous to the electric dipole but with a magnetic current $\vec{M}$ flowing in a specific direction for a given orientation of the dipole. In order to obtain $\vec{E}$ and $\vec{H}$, the electric vector potential $\vec{F}$ will be used. For a generic orientation $\vec{F}$ is

$$\vec{F}(x,y,z) = \frac{\epsilon M_0 l}{4\pi\rho} e^{-jk\rho} \left(\hat{x}\sin\vartheta\cos\varphi + \hat{y}\sin\vartheta\sin\varphi + \hat{z}\cos\vartheta\right) \tag{3.4.8}$$

where M_0 is the constant value of the magnetic current and l is the length of the dipole. Expressing the above in spherical coordinates (see Appendix F)

$$F_\theta = \frac{\epsilon M_0 l}{4\pi\rho} e^{-jk\rho} \left(\sin\vartheta\cos\theta(\cos\varphi\cos\phi + \sin\varphi\sin\phi) - \cos\vartheta\sin\theta\right) \tag{3.4.9a}$$

$$F_\phi = \frac{\epsilon M_0 l}{4\pi\rho} e^{-jk\rho} \sin\vartheta(\sin\varphi\cos\phi - \cos\varphi\sin\phi) \tag{3.4.9b}$$

To obtain the electric and magnetic field intensities $\vec{E}$ and $\vec{H}$ Eq. 3.4.9a and Eq. 3.4.9b has to be introduced into Eq. 2.4.26c and Eq. 2.4.26d

$$E_\theta = -j\frac{kM_0 l}{4\pi\rho} e^{-jk\rho} \sin\vartheta(\sin\varphi\cos\phi - \cos\varphi\sin\phi) \tag{3.4.10a}$$

$$E_\phi = j\frac{kM_0 l}{4\pi\rho} e^{-jk\rho} \left(\sin\vartheta\cos\theta(\cos\varphi\cos\phi + \sin\varphi\sin\phi) - \cos\vartheta\sin\theta\right) \tag{3.4.10b}$$

$$H_\theta = -j\frac{kM_0 l}{\eta 4\pi\rho} e^{-jk\rho} \left(\sin\vartheta\cos\theta(\cos\varphi\cos\phi + \sin\varphi\sin\phi) - \cos\vartheta\sin\theta\right) \tag{3.4.11a}$$

$$H_\phi = -j\frac{kM_0 l}{\eta 4\pi\rho} e^{-jk\rho} \sin\vartheta(\sin\varphi\cos\phi - \cos\varphi\sin\phi) \tag{3.4.11b}$$

Once again, for a desired orientation, the values of the angles ϑ and φ have to be substituted into Eq. 3.4.10a and Eq. 3.4.10b for the electric field intensity $\vec{E}$ and into Eq. 3.4.11a and Eq. 3.4.11b for the magnetic field intensity $\vec{H}$.

3.4.4 Huygens source

If an electric dipole with a specific orientation is combined with a magnetic dipole oriented along the orthogonal direction, with an appropriate value for the ratio of the magnetic to electric current $M_0/I_0 = \eta_0$, a Huygens source is obtained. Following Ludwig-III (see Section 3.4.1) for the definition of the polarisation, the Huygens source is considered a source free of cross-polarisation. If this source is used as a feed in a front-fed parabolic reflector, the field at the aperture plane is also free of

cross-polarisation, as Koffman pointed out [4]. Indeed, as Koffman concluded, in terms of minimising cross-polarisation the ideal reflector for the Huygens source is the paraboloid, for the electric dipole the plane, and for the magnetic dipole the sphere. Three important properties of the Huygens source can be summarized as:

- The ratio of magnetic to electric current is: $M_0/I_0 = \eta_0$.
- It is a source free of cross-polarisation if Ludwig-III is used for the polarisation definition.
- It is an ideal feed for the front-fed parabolic reflector in terms of achieving zero cross-polarisation in the aperture plane.

The Huygens source can be oriented in different ways, but must always fulfil the following statements:

- The orientation of both electric and magnetic dipoles should always be confined in a plane parallel to the reflector aperture plane.
- There must be orthogonality between their orientations and this orthogonality must follow positive values of φ.

However, to be able to assert that the generic Huygens source is also free of cross-polarisation, the Ludwig-II definition has also to be generalised for a generic orientation. Since the aperture plane of the studied reflectors is contained in the xy plane, the last two statements can be simplified to

- Both electric and magnetic dipoles are in the xy plane. Hence $\vartheta = \pi/2$.
- For an electric dipole oriented at an angle $\varphi = \varphi_0$, the magnetic dipole has to be oriented at $\varphi = \varphi_0 + \pi/2$.

Therefore, the electric dipole has the following spherical components for the electric and magnetic field intensities

$$E_\theta^e = -j\eta \frac{kI_0 l}{4\pi\rho} e^{-jk\rho} \cos\theta (\cos\varphi_0 \cos\phi + \sin\varphi_0 \sin\phi) \tag{3.4.12a}$$

$$E_\phi^e = -j\eta \frac{kI_0 l}{4\pi\rho} e^{-jk\rho} (\sin\varphi_0 \cos\phi - \cos\varphi_0 \sin\phi) \tag{3.4.12b}$$

$$H_\theta^e = j\frac{kI_0 l}{4\pi\rho}e^{-jk\rho}(\sin\varphi_0\cos\phi - \cos\varphi_0\sin\phi) \tag{3.4.13a}$$

$$H_\phi^e = -j\frac{kI_0 l}{4\pi\rho}e^{-jk\rho}\cos\theta(\cos\varphi_0\cos\phi + \sin\varphi_0\sin\phi) \tag{3.4.13b}$$

where the superscript e refers to electric dipole, and knowing that $M_0 = \eta I_0$, $\sin(\varphi_0 + \pi/2) = \cos\varphi_0$ and $\cos(\varphi_0 + \pi/2) = -\sin\varphi_0$. The analogous action for the magnetic dipole yields

$$E_\theta^m = -j\eta\frac{kI_0 l}{4\pi\rho}e^{-jk\rho}(\cos\varphi_0\cos\phi + \sin\varphi_0\sin\phi) \tag{3.4.14a}$$

$$E_\phi^m = -j\eta\frac{kI_0 l}{4\pi\rho}e^{-jk\rho}\cos\theta(\sin\varphi_0\cos\phi - \cos\varphi_0\sin\phi) \tag{3.4.14b}$$

$$H_\theta^m = j\frac{kI_0 l}{4\pi\rho}e^{-jk\rho}\cos\theta(\sin\varphi_0\cos\phi - \cos\varphi_0\sin\phi) \tag{3.4.15a}$$

$$H_\phi^m = -j\frac{kI_0 l}{4\pi\rho}e^{-jk\rho}(\cos\varphi_0\cos\phi + \sin\varphi_0\sin\phi) \tag{3.4.15b}$$

where the superscript m refers to magnetic dipole. Adding the components of both dipoles yields to the spherical far-field components of a Huygens source with the electric dipole oriented along a desired angle φ_0

$$E_\theta = -j\eta\frac{kI_0 l}{4\pi\rho}e^{-jk\rho}(1+\cos\theta)\cos(\varphi_0 - \phi) \tag{3.4.16a}$$

$$E_\phi = -j\eta\frac{kI_0 l}{4\pi\rho}e^{-jk\rho}(1+\cos\theta)\sin(\varphi_0 - \phi) \tag{3.4.16b}$$

$$H_\theta = j\frac{kI_0 l}{4\pi\rho}e^{-jk\rho}(1+\cos\theta)\sin(\varphi_0 - \phi) \tag{3.4.17a}$$

$$H_\phi = -j\frac{kI_0 l}{4\pi\rho}e^{-jk\rho}(1+\cos\theta)\cos(\varphi_0 - \phi) \tag{3.4.17b}$$

When using a Huygens source to feed a parabolic reflector, it is common to define its orientation in space by its electric field polarisation at broadside. And usually for positive values of the Cartesian axes. Common orientations are along x, y and slant 45°. Looking at Eq. 3.4.16a and Eq. 3.4.16b, this means to orient the electric dipole along the opposite sense. Also, since the x-axis is usually oriented vertically for reflector antennas, orientations along x and y are usually referred as vertical and horizontal respectively. It should be noticed that a x- or vertically polarised Huygens source will not always have its electric field along x. Only in the principal planes. For the rest of the planes the polarisation will be given by Ludwig-III. The same applies to other polarisations.

In order to obtain a vertically polarised Huygens source, an electric dipole along $-x$ and a magnetic dipole along $-y$ are needed, where $\varphi_0 = \pi$. Following the same procedure for the other two polarisations, it is possible to express these three typical cases in one single equation for each component

$$E_\theta = j\eta \frac{kI_0 l}{4\pi\rho} e^{-jk\rho}(1+\cos\theta)\cos(\beta_0 - \phi) \tag{3.4.18a}$$

$$E_\phi = j\eta \frac{kI_0 l}{4\pi\rho} e^{-jk\rho}(1+\cos\theta)\sin(\beta_0 - \phi) \tag{3.4.18b}$$

$$H_\theta = -j \frac{kI_0 l}{4\pi\rho} e^{-jk\rho}(1+\cos\theta)\sin(\beta_0 - \phi) \tag{3.4.19a}$$

$$H_\phi = j \frac{kI_0 l}{4\pi\rho} e^{-jk\rho}(1+\cos\theta)\cos(\beta_0 - \phi) \tag{3.4.19b}$$

where β_0 defines the orientation of the polarisation: $\beta_0 = 0$ for a x-polarised source, $\beta_0 = \pi/2$ for a y-polarised source, and $\beta_0 = \pi/4$ for a 45°-polarised source.

3.4.5 Gaussian beam

The main disadvantage of the Huygens source is its poor directivity (see Fig.3.6b) of Section 3.4.1). The most common type of ideal source to feed reflectors is the Gaussian beam, whose electric and magnetic amplitude profiles are given by the

Gaussian function. The simplicity and the directivity control of the Gaussian beam are its key features. The Huygens source can behave as a Gaussian beam if a imaginary displacement in the axis of the direction of propagation $(0, 0, -jb)$ is applied [5]. This imaginary displacement controls the beam width. The far-field for this source is

$$\vec{E} = (1 + \cos\theta)\frac{e^{-jk\rho}}{\rho} e^{kb\cos\theta} \left[\hat{\theta}\cos(\beta_0 - \phi) + \hat{\phi}\sin(\beta_0 - \phi)\right] \tag{3.4.20}$$

where

$$b = \frac{20\log((1 + \cos\theta)/2) - taper}{20k(1 - \cos\theta)\log e} \tag{3.4.21}$$

The variable *taper* represents the desired taper for the feed, which is the desired normalised field value in dB at the rims of the reflector. Typical values of tapers are -10dB or -12dB.

3.4.6 Circularly polarised source

An ideal circularly polarised (CP) source is formed by two ideal linearly-polaried (LP) sources of equal magnitude and 90° of phase difference between them. The sense of rotation of the field can be clockwise or right-handed CP (RHCP), or counterclockwise or left-handed CP (LHCP). A commonly used ideal CP source is formed by the phased superposition of two Ludwig-III [17] (see also Section 3.4.1) LP sources. Therefore, following Fig. 3.9, where the observer is looking in the direction of propagation, the two ideal circular polarisations can be formed as [18]

$$\vec{E}_{RH} = \frac{1}{\sqrt{2}}\left(\vec{E}_V - j\vec{E}_H\right) \tag{3.4.22a}$$

$$\vec{E}_{LH} = \frac{1}{\sqrt{2}}\left(\vec{E}_V + j\vec{E}_H\right) \tag{3.4.22b}$$

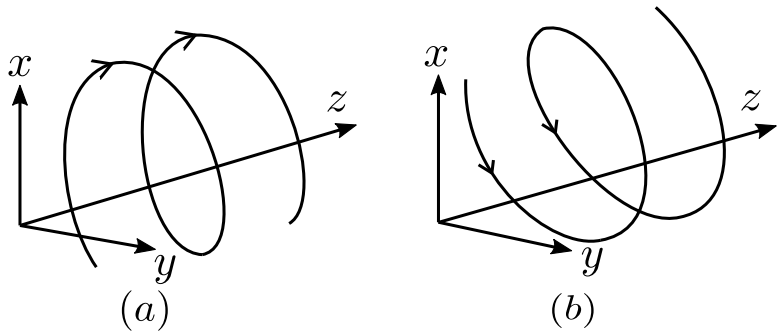

Figure 3.9: Senses of rotation in circularly polarised fields: (a) right-hand and (b) left-hand.

Eq.3.4.22a and Eq.3.4.22b can be expressed in spherical coordinates as

$$\vec{E} = \frac{1}{\sqrt{2}} e^{\mp j\phi} \left(\hat{\theta} E_\theta \mp j \hat{\phi} E_\phi \right) \tag{3.4.23}$$

where the upper signs stand for RHCP and the lower signs for LHCP. Eq.3.4.23 can be found in the literature [1]. The relationship between components can be expressed in matrix form as

$$\begin{bmatrix} E_{RH} \\ E_{LH} \end{bmatrix} = \frac{1}{\sqrt{2}} \begin{bmatrix} 1 & j \\ 1 & -j \end{bmatrix} \begin{bmatrix} E_V \\ E_H \end{bmatrix} \tag{3.4.24}$$

It follows that the trasnformation from RH/LH to vertical/horizontal components is according to:

$$\begin{bmatrix} E_V \\ E_H \end{bmatrix} = \frac{1}{\sqrt{2}} \begin{bmatrix} 1 & 1 \\ -j & j \end{bmatrix} \begin{bmatrix} E_{RH} \\ E_{LH} \end{bmatrix} \tag{3.4.25}$$

It may also be useful to show the transformation from spherical components directly to RH/LH components as

$$\begin{bmatrix} E_{RH} \\ E_{LH} \end{bmatrix} = \frac{1}{\sqrt{2}} \begin{bmatrix} e^{j\phi} & je^{j\phi} \\ e^{-j\phi} & -je^{-j\phi} \end{bmatrix} \begin{bmatrix} E_\theta \\ E_\phi \end{bmatrix} \tag{3.4.26}$$

3.5 Fields at the aperture plane

The aperture plane of the reflector is a plane normal to the reflector axis, usually assumed at the rims of the reflector, as Fig.3.10 shows. At the aperture plane, the paths travelled for all the rays from the feed have the same length, in accordance the definition of the parabola (see Appendix E). By virtue of this property, it can be asserted that the reflector transforms incoming spherical waves into plane waves. This assertion however only holds in the near-field of the reflector.

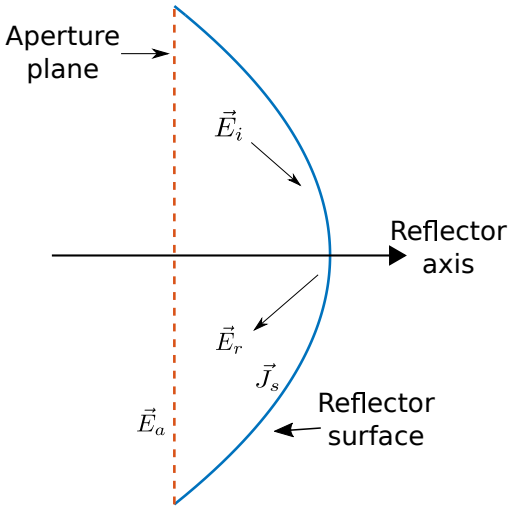

Figure 3.10: Reflector surface and aperture field.

The aperture field for single reflector antennas can be obtained with closed form equations, as will be shown next. These near-fields are especially important when seeking to study the depolarisation properties of single reflector antennas in a simple and compact form. The aperture fields for the front-fed and offset configurations will be obtained for the ideal feeds from Section 3.4 for different orientations.

The polarisation definitions used for each case are summarised in Table 3.2 using the following suppositions (see Section 3.4.1 for Ludwig definitions):

- Before reflection on the reflector surface: far-field spherical wave, whose polarisation definition is given by Ludwig-II or Ludwig-III.
- After reflection on the reflector surface: near-field plane wave, whose polarisation definition is given by Ludwig-I.

Source	**Before reflection**	**After reflection**
Electric dipole	Ludwig-II	Ludwig-I
Magnetic dipole	Ludwig-II	Ludwig-I
Huygens source	Ludwig-III	Ludwig-I
Gaussian beam source	Ludwig-III	Ludwig-I

Table 3.2: Sources and their polarisation definition

First the reflected fields are obtained, expressed in Cartesian coordinates, as a function of the spherical components for a generic feed. Therefore the starting point is the definition of a generic feed in spherical coordinates, whose far-field expression is [11]

$$\vec{E}_i = E^i_\theta \hat{\theta} + E^i_\phi \hat{\phi} \tag{3.5.1}$$

The next step is to obtain the reflected field using Eq. 2.3.37. For a simpler description of the polarisation components, the reflected field will be expressed in Cartesian coordinates, since Ludwig-I applies after reflection. $\vec{E}_i$ and $\hat{n}$ are expressed in Cartesian coordinates as well. Eq. 3.3.9 and Eq. 3.3.24 already give $\hat{n}$ in Cartesian for front-fed and offset configurations respectively. For $\vec{E}_i$, the transformation is (see Appendix F)

$$\vec{E}_i = E^i_x \hat{x} + E^i_y \hat{y} + E^i_z \hat{z} \tag{3.5.2}$$

where

$$E^i_x = E^i_\theta \cos\theta \cos\phi - E^i_\phi \sin\phi \tag{3.5.3a}$$

$$E^i_y = E^i_\theta \cos\theta \sin\phi + E^i_\phi \cos\phi \tag{3.5.3b}$$

$$E^i_z = -E^i_\theta \sin\theta \tag{3.5.3c}$$

Now, a general unit vector normal to the surface $\hat{n}$ in Cartesian coordinates is needed

$$\hat{n} = n_x\hat{x} + n_y\hat{y} + n_z\hat{z} \tag{3.5.4}$$

If Eq. 3.5.2 and Eq. 3.5.4 are substituted into Eq. 2.3.37 the reflected field is obtained for a general feed and the normal unit vector $\hat{n}$ considered above

$$\vec{E}_r = E_x^r\hat{x} + E_y^r\hat{y} + E_z^r\hat{z} \tag{3.5.5}$$

where

$$E_x^r = E_x^i(2{n_x}^2 - 1) + 2n_x(n_yE_y^i + n_zE_z^i) \tag{3.5.6a}$$

$$E_y^r = E_y^i(2{n_y}^2 - 1) + 2n_y(n_xE_x^i + n_zE_z^i) \tag{3.5.6b}$$

$$E_z^r = E_z^i(2{n_z}^2 - 1) + 2n_z(n_xE_x^i + n_yE_y^i) \tag{3.5.6c}$$

It is convenient to express Eq. 3.5.5 in matrix form as

$$\vec{E}_r = \mathbf{N}\vec{E}_i \tag{3.5.7}$$

This 3×3 matrix has been used by Watson and Ghobrial [19], among others:

$$\begin{bmatrix} E_x^r \\ E_y^r \\ E_z^r \end{bmatrix} = \begin{bmatrix} 2{n_x}^2 - 1 & 2n_xn_y & 2n_xn_z \\ 2n_xn_y & 2{n_y}^2 - 1 & 2n_yn_z \\ 2n_xn_z & 2n_yn_z & 2{n_z}^2 - 1 \end{bmatrix} \begin{bmatrix} E_x^i \\ E_y^i \\ E_z^i \end{bmatrix} \tag{3.5.8}$$

Thus, for the reflected field of a desired feed for a desired reflector configuration, each component must be substituted by its specific value in Eq.3.5.8.

3.5.1 Front-fed configuration

Since for the front-fed configuration the non-tilted CS and the feed CS are the same, for simplification purposes only one general CS (ρ, θ, ϕ) will be used. If the reflected

field for the front-fed configuration for a generic feed is desired, the Cartesian components of the normal unit vector in Eq. 3.3.9 have to be introduced into Eq. 3.5.8 yielding

$$\begin{bmatrix} E_x^r \\ E_y^r \\ E_z^r \end{bmatrix} = \begin{bmatrix} (1-\cos\theta)\cos^2\phi - 1 & (1-\cos\theta)\sin\phi\cos\phi & \sin\theta\cos\phi \\ (1-\cos\theta)\sin\phi\cos\phi & (1-\cos\theta)\sin^2\phi - 1 & \sin\theta\sin\phi \\ \sin\theta\cos\phi & \sin\theta\cos\phi & \cos\theta \end{bmatrix} \begin{bmatrix} E_x^i \\ E_y^i \\ E_z^i \end{bmatrix} \tag{3.5.9}$$

Nevertheless, a simplified expression is obtained if the Cartesian components of the feed, i.e., Eq. 3.5.3a, Eq. 3.5.3b and Eq. 3.5.3c, as function of the generic spherical components, are introduced into Eq. 3.5.8

$$\vec{E}_r = \hat{x}(-E_\theta^i\cos\phi + E_\phi^i\sin\phi) + \hat{y}(-E_\theta^i\sin\phi - E_\phi^i\cos\phi) \tag{3.5.10}$$

The simplified equation can be expressed as a 2×2 matrix

$$\begin{bmatrix} E_x^r \\ E_y^r \end{bmatrix} = \begin{bmatrix} d_1 & b_1 \\ -b_1 & d_1 \end{bmatrix} \begin{bmatrix} E_\theta^i \\ E_\phi^i \end{bmatrix} \tag{3.5.11}$$

where $d_1 = -\cos\phi$ and $b_1 = \sin\phi$. The reason for the absence of the z component is due to the definition of the parabola: for an incoming ray, the reflected ray is always parallel to the z-axis, hence there is no z component for any type of point source defined by spherical waves. Therefore, to obtain the reflected field from a front-fed configuration using a specific feed, the spherical components in Eq. 3.5.10 have to be replaced by the spherical components of the desired feed.

Now the feeds from Section 3.4 will be used as primary feeds for the front-fed reflector, obtaining the electric field at the aperture plane for different polarisations.

Electric dipole

Electric dipole along x

For the electric dipole oriented along x the orientation angles are $\vartheta = 90°$ and $\varphi = 0°$ (see Section 3.4.2). Therefore, from Eq. 3.4.6a and Eq. 3.4.6b for the electric

field and Eq. 3.4.7a and Eq. 3.4.7b for the magnetic field, the far-field spherical components of this dipole are

$$E_\theta^i = -j\eta \frac{kI_0 l e^{-jk\rho}}{4\pi\rho} \cos\theta \cos\phi \tag{3.5.12a}$$

$$E_\phi^i = j\eta \frac{kI_0 l e^{-jk\rho}}{4\pi\rho} \sin\phi \tag{3.5.12b}$$

$$H_\theta^i = -j \frac{kI_0 l e^{-jk\rho}}{4\pi\rho} \sin\phi \tag{3.5.13a}$$

$$H_\phi^i = -j \frac{kI_0 l e^{-jk\rho}}{4\pi\rho} \cos\theta \cos\phi \tag{3.5.13b}$$

If the spherical components of the electric field, Eq. 3.5.12a and 3.5.12b, are introduced into the reflected field equation for the front-fed reflector (Eq.3.5.11), along with the phase shift $2f - z_0$ due to the path from the feed to the aperture plane, the field at the aperture plane $\vec{E}_a$ is obtained by

$$\vec{E}_a = j\eta \frac{kI_0 l e^{-jk(2f-z_0)}}{8\pi\rho} \left(\hat{x}(1 + \cos\theta - (1 - \cos\theta)\cos 2\phi) - \hat{y}\sin 2\phi(1 - \cos\theta)\right) \tag{3.5.14}$$

Eq. 3.5.14 was already derived in [3] and [20]. Since Ludwig-I applies after reflection, the x-component belongs to the principal polarisation component and the y-component belongs to the cross polarisation component. As can be seen in Eq. 3.5.14, the y-component of the electric field is non-zero. Therefore, the electric dipole induces some cross-polarisation component at the aperture plane. As can be seen in Eq. 3.5.14, the maximum of the cross-polarised field is obtained at $\phi = 45°$. Fig. 3.11 shows the co- (blue) and cross-polarised (red) components at the aperture plane. It should be noted both components are not in the same scale. As it can be seen in Fig. 3.11, there is a 180° phase shift symmetry in the cross-polarised component between the four quadrants. Toward the principal planes (x- and y-axes) the cross-polarisation tends to 0, disappearing along them.

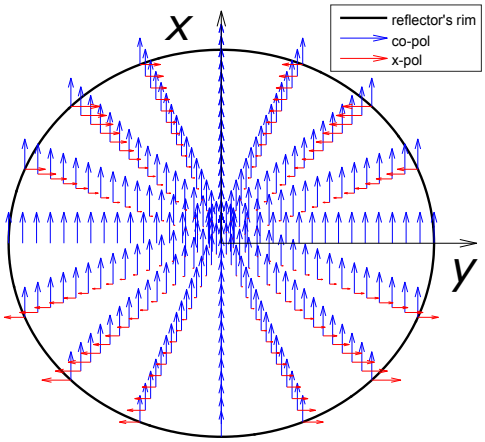

Figure 3.11: Co-polarised and cross-polarised components for a front-fed reflector fed by an electric dipole oriented along x.

Electric dipole along y

For the electric dipole oriented along y the orientation angles are $\vartheta = \varphi = 90°$. Using the same equations that were used for the electric dipole oriented along x (Eq. 3.4.6a and Eq. 3.4.6b, Eq. 3.4.7a and Eq. 3.4.7b) with the new orientation angles, the far-field spherical components of this dipole are

$$E_\theta^i = -j\eta \frac{kI_0 l e^{-jk\rho}}{4\pi\rho} \cos\theta \sin\phi \tag{3.5.15a}$$

$$E_\phi^i = -j\eta \frac{kI_0 l e^{-jk\rho}}{4\pi\rho} \cos\phi \tag{3.5.15b}$$

$$H_\theta^i = j \frac{kI_0 l e^{-jk\rho}}{4\pi\rho} \cos\phi \tag{3.5.16a}$$

$$H_\phi^i = -j \frac{kI_0 l e^{-jk\rho}}{4\pi\rho} \cos\theta \sin\phi \tag{3.5.16b}$$

Once again, the spherical components of the electric field for this new orientation (Eq. 3.5.15a and 3.5.15b) can be introduced into the reflected field equation for the front-fed reflector (Eq. 3.5.11). The phase shift $2f - z_0$ due to the path from the feed to the aperture plane has to be taken into consideration. Then the field at the aperture plane $\vec{E}_a$ is obtained as

$$\vec{E}_a = j\eta \frac{kI_0 l e^{-jk(2f-z_0)}}{8\pi\rho} \left(-\hat{x}\sin 2\phi(1-\cos\theta) + \hat{y}(1+\cos\theta+(1-\cos\theta)\cos 2\phi)\right) \tag{3.5.17}$$

In Eq. 3.5.17, the y-component represents the co-polarised component and the x-component represents the cross-polarised component. Fig.3.12 shows these components at the aperture plane in blue and red respectively. The components are not to scale. As it can be observed in this figure, the symmetry between quadrants is maintained as in the electric dipole oriented along x, and the maximum cross-polarisation is found at 45°.

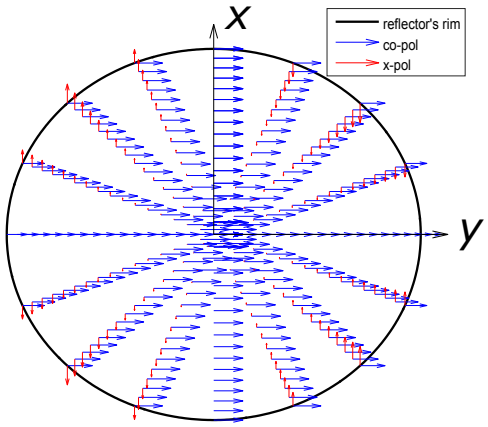

Figure 3.12: Co-polarised and cross-polarised components for a front-fed reflector fed by an electric dipole oriented along y.

Magnetic dipole

Magnetic dipole along x

For the magnetic dipole oriented along x the orientation angles are $\vartheta = 90°$ and $\varphi = 0°$. Therefore, using Eq. 3.4.10a and Eq. 3.4.10b for the electric field and Eq. 3.4.11a and Eq. 3.4.11b for the magnetic field, the spherical components of the magnetic dipole for this orientation are

$$E^i_\theta = j\frac{kM_0 l e^{-jk\rho}}{4\pi\rho}\sin\phi \tag{3.5.18a}$$

$$E^i_\phi = j\frac{kM_0 l e^{-jk\rho}}{4\pi\rho}\cos\theta\cos\phi \tag{3.5.18b}$$

$$H_\theta^i = -j\frac{kM_0 l e^{-jk\rho}}{\eta 4\pi\rho}\cos\theta\cos\phi \tag{3.5.19a}$$

$$H_\phi^i = j\frac{kM_0 l e^{-jk\rho}}{\eta 4\pi\rho}\sin\phi \tag{3.5.19b}$$

Substituting the spherical components of the electric field (Eq. 3.5.18a and 3.5.18b) into the reflected field equation for the front-fed reflector (Eq. 3.5.11), along with the phase shift $2f - z_0$ due to the path from the feed to the aperture plane, the field at the aperture plane $\vec{E}_a$ is given by

$$\vec{E}_a = -j\frac{kM_0 l e^{-jk(2f-z_0)}}{8\pi\rho}\left(\hat{x}\sin 2\phi(1-\cos\theta) + \hat{y}(1+\cos\theta - \cos 2\phi(1-\cos\theta))\right) \tag{3.5.20}$$

Fig.3.13 shows the co- (blue) and cross-polarised (red) components at the aperture plane. They are not to scale. The three characteristics from the electric dipole remain: maximum cross-polarisation at 45°, no cross-polarisation along the principal axes and symmetry between quadrants. Nevertheless, as Fig.3.13 and the sign in Eq.3.5.20 show, there is a shift of 180° in the co-polarised components, if compared with the electric dipole along y.

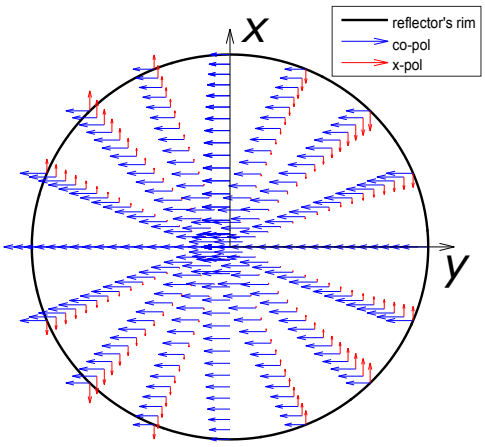

Figure 3.13: Co-polarised and cross-polarised components for a front-fed reflector fed by an magnetic dipole oriented along x.

Magnetic dipole along y

For the magnetic dipole oriented along y the orientation angles are $\vartheta = \varphi =$

90°. Using the same equations that were used for the magnetic dipole oriented along x (Eq. 3.4.10a and Eq. 3.4.10b, Eq. 3.4.11a and Eq. 3.4.11b) with the actual orientation, the spherical components of this dipole are

$$E_\theta^i = -j\frac{kM_0le^{-jk\rho}}{4\pi\rho}\cos\phi \tag{3.5.21a}$$

$$E_\phi^i = j\frac{kM_0le^{-jk\rho}}{4\pi\rho}\cos\theta\sin\phi \tag{3.5.21b}$$

$$H_\theta^i = -j\frac{kM_0le^{-jk\rho}}{\eta 4\pi\rho}\cos\theta\sin\phi \tag{3.5.22a}$$

$$H_\phi^i = -j\frac{kM_0le^{-jk\rho}}{\eta 4\pi\rho}\cos\phi \tag{3.5.22b}$$

If the spherical components of the electric field for this new orientation (Eq. 3.5.21a and 3.5.21b) are introduced into the reflected field equation for the front-fed reflector (Eq. 3.5.11), along with the phase shift $2f - z_0$ due to the path from the feed to the aperture plane, the field at the aperture plane $\vec{E}_a$ is obtained as

$$\vec{E}_a = j\eta\frac{kI_0le^{-jk(2f-z_0)}}{8\pi\rho}\left(\hat{x}(1+\cos\theta+\cos 2\phi(1-\cos\theta)) + \hat{y}\sin 2\phi(1-\cos\theta)\right) \tag{3.5.23}$$

Fig. 3.14 shows the co- (blue) and cross-polarised (red) components at the aperture plane for this dipole. They are not to scale. Once again, the three features associated with the electric dipole (and all cases above) can also be observed here: maximum cross-polarisation at 45°, no cross-polarisation along the principal axes and symmetry between quadrants.

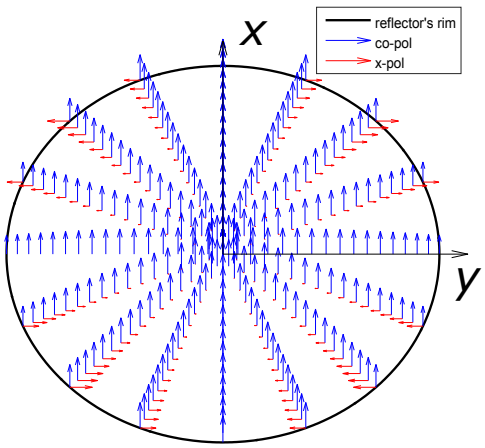

Figure 3.14: Co-polarised and cross-polarised components for a front-fed reflector fed by an magnetic dipole oriented along y.

Huygens source

For the Huygens source two orientations will be applied in reference to the electric dipole: oriented along x and oriented along y.

Huygens source with the electric dipole along x

Following the definitions presented in Section 3.4.4, if a Huygens source with an electric dipole oriented along x is desired, the magnetic dipole should be oriented along y and have for its magnetic current the value $M_0 = \eta I_0$. The orientation angles for the electric dipole along x are $\vartheta = 90°$ and $\varphi_0 = 0°$. If these angles are substituted into Eq. 3.4.12a and Eq. 3.4.12b for the electric field, and into Eq. 3.4.13a and Eq. 3.4.13b for the magnetic field, the spherical components of this Huygens source are respectively obtained

$$E_\theta^i = -j\eta \frac{kI_0 l e^{-jk\rho}}{4\pi\rho} \cos\phi(1+\cos\theta) \tag{3.5.24a}$$

$$E_\phi^i = j\eta \frac{kI_0 l e^{-jk\rho}}{4\pi\rho} \sin\phi(1+\cos\theta) \tag{3.5.24b}$$

$$H_\theta^i = -j \frac{kI_0 l e^{-jk\rho}}{4\pi\rho} \sin\phi(1+\cos\theta) \tag{3.5.25a}$$

$$H_{\phi}^{i} = -j\frac{kI_0 l e^{-jk\rho}}{4\pi\rho}\cos\phi(1+\cos\theta) \tag{3.5.25b}$$

These same expressions can be obtained for the electric field if Eq. 3.5.12a and Eq. 3.5.12b are added to Eq. 3.5.21a and Eq. 3.5.21b, respectively, and for the magnetic field if Eq. 3.5.13a and Eq. 3.5.13b are added to Eq. 3.5.22a and Eq. 3.5.22b, respectively. To obtain the field at the aperture plane, the spherical components of the electric field in Eq. 3.5.24a and Eq. 3.5.24b are introduced into Eq. 3.5.11:

$$\vec{E}_a = j\eta\frac{kI_0 l e^{-jk(2f-z_0)}}{4\pi\rho}\hat{x}\,(1+\cos\theta) \tag{3.5.26}$$

Another way to obtain Eq. 3.5.26 is to add the aperture field of the electric dipole along x (Eq. 3.5.14) and the magnetic field along y (Eq. 3.5.23). Fig. 3.15 shows the field at the aperture plane. As it can be observed in this figure, the aperture field obtained has its co-polarised component along x and is free of cross-polarisation. The cross-polarised component has been cancelled out between the cross-polarisation of the electric dipole along x and the cross-polarisation of the magnetic dipole along y. The field of the transmitting antenna, i.e., $1+\cos\theta$ only depends on θ.

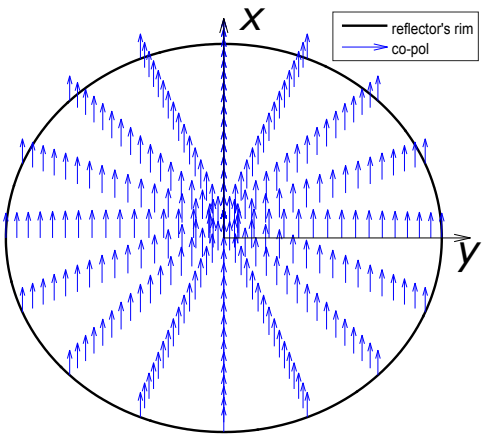

Figure 3.15: Co-polarised and cross-polarised components for a front-fed reflector fed by a Huygens source with the electric dipole oriented along x.

Huygens source with the electric dipole along y

If a Huygens source with an electric dipole oriented along y is desired, the magnetic dipole should be oriented along $-x$ and have again for its magnetic current the value $M_0 = \eta I_0$. The orientation angles for the electric dipole along y are $\vartheta = \varphi_0 = 90°$. If these angles are introduced into Eq. 3.4.12a and Eq. 3.4.12b for the electric field, and

into Eq. 3.4.13a and Eq. 3.4.13b for the magnetic field, the spherical components of this Huygens source are obtained

$$E_\theta^i = -j\eta \frac{kI_0 l e^{-jk\rho}}{4\pi\rho} \sin\phi(1+\cos\theta) \tag{3.5.27a}$$

$$E_\phi^i = -j\eta \frac{kI_0 l e^{-jk\rho}}{4\pi\rho} \cos\phi(1+\cos\theta) \tag{3.5.27b}$$

$$H_\theta^i = j \frac{kI_0 l e^{-jk\rho}}{4\pi\rho} \cos\phi(1+\cos\theta) \tag{3.5.28a}$$

$$H_\phi^i = -j \frac{kI_0 l e^{-jk\rho}}{4\pi\rho} \sin\phi(1+\cos\theta) \tag{3.5.28b}$$

These same expressions can be obtained from the summation of the spherical components of the electric dipole along y and the spherical components of the magnetic dipole along $-x$ (not shown). To obtain the aperture field, the spherical components of the electric field in Eq. 3.5.27a and Eq. 3.5.27b can be introduced into Eq. 3.5.11:

$$\vec{E}_a = j\eta \frac{kI_0 l e^{-jk(2f-z_0)}}{4\pi\rho} \hat{y}(1+\cos\theta) \tag{3.5.29}$$

An alternative way to obtain Eq. 3.5.29 is to add the aperture field of the electric dipole along y (Eq. 3.5.17) and the magnetic field along $-x$ (not shown). Fig.3.16 shows the field at the aperture plane. As Eq.3.5.29 and Fig.3.16 show, the aperture field obtained has its co-polarised component in y and it is free of cross-polarisation. And once again, the field of the transmitting antenna, i.e., $1+\cos\theta$ only depends on θ.

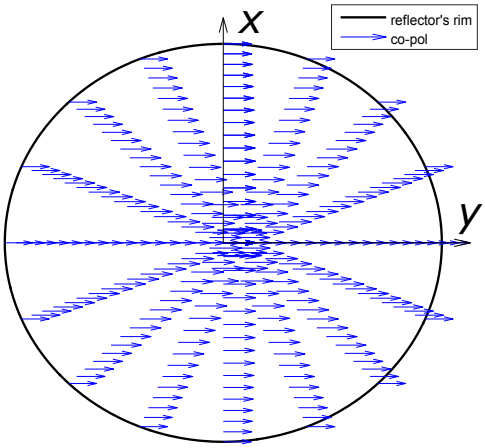

Figure 3.16: Co-polarised and cross-polarised components for a front-fed reflector fed by a Huygens source with the electric dipole oriented along y.

CP source

If a CP source is used as feed, it may be useful to express the Cartesian components of the aperture field as a function of the general CP components. They can be obtained if Eq.3.4.26 is introduced into Eq.3.5.11, yielding

$$E_x^a = -\frac{e^{-jk(2f-z_0)}}{\sqrt{2}\rho}\left(E_{RH}^i(\theta,\phi) + E_{LH}^i(\theta,\phi)\right) \tag{3.5.30a}$$

$$E_y^a = -j\frac{e^{-jk(2f-z_0)}}{\sqrt{2}\rho}\left(-E_{RH}^i(\theta,\phi) + E_{LH}^i(\theta,\phi)\right) \tag{3.5.30b}$$

Then, using Eq.3.5.30a, Eq.3.5.30b and Eq.3.4.24, it is possible to obtain the CP components for the aperture plane field:

$$E_{RH}^a = -\frac{e^{-jk(2f-z_0)}}{\sqrt{2}t\rho}E_{RH}^i(\theta,\phi) \tag{3.5.31a}$$

$$E_{LH}^a = -\frac{e^{-jk(2f-z_0)}}{\sqrt{2}t\rho}E_{LH}^i(\theta,\phi) \tag{3.5.31b}$$

Eq.3.5.31a and Eq.3.5.31b imply that if the CP source is free of cross-polarisation, then the reflected field will be as well.

3.5.2 Offset configuration

In the offset configuration the feed is defined in its own tilted coordinates as

$$\vec{E}_i = E_\theta^{i,s}\hat{\theta}_s + E_\phi^{i,s}\hat{\phi}_s \tag{3.5.32}$$

To express the new tilted feed in non-titled Cartesian coordinates Eq. 3.3.20b and Eq. 3.3.20c should be introduced into Eq. 3.5.32

$$\vec{E}_i = E_x^{i'}\hat{x}' + E_y^{i'}\hat{y}' + E_z^{i'}\hat{z}' \tag{3.5.33}$$

where

$$E_x^{i'} = E_\theta^{i,s}(\cos\theta_s\cos\phi_s\cos\theta_0 - \sin\theta_s\sin\theta_0) - E_\phi^{i,s}\sin\phi_s\cos\theta_0 \tag{3.5.34a}$$

$$E_y^{i'} = E_\theta^{i,s}\cos\theta_s\sin\phi_s + E_\phi^{i,s}\cos\phi_s \tag{3.5.34b}$$

$$E_z^{i'} = E_\theta^{i,s}(-\cos\theta_s\cos\phi_s\sin\theta_0 - \sin\theta_s\cos\theta_0) + E_\phi^{i,s}\sin\phi_s\sin\theta_0 \tag{3.5.34c}$$

The normal unit vector for the offset case in non-tilted Cartesian coordinates was previously obtained in Eq. 3.3.26. Expressing the reflected field for the offset configuration using a matrix form yields

$$\begin{bmatrix} E_x^{r'} \\ E_y^{r'} \\ E_z^{r'} \end{bmatrix} = \frac{1}{t}\begin{bmatrix} b_1^2 - t & b_1\sin\theta_s\sin\phi_s & tb_1 \\ b_1\sin\theta_s\sin\phi_s & \sin^2\theta_s\sin^2\phi_s - t & t\sin\theta_s\sin\phi_s \\ tb_1 & t\sin\theta_s\sin\phi_s & t^2 - t \end{bmatrix}\begin{bmatrix} E_x^{i'} \\ E_y^{i'} \\ E_z^{i'} \end{bmatrix} \tag{3.5.35}$$

where $b_1 = \sin\theta_s\cos\phi_s\cos\theta_0 + \cos\theta_s\sin\theta_0$ and t was defined in Eq.3.3.25. It is possible to reduce this 3×3 matrix to a 2×2 matrix if the Cartesian components of the feed are expressed as a function of the spherical components, since there is only two components (E_θ and E_ϕ). To accomplish this, Eq. 3.5.34a, Eq. 3.5.34b and Eq. 3.5.34c are substituted into Eq. 3.5.35:

$$\vec{E}_r = \hat{x}'E_x^{r'} + E_y^{r'}\hat{y}' + E_z^{r'}\hat{z}' \tag{3.5.36}$$

where

$$E_x^{r'} = \frac{1}{t}\left(E_\theta^{i,s}(\sin\theta_s \sin\theta_0 - \cos\phi_s(1+\cos\theta_s\cos\theta_0)) + E_\phi^{i,s}\sin\phi_s(\cos\theta_s+\cos\theta_0)\right) \tag{3.5.37a}$$

$$E_y^{r'} = \frac{1}{t}\left(-E_\theta^{i,s}\sin\phi_s(\cos\theta_s+\cos\theta_0) + E_\phi^{i,s}(\sin\theta_s \sin\theta_0 - \cos\phi_s(1+\cos\theta_s\cos\theta_0))\right) \tag{3.5.37b}$$

$$E_z^{r'} = 0 \tag{3.5.37c}$$

As the above method is long, a faster way to obtain the reflected field is to substitute Eq. 3.5.32 directly into Eq. 2.3.37. Similar to the front-fed case, Eq. 3.5.36 can be expressed in a matrix form as

$$\begin{bmatrix} E_x^{r'} \\ E_y^{r'} \end{bmatrix} = \frac{1}{t}\begin{bmatrix} c_1 & s_1 \\ -s_1 & c_1 \end{bmatrix}\begin{bmatrix} E_\theta^{i,s} \\ E_\phi^{i,s} \end{bmatrix} \tag{3.5.38}$$

where $c_1 = \sin\theta_s\sin\theta_0 - \cos\phi_s(1+\cos\theta_s\cos\theta_0)$ and $s_1 = \sin\phi_s(\cos\theta_s+\cos\theta_0)$. In order to obtain the reflected field, the spherical components of the desired feed for the offset configuration should be introduced in Eq. 3.5.38.

In the remaining, the aperture field of the offset configuration will be studied for the ideal sources from Section 3.4. As it will be shown, this configuration inherently gives rise to cross-polarisation due to the offset location of the feed and the associated breakdown of rotational symmetry. Since the scope is to investigate the inherent cross-polarisation properties of the offset architecture, only the Huygens and the CP sources are considered. This is due to the fact that the electric and magnetic dipoles give rise to cross-polarisation even in the front-fed case (which is rotationally symmetric).

Huygens source

The orientations for the Huygens source will be the same as in the front-fed case, i.e., electric dipole along x, along y.

Huygens source with the electric dipole along x

The spherical components of both electric and magnetic fields are the same as in Eq.3.5.24a, Eq.3.5.24b, Eq.3.5.25a and Eq.3.5.25b, but expressed in terms of the new tilted coordinate system. The field at the aperture plane is obtained if the spherical components of the electric field are introduced into the equation of the reflected field for the offset reflector (Eq.3.5.38) with the phase shift $2f - z_0$ due to the path from the feed to the aperture plane. The component containing the co-polarisation will be designated as M and the component containing the cross-polarisation as N. This procedure leads to

$$\vec{E}_a = \hat{x}' E_x^{a'} + \hat{y}' E_y^{a'} = \hat{x}' M - \hat{y}' N \tag{3.5.39}$$

where

$$\begin{aligned} M = -j\eta \frac{kI_0 l e^{-jk(2f-z_0)}}{t 4\pi\rho_s}(1+\cos\theta_s)\{&\sin\theta_s\cos\phi_s\sin\theta_0 \\ &-\sin^2\phi_s(\cos\theta_s+\cos\theta_0)-\cos^2\phi_s(1+\cos\theta_s\cos\theta_0)\} \end{aligned} \tag{3.5.40}$$

$$\begin{aligned} N = -j\eta \frac{kI_0 l e^{-jk(2f-z_0)}}{t 4\pi\rho_s}(1+\cos\theta_s)\{&\sin\theta_s\sin\phi_s\sin\theta_0 \\ &-\sin\phi_s\cos\phi_s(1-\cos\theta_s)(1-\cos\theta_0)\} \end{aligned} \tag{3.5.41}$$

It is noted that if the offset angle is $\theta_0 = 0°$, Eq. 3.5.40 and Eq. 3.5.41 give the same result as Eq. 3.5.26, where $N = 0$. This implies that the new component N is the cross-polarisation due to the offset configuration, and the co-polarised component is M, along the x-axis.

Fig. 3.17 shows the co- (blue) and cross-polarised (red) components from Eq. 3.5.40 and Eq. 3.5.41 respectively, at the aperture plane. For an offset in the $x'z'$-plane, the vertical parabola will be free of cross-polarisation due to the fact that the feed is placed at the focus and therefore its vertical plane matches this vertical parabola that crosses the vertex (see Appendix E). For other parabolas (ϕ' planes) however, some cross-polarisation will arise due to the fact that the feed horizontal plane and the reflector main horizontal parabola (the horizontal parabola that crosses the vertex) do not match. Therefore the cross-polarised component will increase as we

move away from the vertical plane ($\phi' = 0°$) until its maximum at the feed horizontal plane ($\phi' = 90°$). For an offset in the $y'z'$-plane, the reflector parabola free of cross-polarisation will be the horizontal, and the maximum cross-polarisation will appear at $\phi' = 0°$. Hence, at the present case, the reflector is free of cross-polarisation at $\phi' = 0°$, and with maximum cross-polarisation at $\phi' = 90°$, as can be seen in Fig.3.17.

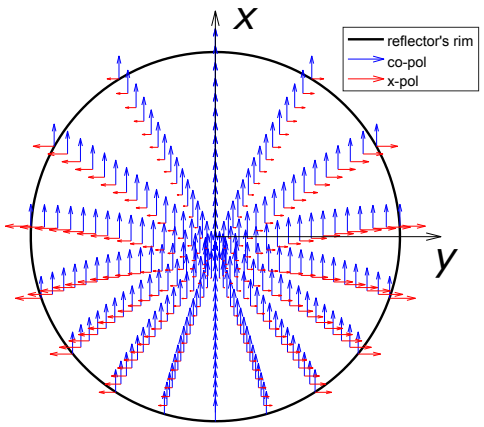

Figure 3.17: Co-polarised and cross-polarised for the offset reflector fed by a Huygens source with the electric dipole along x, for $\theta_0 = 45°$.

It can also be observed that at the plane $\Phi = 0°$ in the far-field (vertical plane), all the contributions from left and right sides will be added, leading to a cancellation of the cross-polarisation. On the contrary, at the plane $\Phi = 90°$, all the contributions from the upper and lower parts will be added, leading to maximum cross-polarisation.

Huygens source with the electric dipole along y

The spherical components of both electric and magnetic fields were obtained in Eq.3.5.27a, Eq.3.5.27b, Eq.3.5.28a and Eq.3.5.28b. To obtain the aperture field for the electric field, Eq.3.5.27a and Eq.3.5.27b are introduced into the equation of the reflected field for the offset reflector (Eq.3.5.38) with the phase shift $2f - z_0$ due to the path from the feed to the aperture plane. The aperture field for this orientation is

$$\vec{E}_a = \hat{x}' E_x^{a'} + \hat{y}' E_y^{a'} = \hat{x}' N + \hat{y}' M \tag{3.5.42}$$

where

$$N = -j\eta \frac{kI_0 l e^{-jk(2f-z_0)}}{t4\pi\rho_s}(1+\cos\theta_s)\{\sin\theta_s \sin\phi_s \sin\theta_0 - \sin\phi_s \cos\phi_s(1-\cos\theta_s)(1-\cos\theta_0)\} \tag{3.5.43}$$

$$M = -j\eta \frac{kI_0 l e^{-jk(2f-z_0)}}{t4\pi\rho_s}(1+\cos\theta_s)\{\sin\theta_s \cos\phi_s \sin\theta_0 - \sin^2\phi_s(\cos\theta_s+\cos\theta_0) - \cos^2\phi_s(1+\cos\theta_s\cos\theta_0)\} \tag{3.5.44}$$

If the offset angle is $\theta_0 = 0°$, Eq. 3.5.44 and Eq. 3.5.43 give the same result as Eq. 3.5.29, where $N = 0$. The cross-polarisation N is now in the x-axis and the co-polarisation in the y-axis.

Fig.3.18 shows the co- (blue) and cross-polarised components from Eq. 3.5.44 and Eq. 3.5.43 respectively, at the aperture plane. As in the vertical Huygens source case, the $\phi' = 0°$ plane is free of cross-polarisation, and maximum cross-polarisation appears at $\phi' = 90°$, as it can be seen in Fig.3.18. The same properties are maintained in the far-field, where due to cancellation the $\Phi = 0°$ plane will be free of cross-polarisation and again maximum cross-polarisation arises at $\Phi = 90°$.

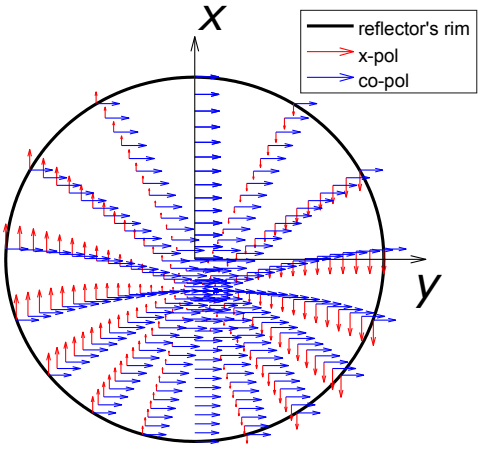

Figure 3.18: Co-polarised and cross-polarised for the offset reflector fed by a Huygens source with the electric dipole along y, for $\theta_0 = 45°$.

CP source

A CP source formed by a phased superposition of two Huygens sources oriented in orthogonal directions can be used as feed. It is then useful to express the Cartesian components of the aperture field for the offset configuration as function of the general CP components. This is obtained if Eq.3.4.26 is introduced into Eq.3.5.38, which yields

$$E_x^{a'} = \frac{e^{-jk(2f-z_0)}}{\sqrt{2}t\rho_s}\left(E_{RH}^{i,s}(\theta,\phi)e^{-j\phi_s}a_1 + E_{LH}^{i,s}(\theta,\phi)e^{j\phi_s}a_2\right) \tag{3.5.45a}$$

$$E_y^{a'} = \frac{e^{-jk(2f-z_0)}}{\sqrt{2}t\rho_s}\left(-jE_{RH}^{i,s}(\theta,\phi)e^{-j\phi_s}a_1 + jE_{LH}^{i,s}(\theta,\phi)e^{j\phi_s}a_1\right) \tag{3.5.45b}$$

where

$$a_1 = \sin\theta_s\sin\theta_0 - \cos\phi_s(1+\cos\theta_s\cos\theta_0) + j\sin\phi_s(\cos\theta_s+\cos\theta_0) \tag{3.5.46a}$$

$$a_2 = \sin\theta_s\sin\theta_0 - \cos\phi_s(1+\cos\theta_s\cos\theta_0) - j\sin\phi_s(\cos\theta_s+\cos\theta_0) \tag{3.5.46b}$$

Then, using Eq.3.5.45a, Eq.3.5.45b and Eq.3.4.24, it is possible to obtain the circular components for the aperture plane field for the offset configuration:

$$E_{RH}^{a'} = \frac{e^{-jk(2f-z_0)}}{t\rho_s}\left(E_{RH}^{i,s}(\theta,\phi)e^{-j\phi_s}a_2\right) \tag{3.5.47a}$$

$$E_{LH}^{a'} = \frac{e^{-jk(2f-z_0)}}{t\rho_s}\left(E_{LH}^{i,s}(\theta,\phi)e^{j\phi_s}a_1\right) \tag{3.5.47b}$$

Eq.3.5.47a and Eq.3.5.47b imply that even for the offset configuration, if the CP source is free of cross-polarisation, then the reflected field will be as well. Furthermore, it is well known that a CP source feeding an offset parabolic reflector will cause a beam tilt in the far-field [6]. The direction of this beam tilt will depend on the sense of rotation of the feed. However, from Eq.3.5.47a and Eq.3.5.47b it is not possible to predict the beam tilt, since it will appear in the far-field, where all the components from the discretized points on the reflector will add up.

3.6 Far field

The field reaching the reflector from the feed is known as the primary field, whereas the field emanating from the reflector is known as the secondary field. For this reason, the far-field pattern of the antenna after reflection can be denoted as the secondary pattern.

Two classes of methodologies are commonly used in order to obtain the secondary pattern from a reflector antenna, as it was mentioned in Section 2.3. One relies on the derivation of the far-field characteristics from the near-fields on the aperture plane (as discussed in Section 3.5). This is known as the *aperture distribution method* or the *geometrical optics (GO) method*. The other obtains far-field characteristics using the currents excited on the reflector surface (which may be curved) by the incoming field. It is known as the *current distribution method* or the *physical optics (PO) method*.

Both methods are based on quasi-optical approaches, where by employing ray tracing tools the rays are followed from the feed to the reflector surface. According to the theory explained in Section 2.3 the rays carry information about their amplitude, phase and polarization. For the GO method, the rays are reflected on the surface and they are followed up to the aperture plane where the phase distance is the same for all of them as in Fig. 3.19. For the PO method, the incident magnetic field is used to obtain the surface currents. Knowing the aperture fields (GO) or the surface currents (PO), the radiation integrals from Eq. 2.4.28a and Eq. 2.4.28b can be computed. These integrals, also know as the *far-field integrals*, represent the summation at a specific far-field point from all the contributions along the reflector surface or aperture plane.

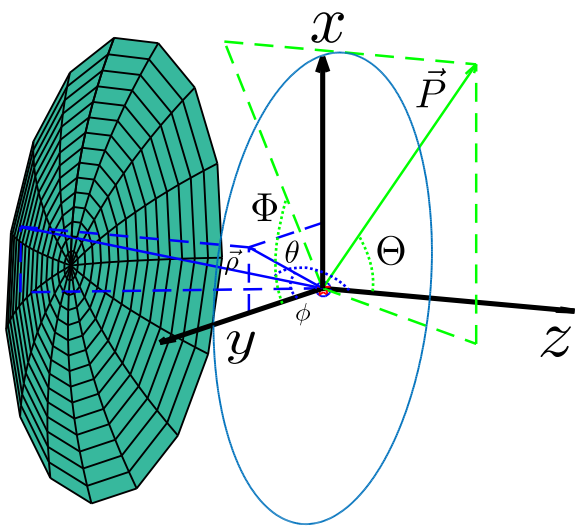

Figure 3.19: Far-field Coordinates system placed at the aperture plane.

A key difference between the two classes of methodologies relies on the evaluation of the far-field integral. Referring to the GO method, the far-field integral is evaluated over the circular aperture formed by the aperture plane, which results in a surface (2D) integral. Referring to the PO method, the far-field integral is evaluated over the reflector surface, which results in a volumetric (3D) integral. As will be discussed, when analysing parabolic reflectors, PO is more accurate than GO mainly due to the fact that the integral is performed over the 3D reflector surface.

3.6.1 Aperture distribution/GO method

In the *aperture distribution* or *GO* method it can be supposed that the aperture plane is an aperture antenna with some associated surface electric and magnetic current densities. The aperture antennas theory from Section 2.4.3 can be then applied.

The aperture is neither an electric conductor or a magnetic conductor. Therefore, by the *Love's equivalent principle*, it is a closed surface with null electric and magnetic fields inside (V in Fig.C.1 from Appendix C), and electric and magnetic surface currents $\vec{J}_a$ and $\vec{M}_a$. These surface currents are functions of the magnetic and electric fields $\vec{H}_a$ and $\vec{E}_a$ at the surface, respectively. Then, from Appendix C and

Eq.2.4.29

$$\vec{J}_a = \hat{n} \times \vec{H}_a = \hat{x}J_x^a + \hat{y}J_y^a + \hat{z}J_z^a \tag{3.6.1a}$$

$$\vec{M}_a = \vec{E}_a \times \hat{n} = -\hat{n} \times \vec{E}_a = \hat{x}M_x^a + \hat{y}M_y^a + \hat{z}M_z^a \tag{3.6.1b}$$

This approximation is known as the *Field Equivalence Principle* [11]. This principle allows to obtain the radiated field from a source with specific electric and magnetic currents $\vec{J}_a$ and $\vec{M}_a$ by replacing the source for a closed surface which boundary conditions are known. The normal to the aperture is $\hat{z}$, and the direction of propagation is also $\hat{z}$, since the reflected wave is a plane wave. Therefore,

$$\vec{E}_a = \hat{x}E_x^a + \hat{y}E_y^a \tag{3.6.2a}$$

$$\vec{H}_a = \frac{1}{\eta}(\hat{z} \times \vec{E}_a) = -\hat{x}\frac{E_y^a}{\eta} + \hat{y}\frac{E_x^a}{\eta} \tag{3.6.2b}$$

As it was stated in Section 3.5, the aperture electric field is obtained from the reflected field (Eq.2.3.37) in the far-field CS. The displacement from the feed origin to the aperture plane has to be taken into account. It should be noted that the aperture plane is in the $x'y'$ or xy plane (see Fig. 3.1d). Therefore, this displacement can be taken with respect to the non-tilted CS: $\rho' \cos\theta'$. No amplitude change is usually applied from the reflector to the aperture plane since all the rays travel the same distance. Therefore, this displacement is only applied to the phase. The resulting aperture plane field is

$$\begin{aligned} \vec{E}_a &= \vec{E}_r e^{-jk\rho'\cos\theta'} = (2\hat{n}(\hat{n}\cdot\vec{E}) - \vec{E})e^{-jk\rho'\cos\theta'} \\ &= (\hat{x}E_x^r + \hat{y}E_y^r + \hat{z}E_z^r)e^{-jk\rho'\cos\theta'} = \hat{x}E_x^a + \hat{y}E_y^a \end{aligned} \tag{3.6.3}$$

The electric and magnetic currents can be expressed as functions of the electric field

at the aperture, as

$$\vec{J}_a = \hat{z} \times \vec{H}_a = -\hat{x}\frac{E_x^a}{\eta} - \hat{y}\frac{E_y^a}{\eta} \tag{3.6.4a}$$

$$\vec{M}_a = -\hat{z} \times \vec{E}_a = \hat{x}E_y^a - \hat{y}E_x^a \tag{3.6.4b}$$

Therefore the different current components for these electric field are: $J_x^r = -E_x^a/\eta$, $J_y^a = -E_y^a/\eta$, $J_z^a = 0$, $M_x^a = E_y^a$, $M_y^a = -E_x^a$ and $M_z^a = 0$. The differential path $R' \cos\psi$ from Section 2.4.3 can be express as the aperture Cartesian coordinates (x, y)

$$\begin{aligned} R' \cos\psi = \vec{R}' \cdot \hat{\rho} &= (\hat{x}x + \hat{y}y) \cdot (\hat{x}\sin\Theta\cos\Phi + \hat{y}\sin\Theta\sin\Phi + \hat{z}\cos\Theta) \\ &= x\sin\Theta\cos\Phi + y\sin\Theta\sin\Phi \end{aligned} \tag{3.6.5}$$

It is also possible to express the differential path $R' \cos\psi$ as function of the aperture's cylindrical coordinates (r, ϕ) or function of the aperture's spherical coordinates (θ, ϕ) respectively as

$$R' \cos\psi = r\sin\Theta\cos(\Phi - \phi) \tag{3.6.6}$$

$$R' \cos\psi = \rho\sin\theta\sin\Theta\cos(\Phi - \phi) \tag{3.6.7}$$

where the equations in Appendix F were used for the coordinate changes. For the differential area ds', the variables of the far-field CS should be used, since it is where the radiation integrals (see Section 2.4.3) are performed:

$$ds' = dxdy \tag{3.6.8a}$$

$$ds' = rdrd\phi \tag{3.6.8b}$$

$$ds' = \rho^2\sin\theta d\theta d\phi \tag{3.6.8c}$$

The far-field spherical components in Cartesian coordinates can be obtained from Eq.2.4.40a, Eq.2.4.40b and Eq.2.4.40c after introducing the following information: the currents function of the aperture field (Eq. 3.6.4a and Eq. 3.6.4b), the phase differential path (Eq. 3.6.5) and the differential area (Eq. 3.6.8a). This yields

$$E_\Theta = \frac{jke^{-jkP}}{4\pi P}(1+\cos\Theta)\int_{-\frac{d}{2}\sin\phi}^{\frac{d}{2}\sin\phi}\int_{-\frac{d}{2}\cos\phi}^{\frac{d}{2}\cos\phi}(E_x^a\cos\Phi + E_y^a\sin\Phi) \cdot e^{jk(x\sin\Theta\cos\Phi + y\sin\Theta\sin\Phi)}dxdy \tag{3.6.9}$$

$$E_\Phi = \frac{jke^{-jkP}}{4\pi P}(1+\cos\Theta)\int_{-\frac{d}{2}\sin\phi}^{\frac{d}{2}\sin\phi}\int_{-\frac{d}{2}\cos\phi}^{\frac{d}{2}\cos\phi}(-E_x^a\sin\Phi + E_y^a\cos\Phi) \cdot e^{jk(x\sin\Theta\cos\Phi + y\sin\Theta\sin\Phi)}dxdy \tag{3.6.10}$$

For cylindrical coordinates, using Eq. 3.6.6 for the phase differential path and Eq. 3.6.8b for the differential area, the spherical components are

$$E_\Theta = \frac{jke^{-jkP}}{4\pi P}(1+\cos\Theta)\int_0^{2\pi}\int_0^{\frac{d}{2}}(E_x^a\cos\Phi + E_y^a\sin\Phi) \cdot e^{jkr\sin\Theta\cos(\Phi-\phi)}rdrd\phi \tag{3.6.11}$$

$$E_\Phi = \frac{jke^{-jkP}}{4\pi P}(1+\cos\Theta)\int_0^{2\pi}\int_0^{\frac{d}{2}}(-E_x^a\sin\Phi + E_y^a\cos\Phi) \cdot e^{jkr\sin\Theta\cos(\Phi-\phi)}rdrd\phi \tag{3.6.12}$$

For spherical coordinates, using Eq. 3.6.7 for the phase differential path and Eq. 3.6.8c for the differential area, the spherical components are

$$E_\Theta = \frac{jke^{-jkP}}{4\pi P}(1+\cos\Theta)\int_0^{2\pi}\int_0^{\theta_c}(E_x^a\cos\Phi + E_y^a\sin\Phi) \cdot e^{jk\rho\sin\theta\sin\Theta\cos(\Phi-\phi)}\rho^2\sin\theta d\theta d\phi \tag{3.6.13}$$

$$E_\Phi = \frac{jke^{-jkP}}{4\pi P}(1+\cos\Theta)\int_0^{2\pi}\int_0^{\theta_c}(-E_x^a\sin\Phi + E_y^a\cos\Phi) \cdot e^{jk\rho\sin\theta\sin\Theta\cos(\Phi-\phi)}\rho^2\sin\theta d\theta d\phi \tag{3.6.14}$$

3.6.2 Current distribution/PO method

In the *current distribution* or *PO* method, the currents at the reflector surface are taken to perform the far-field integral. Initially we consider a perfect electric conductor (PEC) surface for the reflector. Therefore, only the electric currents $\vec{J}_s$ are present. The far-field is then obtained from Eq.2.4.40a, Eq.2.4.40b and Eq.2.4.40c as

$$\vec{E}_F = -jk\eta \frac{e^{-jkP}}{4\pi P}(\hat{\theta}N_\Theta + \hat{\phi}N_\Phi) \tag{3.6.15}$$

where $\vec{N}$ is now a surface integral over the 3D reflector surface Σ, and it is known as physical optics integral:

$$\vec{N} = \int_\Sigma \vec{J}(\vec{\rho}) e^{jk\vec{R}'\cdot\hat{\rho}} ds' \tag{3.6.16}$$

Since the third dimension of the surface (z or ρ) is expressed as function of the other two, Eq. 3.6.16 can be transformed into an integral over the projected circular aperture by multiplying the integrand by the Jacobian [21]. First, the function $g(x, y)$ that defines the reflector geometry for a general offset case has to be defined as

$$g(x, y) = z = -f + \frac{(x + x_c)^2 + y^2}{4f} + z_f \tag{3.6.17}$$

where z_f is a constant to displace the origin to the centre of the aperture

$$z_f = -f + \frac{(x_c)^2}{4f} \tag{3.6.18}$$

The Jacobian can be expressed as

$$J_\Sigma = N = \sqrt{\left(\frac{\partial g}{\partial x}\right)^2 + \left(\frac{\partial g}{\partial y}\right)^2 + 1} = \sqrt{\left(\frac{x + x_c}{2f}\right)^2 + \left(\frac{y}{2f}\right)^2 + 1} \tag{3.6.19}$$

where N is the modulus of the normal vector $\vec{N}$ ($\hat{n} = \vec{N}/N$). Eq.3.6.16 can be then reduced to

$$\vec{N} = \iint \vec{J}(\vec{\rho}) N e^{jk\vec{R}'\cdot\hat{\rho}} ds \tag{3.6.20}$$

In a similar way as in the GO method (see Section 3.6.1), the phase term $\vec{R}' \cdot \hat{\rho}$ is obtained as

$$\begin{aligned} \vec{R}' \cdot \hat{\rho} &= (\hat{x}x + \hat{y}y + \hat{z}z) \cdot (\hat{x}\sin\Theta\cos\Phi + \hat{y}\sin\Theta\sin\Phi + \hat{z}\cos\Theta) \\ &= x\sin\Theta\cos\Phi + y\sin\Theta\sin\Phi + z\cos\Theta \end{aligned} \tag{3.6.21}$$

The differential area ds' is obtained in the same way as in Eq.3.6.8a, Eq.3.6.8b and Eq.3.6.8c. The surface currents are obtained using Eq.C.0.6. Finally, the spherical components of the far-field in Cartesian coordinates can be express as

$$\begin{aligned} E_\Theta = -jk\eta\frac{e^{-jkP}}{4\pi P}\int_{-\frac{d}{2}\sin\phi}^{\frac{d}{2}\sin\phi}\int_{-\frac{d}{2}\cos\phi}^{\frac{d}{2}\cos\phi} N(\cos\Theta(J_x^s\cos\Phi + J_y^s\sin\Phi) - J_z^s\sin\Theta) \\ \cdot e^{jk(\sin\Theta(x\cos\Phi + y\sin\Phi) + z\cos\Theta)} dxdy \end{aligned} \tag{3.6.22}$$

$$\begin{aligned} E_\Phi = -jk\eta\frac{e^{-jkP}}{4\pi P}\int_{-\frac{d}{2}\sin\phi}^{\frac{d}{2}\sin\phi}\int_{-\frac{d}{2}\cos\phi}^{\frac{d}{2}\cos\phi} N(-J_x^s\sin\Phi + J_y^s\cos\Phi) \\ \cdot e^{jk(\sin\Theta(x\cos\Phi + y\sin\Phi) + z\cos\Theta)} dxdy \end{aligned} \tag{3.6.23}$$

For cylindrical coordinates,

$$\begin{aligned} E_\Theta = -jk\eta\frac{e^{-jkP}}{4\pi P}\int_0^{2\pi}\int_0^{\frac{d}{2}} N(\cos\Theta(J_x^s\cos\Phi + J_y^s\sin\Phi) - J_z^s\sin\Theta) \\ \cdot e^{jk(r\sin\Theta\cos(\Phi-\phi) + z\cos\Theta)} r dr d\phi \end{aligned} \tag{3.6.24}$$

$$\begin{aligned} E_\Phi = -jk\eta\frac{e^{-jkP}}{4\pi P}\int_0^{2\pi}\int_0^{\frac{d}{2}} N(-J_x^s\sin\Phi + J_y^s\cos\Phi) \\ \cdot e^{jk(r\sin\Theta\cos(\Phi-\phi) + z\cos\Theta)} r dr d\phi \end{aligned} \tag{3.6.25}$$

For spherical coordinates,

$$E_\Theta = -jk\eta\frac{e^{-jkP}}{4\pi P}\int_0^{2\pi}\int_0^{\theta_c} N(\cos\Theta(J_x^s\cos\Phi + J_y^s\sin\Phi) - J_z^s\sin\Theta) \cdot e^{jk\rho(\sin\theta\sin\Theta\cos(\Phi-\phi)+\cos\theta\cos\Theta)}\rho^2\sin\theta d\theta d\phi \tag{3.6.26}$$

$$E_\Phi = -jk\eta\frac{e^{-jkP}}{4\pi P}\int_0^{2\pi}\int_0^{\theta_c} N(-J_x^s\sin\Phi + J_y^s\cos\Phi) \cdot e^{jk\rho(\sin\theta\sin\Theta\cos(\Phi-\phi)+\cos\theta\cos\Theta)}\rho^2\sin\theta d\theta d\phi \tag{3.6.27}$$

3.7 Tool for the Analysis of Reflector Antennas

The most common way to analyse and design reflector antennas is the software package GRASP from TICRA [5]. This software uses PO/PTD to obtain the far-field of the reflector antenna in a very efficient way. It can also use MoM at the expense of much longer computation times. Even though it has no real competitor when it comes to the analysis and design of reflector antennas, its price could be discouraging specially for universities. However, for simple analyses (ideal sources, no struts, PEC surfaces, etc) there is a very convenient and fairly complete free student version.

For the present thesis, the student version of GRASP was not enough since it only allows to obtain the far-field and does not use GO. The study of the fields at the reflector aperture has proven to be a very convenient theoretical way to study the depolarisation properties of single reflector antennas (see Section 3.5). Also, even though GO is not used anymore for reflector antennas (it is used for reflectarrays), a theoretical comparison between GO and PO can give useful insight. Furthermore, as it will be shown in the following chapters, it is also needed for this thesis the use of practical feeds and metallodielectric arrays (FSSs, reflectarrays).

Taking into account all the above, a tool programmed in MATLAB [8] has been developed to analyse single reflector antennas. This section is structured as followed: first some hints on how the tool is programmed will be presented. Then the tool will be used to compare GO and PO, validating the results with GRASP. Finally, two different numerical methods to compute the far-field will be presented and compared.

3.7.1 Implementation of the tool

The tool consists on the implementation in MATLAB of the different sections of this chapter: the different CS changes to move between coordinate systems (see Section 3.2), the definition of the reflector geometry (see Section 3.3) and the definition of the ideal source to feed the reflector (see Section 3.4). Then, for the case of Section 3.5, the fields at the aperture plane are obtained by computing the reflected field (using Eq. 2.3.37) to study the depolarisation properties of the selected reflector and source. Once the aperture fields or the surface currents are known, the equations from Section 3.6 are used to compute the far-field by using GO or PO respectively.

For simplicity reasons, it should be noted that the code uses only the feed far-field and no diffraction effects or feed contributions to the far-field are taken into account. As an example, Fig. 3.20 shows a simple flow chart of the different steps in order to obtain the far-field of a single reflector fed by a single feed using PO.

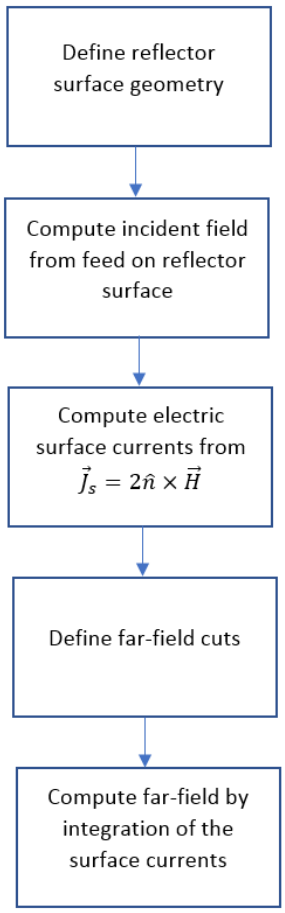

Figure 3.20: Simple flow chart showing the different steps to obtain the far-field of a single reflector antenna fed by one feed using Physical Optics.

3.7.2 Comparison of Geompetrical Optics and Physical Optics methods

A substantial volume of the literature has focused on the analysis of the depolarisation properties of front-fed and offset configurations [3, 4, 6, 14, 19, 20, 22–24]. Historically, the preferred analysis method to obtain the far-field pattern of the antenna has been GO due to its simplicity. More recently, it has been demonstrated that GO may lead to some inaccuracies that can be addressed with PO. For example, Rahmat-Samii showed that GO leads to some errors in the estimation of the sidelobe levels and null positions, compared with PO [7].

This subsection presents a comparison between GO and PO focusing in their accuracy to analyse the depolarisation properties of single front-fed and offset reflector antennas for both linearly (LP) and circularly polarised (CP) feeds. The conclusions reached for different authors will be reviewed. The common statement that the front-fed configuration is free of cross-polarisation in all the far-field's planes when fed by a Huygens source will be refuted by the use of the PO method. Also, new insight on the origin of the far-field beam tilt in offset configurations when fed by CP sources will be provided. The study is based on the tool reviewed in Section 3.7.1 and is further corroborated using TICRA's GRASP software [5].

Front-Fed Configuration

In this subsection, the far-field pattern of a front-fed reflector antenna for both LP and CP feeds will be discussed for both GO and PO methods.

It is useful to generalise the ideal source to feed a parabolic reflector antenna. This generic source was denoted as *balanced feed* in [6]. As it is known from Section 3.5, this source follows Ludwig-III for the definition of the polarisation [17] (see also Section 3.4.1). Following the properties of the Huygens source (see Section 3.4.4), this generic feed should have a circularly symmetric radiation pattern independent of ϕ. After all these considerations, the generic feed can be expressed as

$$\begin{bmatrix} \vec{E}_{co} \\ \vec{E}_{xp} \end{bmatrix} = \begin{bmatrix} \cos(\beta_0 - \phi_s) & \sin(\beta_0 - \phi_s) \\ \cos(\beta_0 \pm \frac{\pi}{2} - \phi_s) & \sin(\beta_0 \pm \frac{\pi}{2} - \phi_s) \end{bmatrix} \begin{bmatrix} \hat{\theta}_s \\ \hat{\phi}_s \end{bmatrix} F(\theta_s) \frac{e^{-jk\rho_s}}{\rho_s} \tag{3.7.1}$$

where β_0 defines the orientation of the polarisation: $\beta_0 = 0°$ and $+\phi/2$ for a vertically polarised source, $\beta_0 = 90°$ and $-\phi/2$ for a horizontally polarised source and $\beta_0 = 45°$ and $-\phi/2$ for a slant 45°-polarised source.

As it was stated in Section 3.5.1, and previously reported in [3,4], a Huygens source with vertical/horizontal polarisation placed at the focus of a front-fed parabolic reflector will not give rise to surface currents/reflected field in the orthogonal direction. This statement can be easily understood if the ideal source is decomposed into an electric dipole and an orthogonal magnetic dipole with equal amplitude (see Section 3.4.4). The cross-polarised surface currents/reflected field of one dipole are cancelled out by the cross-polarised currents/reflected field of the other, as Fig.3.11 + Fig.3.14 = Fig.3.15 shows. However, the cross-polarisation prediction in the far-field can vary depending on the method used.

From the spherical components of the far-field and the ideal feed from Eq.3.7.1, it is possible to arrive to a generic equation for the cross-polarised component of the far-field pattern using GO:

$$E_{xp}^{GO} \propto (1 + \cos\Theta)(g_x \sin\beta_0 + g_y \cos\beta_0) \tag{3.7.2}$$

where

$$\vec{g}(\Theta, \Phi) = \int_0^{d/2} \int_0^{2\pi} \vec{E}_a e^{jkr \sin\Theta \cos(\phi - \Phi)} \tag{3.7.3}$$

and where $\vec{g}(\Theta, \Phi)$ is the GO Fourier Transform (FT) and $d = D$ for the front-fed case. Therefore, if the source is vertically polarised, then the cross-polarisation in Eq.3.7.2 only arises from the cross-polarised component (y-component) due to the reflector geometry, which for the present ideal source is zero. It can also be observed that the cross-polarisation is independent of the cut in Φ. The same applies for any other polarisation.

The cross-polarised component of the far-field can be obtained as well for the PO method. If the above procedure is applied, one yields

$$E_{xp}^{PO} \propto \mp \sin\beta_0 \left(p_x(\cos\Theta\cos^2\Phi + \sin^2\Phi) + \frac{p_y}{2}\sin 2\Phi(\cos\Theta - 1) - p_z \sin\Theta\cos\Phi \right)$$

$$\pm \cos\beta_0 \left(\frac{p_x}{2}\sin 2\Phi(\cos\Theta - 1) + p_y(\cos\Theta\cos^2\Phi + \sin^2\Phi) - p_z \sin\Theta\sin\Phi \right) \tag{3.7.4}$$

where

$$\vec{p}(\Theta,\Phi) = \int_0^{d/2}\int_0^{2\pi} \vec{J}_s N e^{jk(r\sin\Theta\cos(\phi-\Phi)+z\cos\Theta)} \tag{3.7.5}$$

and where $\vec{p}(\Theta,\Phi)$ is the PO FT. Adatia [25] obtained an equation for the y-polarised case, while Eq.3.7.4 represents the general case for any linear polarisation. For the PO method, the cross-polarised component in Eq.3.7.4 has contributions from the three Cartesian components of the surface currents. An ideal feed as the one in Eq.3.7.1 polarised at an angle β_0 gives no cross-polarised surface currents. Therefore, the far-field will be free of cross-polarisation at the principal planes. But some cross-polarisation will appear in the rest of the planes.

The different conclusion when comparing Eq.3.7.2 (GO) and Eq.3.7.4 (PO) comes from the different methodologies employed to obtain the currents. In GO, the aperture field is obtained from the equivalent electric and magnetic surface currents along the aperture plane, where the unit normal is $\hat{n} = \hat{z}$, leading to a surface integral (see Section 3.6.1). In PO, the surface currents are taken over the surface geometry. The unit normal vector follows the paraboloid geometry, leading to a volumetric integral (see Section 3.6.2).

The discrepancy between the two methods in obtaining cross-pol estimations is shown by means of an example. The chosen example has been the front-fed configuration used by Jones [3], with diameter $D = 37.1973\lambda$ and ratio focal distance to diameter $f/D = 0.6$ at 18.5 GHz. Fig. 3.21 shows the far-field directivity for this example, fed by a vertically LP source. The plane shown is $\Phi = 45°$, where maximum cross-polarisation is expected. GO and PO match very well in the co-polarised component, but GO fails to obtain the cross-polarised component. The implemented PO matches very well with GRASP's PO.

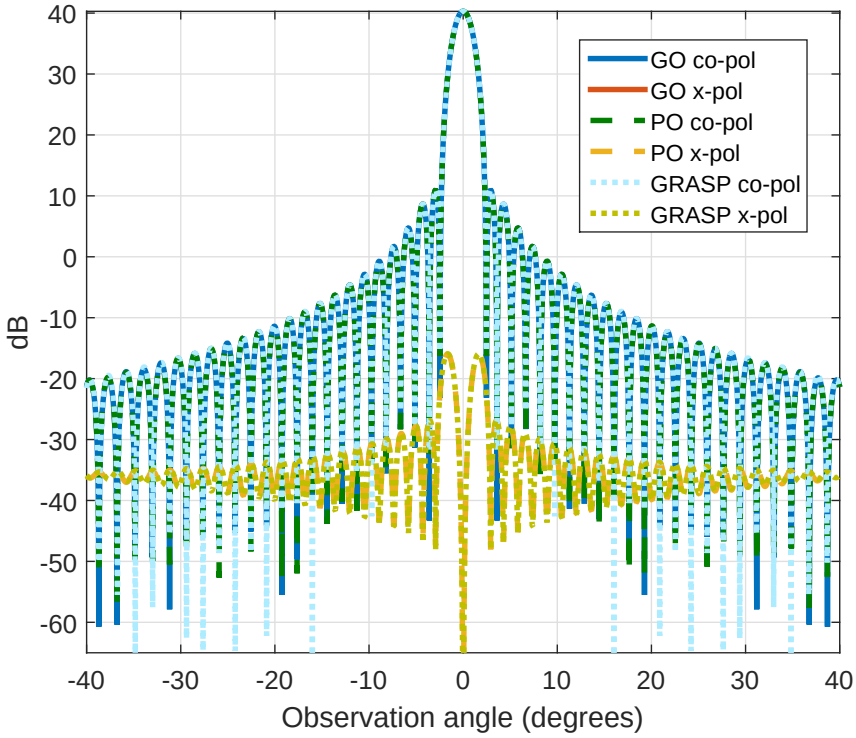

Figure 3.21: Directivity (dB) for a single front-fed reflector antenna with $D = 37.1973\lambda$, $f/D = 0.6$, and $f_0 = 18.5$ GHz, fed by a vertically LP source for a $\Phi = 45°$ plane.

It is well known that a CP feed with a specific sense or rotation gives the contrary rotation in the far-field pattern [24]. This statement is true as long as the observer is always placed at the origin of each coordinate system, as it is usually supposed for CP feeds (see Section 3.4.6). For example, an ideal right-hand CP (RHCP) source feeding a front-fed reflector can be used to understand this statement. Only the main ray (broadside direction) is used in this explanation for simplicity. Looking at Fig. 3.9a, the field rotation goes from the vertical axis (x-axis) to the horizontal axis (y-axis). From the far-field CS origin, this ray arriving from the feed CS origin has a left-hand sense of rotation (rotating from the y-axis to the x-axis). After reflection, it is known from Eq.2.3.37 that only the x and y components will change sign. However, compared to the feed CS, the far-field CS has the y- and z-axes inverted. Taking all these into account, it can be deduced that the field rotation after reflection goes from the $-x$-axis to the y-axis. Hence, the sense of rotation after reflection is left-hand.

It is also discussed in the literature that a front-fed metallic reflector does not depolarize the signal [6]. This statement can be confirmed with the aperture fields

for the front-fed configuration in Eq.3.5.31a and Eq.3.5.31b. To go further into this statement, Fig. 3.22 shows the directivity of the front-fed reflector considered in Fig.3.21 fed by a right handed circularly polarised (RHCP) source for a $\Phi = 0°$ plane. Results obtained by GO and PO are presented. As expected, GO shows no depolarisation. However, PO shows there is cross-pol (RHCP) in every plane. This discrepancy can be attributed to the way both methods obtain and compute the currents as discussed in the LP case above.

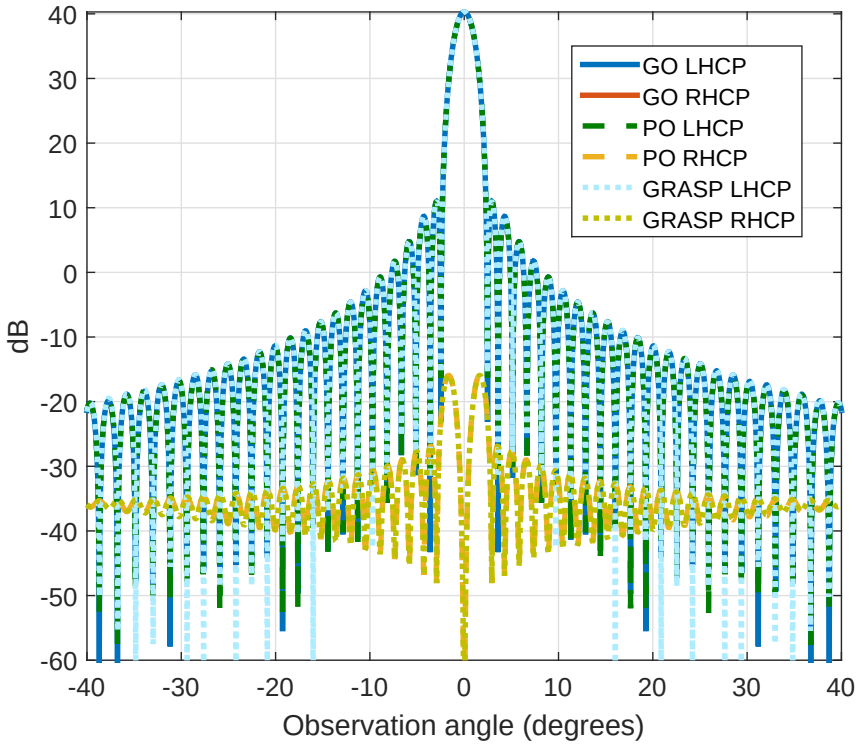

Figure 3.22: Directivity (dB) for a single front-fed reflector antenna with $D = 37.1973\lambda$, $f/D = 0.6$, and $f_0 = 18.5$ GHz, fed by an RHCP source for a $\Phi = 0°$ plane.

Offset Configuration

Analysing the depolarisation properties of the offset case is more complex because of the cross-polarised currents that appears due to the offset.

Before continuing, a comment should be made: in the classic literature such as [6], the angle between the feed CS z-axis and the non-tilted CS z-axis has been considered to be θ_0, i.e., the offset angle (see Fig. 3.4). However θ_0 does not necessarily impose for the feed to point towards the centre of the aperture, which could lead to slightly increased sidelobes in the far-field. The angle that should be

used (and will be used from now on) to point the feed towards the centre of the aperture is θ_f:

$$\theta_f = 2\tan^{-1}\left(\frac{d/2+h}{2f}\right) \tag{3.7.6}$$

An offset parabolic reflector can be regarded as the illuminated offset section of a bigger imaginary paraboloid (see Section 3.3.2). Therefore, the feed is still placed at the focus of the paraboloid, but its broadside direction does not match with the vertex of the paraboloid anymore. This asymmetry is the cause of the cross-polarised surface currents/reflected field. This can be understood looking at the Cartesian components of the reflected field. They were obtained in Eq.3.5.38. But a better insight can be gained if they are expressed as function of the generic co-polarised and cross-polarised components:

$$E_x^{r'} = E_{co}^{i,s}(a_1\cos\beta_0 + a_2\sin\beta_0) \pm E_{xp}^{i,s}(-a_1\sin\beta_0 + a_2\cos\beta_0) \tag{3.7.7a}$$

$$E_y^{r'} = E_{co}^{i,s}(a_2\cos\beta_0 - a_1\sin\beta_0) \pm E_{xp}^{i,s}(a_2\sin\beta_0 - a_1\cos\beta_0) \tag{3.7.7b}$$

where

$$a_1 = \frac{1}{t}\Big(\sin\theta_s\cos\phi_s\sin\theta_f - \sin^2\phi_s(\cos\theta_s+\cos\theta_f) - \cos^2\phi_s(1+\cos\theta_s\cos\theta_f)\Big) \tag{3.7.8a}$$

$$a_2 = \frac{1}{t}\left(\sin\theta_s\sin\phi_s\sin\theta_f + \sin\phi_s\cos\phi_s(1-\cos\theta_f)(\cos\theta_s-1)\right) \tag{3.7.8b}$$

and where t was defined in Eq.3.3.25 and θ_f in Eq.3.7.6. It can be observed from Eq.3.7.7a and Eq.3.7.7b that even if the source does not introduce any cross-polarisation, the cross-polarised reflected field (x for HLP source or y for VLP source) still depends on the co-polarised component. They are only suppressed if $\theta_f = 0°$.

The linearly polarised fed offset reflector has been fully analysed in [6] or [7]. As Rahmat-Samii pointed out [7], the GO method leads to a wrong sidelobe level and null positions as well as a false symmetry. This is illustrated by means of an example

in Fig. 3.23. The selected example is the one used in [6], with diameter $d = 18.796\lambda$ and ratio focal distance to diameter $f/D = 0.5$ at 18.5 GHz. The reflector is fed by a vertically LP source. The plane shown is $\Phi = 0°$, where no cross-polarisation is expected.

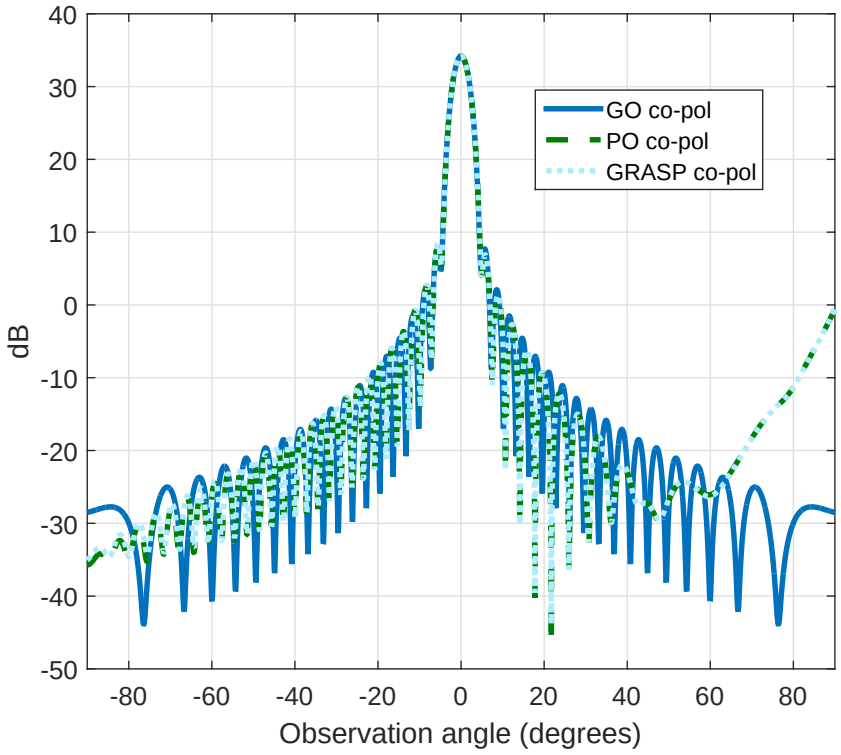

Figure 3.23: Directivity (dB) for a single offset reflector antenna with $d = 18.796\lambda$, $f/D = 0.5$, and $f_0 = 18.5$ GHz, fed by a vertically LP source for a $\Phi = 0°$ plane.

For the front-fed case with no cross-polarised surface currents, the maximum cross-polarisation for PO appears at the plane $\Phi = 45°$ (see Fig.3.21). This difference is present in the offset case as well. The far-field from an offset reflector using this method will present a wrong symmetry. This wrong symmetry is due to the aforementioned two facts: the path travelled from the focus to the aperture plane is the same for all the rays, and the FT used by GO (see Eq.3.7.3) is symmetric. This wrong symmetry is illustrated in Fig.3.23 and Fig.3.24. However, PO considers the currents at the reflector surface, where the field is not symmetric. Also, the FT in Eq.3.7.5 considers the 3D surface, which is not symmetric. These asymmetries in the surface currents and the geometry explain the asymmetries in the far-field.

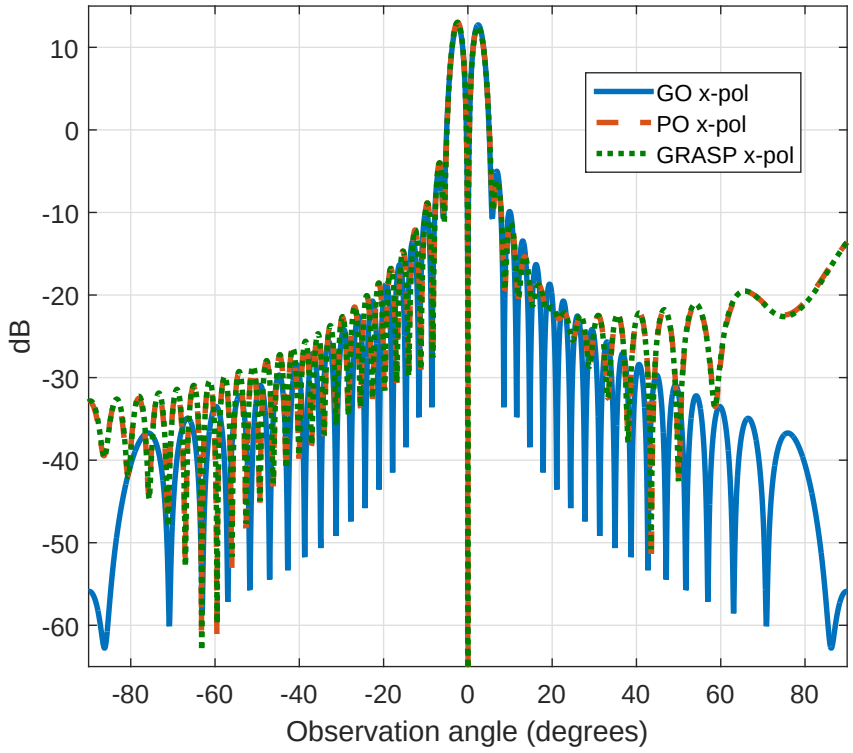

Figure 3.24: cross-pol components (dB) for a single offset reflector antenna with $d = 18.796\lambda$, $f/D = 0.5$, and $f_0 = 18.5$ GHz, fed by a vertically LP source for a $\Phi = 45°$ plane.

When a CP source is used to feed the offset reflector, Chu and Turrin stated that no cross-pol appears in the far-field [6], but instead the offset feed results in a beam tilt. This tilt can be understood as follows: the CP source can be regarded as a superposition of a vertically and a horizontally LP sources with a 90° phase shift. If they are treated separately, each of them introduce a LP cross-polarised component due to the offset. If all the vertical and horizontal components (from co-polarisation and cross-polarisation) are added in the far-field, the beam tilt is observed. But if the individual LP cross-polarised components are suppressed, no tilt will be present. Therefore, the above indicate that the tilt comes as a result of the LP cross-polarisation of the two individual sources.

Both GO and PO are very similar in the tilt prediction. This could be the reason why some authors [24], [26] preferred GO to obtain an equation for the beam tilt, since it is mathematically simpler. But using GO, no CP cross-polarisation is obtained. On the contrary, it can be seen in Fig. 3.25, where a $\Phi = 90°$ cut was chosen since it is where maximum tilt is expected, that CP cross-pol will appear if PO is used.

The explanation of this cross-polarisation is the same as in the front-fed case.

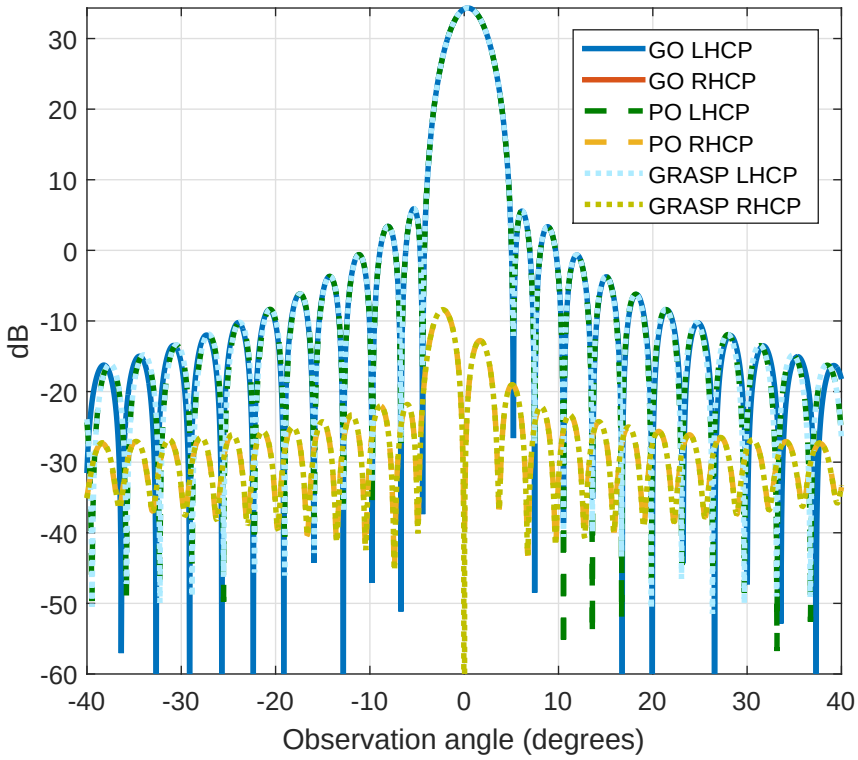

Figure 3.25: Directivity (dB) for a single offset reflector antenna with $d = 18.796\lambda$, $f/D = 0.5$, and $f_0 = 18.5$ GHz, fed by an RHCP source for a $\Phi = 90°$ plane.

Fig. 3.26 shows, for the same plane, both LP components with the LP cross-polarised components suppressed. It is seen that the suppression of the LP cross-polarised components corrects the tilt and lower the CP cross-polarisation level. However some CP cross-polarisation will be always present.

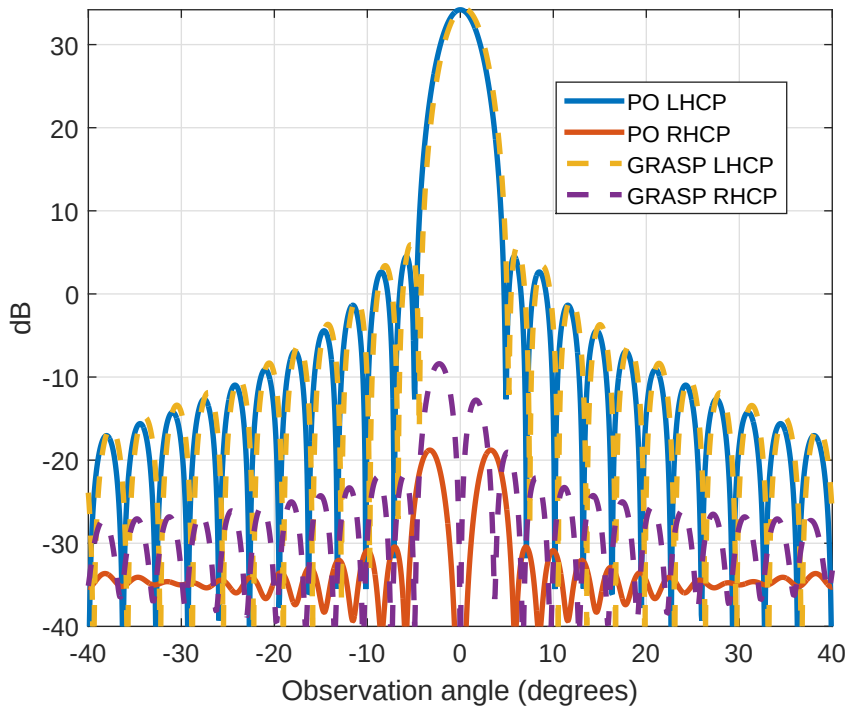

Figure 3.26: Directivity (dB) for a single offset reflector antenna with $d = 18.796\lambda$, $f/D = 0.5$, and $f_0 = 18.5$ GHz, fed by two orthogonal LP sources with a 90° phase shift between them, and with their LP cross-pol suppressed. $\Phi = 90°$.

As conclusion of the study on the far-field cross-polarisation performance of front-fed and offset configurations, it can be stated that for the front-fed configuration some cross-polarisation will arise in the far-field if the PO method is used. This is true even for a source (LP or CP) free of cross-polarisation. This feature is not predicted with GO. In the offset configuration, both methods accurately obtain the beam tilt in the CP feeding. However GO fails to obtain the correct sidelobe levels, while a further discrepancy between the two methods is observed in the estimation of the CP cross-polarisation. Furthermore, it has been shown that the beam tilt in CP arises from the cross-polarisation contributions from two orthogonal LP feeds due to the offset. These LP feeds are obtained if the CP feed is decomposed into two orthogonal LP feeds with 90° of phase difference between them.

3.7.3 Numerical methods to solve the far-field integrals

So far nothing has been said about the numerical computation the far-field integrals. In this subsection two numerical methods will be reviewed to compute the

PO far-field integrals (Eq. 3.6.22-3.6.27), since in Section 3.7.2 has already been demonstrated that PO is more accurate than GO.

The implementation of the far-field integrals has received a lot of attention in the literature [27, 28]. They can be divided in two big groups: the ones that try to simplify the integrals or try to solve them in an analytical way, such as the FFT method [29, 30] or the Rusch's method [28], and the ones that try to improve the speed or the accuracy of the way in which the integrals are computed, such as Ludwig's method [31, 32], Levin's method [33] or Jacobi-Bessel method [21, 34].

The first group has the limitation of being only valid for special cases. For example, the fast Fourier Transform (FFT) method performs a 2D integral. Therefore, it is only valid for the GO integrals performed at the aperture plane. Some authors have tried to implement the PO integrals as a series of FFTs, where the accuracy/speed trade-off has to be taken into account [30]. Another disadvantage is that the number of points in the reflector grid and the far-field grid has to be the same. The Rusch's method try to present analytical equations both for the feed and for the PO integrals, with the limitations that this implies for other cases not considered in the method [28].

The second group presents the most common ways to implement the PO integrals. Comments and comparisons on these methods can be found in Chapters 1 and 6 of [27] and in [28].

In the present thesis, two methods will be compared. The first is the implementation of the trapezoidal rule. The main advantage of the method is that it is already implemented in a very efficient way in MATLAB, being simple and fast. The second method is the Ludwig's method, since it represents a numerical-efficient way to perform the PO integrals for virtually any kind of configuration and feed.

Before continuing, it should be noted that slightly different results will be obtain if spherical, cylindrical or Cartesian grids are used to discretize the reflector. These differences are usually relevant for observation angles far from the main beam. Cylindrical and spherical grids will concentrate more points around the centre of the reflector than the Cartesian grid, as Fig.3.27a shows for a cylindrical grid and Fig.3.27b shows for a Cartesian grid. Therefore, since more energy from the feed will be concentrated around the centre, for the same number of points, cylindrical

and spherical grids will give more accurate results than the Cartesian grid.

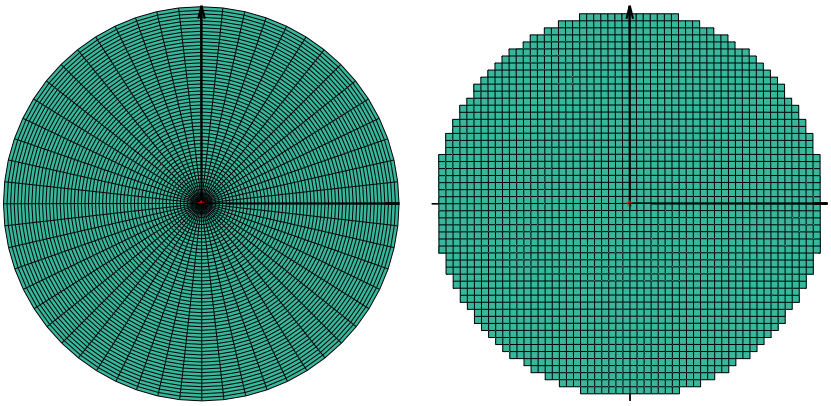

(a) Cylindrical grid (b) Cartesian grid

Figure 3.27: Reflector grids: a) cylindrical grid, b) Cartesian grid.

Trapezoidal rule

The trapezoidal rule is one of the more common ways to perform integrals. It approximates a discretized region of the function by a trapezoid, being easier to obtain its area. It can be expressed mathematically as [35]

$$\int_{x_1}^{x_2} f(x)dx \simeq (x_2 - x_1)\left(\frac{f(x_1) + f(x_2)}{2}\right) \tag{3.7.9}$$

Ludwig's method

The Ludwig's method [31, 32] is going to be reviewed for a cylindrical grid. The same procedure applies to spherical or Cartesian grids. The first step is to assume an incremental area across the grid as

$$\Delta S_{mn} = \{(r, \phi) : \, r_m \leq r \leq r_{m+1}, \, \phi_n \leq \phi \leq \phi_{n+1}\} \tag{3.7.10}$$

If ΔS_{mn} is supposed to be in the order of λ, then the phase term cannot vary more than 360°. On the other hand, for this same interval the magnitude of the fields cannot generally vary abruptly. Following this assumption, the function to be integrated (Eq.3.7.5) can be separated into magnitude and phase. The magnitude is referred to the magnitude of the currents (they can be complex):

$$\vec{F} = \frac{\vec{J}_s'}{\rho_s} N r \tag{3.7.11}$$

being $\vec{J}_s = \vec{J}_s' e^{-jk\rho_s}/\rho_s$. The phase factor due to the geometrical path from the feed to the reflector surface can be expressed as

$$\gamma = r \sin\Theta \cos(\Phi - \phi) + z \cos\Theta - \rho_s \tag{3.7.12}$$

These functions can be expanded into a summation of coefficients as

$$\vec{F} \simeq \vec{a}_{mn} + \vec{b}_{mn}(r - r_m) + \vec{c}_{mn}(\phi - \phi_n) \tag{3.7.13a}$$

$$\gamma \simeq \alpha_{mn} + \beta_{mn}(r - r_m) + \xi_{mn}(\phi - \phi_n) \tag{3.7.13b}$$

being $(r, \phi) \in \Delta S_{mn}$. Since these functions are considered linear within the interval, they can be expanded as a Taylor series. To obtain the coefficients in Eq.3.7.13a and Eq.3.7.13b a plane is fit to the four corners of the interval ΔS_{mn}: (r_m, ϕ_n), (r_{m+1}, ϕ_n), (r_m, ϕ_{n+1}) and (r_{m+1}, ϕ_{n+1}). For the fitting, the least square method is applied:

$$\left(\vec{F}(r, \phi) - (\vec{a}_{mn} + \vec{b}_{mn}(r, r_m) + \vec{c}_{mn}(\phi, \phi_n))\right)^2 \tag{3.7.14a}$$

$$(\gamma(r, \phi) - (\alpha_{mn} + \beta_{mn}(r, r_m) + \xi_{mn}(\phi, \phi_n)))^2 \tag{3.7.14b}$$

Therefore, the four corners are substituted in Eq.3.7.14a and Eq.3.7.14b, added together for each function, and their derivatives with respect to each coefficient are imposed to be zero in order to find the coefficients. This procedure yields

$$\vec{a}_{mn} = \frac{1}{4}\left(3\vec{F}(r_m, \phi_n) + \vec{F}(r_{m+1}, \phi_n) + \vec{F}(r_m, \phi_{n+1}) - \vec{F}(r_{m+1}, \phi_{n+1})\right) \tag{3.7.15a}$$

$$\vec{b}_{mn} = \frac{1}{2\Delta r_m}\left(-\vec{F}(r_m, \phi_n) + \vec{F}(r_{m+1}, \phi_n) - \vec{F}(r_m, \phi_{n+1}) + \vec{F}(r_{m+1}, \phi_{n+1})\right) \tag{3.7.15b}$$

$$\vec{c}_{mn} = \frac{1}{2\Delta\phi_n}\left(-\vec{F}(r_m,\phi_n) - \vec{F}(r_{m+1},\phi_n) + \vec{F}(r_m,\phi_{n+1}) + \vec{F}(r_{m+1},\phi_{n+1})\right) \tag{3.7.15c}$$

The same applies to α_{mn}, β_{mn} and ξ_{mn}. Now, if Eq.3.7.14a and Eq.3.7.14b are introduced into the PO integrals from Eq.3.7.5, it can be observed that the integrals can be solved analytically. Therefore, the PO integrals can be expressed as

$$\begin{aligned}\vec{p}(\Theta,\Phi) = \sum_{mn} e^{jk\alpha_{mn}}\Bigg[&\vec{a}_{mn}\frac{e^{jk\beta_{mn}\Delta r_m}-1}{jk\beta_{mn}}\frac{e^{jk\xi_{mn}\Delta\phi_n}-1}{jk\xi_{mn}} \\ &+\vec{b}_{mn}\left(\frac{\Delta r_m}{jk\beta_{mn}}e^{jk\beta_{mn}\Delta r_m} - \frac{e^{jk\beta_{mn}\Delta r_m}-1}{(jk\beta_{mn})^2}\right)\frac{e^{jk\xi_{mn}\Delta\phi_n}-1}{jk\xi_{mn}} \\ &+\vec{c}_{mn}\frac{e^{jk\beta_{mn}\Delta r_m}-1}{jk\beta_{mn}}\left(\frac{\Delta\phi_n}{jk\xi_{mn}}e^{jk\xi_{mn}\Delta\phi_n} - \frac{e^{jk\xi_{mn}\Delta\phi_n}-1}{(jk\xi_{mn})^2}\right)\Bigg]\end{aligned} \tag{3.7.16}$$

It can be observed in Eq.3.7.16 that a problem will arise when the denominator goes close to 0, leading to an indetermination when is 0. Ludwig mentioned this issue in [31], but didn't provide with a solution. Nevertheless, as with any indetermination of the kind 0/0, L'Hospital's rule can be applied to solve it. There are three cases: only $k\beta_{mn} \simeq 0$, only $k\xi_{mn} \simeq 0$ and both $k\beta_{mn} \simeq 0$ and $k\xi_{mn} \simeq 0$. Meng et al. [36] presented a work in which they say that L'Hospital's rule is not a good method to solve the problem when the denominator is close to 0. To solve the problem they present a solution based on a Taylor series expansion. However, since L'Hospital rule presents a way to solve the problem in the limit of the indetermination, for values close enough to 0 it still is a good method. Therefore, it is the method used in the present dissertation.

The $k\beta_{mn} \leq L_i$ case yields

$$\begin{aligned}\vec{p}_{mn} = e^{jk\alpha_{mn}}\Delta r_m\Bigg[&\left(\vec{a}_{mn} + \frac{\Delta r_m}{2}\vec{b}_{mn}\right)\frac{e^{jk\xi_{mn}\Delta\phi_n}-1}{jk\xi_{mn}} \\ &+\vec{c}_{mn}\left(\frac{\Delta\phi_n}{jk\xi_{mn}}e^{jk\xi_{mn}\Delta\phi_n} - \frac{e^{jk\xi_{mn}\Delta\phi_n}-1}{(jk\xi_{mn})^2}\right)\Bigg]\end{aligned} \tag{3.7.17}$$

The $k\xi_{mn} \leq L_i$ case yields

$$\vec{p}_{mn} = e^{jk\alpha_{mn}}\Delta\phi_n\Bigg[\left(\vec{a}_{mn} + \frac{\Delta\phi_n}{2}\vec{c}_{mn}\right)\frac{e^{jk\beta_{mn}\Delta r_m} - 1}{jk\beta_{mn}} + \vec{b}_{mn}\left(\frac{\Delta r_m}{jk\beta_{mn}}e^{jk\beta_{mn}\Delta r_m} - \frac{e^{jk\beta_{mn}\Delta r_m} - 1}{(jk\beta_{mn})^2}\right)\Bigg] \tag{3.7.18}$$

Finally, for $k\beta_{mn} \leq L_i$ and $k\xi_{mn} \leq L_i$ case yields

$$\vec{p}_{mn} = e^{jk\alpha_{mn}}\Delta r_m\Delta\phi_n\left(\vec{a}_{mn} + \frac{\Delta r_m}{2}\vec{b}_{mn} + \frac{\Delta\phi_n}{2}\vec{c}_{mn}\right) \tag{3.7.19}$$

Comparison between Trapezoidal rule and Ludwig's method

The main difference between the two methods is the way they perform the integral. MATLAB trapezoidal implementation approximates the local function between two points by a straight line. Therefore, as the grid size is increased, the distance between the two points is decreased and therefore the trapezoids will be closer to the original function. On the other hand, Ludwig's method approximates the original function by fitting a plane in four corners using the least square method.

Close to the far-field broadside, the phase of the function γ (see Eq. 3.7.12) to be integrated is smooth. This is illustrated in Fig.3.28a, which shows the function γ for $\Theta = 2.3°$ and $\Phi = 90°$. Therefore, both trapezoid rule and Ludwig's method perform the integration accurately. However, for far-field points far from broadside γ varies more sharply, as Fig.3.28b shows for $\Theta = -70°$ and $\Phi = 90°$. In these regions, Ludwig's method finds a fitting function that captures better than the trapezoidal rule these more sharply variations.

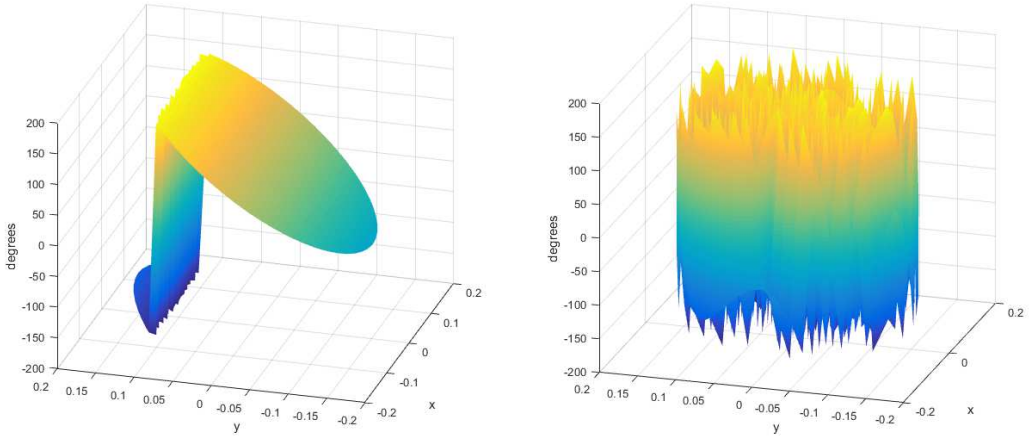

(a) γ for $\Theta = 2.3°$ and $\Phi = 90°$ (b) γ for $\Theta = -70°$ and $\Phi = 90°$

Figure 3.28: Function γ across the reflector aperture for: a) $\Theta = 2.3°$ and $\Phi = 90°$, b) $\Theta = -70°$ and $\Phi = 90°$.

Fig.3.29a shows the far-field for the vertical plane of the offset parabolic reflector used in [6] comparing both numerical methods, and also GRASP results. Fig.3.29b do the same for the horizontal plane. Both methods have the same grid of $ceil\left(\frac{d}{\lambda/3}\right)$. Both figures confirm the mentioned above: around broadside, both methods yield accurate results (when compared with GRASP). However, for angles far from broadside, Ludwig's method yields more accurate results than the trapezoid rule.

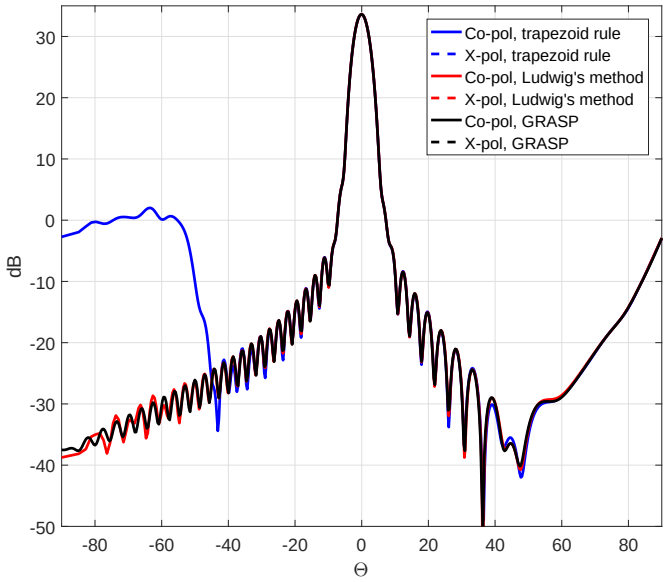

(a)

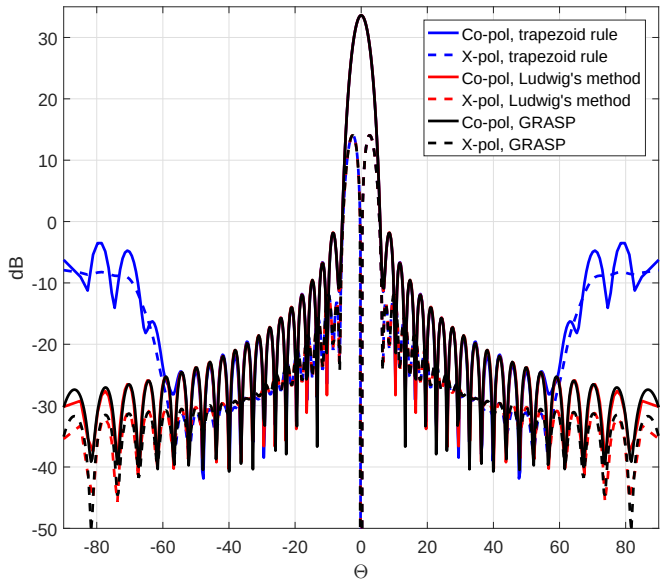

(b)

Figure 3.29: Directivity (dB) comparison of numerical methods for a single offset reflector antenna with $d = 18.796\lambda$, $f/D = 0.5$, and $f_0 = 18.5$ GHz for (a) the vertical plane ($\Phi = 0°$) and (b) the horizontal plane ($\Phi = 90°$), fed by an ideal Gaussian beam: trapezoidal rule (blue lines), Ludwig's method (red lines) and GRASP (black lines).

3.8 Summary

This chapter has aimed to describe the basic theory to analyse single parabolic reflector antennas and their depolarisation properties. First, in Section 3.2 the different coordinate systems used in this thesis and their transformations have been presented. Then, in Section 3.3 the geometry of single front-fed and offset reflectors has been reviewed. Section 3.4 has carried out a review of the most typical sources to feed these reflectors, i.e., electric dipole, magnetic dipole, Huygens source, Gaussian beam and circularly polarised source. In Section 3.5 these sources has been used as feeds for the front-fed and offset reflectors to study their depolarisation properties at the aperture plane, yielding the same conclusions than other authors: the Huygens source (and by extension the Gaussian beam) is the ideal linearly-polarised source to feed a front-fed parabolic reflector, as it is a circularly polarised source formed by two Huygens sources (or Gaussian beams) with equal magnitude and 90° of phase shift. Some extra comments on the rise of cross-polarisation in the offset configuration have been included.

The two more common methods to obtain the far-field of these antennas have been reviewed in Section 3.6, i.e., geometrical optics and physical optics. A new tool programmed in MATLAB has been developed to analyse single reflector antennas. This tool has been used to compare geometrical and physical optics validating the results with GRASP. Same conclusion as other authors has been reached (physical optics is more accurate) along with proper explanations of their accuracy to predict cross-polarisation and first sidelobes levels. The physical optics method has been used to show that even the front-fed configuration fed by a source free of cross-polarisation can present cross-polarisation in the far-field. New insight into the origin of the far-field beam tilt in the offset configuration when fed by a circularly polarised feed has been provided. Finally, two numerical tools to solve the integrals have been reviewed and compared as well, leading to slightly different results specially for points far from the broadside direction.

References

[1] S. T. Sharma, S. Rao, and L. Shafai, *Handbook of Reflector Antennas and Feed Systems, vol. I: Theory and Design of Reflectors.* Artech House, 2013.

[2] Y. Rahmat-Samii and R. Haupt, "Reflector antenna developments: A perspective on the past, present, and future," *IEEE Antennas and Propag. Mag.*, vol. 57, no. 2, pp. 85–95, April 2015.

[3] E. M. T. Jones, "Parabolic reflector and hyperboloid lens antennas," *Trans. of the IRE Prof. Group on Antennas and Propag.*, vol. 2, no. 3, pp. 119–127, July 1954.

[4] I. Koffman, "Feed polarization for parallel currents in reflectors generated by conic sections," *IEEE Trans. Antennas Propag.*, vol. 20, no. 1, pp. 37–40, Jan 1966.

[5] TICRA staff, *GRASP Technical Description, TICRA, Copenhagen, 2005-2008.*

[6] T. S. Chu and R. H. Turrin, "Depolarization properties of offset reflector antennas," *IEEE Transactions on Antennas and Propagion*, vol. 21, no. 3, pp. 339–345, May 1973.

[7] Y. Rahmat-Samii, "A comparison between GO/aperture field and Physical-Optics methods for offset reflectors," *IEEE Trans. Antennas Propag.*, vol. 32, no. 53, pp. 301–306, Mar 1984.

[8] MATLAB® Toolbox [Online]. Available: https://uk.mathworks.com/products/matlab.html.

[9] Y. Rahmat-Samii, "Useful coordinate transformations for antenna applications," *IEEE Trans. Antennas Propag.*, vol. 27, no. 4, pp. 571–574, July 1979.

[10] S. Silver, *Microwave Antenna Theory and Design.* McGraw-Hill, 1949.

[11] C. A. Balanis, *Antenna Theory: Analysis and Design*, 3rd ed. Wiley & Sons, 2015.

[12] A. W. Rudge, A. W. Love, and A. D. Olver, *The Handbook of Antenna Design, Volume I.* Peter Peregrinus Ltd., 1982.

[13] J. D. Hanfling, "Aperture fields of paraboloidal reflectors by stereographic mapping of feed polarization," *IEEE Trans. Antennas Propag.*, vol. 18, no. 3, pp. 392–396, Sept 1969.

[14] A. W. Rudge and N. A. Adatia, "Offset-parabolic-reflector antennas: A review," *Proceedings of the IEEE*, vol. 66, no. 12, pp. 1592–1618, Dec 1978.

[15] J. S. Cook, E. M. Elam, and H. Zucker, "The open Cassegrain antenna: Part I. electromagnetic design and analysis," Bell Sys. Tech. J., Vol. 44, Tech. Rep., Sept 1965.

[16] "IEEE standard definitions of terms for antennas," *IEEE Std 145-1993*, vol. 21, no. 1, pp. 116–119, Jan 1973.

[17] A. C. Ludwig, "The definition of cross polarization," *IEEE Trans. Antennas Propag.*, vol. 21, no. 1, pp. 116–119, Jan 1973.

[18] B. Y. Toh, R. Cahill, and V. F. Fusco, "Understanding and measuring circular polarization," *IEEE Trans. Edu.*, vol. 46, no. 3, pp. 313–318, Aug 2003.

[19] P. A. Watson and S. I. Ghobrial, "Off-axis polarization characteristics of cassegrainian and front-fed paraboloidal antennas," *IEEE Trans. Antennas Propag.*, vol. 20, no. 6, pp. 691–699, Nov 1972.

[20] J. Dijk, C. T. W. van Diepenbeek, E. J. Maanders, and L. F. G. Thurlings, "The polarization losses of offset paraboloid antennas," *IEEE Trans. Antennas Propag.*, vol. 22, no. 4, pp. 513–520, July 1974.

[21] Y. Rahmat-Samii and V. Galindo-Israel, "Shaped reflector antenna analysis using the jacobi-bessel series," *IEEE Trans. Antennas Propag.*, vol. 28, no. 4, pp. 571–574, July 1980.

[22] A. W. Rudge, "Multiple-beam antennas: Offset reflectors with offset feeds," *IEEE Transactions on Antennas and Propagion*, vol. 23, no. 3, pp. 317–322, Nov 1975.

[23] J. Jacobsen, "On the cross polarization of asymmetric reflector antennas for satellite applications," *IEEE Trans. Antennas Propag.*, vol. 25, no. 2, pp. 276–283, Mar 1977.

[24] D. W. Duan and Y. Rahmat-Samii, "Beam squint determination in conic-section reflector antennas with circularly polarized feeds," *IEEE Trans. Antennas Propag.*, vol. 39, no. 5, pp. 612–619, May 1991.

[25] N. A. Adatia, "Cross-polarisation of reflector antennas," Ph.D. dissertation, Surrey University, England, UK, Dec 1974.

[26] N. A. Adatia and A. W. Rudge, "Beam-squint in circularly polarised offset reflector antennas," *Electr. Lett.*, vol. 11, no. 21, pp. 513–515, Oct 1975.

[27] A. C. Densmore, "Algorithms for rapid characterization and optimization of aperture and reflector antennas," Ph.D. dissertation, UCLA, USA, 2014.

[28] C. Scott, *Modern Methods of Reflector Antenna Analysis and Design*. Artech House, 1990.

[29] Z. H. Firouzeh, A. Zeidaabadi-Nezhad, and H. Mirmohammad-Sadeghi, "An optimum meshing to compute the radiation integrals of reflector antennas by FFT method," *Proc. of the ASPC*, pp. 1–4, 2007.

[30] R. Mittra, V. Galindo-Israel, and R. Norman, "An efficient technique for the computation of vector secondary patterns of offset parabolic reflectors," *IEEE Trans. Antennas Propag.*, vol. 27, no. 3, pp. 294–304, May 1979.

[31] A. C. Ludwig, "Computation of radiation patterns involving numerical double integration," *IEEE Trans. Antennas Propag.*, vol. 16, no. 6, pp. 767–769, July 1968.

[32] ——, "Calculation of scattered patterns from asymmetrical reflectors," JPL TR 32-1430, Tech. Rep., Feb 1970.

[33] D. Levin, "Fast integration of rapidly oscillatory functions," *J. Comput. Appl. Math.*, vol. 67, no. 1, pp. 95–101, Feb 1996.

[34] V. Galindo-Israel and R. Mittra, "A new series representation of the radiation integral with application to reflector antennas," *IEEE Trans. Antennas Propag.*, vol. 25, no. 5, pp. 631–641, Sept 1977.

[35] M. Abramowitz and I. A. Stegun, *Handbook of Mathematical Functions*. National Bureau of Standards, Applied Math. Series no. 55, 1964.

[36] W. Meng, W. Nan, and L. Changhong, "Problem of singularity in Ludwig's algorithm," *Microw. Opt. Technol. Lett.*, vol. 49, no. 2, pp. 400–403, Feb 2007.

Chapter 4

Cross-polarisation reduction of linear-to-circular polarising offset reflectors

4.1 Introduction

As it was mentioned in Section 1.2.3, reflector antennas have been extensively used in multi-beam antennas for satellite communications [1]. Their high gain per beam and frequency re-use capabilities for different beams have been the keys of their success [2]. The more popular multi-beam antenna configuration consists on four reflectors using a single-feed-per-beam (SFB) architecture to provide a four-colour frequency and polarisation reuse scheme [1]. SFB architectures are usually preferred in many applications over multi-feed-per-beam (MFB) architectures since they do not need any beam forming network (BFN). The BFN in MFB allows to generate adjacent beams by a single reflector, which reduces the number of reflectors used [3].

The simplification of the antenna system by using SFB architectures and the minimum number of reflectors has been a top priority in modern satellite communications [4]. Early attempts to achieve the aforementioned characteristics include the use of dual-gridded reflectors [5]. However, the proposed technologies worked in linear polarisation (LP), while the new trend in satcoms is to use circular polarisation (CP) both for uplink and downlink [6]. Frequency selective surfaces (FSS) in CP [7,8] or circular polarisation selective surfaces (CPSS) [9–12] have been proposed

to reduce the number of reflectors while using CP feeds. However, they are still not sufficiently mature to be able to provide the needed RF performances.

A concept presented in different works maintain the optics in LP up to the main reflector surface, where the LP to CP conversion takes place [4, 6, 13–15]. One big challenge of this concept is the manufacturing of the polarising curved reflector. As a first approach, a multi-beam Ku-band reflector antenna prototype comprising a cylindrical polarising reflector fed by a quasi-optical beamformer was manufactured and measured [15] by our research group. Good agreement with simulations validates the use of 1D polarising conformal surfaces. Now efforts are focused on developing the technology to manufacture the polarising surfaces in 2D conformal shapes.

The other big challenge of the main polarising surface is the design of the dual-band LP-CP polarising unit-cell that converts each LP band to an orthogonal CP. A unit-cell with these characteristics was already presented in [4]. However, its large electrical length limits its performance due to the appearance of grating lobes for angles different from broadside. More recently, a more compact unit-cell in Ku-band based on similar working principles has been proposed in [14]. Due to the large dimensions of the main surface, another key feature of the unit-cell is a broad angular stability to obtain reasonable levels of cross-polarisation in the far-field. The unit-cell from [14] maintains reasonable performance for local angle of incidence θ up to 30° along the main plane of incidence. But the large set of angles of incidence imposed by the main reflector forces the use of an optimisation procedure to improve the cross-polarisation performance of these kind of structures.

This chapter presents an optimisation procedure to improve the cross-polarisation performance of linear-to-circular polarising offset reflectors based on two steps: geometrical optimisation of the unit-cell and unit-cell rotation. The former performs a local axial ratio (AR) optimisation and it decreases the far-field cross-polarisation in the vertical plane mainly. The latter performs a global optimisation of the far-field cross-polarisation based on unit-cell rotation and it affects mainly the far-field horizontal plane. The optimisation procedure will be validated by comparison with measurements for an offset flat reflector fed by a standard Flann's horn. The breadboards have been manufactured and measured at Heriot-Watt University's Microwave Lab.

The tool developed for Chapter 3 (see Section 3.7) for the analysis of reflector

antennas is going to be updated with the theory presented here, i.e., modelling of practical feeds and analysis of metallodieletric arrays. It should be noted that at the moment there is no such tool in the market. This tool will then resemble similar tools developed by other research groups to analyse reflectarrays.

4.2 Analysis of polarising reflectors

As discussed in the introduction, polarising reflectors may be encountered in a flat or conformal surface and illuminated by far-fields or near-fields of primary feeds. In this section, an overview of the generic analysis methodologies that can be used to simulate the radiation characteristics from this class of structures is presented. These techniques are: the Floquet modal expansion of the fields impinging doubly periodic surfaces, the modelling of the feed's near-field and the physical optics method to obtain the reflector antenna far-field. It should be noted that these techniques resemble techniques used in reflectarray analysis [16–18].

The Floquet modal expansion and the physical optics method were described in Section 2.5 and Section 3.6.2 respectively. Therefore, only special emphasis will be put on the description of the near-field modelling by means of an example. Then, the radiation characteristics associated with a curved polarising reflector when illuminated by an ideal LP feed will be analysed. By means of comparison with the case of a pure metal reflector with the same geometry and illuminated by a feed with similar characteristics but in CP, the margin for improvement in the cross-polarisation response will be demonstrated.

4.2.1 Numerical technique

As it was mentioned in Section 2.5, periodic structures such as FSS [19] or reflectarrays [16] are commonly analysed using Floquet modal expansion of the fields under some approximations. These approximations are: local periodicity, infinite structure locally flat unit-cells and plane wave incidence. In particular, the local periodicity approximation suggests that the interaction of the incoming wave with each unit-cell can be obtained on the assumption of an infinite periodic structure. This approximation is more accurate for slowly varying geometries along the reflector, since the

mutual coupling effects in these arrays are predominantly associated with neighbouring unit-cells. It is consistently valid in the structures under consideration in this thesis. The approximation of locally flat unit-cells is quite accurate for typical reflectors of large electrical dimensions. Each unit-cell is therefore modelled under plane wave incidence and fully periodic boundary conditions.

Under these assumptions, the reflection characteristics of a unit-cell can be obtained using spectral domain method of moments (MoM) tools [17,18,20,21]. The resulting output would be the S-parameters describing the co- and cross-polarised reflection coefficients for each Floquet space harmonic associated with every unit-cell on the surface. For unit-cells that do not generate grating lobes [22] and where the feed is sufficiently far such that the propagating element dominates the incoming radiation, it is sufficient to only consider the fundamental harmonic. However this methodology can be generalised to consider effects associated with higher order harmonics.

The large reflector dimensions in terms of the wavelength allow the use of ray tracing techniques such as geometrical optics to model the incident and reflected field (see Chapter 3). If the reflector is placed in the far-field of the feed, the feed can be assumed a point source. Therefore, the incidence on the unit-cells is dictated by the angle of incidence of the spherical wave emanating from the feed origin.

For many practical configurations, where the reflector is not sufficiently far to assume spherical wave incidence, an accurate modelling of the feed's near-field is needed [23, 24]. The feed's near-field (both electric and magnetic) at the reflector surface can be directly obtained using any integral equation solver (or similar) such as CST Microwave Studio [25], or from the far-field characteristics together with a spherical wave expansion [26]. In general, the near-field contains both propagating and non-propagating fields. As mentioned above, it is often sufficient to consider only the propagating component of the near-field. This corresponds to the fields associated with the fundamental Floquet space harmonic. The local angles of incidence of the propagating element of the field can be extracted from the normalised real part of the Poynting vector:

$$\hat{k}_0 = \frac{\vec{P}}{|P|} = \frac{\frac{1}{2} real\{\vec{E} \times \vec{H}^*\}}{|P|} \tag{4.2.1}$$

where $\vec{E}$ and $\vec{H}$ are referred to the total near-fields. The configuration shown in

Fig. 4.1 is used as example, where a reflector with dimensions $d_x = d_y = 270$ mm is fed by a standard Flann's horn model 19240 [27] at 17.7 GHz, placed at a distance $f = 250$ mm from the reflector with offset angle $\theta_f = 35°$. The angles of incidence for this horn across the reflector surface are depicted in Fig. 4.2. It is noted that for a real feed as the one under consideration, this plot is frequency dependent. For comparison, the angles of incidence associated with an ideal point source are superimposed (frequency independent).

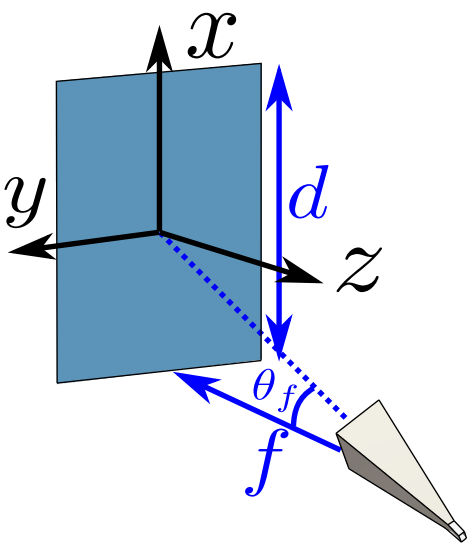

Figure 4.1: Offset flat reflector of dimensions $d_x = d_y = 270$ mm fed by a standard Flann's horn model 19240 at 17.7 GHz polarised at slant 45°, placed at a distance $f = 250$ mm and offset angle $\theta_f = 35°$.

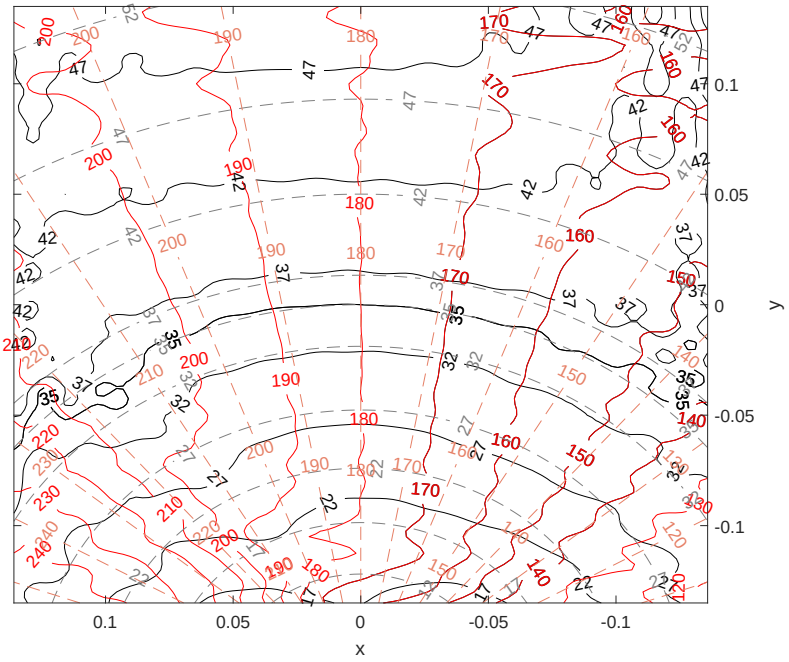

Figure 4.2: Local angles of incidence θ_l (black lines) and ϕ_l (red lines) across an offset flat reflector with dimensions $d_x = d_y = 270$ mm fed by a standard Flann's horn model 19240 at 17.7 GHz placed at a distance $f = 250$ mm and offset angle $\theta_f = 35°$, superimposed with the angles of incidence for the same configuration and a point source (lighter colour).

The procedure above yields the direction of the incoming propagating field locally at each unit-cell of the array. The derivation of the reflected field at each unit cell further requires the associated magnitude and phase. This is captured in the complex magnitude a_{m00} of the fundamental Floquet space harmonic, where the subscript $m = 1, 2$ represents the TM and TE polarisation respectively. This coefficient can be estimated considering that the total near-field can be as a superposition of Floquet space harmonics and exploiting the associated orthogonality property:

$$a_{m00} = \iint \vec{H} \cdot \vec{\kappa}_{m00} \psi^*_{00}(x, y) dx dy \tag{4.2.2}$$

where it is assumed that the periodic surface lies on the xy-plane. In Eq. 4.2.2, $\vec{\kappa}_{m00}$ is a unit vector along the xy-plane representing the direction of the tangential magnetic field for the TM and TE modes respectively while ψ_{00} is the Floquet phasor of the fundamental harmonic, defined by the tangential components k_{x00} and k_{y00} of the wavenumber k_0 along the x- and y-axes respectively [19] (see Eq. 2.5.5). Solving

Eq. 4.2.2 yields

$$a_{100} = -\eta_0 C_0 Q_0 \cos\theta_l \left(-H_x \sin\phi_l + H_y \cos\phi_l\right) \tag{4.2.3a}$$

$$a_{200} = \frac{\eta_0 C_0 Q_0}{\cos\theta_l} \left(H_x \cos\phi_l + H_y \sin\phi_l\right) \tag{4.2.3b}$$

where H_x and H_y refer to the tangential near-field, C_0 is a needed coefficient to maintain the same power magnitude as the real part of the original Poynting vector, and

$$Q_0 = \iint \psi_{00}(x,y)dxdy = 4\frac{\sin(k_{00}^y \frac{D_y}{2})\sin(k_{00}^x \frac{D_x}{2})}{k_{00}^y k_{00}^x} \tag{4.2.4}$$

D_y and D_x in Eq. 4.2.4 refer to the unit-cell dimensions. Since the Floquet expansion works here as an approximation, selecting sufficient small virtual unit-cells ($D_y = \lambda_0/6$ and $D_x = \lambda_0/6$) gives accurate enough results.

This way of modelling the near-field has been included in the tool presented in Section 3.7. Fig. 4.3 shows the far-field vertical and horizontal planes for the configuration from Fig. 4.1, where the reflector is supposed to be metallic using the updated tool. In blue is shown the co- and cross-polarisation components if the total near-field at the reflector surface is used to obtain the surface currents. In red is shown the co- and cross-polarisation components if only the fundamental TE and TM modes (extracted from the total near-field by the procedure explained above) are used to obtain the surface currents. As it can be seen, both set of curves produce the same results, which confirm the assumption of supposing that only the fundamental (radiative) modes of the total near-field will contribute to the far-field. It also validates the proposed way to extract these fundamental modes. Using this methodology, the amplitudes of the fundamental TE and TM modes of the incident near-field and their associated incident angles at each unit-cell can be obtained.

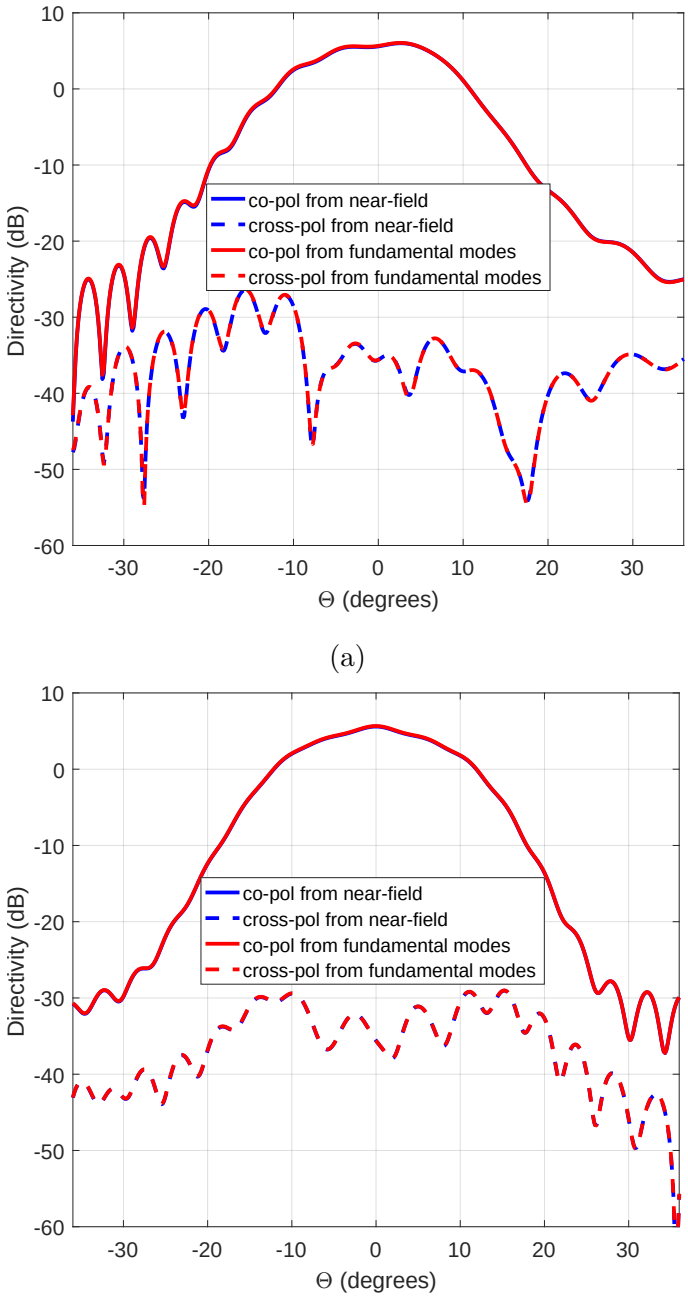

(a)

(b)

Figure 4.3: Comparison of the far-field from a metallic offset flat reflector using the near-field and using the fundamental modes only at 17.7 GHz for (a) the vertical plane ($\Phi = 0°$) and (b) the horizontal plane ($\Phi = 90°$).

Once the S-parameters and the incident field at each unit-cell are known, the reflected field can be obtained by using the relations from Section 2.5.5. Then, the equivalent electric and magnetic surface currents $\vec{J}_s$ and $\vec{M}_s$ can be obtained from the reflected fields using Love's Equivalence Principle [28]. It is usually supposed that the field behind the reflector is zero, which makes possible to place a perfect electric

or magnetic conductor to short-circuit one of the equivalent currents [29]. Then the equivalent current that has been short-circuited can be eliminated by means of the image principle [28]. If both equivalent currents are used, radiation over the entire 3D far-field sphere can be computed [30]. This approach has been validated against measurements in [15] and in [30] (technique II). These equivalent surface currents are integrated over the surface geometry to obtain the far-field by using aperture antenna theory [28]. This way of obtaining the reflected field (no PEC) has been added to the tool. Therefore, the results presented from now on only use the electric surface currents $\vec{J}_s$, but it should be noted that the magnetic surface currents $\vec{M}_s$ could be easily used as well at the expense of longer computing time.

4.2.2 Cross polarisation response from uniform arrays

Based on the design from [15], an offset cylindrical reflector is used as an example to illustrate the performance of fully periodic polarising reflectors. The antenna architecture is shown in Fig. 4.4a. Its dimensions are $d_x = d_y = 700$ mm, focal length $f = 500$ mm, and offset angle $\theta_f = 50°$. The reflector is fed by a Gaussian beam source at slant 45° (see Section 3.4.5), placed at the parabola focus. Due to the parabolic geometry in the vertical plane, the reflector will collimate the primary field only in the vertical plane of the far-field. Therefore, a fan-beam type radiation pattern is therefore produced in this example. Fig. 4.4a also shows the local coordinate system (in red) for a random location on the reflector, where the z-axis coincides with the normal to the surface.

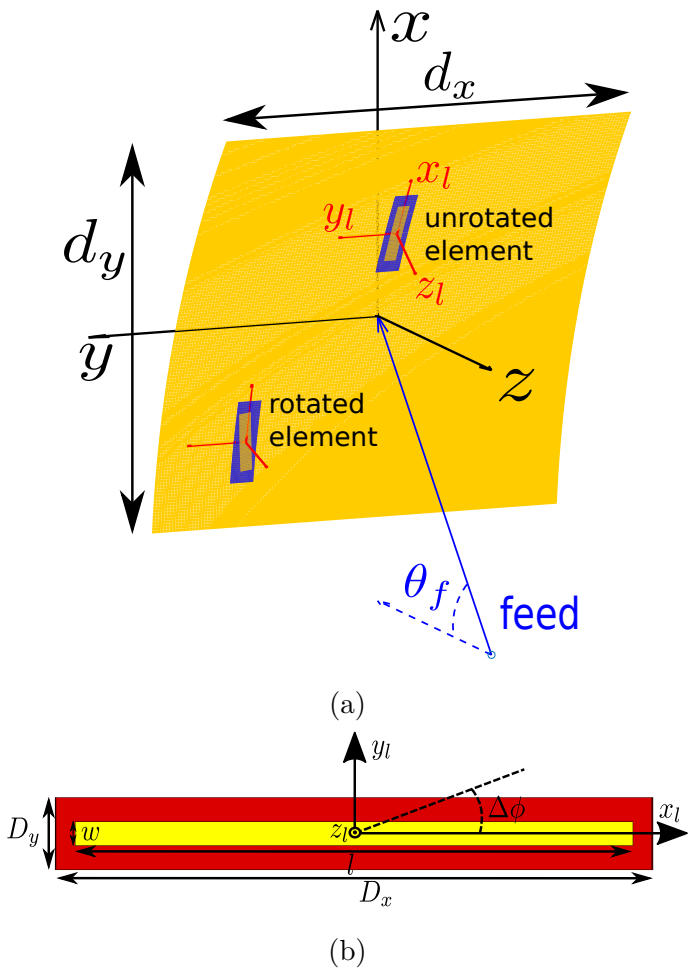

(a)

(b)

Figure 4.4: (a) Antenna architecture formed by an offset cylindrical parabolic reflector with dimensions $d_x = d_y = 700$ mm, focal length $f = 500$ mm and offset angle $\theta_f = 50°$, fed by an ideal Gaussian beam. (b) Geometry of the selected dipole unit-cell.

The multi-beam reflector antenna concept commented in the introduction [4] rely on dual-band LP to CP unit-cells working in orthogonal polarisations. However, in order to demonstrate the optimisation procedure presented in this chapter, a simpler unit-cell geometry based on the dipole element from [31] has been selected. The unit-cell is shown in Fig. 4.4b, where the dipole is assumed oriented along the x-axis. For the configuration shown in Fig. 4.4a, where the offset is in the xz plane, the dipole orientation along the x-axis gives a more deteriorated performance than if oriented along the y-axis. This orientation provides levels of cross-polarisation that can be easily measured in the Microwave Lab of Heriot-Watt University, as it will be shown in Section 4.4. The unit-cell has been optimised for the local incidence angles ($\theta_l = 25°$, $\phi_l = 180°$) experienced by the unit-cell at the centre of the reflector. The

unit-cell dimensions with respect to Fig. 4.4b are $D_x = 7.5$ mm, $D_y = 0.9$ mm, $l = 7$ mm and $w = 0.3$ mm. This polariser, which transforms an incident slant 45° LP wave into a left-handed CP (LHCP) wave, presents good performance (AR< 0.5 dB) for frequencies in the range 13.5-21.7 GHz, as shown in Fig. 4.5 (solid black line). Fig. 4.5 (solid lines) also show the AR produced by this polariser as the incidence angle θ_l varies in the range 10°-40° roughly corresponding to the lower and upper edges of the reflector along the vertical plane of symmetry. As shown, at 17.7 GHz the AR deteriorates up to > 2.5 dB within this angular range.

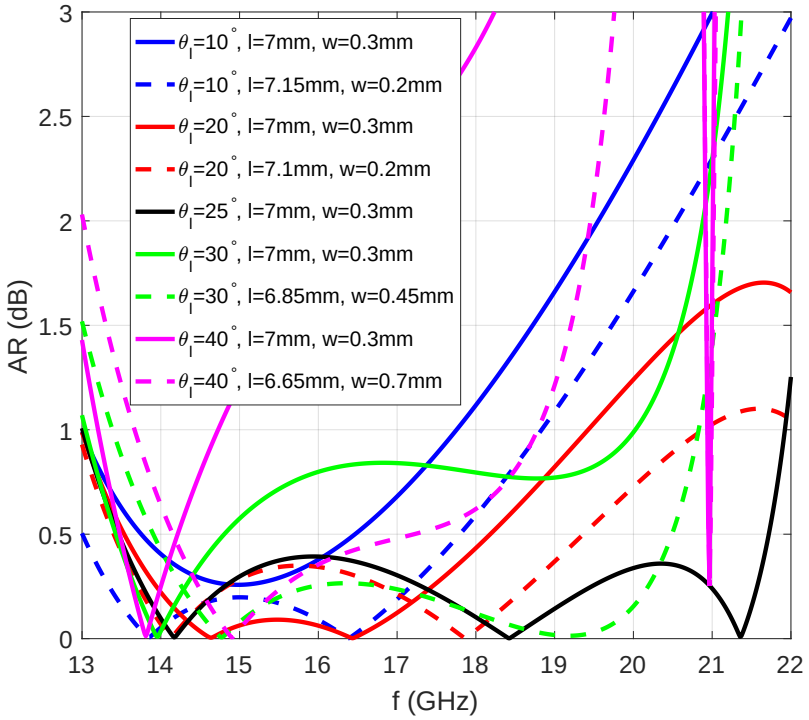

Figure 4.5: AR (dB) of the original (solid lines) and optimised (dashed lines) unit-cell for different θ_l.

This polarising reflector has been analysed with the technique outlined in the previous section. Fig. 4.6a and Fig. 4.6b show in blue lines the far-field characteristics at 17.7 GHz for the vertical ($\Phi = 0°$) and horizontal ($\Phi = 90°$) planes respectively. For comparison, the far-field characteristics from the same antenna architecture but assuming a perfect electric conductor (PEC) reflector and an ideal CP feed (which otherwise has the same characteristics and is placed in the same location) is also shown in Fig. 4.6a and Fig. 4.6b in red lines for the same frequency. As shown, the co-polarisation characteristics are very similar for the two cases. However, the cross-polarisation characteristics for the reflector with a uniform polarising array

are compromised by over 25 dB in some cases, including the broadside. For applications requiring good cross-polarisation discrimination, clearly this figure indicates significant margin for improvement of the polariser design.

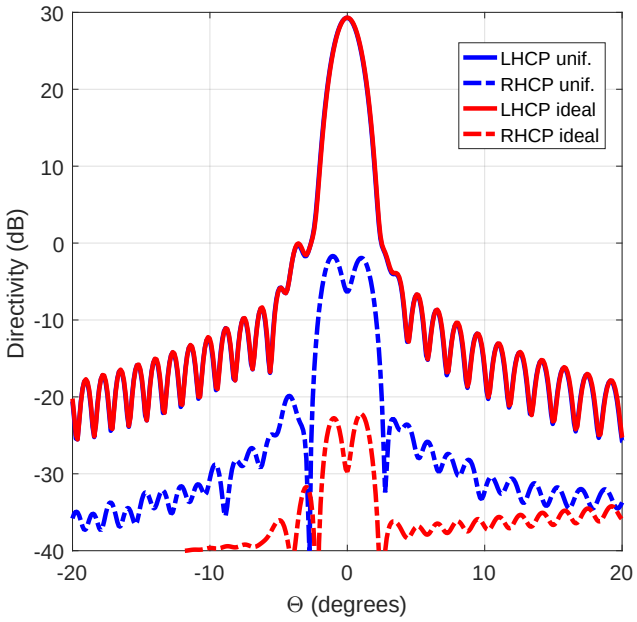

(a)

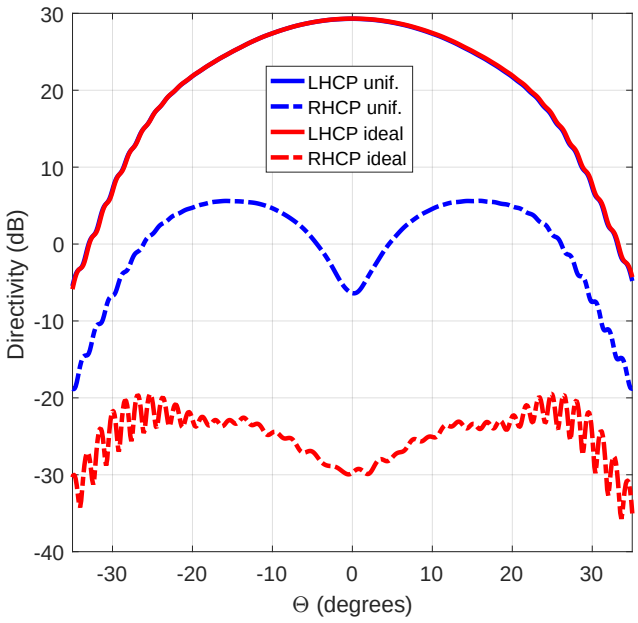

(b)

Figure 4.6: Far-field directivity (dB) at 17.7 GHz for (a) the vertical plane ($\Phi = 0°$) and (b) the horizontal plane ($\Phi = 90°$) for the metallic reflector fed by an ideal LHCP source (red) and the uniform unit-cell polariser fed by an ideal 45° LP source (blue).

4.3 Synthesis for reduced cross polarisation

Rectangular unit-cells, such as the one depicted in Fig. 4.4b, under plane wave illumination are associated with two principal planes of incidence. In Fig. 4.4 these are the xz- and the yz-planes. Along the principal planes and for regular element geometries (such as the dipole of Fig. 4.4b but also more complex variations [14]), the cross-polarisation reflection coefficient vanishes. The operation of the polarising surfaces can therefore be readily achieved ensuring a 90° differential phase between the TE and TM reflection coefficients, provided that the magnitudes of the two incident polarisations are balanced. The latter assumption is valid along the principal planes of incidence for primary feeds polarised at slant 45° (in Fig. 4.4 with respect to the z-axis). This polarisation is therefore considered here but also in other works [4, 6, 8, 14, 31].

For the antenna architecture under consideration, unit-cells along the vertical plane of symmetry in Fig. 4.4a are illuminated along a principle plane in Fig. 4.4b. For these unit-cells it is relatively straightforward to optimise the geometry in order to improve the AR of the locally reflected field, as shown in Fig. 4.5. All other unit-cells are illuminated along oblique planes of incidence. At oblique planes of incidence and for a primary feed polarisation fixed at slant 45°, the magnitude ratio between the TE and TM polarised components is no longer unitary but depends on ϕ_l. Due to the magnitude imbalance between the incoming TM and TE components, LP to CP conversion requires determining both co- and cross-polarisation reflection characteristics of the unit-cell. It has indeed been confirmed by full-wave simulations that for these unit-cells the AR of the locally reflected field cannot be significantly improved by adjusting the dipole dimensions.

The level of cross-polarisation in reflection for the dipole element of Fig. 4.4b and other geometries with similar working principle can be controlled by rotating the unit-cell's element around its centre. Consequently, local rotation of the element enables to significantly improve the AR. This is illustrated in Fig. 4.7 for the dipole geometry from Fig. 4.5 (black lines). The blue line shows the AR for the centre unit-cell (which experiences local incidence angles $\theta_l = 25°$, $\phi_l = 180°$). As ϕ_l moves away from this point and along a line of constant local θ ($\theta_l = 25°$), the AR deteriorates, as shown by the solid red and solid black lines for $\phi_l = 177°$ and $\phi_l = 170°$

respectively. However, once the element is rotated, the AR can be decreased close to the original levels. This is illustrated by the dashed red and dashed black lines, where local rotations of $\Delta\phi = -3°$ and $\Delta\phi = -10°$ with respect to the x-axis have been applied for the unit-cells at $\phi_l = 177°$ and $\phi_l = 170°$ respectively. Based on these observation, this section describes the proposed optimisation procedure to reduce the far-field cross-polarisation of LP-CP reflection polarisers. The procedure is applied to the example of Fig. 4.4. Then, the far-field performance of the optimised array is analysed and compared with the uniform array and the target case formed by the metallic reflector and the CP feed.

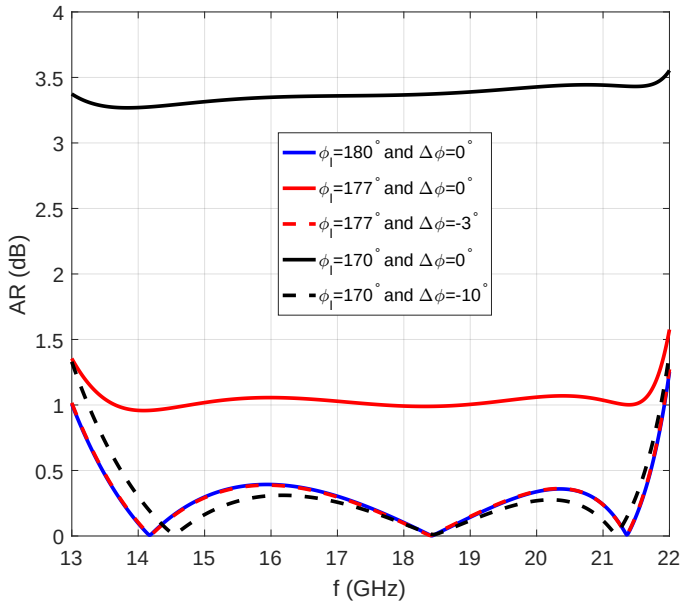

Figure 4.7: Effects of the unit-cell's element rotation on its performance using a dipole geometry. AR upon reflection for the unit-cell at the centre of the reflector (experiencing incidence at $\theta_l = 25°$, $\phi_l = 180°$, blue line), off-principal plane incidences ($\theta_l = 25°$, $\phi_l = 177°$, solid red line) and ($\theta_l = 25°$, $\phi_l = 170°$, solid black line). AR for the latter two unit-cells upon local rotations of $\Delta\phi = -3°$ (in dashed red line) and $\Delta\phi = -10°$ (in dashed black line).

4.3.1 Proposed optimisation procedure

In order to illustrate the proposed optimisation procedure, the target far-field characteristics should be first defined. For the present case, the far-field of the metallic reflector fed by the ideal CP feed shown in Fig. 4.6a and Fig. 4.6b (red lines) is selected as target. Similar to the strategy described in [18], the ideal reflection prop-

erties of each unit-cell on the reflector can be obtained by back-projecting the target far-field onto the reflector surface and taking the ratio locally with the incoming field produced by the primary feed. The outcome of this process is a set of target co- and cross-polarisation reflection coefficients for each unit-cell in the reflector. Then the set of ideal reflection coefficients for each unit-cell can be expressed as a 2×2 scattering matrix as in Section 2.5.5. It is noted that the ideal S-parameters obtained in this fashion for each unit-cell on the reflector do not necessarily correspond to realisable values but instead represent some target in the optimisation procedure. In the present case, since no change is applied to the target far-field, which is obtained from the metallic reflector fed by the CP source, the target S-parameters are realisable.

Performing the above procedure at 17.7 GHz, the target s-matrices across the reflector are obtained. They are plotted in Fig. 4.8 (red lines) against the angle of incidence (θ_l, ϕ_l) experienced locally at the reflector. For comparison, Fig. 4.8 also superimposes the scattering coefficients associated with the uniform unit-cell array (blue lines). It can be observed in Fig. 4.8e-4.8h that the reciprocity condition $s_{21} = s_{12}$ is fulfilled even for oblique incidences since the unit-cell geometry is symmetric in its two main planes [32]. For this same type of unit-cell, the energy conservation sets the following conditions [32]:

$$|s_{11}|^2 + |s_{21}|^2 = 1 \tag{4.3.1a}$$

$$|s_{22}|^2 + |s_{21}|^2 = 1 \tag{4.3.1b}$$

$$s_{11}^* s_{12} + s_{21}^* s_{22} = 0 \tag{4.3.1c}$$

If Eq. 4.3.1c is substituted into Eq. 4.3.1a and Eq. 4.3.1b one concludes that $|s_{11}| = |s_{22}|$. This last condition can be observed in Fig. 4.8a and Fig. 4.8c. The aforementioned reciprocity and energy conservation conditions are met for both set of S-parameters.

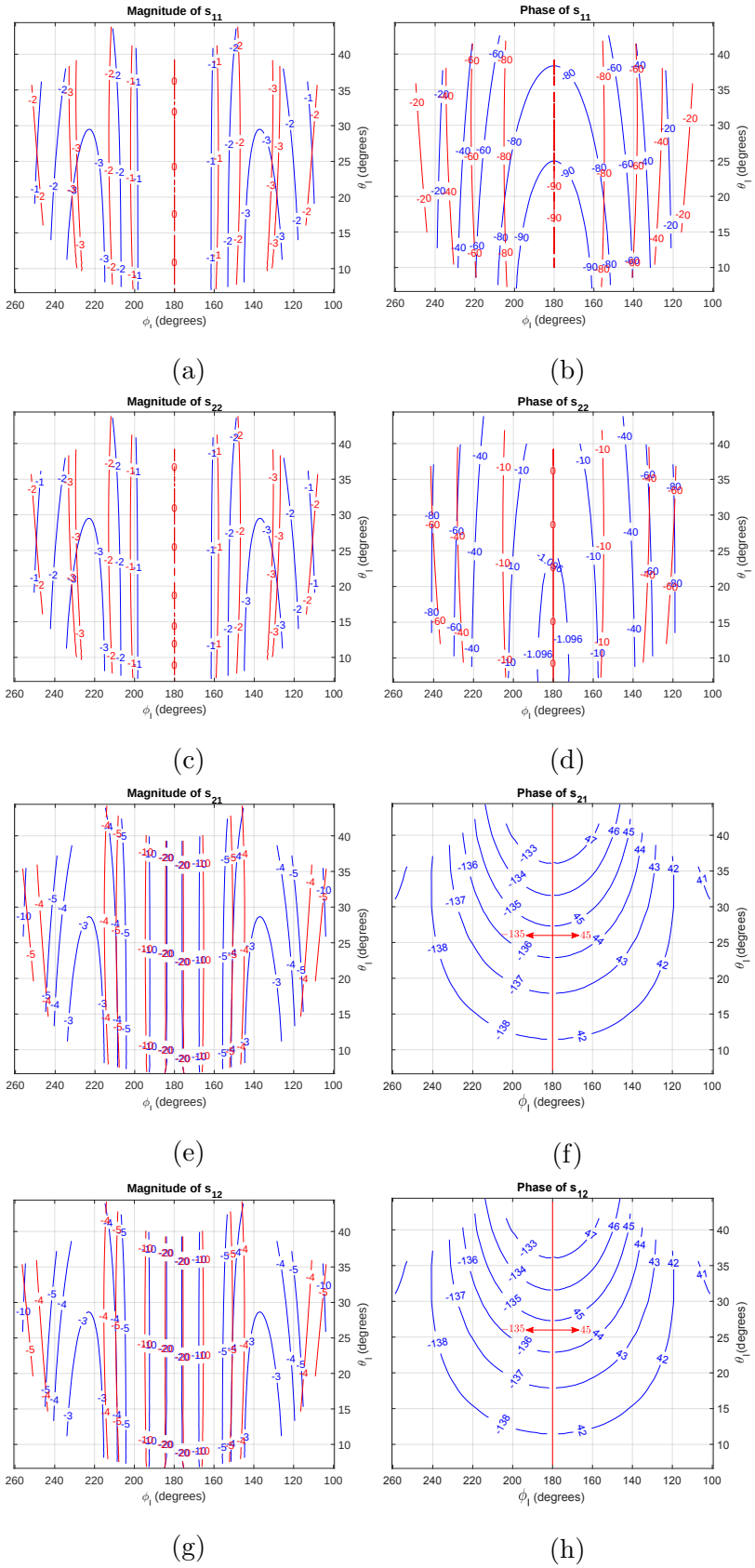

Figure 4.8: Contours for the magnitude and phases of the S-parameters at 17.7 GHz for the uniform unit-cell array (blue lines) and the target case consisting on a metallic reflector fed by a CP source (red lines).

The target S-parameters along the vertical plane of symmetry indicate a 90° differential phase requirement between the TM and TE reflection coefficients (phase of s_{11} and s_{22} respectively) and a vanished cross-polarised reflection coefficients ($|s_{12}|$ and $|s_{21}|$). As discussed above, this is a typical design target for this class of polarisers. It is noted that when the properties of the incident waves are considered locally at other points along the reflector, the target axial ratio of the reflected field is also 0 dB. This is due to the consideration of an ideal CP source for the definition of the target reflected field. However the target S-parameters at other points do not match the classical S-parameter requirements (as e.g. in [31]) since the incoming field can no longer be decomposed into TE and TM components with balanced amplitude.

As observed in Fig. 4.8b and Fig. 4.8d, the two sets of curves coincide at the centre of the reflector ($\theta_l = 25°$ and $\phi_l = 180°$) for the phases of s_{11} and s_{22} respectively. This reflects the fact that the unit-cell has been optimised for this set of incidence angles. However, away from the centre, the two sets of curves diverge. In particular, the target reflection characteristics remain constant along the vertical plane ($\phi_l = 180°$) but instead, the uniform array leads to some variation associated with the angular response of the unit-cell along the xz-plane (Fig. 4.5).

Along the horizontal plane, i.e. $\theta_l = const$, the uniform array provides reflection characteristics that would approach the target if the obtained responses were observed further away from the vertical plane of symmetry. This can be consistently observed in Fig. 4.8 if one follows a line of constant θ_l-value across all three plots; it then become obvious that improved agreement between the two sets of curves will be observed upon scaling up the ϕ_l-axis associated with the blue set of curves. The scaling factor depends on the value of θ_l and is not the exactly the same for all three plots presented.

On these principles, the optimisation along the vertical plane is quite straightforward. It can be achieved with the adjustment of the unit-cell dimensions (D_x, D_y, l, w) as θ_l varies. It is noted that along the vertical plane of incidence, the target S-parameters call for vanishing cross-polarisation reflection coefficients ($s_{21} = s_{12} = 0$) and a differential reflection phase between the two co-polarised coefficients of 90°. As shown in Fig. 4.5, this can be achieved within the given unit-cell dimensions (fixed D_x, D_y) by adjusting the dipole dimensions (l, w), for a wide frequency band. The improvement in the phases of the s_{11} and s_{22} parameters at 17.7 GHz obtained by

the geometrical optimisation can be seen in Fig. 4.9 for the targeted vertical plane, where the optimised S-parameters (darker blue) go closer to the target S-parameters (red), compared with the uniform unit-cell array (lighter blue), especially in the vertical plane. The s_{21} and s_{12} parameters are not shown since it vanishes in the vertical plane.

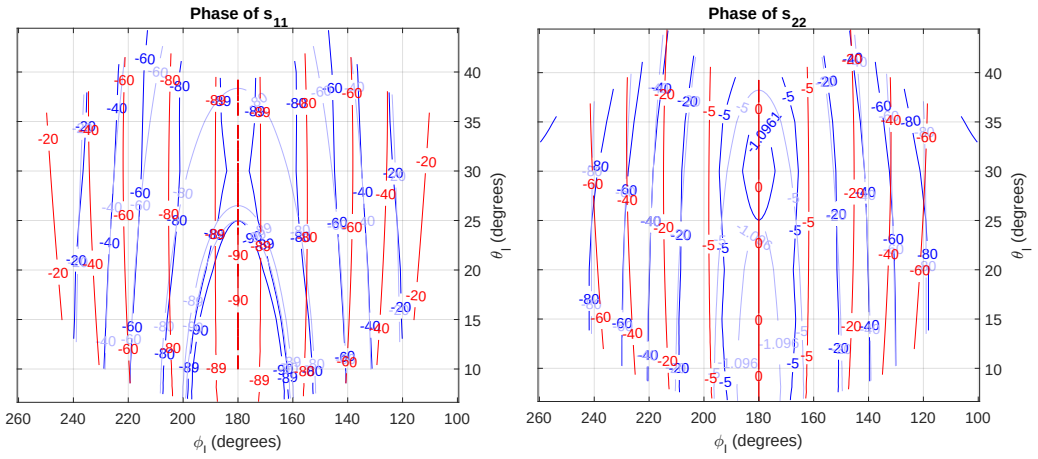

(a) (b)

Figure 4.9: Phases of the (a) s_{11} and (b) s_{22} parameters at 17.7 GHz for the uniform unit-cell array (lighter blue lines), array with unit-cell's element geometrical optimisation (darker blue lines) and the target case consisting on a metallic reflector fed by a CP source (red lines).

However, as mentioned above, it was found that other combinations of (l, w) outside the unit-cell principle planes of incidence do not lead to significant improvement of scattering coefficients achieved. Considering in the first instance the magnitudes of s_{21} and s_{12} plotted in Fig. 4.8e and Fig. 4.8g, it is quite straightforward to appreciate why the optimization of the unit-cell characteristics outside the vertical plane cannot be achieved by simply optimising the unit-cell dimensions: the cross-polarisation reflection of a linear element (such as the dipole considered here) depends primarily on the orientation of the element in relation to the tangential projection of the incoming field, defying by Ludwig-III (see Section 3.4.1). However, one can exploit an additional degree of freedom associated with the rotation of the unit-cell's element in relation to the x-axis [33].

The element rotation affects the plane of incidence of the unit-cell (defined by ϕ_l), and hence the alignment between the unit-cell geometry and the incoming field

polarisation, defined by Ludwig-III. Therefore, an optimisation by element rotation is expected to be able to bring the S-parameters associated with the uniform array (blue lines in Fig. 4.8) closer to the target values (red lines in Fig. 4.8) as we vary ϕ_l for constant θ_l. However, if the phases of s_{11} and s_{22} in Fig. 4.8b and Fig. 4.8d are compared for a fixed set of (θ_l, ϕ_l), it can be deduced that different rotations will be needed to bring the phases of these parameters closer to their target values.

Morevoer, outside the vertical plane ($\phi_l = 180°$), the projection of the incident field onto the unit-cell and the plane of incidence vary in different ways. The incidence field varies following Ludwig-III definition (see Fig. 3.6), while the plane of incidence varies with ϕ_l. Therefore, as shown in Fig. 4.10, two different set of rotations are needed to be aligned with projection of the incoming field (black lines) and with the plane of incidence.

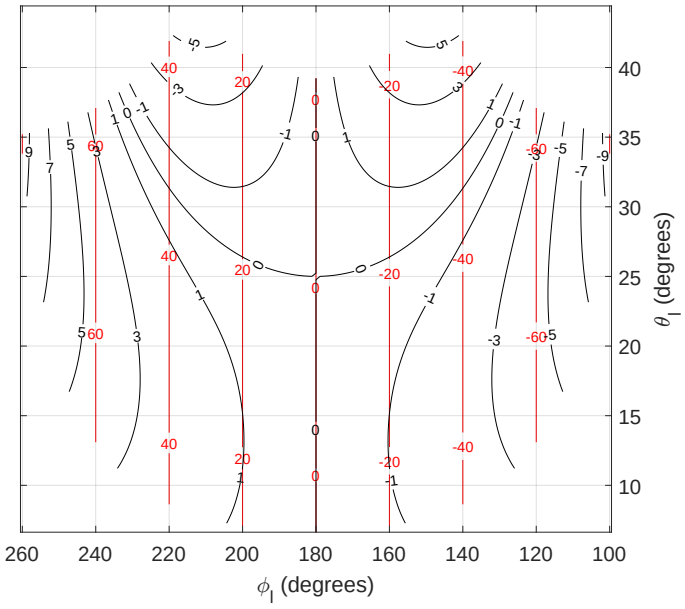

Figure 4.10: Rotations needed to be aligned with the projection of the incoming field onto the unit-cell (black lines) and with the plane of incidence (red lines).

For the reasons above, the element rotation should be applied under an optimisation routine where the cross-polarisation (or AR) of the unit-cell is the function to be minimised [34]. A more general approach can be used if the far-field cross-polarisation is chosen as the function to be minimised.

An optimisation routine based on unit-cell's element rotation using the far-field cross-polarisation as target to be minimised has been implemented, using MAT-

LAB's implementation of the Nelder-Mead algorithm [35]. This method was chosen because is a gradient-free local search method which does not require to calculate any derivatives of the cross-polarisation while achieving relatively rapid convergence rate. The function to describe the unit-cell rotation can be a polynomial function with the local angles of incidence θ_l and ϕ_l as inputs:

$$\Delta\phi = c_1\phi_l' + c_2\theta_l\phi_l' + c_3\phi_l'^2 + c_4\theta_l^2\phi_l' + c_5\theta_l\phi_l'^2 + c_6\phi_l'^3 + c_7\theta_l^3\phi_l' + c_8\theta_l^2\phi_l'^2 + c_9\theta\phi_l'^3 + c_{10}\phi_l'^4 + c_{11}\theta_l^4\phi_l' + c_{12}\theta_l^3\phi_l'^2 + c_{13}\theta_l^2\phi_l'^3 + c_{14}\theta_l\phi_l'^4 + c_{15}\phi_l'^5 \tag{4.3.2}$$

where $\phi_l' = \phi_l - 180°$ to ensure that $\Delta\phi = 0°$ for the central vertical line, and where c_i are the unknown coefficients to be obtained. Lower or higher order functions can be used taking into account that the search space increases with the function order.

Since the performance of the array should be improved within the whole bandwidth of the unit-cell, the function to be minimised $g(\Delta\phi)$ includes the far-field cross-polarisation for three frequencies (extremes of the band and around the centre):

$$g(\Delta\phi) = C^{f_1}|E_{RH}^{f_1}|^2 + C^{f_2}|E_{RH}^{f_2}|^2 + C^{f_3}|E_{RH}^{f_3}|^2 \tag{4.3.3}$$

where $f_1 = 14.5$ GHz, $f_2 = 17.7$ GHz and $f_3 = 20$ GHz; $E_{RH}^{f_i}$ refers to the RHCP component (cross-polarisation) for each frequency; and C^{f_i} refers to constant coefficients to weight each frequency component. Fig. 4.11 shows the resulting $\Delta\phi$ after the optimisation process is finished. The coefficients are shown in Table 4.1.

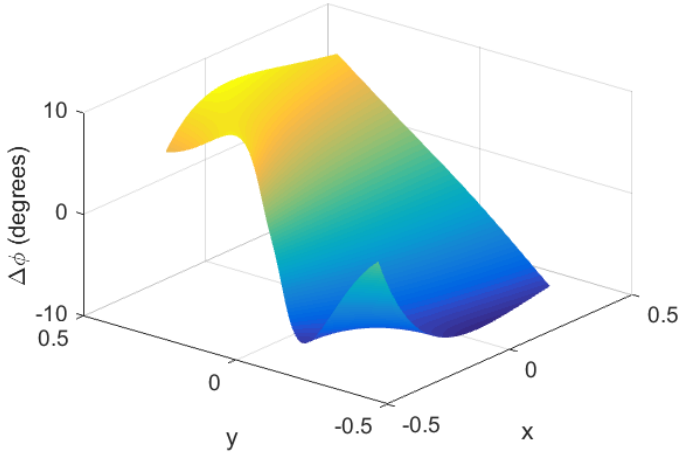

Figure 4.11: Resulting unit-cell's element rotation function $\Delta\phi$ across the reflector surface.

Fig. 4.12 shows the phases of the s_{11} and s_{22} parameters as well as the magnitude of the s_{21} at 17.7 GHz for the uniform unit-cell array (lighter blue), the array with element rotation optimisation (darker blue) and target values (red). It can be seen how the S-parameters of the optimised array converge to the target S-parameters, compared with the uniform unit-cell array.

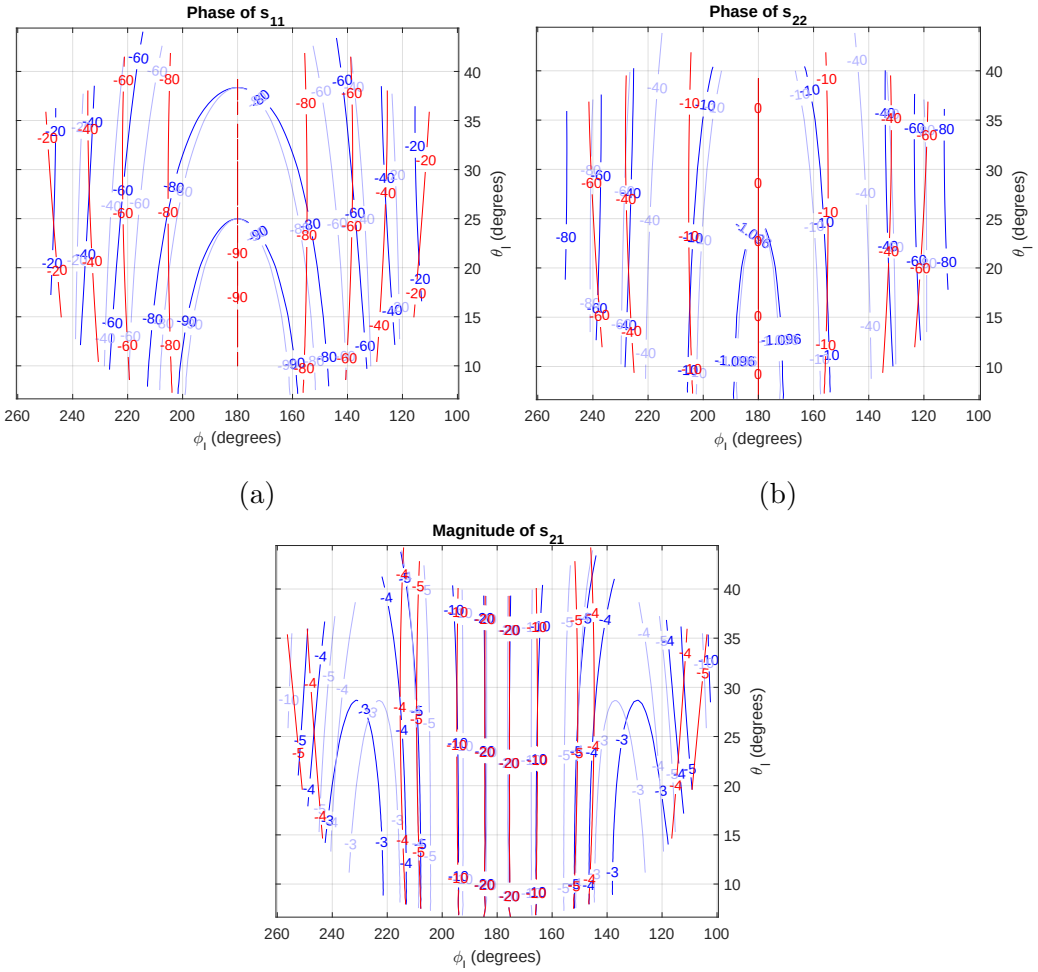

Figure 4.12: Phases of the (a) s_{11} and (b) s_{22} parameters, and (c) magnitude of the s_{21} parameter at 17.7 GHz for the uniform unit-cell array (lighter blue lines), array with unit-cell's element rotation optimisation (darker blue lines) and the target case consisting on a metallic reflector fed by a CP source (red lines).

The unit-cell's element geometrical optimisation and rotation are applied in orthogonal directions, i.e. along θ_l and along ϕ_l respectively. Therefore, it can be seen as the natural next step to combine them in one optimisation procedure in two steps, where first a geometrical optimisation as the one in Fig. 4.5 is performed, followed by the element rotation optimisation described above. Fig. 4.13 shows the phases of

the s_{11} and s_{22} parameters for the uniform array (lighter blue lines), the optimised array (blue lines) and the target values (red lines). It can be observed how the S-parameters associated with the optimised array a better convergence to the target values than the S-parameters associated with the element geometrical optimisation (Fig. 4.9) or the element rotation (Fig. 4.12) applied independently. The resulting $\Delta\phi$ is shown in Fig. 4.14 and the coefficients are shown in Table 4.1.

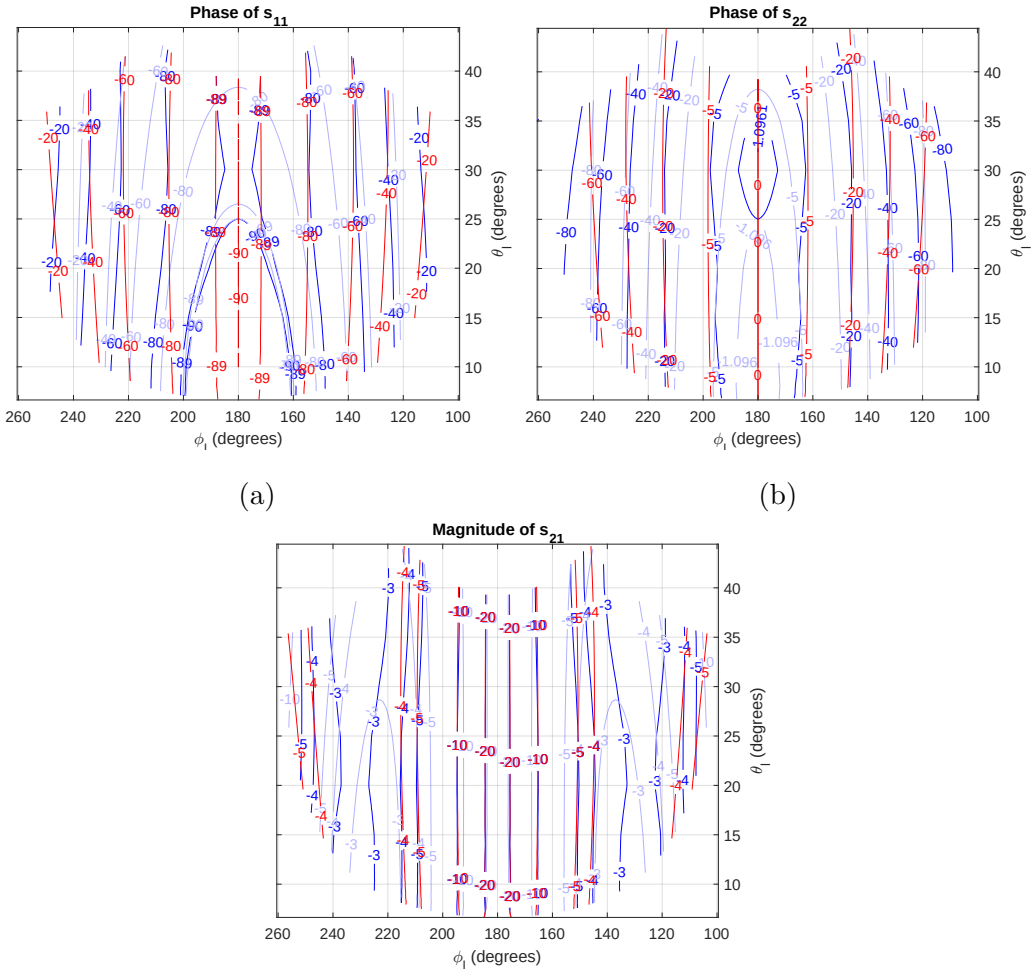

Figure 4.13: Phases of the (a) s_{11} and (b) s_{22} parameters, and (c) magnitude of the s_{21} parameter at 17.7 GHz for the uniform unit-cell array (lighter blue lines), array optimised by unit-cell' element geometrical optimisation and rotation (darker blue lines) and the target case consisting on a metallic reflector fed by a CP source (red lines).

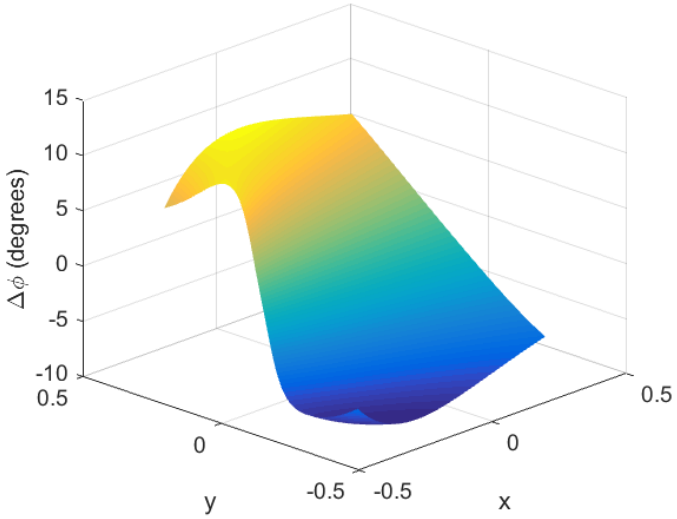

Figure 4.14: Resulting unit-cell rotation function $\Delta\phi$ across the reflector surface after the two-step optimisation process.

coefficient	**rot.**	**GO+rot.**
c_1	0.1099	0.1121
c_2	−0.0272	0.0492
c_3	−0.0100	0.0101
c_4	0.1653	0.1193
c_5	−0.0051	−0.0485
c_6	0.1384	0.0705
c_7	0.0224	−0.0129
c_8	0.0106	−0.0150
c_9	−0.1662	−0.0278
c_{10}	0.0022	0.0109
c_{11}	0.1494	0.0056
c_{12}	−0.0577	0.1417
c_{13}	0.0065	−0.0701
c_{14}	0.0403	−0.0305
c_{15}	−0.0589	−0.0413

Table 4.1: Coefficients of the unit-cell's element rotation optimisation (rot.) and the two-step optimisation procedure (GO+rot.).

4.3.2 Far-field comparison

In order to validate each step of the optimisation process, four breadboards have been simulated and compared: uniform unit-cell array, array with geometrically optimised unit-cells, array with optimisation by element rotation, and array with a combination of the two procedures.

To this end, Fig. 4.15a and Fig. 4.15b show the far-field directivity for the vertical ($\Phi = 0°$) and horizontal ($\Phi = 90°$) planes respectively, at 14.5 GHz. Fig. 4.16a and Fig. 4.16b show the far-field directivity for the same two planes at 17.7 GHz. Fig. 4.17a and Fig. 4.17b show the far-field directivity for the same two planes at 20 GHz. These three frequencies represent the lower band frequency (14.5 GHz), the higher band frequency (20 GHz) and a frequency in the middle of the band (17.7 GHz).

At the lower limit of the band (14.5 GHz), it seems that the unit-cell's element geometrical optimisation does not improve the far-field vertical plane, except for broadside (see Fig. 4.15a). This could be due to the AR deterioration for frequencies between 14.5-17 GHz at the expense of an improvement at higher frequencies for around $\theta_l = 20°$ (see red solid/dashed lines in Fig. 4.5). However, the deteriorated values are still acceptable since they are below 0.5 dB. The unit-cell (both original and optimised) shows better performance overall for the lower part of the band. This is translated in the far-field into acceptable cross-polarisation levels even for the original uniform unit-cell array. At mid-band (17.7 GHz) the geometrical optimisation has a bigger impact, being translated in the far-field into cross-polarisation improvements up to 16 dB, as Fig. 4.16a shows. At around the higher limit of the band (20 GHz) the unit-cell deterioration is more severe. Therefore, the geometrical optimisation only achieves improvements up to 6 dB, as Fig. 4.17a shows. Moreover, the unit-cell's element rotation has no impact in the far-field vertical plane.

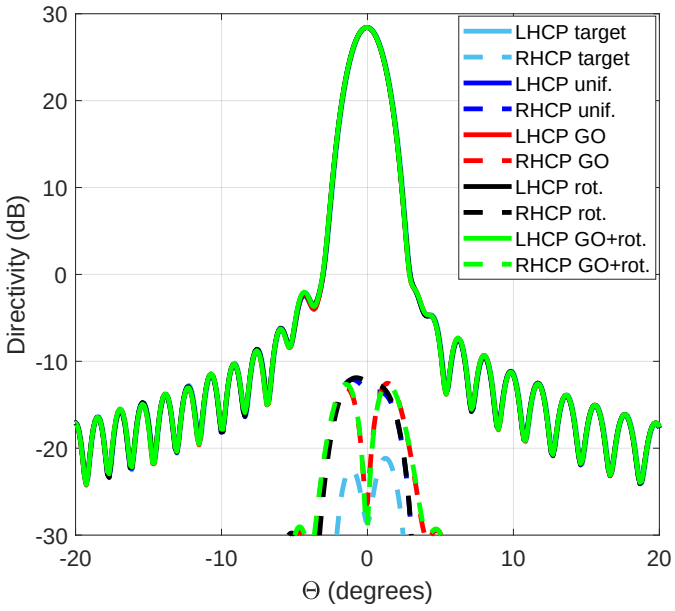

(a)

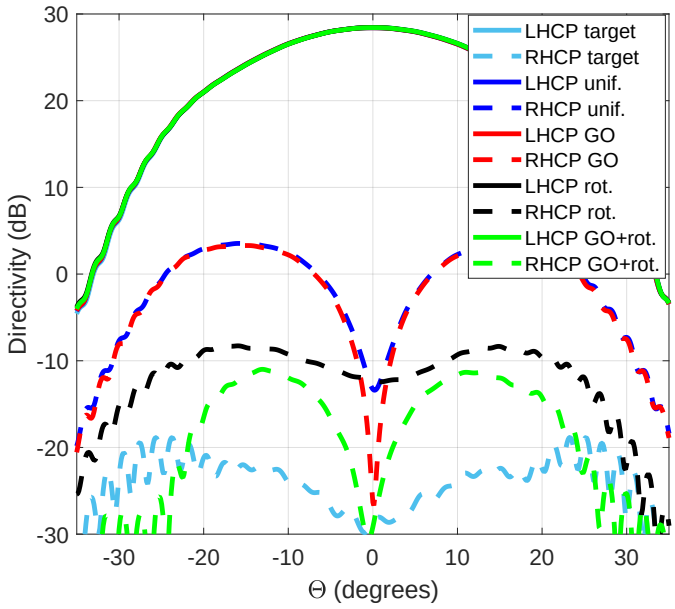

(b)

Figure 4.15: Far-field directivity (dB) at 14.5 GHz for (a) the vertical plane ($\Phi = 0°$) and (b) the horizontal plane ($\Phi = 90°$).

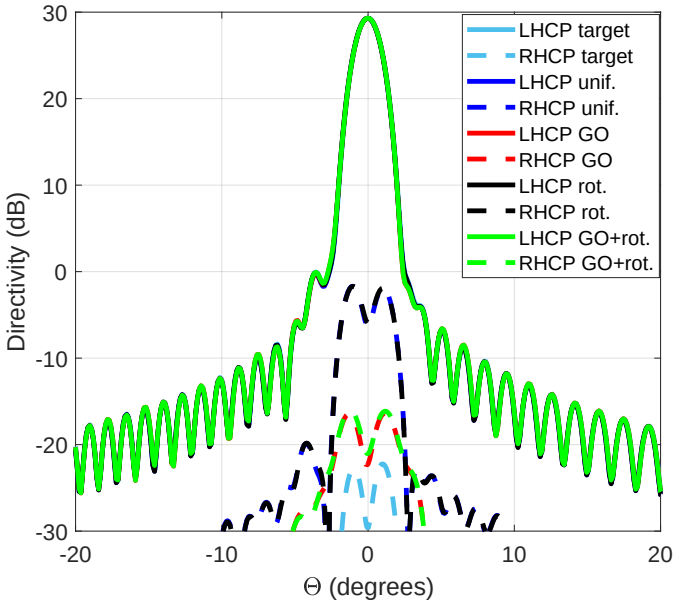

(a)

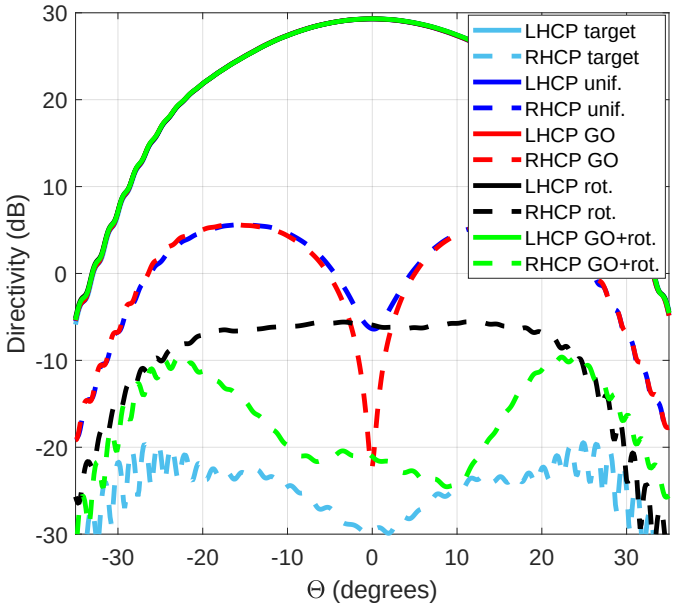

(b)

Figure 4.16: Far-field directivity (dB) at 17.7 GHz for (a) the vertical plane ($\Phi = 0°$) and (b) the horizontal plane ($\Phi = 90°$).

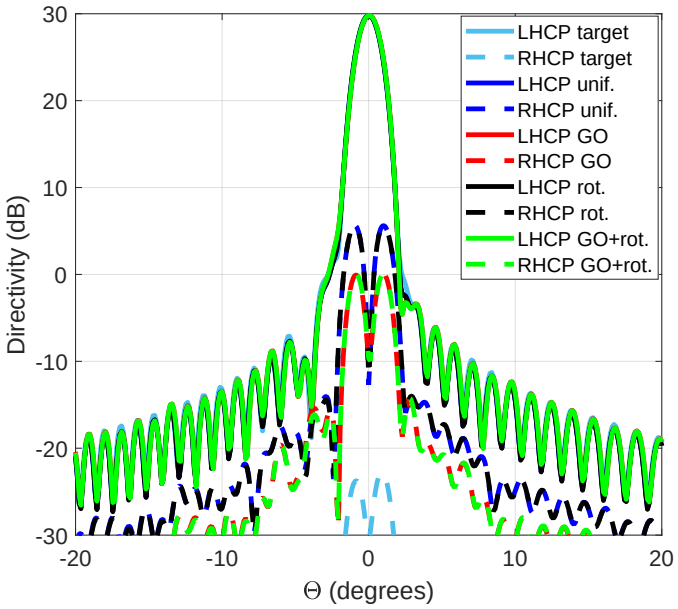

(a)

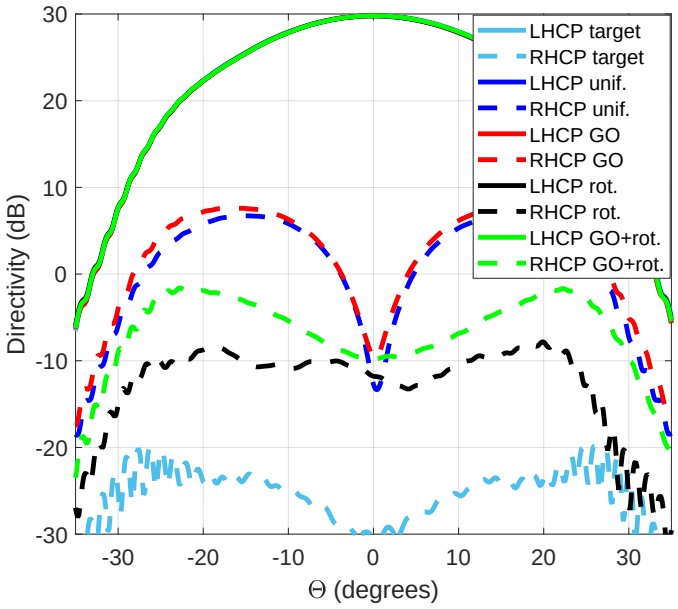

(b)

Figure 4.17: Far-field directivity (dB) at 20 GHz for (a) the vertical plane ($\Phi = 0°$) and (b) the horizontal plane ($\Phi = 90°$).

With respect to the far-field horizontal plane, it can be seen in Fig. 4.15b, Fig. 4.16b and Fig. 4.17b that the element geometrical optimisation has almost no impact. Nevertheless, there seems to be a small deterioration of the cross-polarisation for the higher limit of the band (20 GHz). This could be due to a slightly deterioration in the angular stability (for ϕ_l far from 180°) of the geometrically optimised unit-cells compared to the original around the higher limit of the band. On the other

hand, the element rotation shows a more consistent performance across the whole band, whether if it is applied alone (black lines) of after the element geometrical optimisation (green lines). It is expected that it achieves better results if applied after the geometrical optimisation since it presents a better starting point (lower cross-polarisation at broadside). This is generally true, as it can be seen in Fig. 4.15b and Fig. 4.16b. Nevertheless, due to the deterioration in the angular stability of the geometrically optimised unit-cell, and its bigger impact towards the higher limit of the band, it seems that the two-step optimisation procedure (green lines) achieves less improvement than the element rotation applied alone (black lines) at 20 GHz, as Fig. 4.17b shows. However, the improvements achieved by the two-step optimisation procedure in the horizontal plane are very significant, ranging between 8-15 dB.

4.4 Validation and measurements

To validate the optimisation procedure, an offset flat reflector has been proposed to ease the manufacturing process. It has $d = 270$ mm of height and width, distance between feed and reflector $f = 250$ mm and offset angle $\theta_f = 35°$. It is fed by a standard Flann's gain horn, model 19240 [27], polarised at slant 45°. The unit-cell presented in Section 4.2.2 is used again for the initial uniform array.

4.4.1 Optimisation procedure, manufacturing and set-up

Then the optimisation procedure described in Section 4.3.1 is used to optimise the polarising surface.

Considering the distance between reflector and horn, and the frequency band of the horn, the far-field approximation for the feed is no longer valid. The procedures described in Section 4.2.1 are used to obtain the fundamental modes (TM and TE) of the near-field and their angles of incidence (see Fig. 4.2), and subsequently the S-parameters, reflected field, equivalent currents and far-field. Then the optimisation procedure described in Section 4.2.2 is used to optimise the polarising surface. The uniform array is comprised by the unit-cell introduced in Section 4.3 optimised for the offset angle of the configuration shown in Fig. 4.1, i.e., $\theta_f = \theta_l = 35°$. Since

the angles of incidence referred to the fundamental modes are frequency dependent, an average of the optimised geometries (lower, central and upper part of the band) should be taken during the unit-cell's element geometrical optimisation.

This dependency with frequency should also be taken into account for the unit-cell's element rotation. For a point source, the input parameters for the quadratic function $\Delta\phi$ in Eq. 4.3.2 are its associated frequency-independent local angles of incidence. These angles were smooth compared to the ones referred to the horn's, as it can be seen in Fig. 4.2. If a global-minima type optimisation routine and higher enough order for $\Delta\phi$ are used, the inputs of $\Delta\phi$ could be virtually anything, since they would reach the global minimum. However, a local-minima type optimisation routine is used in this thesis (See Section 4.3) to speed up the process. Also for speeding up reasons, the aforementioned quadratic function is used. The success of the optimisation routine will depend on the selected inputs. Therefore, since the angles of incidence referred to the point source are smoother, it has been found they reach better results.

Once the optimisation procedures have been applied, the masks have to been prepared for printing. In order to validate each step of the optimisation process, four breadboard were manufactured: a uniform unit-cell array, an array optimised by unit-cell's element geometrical optimisation, an array optimised by unit-cell's element rotation and a final array with the two-step optimisation procedure.

The vector graphics editor Inkscape [36] has been the preferred tool for the masks design. It is written in C++ with *gtkmm* (interface for GUI library). A small program has been written in MATLAB that generates the "*.vsg*" file with all the unit-cells.

Taking into account the unit-cell size and the original reflector size (270×270 mm) the total number of unit-cells is 37×303. The final reflector size to fit this number of unit-cells is 277.5×272.7 mm. An extra space surrounding the reflector is added with four crosses for reference in the measurements. The mask for the two-step optimisation procedure is shown in Fig. 4.18, where the geometrical modulations and rotations can be clearly appreciated.

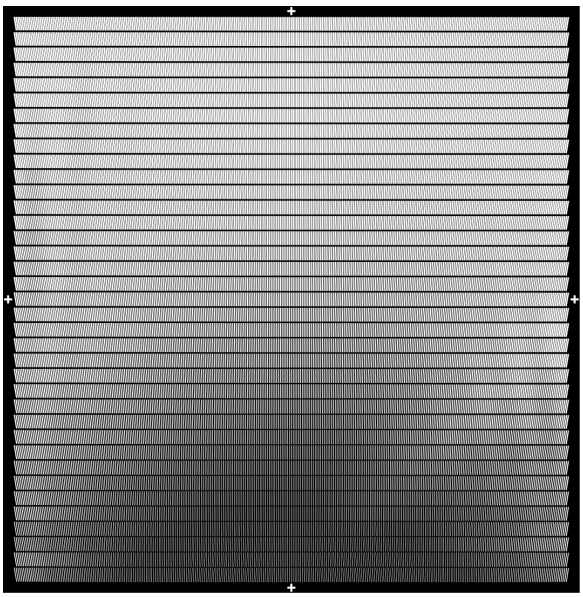

Figure 4.18: Mask for the breadboard with the two-step optimisation procedure.

The four masks were printed on one side of the Taconic TLY-5 laminates. The backs were left grounded. Fig. 4.19 shows a photo zoom of the breadboard with the two-step optimisation procedure.

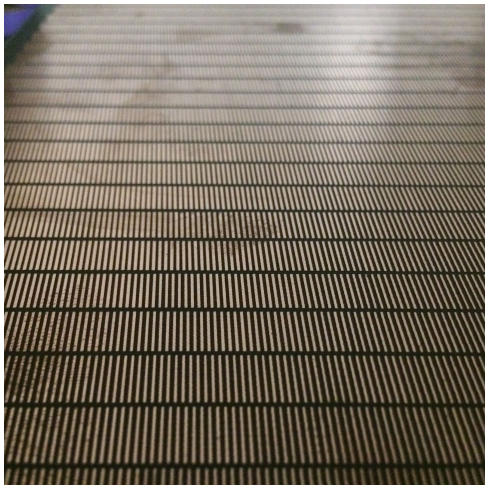

Figure 4.19: Photograph of the breadboard with the two-step optimisation procedure.

The reflector and the horn have been mounted on a supporting structure, as shown in Fig. 4.20. A near-field measurement system from NSI [37] has been used to performed the measurements, where the near-field reflected from the surface is measured in a 2D plane. Then the software performs a near-to-far-field transformation and the vertical and horizontal components of the far-field are extracted. The whole

configuration has been rotated so that the broadside direction of the antenna under test (AUT) matches with the broadside direction of the near-field probe.

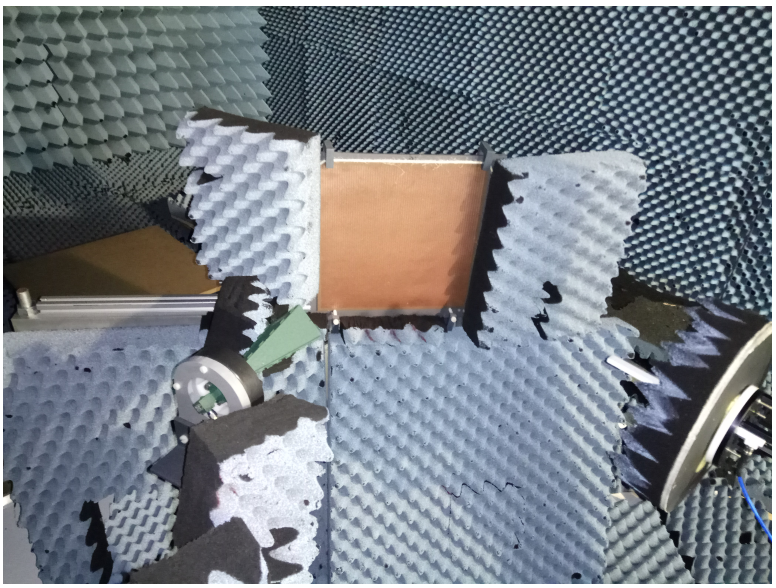

Figure 4.20: Photograph of the measured configuration.

4.4.2 Far-field comparison

Fig. 4.21a and Fig. 4.21b show a comparison of simulations and measurements for the normalised directivity vertical ($\Phi = 0°$) and horizontal ($\Phi = 90°$) planes respectively at 17.7 GHz. Both the breadboard optimised by unit-cell's element geometrical optimisation and the uniform unit-cell breadboard are shown. As described in Section 4.3.2, the optimised breadboard presents cross-polarisation improvement in the vertical plane, while maintaining almost the same levels for the horizontal plane. Fig. 4.22a and Fig. 4.22b show the same comparison for the same planes and frequency for the breadboard optimised by unit-cell's element rotation and the uniform unit-cell breadboard. As described in Section 4.3.2, the optimised breadboard presents cross-polarisation improvement in the horizontal plane, while maintaining almost the same levels for the vertical plane. Finally, Fig. 4.23a and Fig. 4.23b show the same comparison for the same planes and frequency for the breadboard optimised by the two-step optimisation procedure and the uniform unit-cell breadboard. As described in Section 4.3.2 as well, the optimised breadboard presents cross-polarisation improvement in both planes.

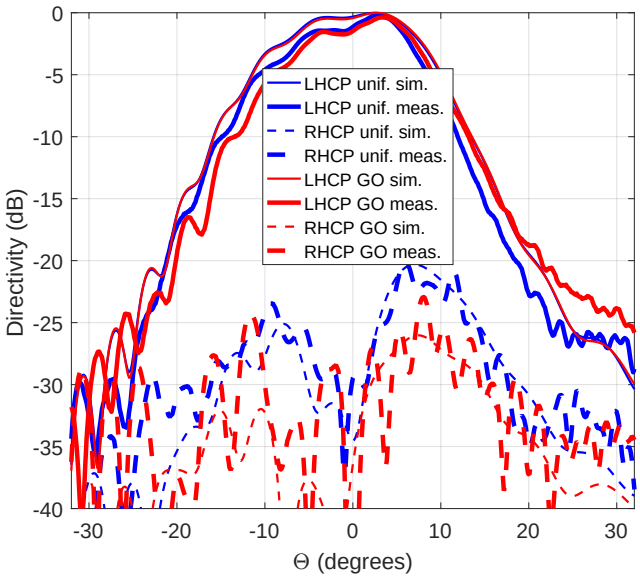

(a)

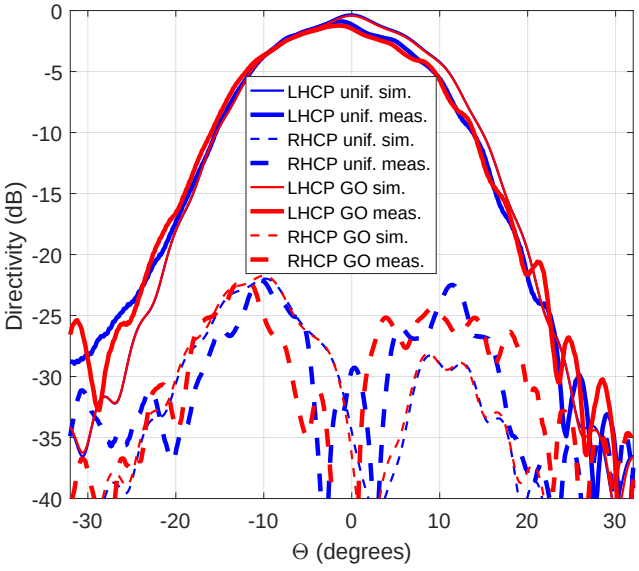

(b)

Figure 4.21: Simulation and measurements comparison of the normalised far-field directivity (dB) for the unit-cell's element geometrical optimisation at 17.7 GHz for (a) the vertical plane ($\Phi = 0°$) and (b) the horizontal plane ($\Phi = 90°$).

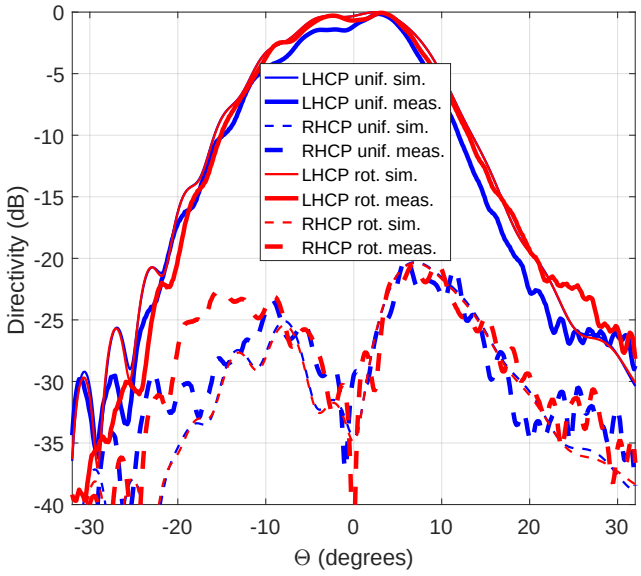

(a)

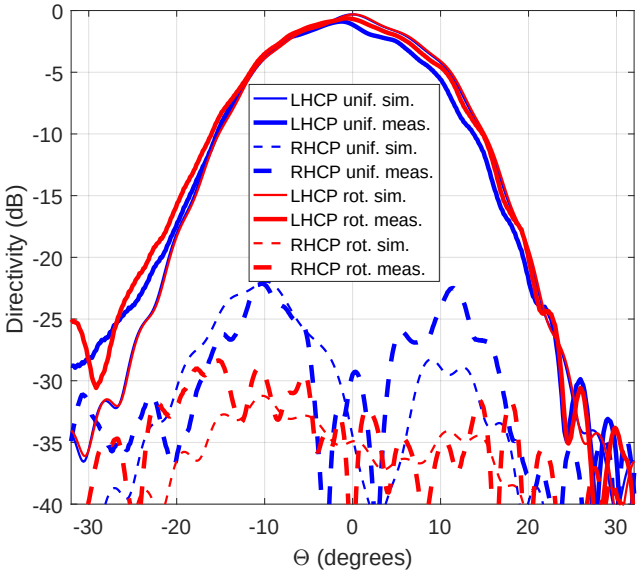

(b)

Figure 4.22: Simulation and measurements comparison of the normalised far-field directivity (dB) for the unit-cell's element rotation optimisation at 17.7 GHz for (a) the vertical plane ($\Phi = 0°$) and (b) the horizontal plane ($\Phi = 90°$).

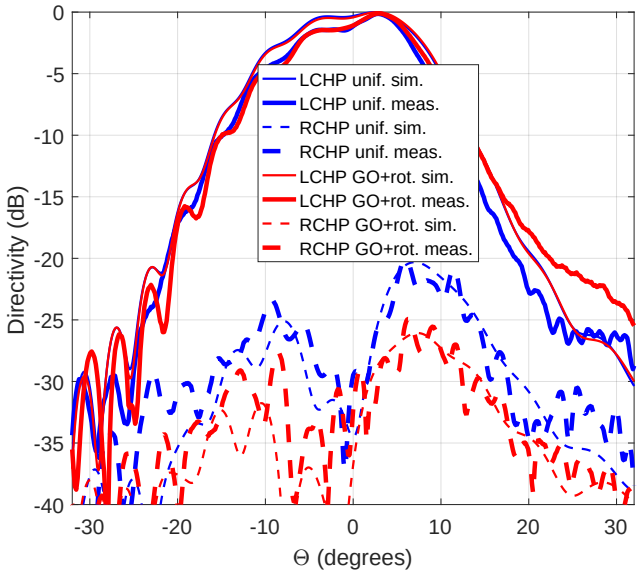

(a)

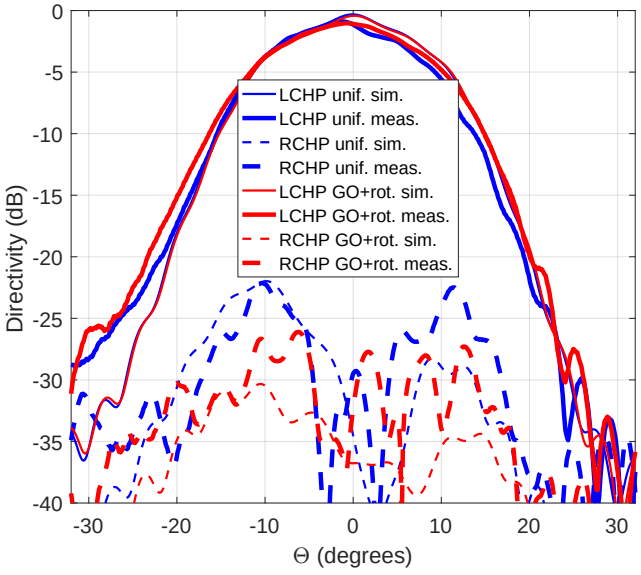

(b)

Figure 4.23: Simulation and measurements comparison of the normalised far-field directivity (dB) for the two-step optimisation procedure at 17.7 GHz for (a) the vertical plane ($\Phi = 0°$) and (b) the horizontal plane ($\Phi = 90°$).

Overall the measured results agree well with the simulations, indicating the anticipated improvement in cross-polarisation performance in each case. Some minor disagreements between simulations and measurements are observed. These disagreements are present both in the co-polarisation and cross-polarisation components. Af-

ter a close look at the co-polarisation components, it seems that disagreements come from misalignments in the measurements. Mainly, two types of misalignments can be present: between reflector and near-field probe and between horn and reflector. Extra errors in the rotation of the feed could be present as well. Diffraction effects (not considered in the simulations) and errors in the breadboard manufacturing also add uncertainties to the measurements.

4.5 Summary

A two-step design procedure to reduce the cross-polarisation levels of linear-to-circular reflection polarisers has been presented. The procedure to obtain the far-field from this kind of structures has been outlined in Section 4.2, along with the need for cross-polarisation improvement. Then, the proposed optimisation procedure to reduce the far-field cross-polarisation has been detailed in Section 4.3. The procedure exploits physical insight and leads to computational efficiencies. This in turn allows the simultaneous optimisation of the cross-polarisation across a wide bandwidth. Design examples are presented demonstrating improvements that reach up to 16 dB. The procedure is validated experimentally in Section 4.4. It is noted that the proposed procedure can be used as a starting point for more advanced optimisation.

The simulations presented in this chapter have been performed with the tool developed for the previous chapter for the analysis of reflector antennas where new features have been added, i.e. modelling of practical feeds and substitution of the PEC surface by a FSS where the S-parameters have been computed with CST.

References

[1] S. K. Rao, "Parametric design and analysis of multiple-beam reflector antennas for satellite communications," *IEEE Antennas Propag. Mag.*, vol. 45, no. 4, p. 2634, Aug 2003.

[2] S. T. Sharma, S. Rao, and L. Shafai, *Handbook of Reflector Antennas and Feed Systems, vol. III: Applications of Reflectors*. Artech House, 2013.

[3] B. Palacin *et al.*, "Multibeam antennas for very high throughput satellites in europe: technologies and trends," *Proc. 11th Eur. Conf. Antennas Propag. (EuCAP'17)*, p. 24132417, 2017.

[4] N. J. G. Fonseca and C. Mangenot, "High-performance electrically thin dual-band polarizing reflective surface for broadband satellite applications," *IEEE Trans. Antennas Propag.*, vol. 64, no. 2, pp. 640–649, Feb 2015.

[5] M. Baunge, H. Ekstrom, P. Ingvarson, and M. Peterson, "A new concept for dual gridded reflectors," *Proc. 4th Eur. Conf. Antennas Propag. (EuCAP'10)*, 2010.

[6] N. J. G. Fonseca and C. Mangenot, "Low-profile polarizing surface with dual-band operation in orthogonal polarizations for broadband satellite applications," *Proc. 8th Eur. Conf. Antennas Propag. (EuCAP'14)*, 2014.

[7] R. Orr *et al.*, "Circular polarization frequency selective surface operating in ku and ka band," *IEEE Trans. Antennas Propag.*, vol. 63, no. 11, pp. 5194–5197, Nov 2015.

[8] R. Orr, G. Goussetis, V. Fusco, and E. Sáenz, "Linear-to-circular polarization reflector with transmission band," *IEEE Trans. Antennas Propag.*, vol. 63, no. 5, pp. 1949–1956, May 2015.

[9] J. Sanz-Fernández, E. Sáenz, and P. de Maagt, "A circular polarization selective surface for space applications," *IEEE Trans. Antennas Propag.*, vol. 63, no. 6, pp. 2460–2470, June 2015.

[10] W. Tang *et al.*, "Coupled split-ring resonator circular polarization selective surface," *IEEE Trans. Antennas Propag.*, vol. 65, no. 9, pp. 4664–4675, Sept 2017.

[11] A. Ericsson and D. Sjoberg, "Design and analysis of a multilayer meander line circular polarization selective surface structure," *IEEE Trans. Antennas Propag.*, vol. 65, no. 8, pp. 4089–4101, Aug 2017.

[12] A. Ericsson, J. Lundgren, and D. Sjoberg, "Experimental characterization of circular polarization selective surface structures using linearly-polarized antennas," *IEEE Trans. Antennas Propag.*, vol. 65, no. 8, pp. 4239–4249, Aug 2017.

[13] M. Albani *et al.*, "Concepts for polarising sheets & "dual-gridded" reflectors for circular polarisation," *Proc. ICEComp*, 2010.

[14] W. Tang, S. Mercader-Pellicer, G. Goussetis, H. Legay, and N. J. G. Fonseca, "Low-profile compact dual-band unit cell for polarising surfaces operating in orthogonal polarizations," *IEEE Trans. Antennas Propag.*, vol. 65, no. 3, pp. 1472–1477, March 2017.

[15] W. Tang, D. Bresciani, H. Legay, G. Goussetis, and N. J. G. Fonseca, "Circularly polarised multiple beam antenna for satellite applications," *Proc. 11th Eur. Conf. Antennas Propag. (EuCAP'17)*, 2017.

[16] J. Huang and J. A. Encinar, *Reflectarray Antennas*. Wiley & Sons, 2008.

[17] M. Zhou *et al.*, "The generalized direct optimization technique for printed reflectarrays," *IEEE Trans. Antennas Propag.*, vol. 62, no. 4, pp. 1690–1700, April 2014.

[18] H. Legay *et al.*, "A 1.3 m facetted reflectarray in ku band," *15th ANTEM*, 2012.

[19] J. C. Vardaxoglou, *Frequency Selective Surfaces: Analysis and Design*. Wiley & Sons, 1997.

[20] D. R. Prado, D. Arrebola, M. R. Pino, and F. Las-Heras, "Efficient crosspolar optimization of shaped-beam dual-polarized reflectarrays using full-wave anal-

ysis for the antenna element characterization," *IEEE Trans. Antennas Propag.*, vol. 65, no. 2, pp. 623–635, Feb 2017.

[21] C. Mateo-Segura, G. Goussetis, and A. P. Ferisidis, "Resonant effects and near-field enhancement in perturbed arrays of metal dipoles," *IEEE Trans. Antennas Propag.*, vol. 58, no. 8, pp. 2523–2530, Aug 2010.

[22] E. Doumanis *et al.*, "Design of engineered reflectors for radar cross section modification," *IEEE Trans. Antennas Propag.*, vol. 61, no. 1, pp. 232–239, Jan 2010.

[23] M. Zhou *et al.*, "Direct optimization of printed reflectarrays for contoured beam satellite antenna applications," *IEEE Trans. Antennas Propag.*, vol. 61, no. 1, pp. 232–239, April 2013.

[24] M. Arrebola, Y. Álvarez, J. A. Encinar, and F. Las-Heras, "Accurate analysis of printed reflectarrays considering the near field of the primary feed," *IET Microw. Antennas and Propagat.*, vol. 3, no. 2, pp. 187–194, 2009.

[25] CST Microwave Studio® [Online]. Available: https://www.cst.com/products/cstmws/.

[26] A. C. Ludwig, "Near-field far-field transformations using spherical-wave expansions," *IEEE Trans. Antennas Propag.*, vol. 19, no. 2, pp. 214–220, March 1971.

[27] Standard Gain Horns, Series 240, Flann Microwave Ltd.

[28] C. A. Balanis, *Antenna Theory: Analysis and Design*, 3rd ed. Wiley & Sons, 2015.

[29] K. Barkeshli, *Advanced Electromagnetic and Scattering Theory.* Springer, 2015.

[30] M. Zhou *et al.*, "An accurate technique for calculation of radiation from printed reflectarrays," *IEEE Antennas Wireless Propag. Lett.*, vol. 10, pp. 1081–1084, Jan 2011.

[31] E. Doumanis, G. Goussetis, J. Gómez-Tornero, R. Cahill, and V. Fusco, "Anisotropic impedance surfaces for linear to circular polarization conversion," *IEEE Trans. Antennas Propag.*, vol. 60, no. 1, pp. 212–219, Jan 2012.

[32] X. Artiga, D. Bresciani, H. Legay, and J. Perruisseau-Carrier, "Polarimetric control of reflective metasurfaces," *IEEE Antennas and Wireless Propag. Lett.*, vol. 11, pp. 1489–1492, Dec 2012.

[33] J. A. Encinar, M. Arrebola, W. Menzel, and G. Toso, "Antena reflectarray de polarización dual linear con propiedades de polarización cruzada mejoradas," Spanish pattent P200931140, Tech. Rep., 2010.

[34] R. Florencio, J. A. Encinar, R. R. Boix, G. Pérez-Palomino, and G. Toso, "Cross-polar reduction in reflectarray antennas by means of element rotation," *Proc. 10th Eur. Conf. Antennas Propag. (EuCAP'16)*, 2016.

[35] J. A. Nelder and R. Mead, "A simplex method for function minimization," *The Computer Journal*, vol. 7, no. 4, pp. 308–313, Jan 1965.

[36] Inkscape Vector Graphics Editor [Online]. Available: https://inkscape.org/en/.

[37] NSI-MI Technologies [Online]. Available: https://www.nsi-mi.com/products/system-solutions/near-field-systems.

Chapter 5

Cross-polarisation reduction of linear-to-circular polarising offset reflectors for multiple primary feeds

5.1 Introduction

Chapter 4 introduced an optimisation procedure to reduce the cross-polarisation of linear-to-circular reflection polarisers in single offset configurations for single primary feeds. The main application was multi-beam reflector antennas in single feed per beam (SFB) configurations for space communications [1,2]. Due to the current trend of using circular polarisation (CP) for the up/down links, it was proposed in [3,4] to maintain the feeds and subreflectors in linear polarisation (LP) and perform the LP-CP conversion at the main reflector surface. The key innovation of this architecture is to keep all the optics in LP, since the subsreflector technologies (e.g. gridded subreflectors [5, 6]) are more mature for LP. However, the large dimensions of the main reflector impose a broad range of angles of incidence for the unit-cells. This is translated into high levels of far-field cross-polarisation. Therefore, in order to cope with the stringent mission requirements [7], a way to lower the far-field cross-polarisation is needed. The optimisation procedure presented in Chapter 4 achieved improvements of around $5 - 15$ dB by simulation.

However, as it was mentioned in Chapter 1.2.3, several feeds are used in multi-beam reflector antennas (in SFB architectures) to provide the desired beams (feed per beam). Therefore, a single unit-cell will have different angles of incidence belonging to the different feeds. Nevertheless, the unit-cell has to maintain its good performance for all the feeds. Consequently, the optimisation procedure should be applied for different feeds (and frequencies) at the same time. As in Chapter 4, in order to simplify the problem, only single offset configurations are taken into account. Therefore, this chapter presents preliminary results on the cross-polarisation reduction for single offset polarisers fed by three feeds. Only the unit-cell's element rotation technique shown in Section 4.3.1 will be applied. The code developed for Chapter 3 and extended in Chapter 4 will be used to perform these simulations.

5.2 Reflector antenna architecture and unit cell geometry

The optimisation procedure is demonstrated for an offset parabolic reflector antenna, shown in Fig. 5.1. The reflector has a diameter of $d = 600$ mm, focal length of $f = 400$ mm and offset angle of $\theta_f = 50°$. It is fed by three ideal Gaussian beam sources (see Section 3.4.5) linearly polarised at 45°. In order to obtain good illumination efficiencies, their broadside direction points towards the centre of the reflector. One feed, numbered as 0, is placed at the reflector focus, while the other two feeds, numbered as 1 and 2, are displaced along the y-axis by 94 mm and -94 mm respectively. This displacement along the y-axis has been chosen over the x-axis since a more deteriorated cross-polarisation in the far-field is expected, especially in the horizontal plane. The bigger deterioration in the horizontal plane is thought to be due to the wide range of ϕ_l across the reflector (especially for θ_l different from the centre unit-cell).

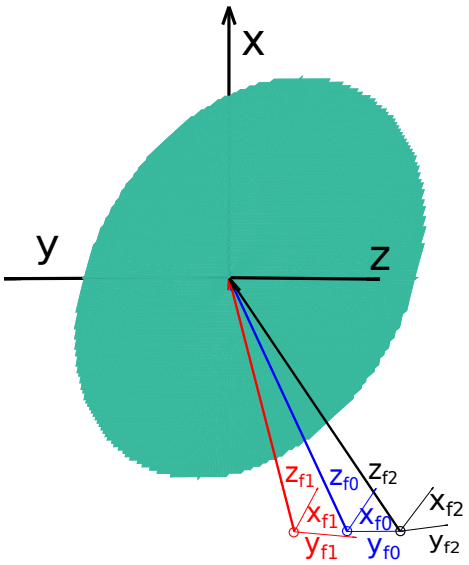

Figure 5.1: Antenna configuration fed by three Gaussian beams pointing towards the centre of the reflector and with 600 mm of reflector diameter, focal length of 400 mm and 50° of offset.

The same dipole unit-cell as in Chapter 4 (originally from [8]) is used here for the polarising surface. It is oriented along the x-axis, and optimised for the centre unit-cell ($\theta = 25°$ and $\phi_l = 180°$). Then the optimised unit-cell is repeated uniformly over the reflector surface. The polarising surface transforms the 45° LP incident field into a left-handed circularly polarised (LHCP) field.

As it was mentioned in the introduction, the angles of incidence that each unit-cell experiences are different for each feed. In the remaining we use the notation (θ_0^l, ϕ_0^l), (θ_1^l, ϕ_1^l) and (θ_2^l, ϕ_2^l) for the angles of incidence in the local coordinate system due to radiation from feeds 0, 1 and 2 respectively. Fig. 5.2 shows contours for a few angles of incidence, where blue, red and black colours correspond to feeds 0, 1 and 2, respectively. Solid lines correspond to θ_l and dash-dotted lines to ϕ_l.

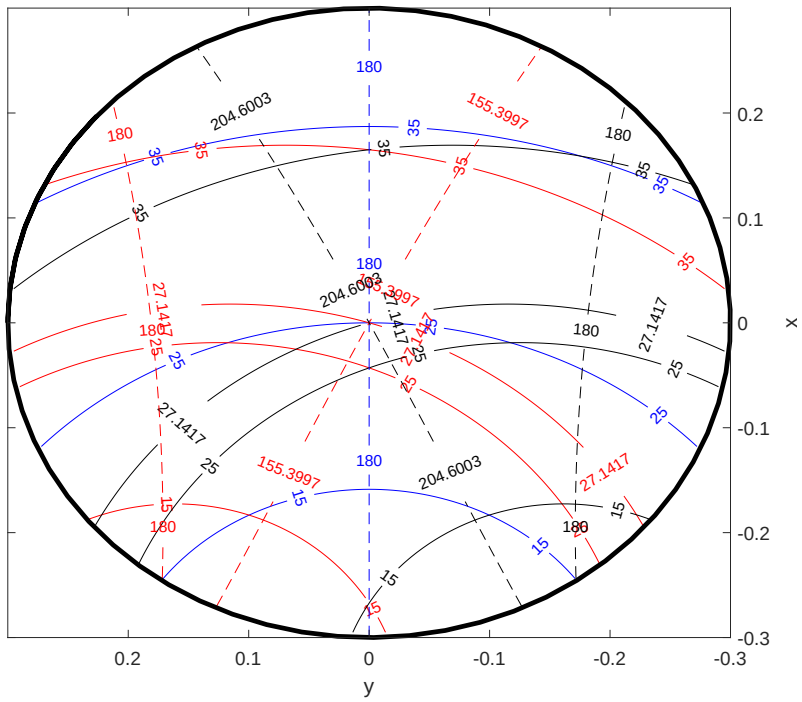

Figure 5.2: Contours for angles of incidence θ_l and ϕ_l: feed at the focus (feed 0, blue lines), feed displaced to the left (feed 1, red lines) and feed displaced to the right (feed 2, black lines).

The far-field has been obtained using the tool developed for Chapters 3 and 4, where the S-parameters computed by CST [9] are used to obtained the reflected magnetic field. Then, from the reflected magnetic field the electric surface currents are obtained, and the PO method is used to compute the far-field.

5.3 Optimisation procedure

As explained in Chapter 4, for an offset reflector with the feed placed at its focus (feed 0), there will be a misalignment between unit-cell and incoming field polarisation outside the vertical principal plane (vertical blue line $\phi_0^l = 180°$ in Fig. 5.2). Therefore, a unit-cell's element rotation is expected to improve the far-field horizontal plane, leaving the far-field vertical plane almost unaltered.

This quasi-independence in the far-field vertical plane is not present for the displaced feeds. To help understand, Fig. 5.3 shows a few contours for θ' and ϕ' in the non-tilted coordinate system (CS, see Section 3.2) for the three feeds where blue, red and black colours correspond to feeds 0, 1 and 2, respectively. Solid lines correspond to

θ_l and dash-dotted lines to ϕ_l. For feed 0, there are three planes that coincide: the vertical main plane of the feed ($\phi_s = 0°$ or $\phi' = 0°$ in Fig. 5.3), the vertical main plane of incidence for the unit-cells ($\phi_l = 180°$ in Fig. 5.2) and the vertical main plane of the reflector ($y = 0$). This alignment is the cause of the quasi-independence of the far-field vertical plane for feed 0. However, for the lateral feeds, their vertical main plane ($\phi^s_{1,2} = 0°$ or $\phi'_{1,2} = 0°$ in Fig. 5.3), the vertical main plane of incidence for the unit-cells ($\phi^l_{1,2} = 180°$ in Fig. 5.2) and the reflector main plane ($y = 0$) do not match. These misalignments produce that the element rotation affects to the far-field vertical plane for the displaced feeds, as it will be seen in Section 5.4.

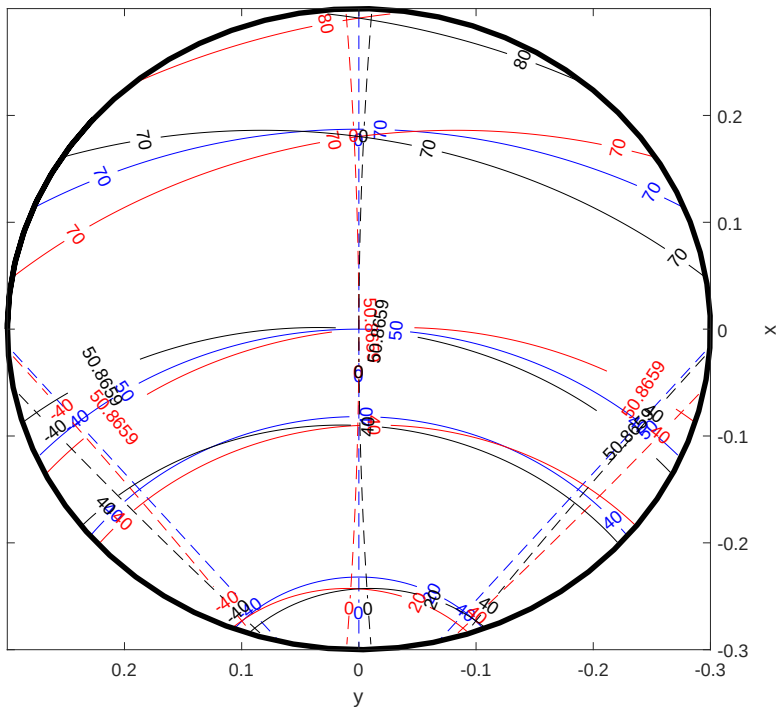

Figure 5.3: Contours for θ' and ϕ' in the non-tilted CS: feed at the focus (feed 0, blue lines), feed displaced to the left (feed 1, red lines) and feed displaced to the right (feed 2, black lines).

The design procedure is performed in two steps. First, an individual optimisation by element rotation is performed for each feed in isolation. As in Section 4, the element rotation is defined by a polynomial function denoted $\Delta\phi_i$, which input parameters are the local angles of incidence of the each feed:

$$\Delta\phi_i = a_i\theta_i^{l2}\gamma_i^2 + b_i\theta_i^{l2}\gamma_i + c_i\theta_i^l\gamma_i^2 + d_i\theta_i^{l2} + e_i\gamma_i^2 + f_i\theta_i^l\gamma_i + g_i\theta_i^l + h_i\gamma_i + i_i \quad (5.3.1)$$

where $\gamma_i = \phi_i^l - \phi_i^{l0}$ and ϕ_i^{l0} is the value of ϕ_i^l at the centre unit-cell, i.e., 180°, 155.4° and 204.6° for feeds 0, 1 and 2 respectively (see Fig. 5.2). The optimisation found the values for a_i, b_i, c_i, d_i, e_i and f_i to optimise each feed individually, taking into account that $d_0 = g_0 = i_0 = 0$ for feed 0 to ensure no rotation in the centre vertical plane ($y = 0$). The coefficients are summarized in Table 5.1.

coefficient	**feed** 0	**feed** 1	**feed** 2
a_i	0.0352	−0.1880	−0.0325
b_i	0.6069	0.1189	0.2877
c_i	−0.0215	−0.0476	0.0056
d_i	0	0.2186	0.0857
e_i	0.0051	−0.0848	0.5590
f_i	−0.1560	0.0004	0.0646
g_i	0	−0.0948	−0.2949
h_i	0.1750	0.1132	0.1470
i_i	0	0.0767	−0.0021

Table 5.1: Coefficients of the optimisation by unit-cell's element rotation for each feed.

The second step exploits the fact that the optimisation for one feed may not work for the others, as it can be deduced from the curves in Fig. 5.2 and Fig. 5.3. Therefore, a global $\Delta\phi_G$ is obtained by an average of the three $\Delta\phi_i$ functions weighted by the field intensities as

$$\Delta\phi_G = \frac{E_0^{norm}\Delta\phi_0 + E_1^{norm}\Delta\phi_1 + E_2^{norm}\Delta\phi_2}{E_0^{norm} + E_1^{norm} + E_2^{norm}} \quad (5.3.2)$$

where E_i^{norm} is the normalised field intensity for each feed, which can be seen in Fig. 5.4. An extra global optimisation for the three feeds together was performed with the weighted $\Delta\phi_G$ as input together with the local angles of incidence of feed 0. In order to have enough accuracy, polynomials of order 5 were needed for both θ_0^l and γ_0. The resulting $\Delta\phi_T$ is

$$\Delta\phi_T = c_1\theta_l^5 + c_2\gamma^5 + c_3\theta_l^4\gamma + c_4\theta_l\gamma^4 + c_5\theta_l^3\gamma^2 + c_6\theta_l^2\gamma^3 + c_7\theta_l^4 + c_8\gamma^4$$

$$+ c_9\theta_l^3\gamma + c_{10}\theta_l\gamma^3 + c_{11}\theta_l^2\gamma^2 + c_{12}\theta_l^3 + c_{13}\gamma^3 + c_{14}\theta_l^2\gamma + c_{15}\theta_l\gamma^2 \tag{5.3.3}$$

$$+ c_{16}\theta_l^2 + c_{17}\gamma^2 + c_{18}\theta_l\gamma + c_{19}\theta_l + c_{20}\gamma + c_{21}$$

where for simplicity in the formulation it has been supposed that θ_l and γ correspond to feed 0. The final $\Delta\phi_T$ is shown in Fig. 5.5, and its 21 coefficients are summarised in Table 5.2. As in Chapter 4, the optimisation by rotation has been performed by using the Nelder-Mead algorithm [10] implemented in MATLAB.

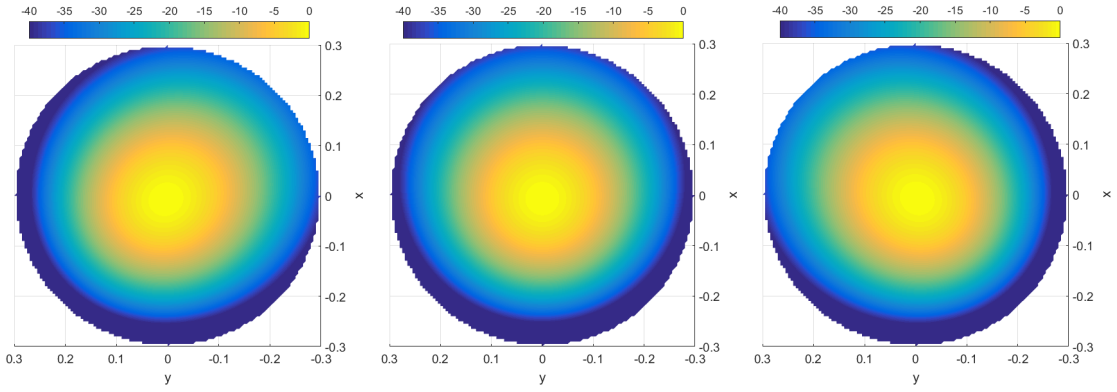

(a) (b) (c)

Figure 5.4: Field intensities across the parabolic reflector for the three feeds pointing towards the centre of the reflector: (a) feed 1 (offset in the vertical plane and displacement in the y-axis), (b) feed 0 (offset in the vertical plane) and feed 2 (offset in the vertical plane and displacement in the y-axis).

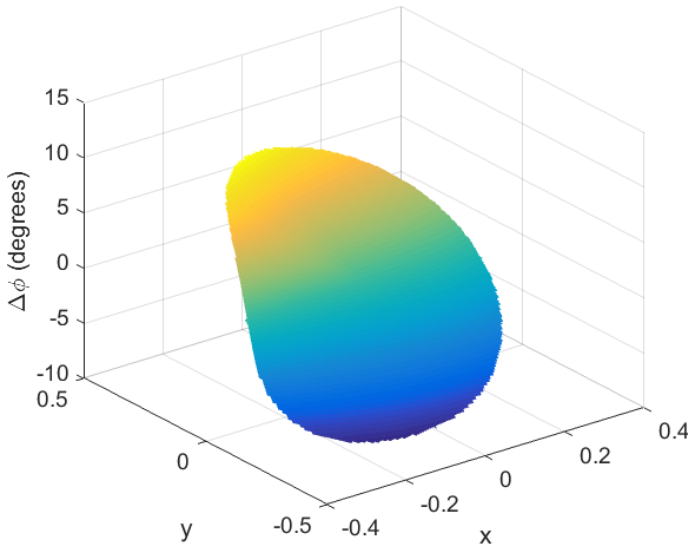

Figure 5.5: Resulting unit-cell's element rotation function $\Delta\phi_T$ across the reflector surface for the three feeds.

coefficient	**value**
c_1	-0.0051
c_2	0.0763
c_3	0.1797
c_4	-0.4346
c_5	-0.5426
c_6	0.0281
c_7	1.1150
c_8	3.3338
c_9	-0.3804
c_{10}	-0.0074
c_{11}	-1.1309
c_{12}	-5.9242
c_{13}	1.2948
c_{14}	-0.0085
c_{15}	0.0232
c_{16}	0.2081
c_{17}	4.2247
c_{18}	-1.3645
c_{19}	-0.0997
c_{20}	-0.0410
c_{21}	0.0095

Table 5.2: Coefficients of the final optimisation by unit-cell's element rotation for the three feeds.

5.4 Results

The results by simulation in Fig. 5.6a-5.8b show the CP components (LHCP and RHCP) of the far-field directivity for the three feeds, for two reflectors: one with a polarising surface based on the original unit-cell uniformly distributed serving as benchmark, and one with the optimisation by unit-cell's element rotation explained in Section 5.3. Fig. 5.6a and 5.6b show the vertical and horizontal planes respectively

at 14.5 GHz, Fig. 5.7a and 5.7b show the two planes at 17.7 GHz, and Fig. 5.8a and 5.8b show the two planes at 20 GHz.

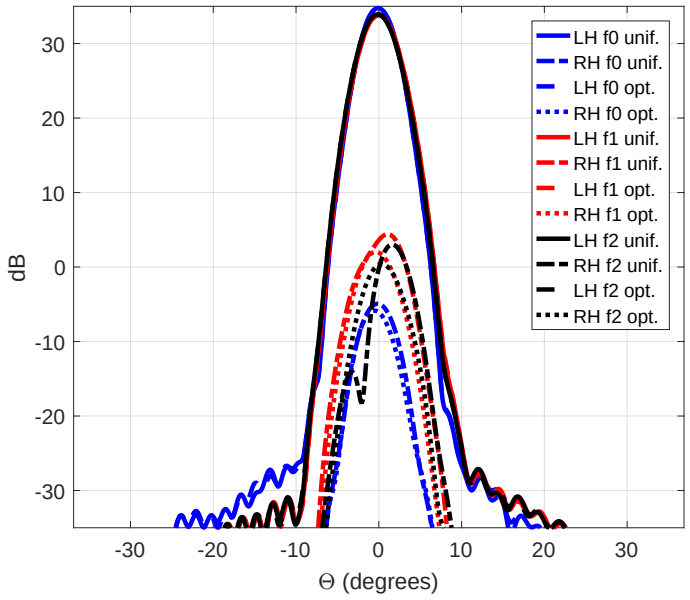

(a)

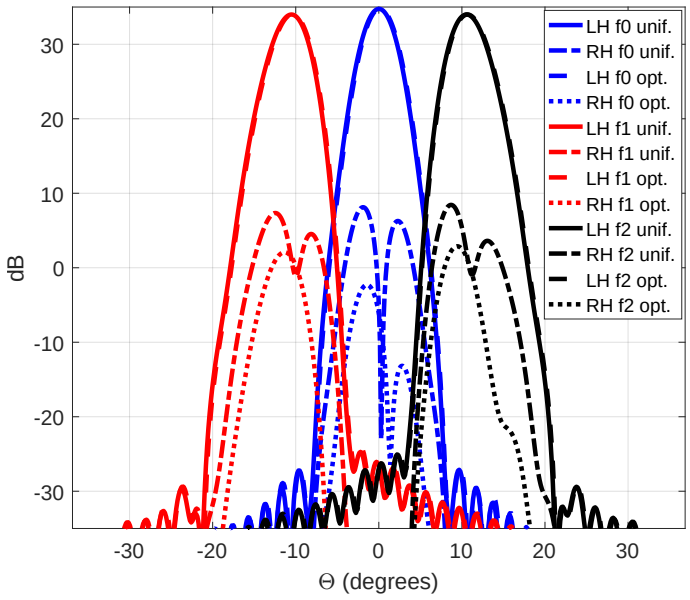

(b)

Figure 5.6: Far-field directivity (dB) at 14.5 GHz for (a) the vertical plane ($\Phi = 0°$) and (b) the horizontal plane ($\Phi = 90°$) for the three feeds (f0, f1 and f2) and the two polarising surfaces: array with uniform unit-cells and array with optimised unit-cells.

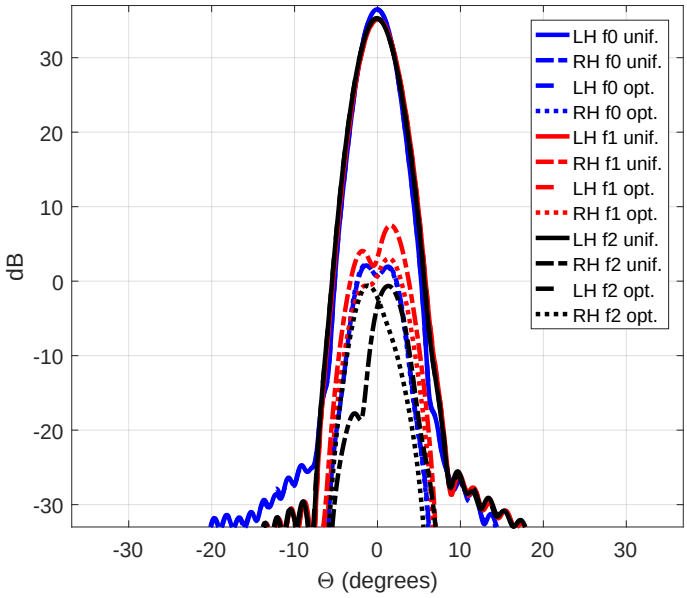

(a)

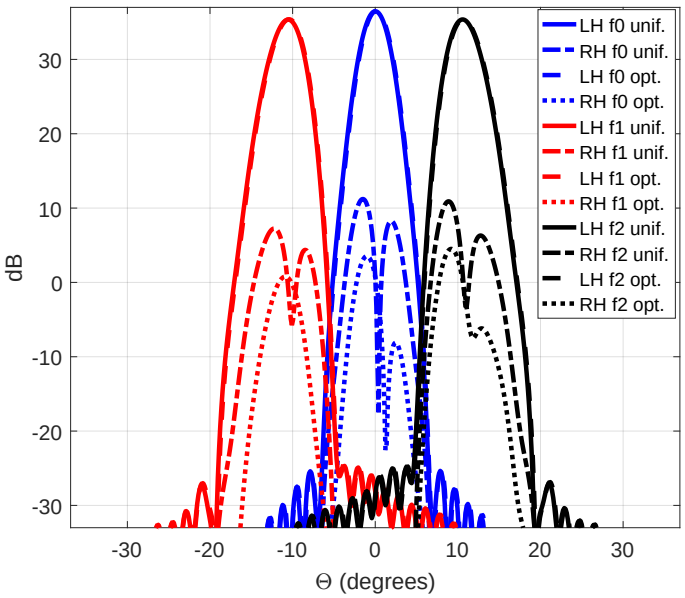

(b)

Figure 5.7: Far-field directivity (dB) at 14.5 GHz for (a) the vertical plane ($\Phi = 0°$) and (b) the horizontal plane ($\Phi = 90°$) for the three feeds (f0, f1 and f2) and the two polarising surfaces: array with uniform unit-cells and array with optimised unit-cells.

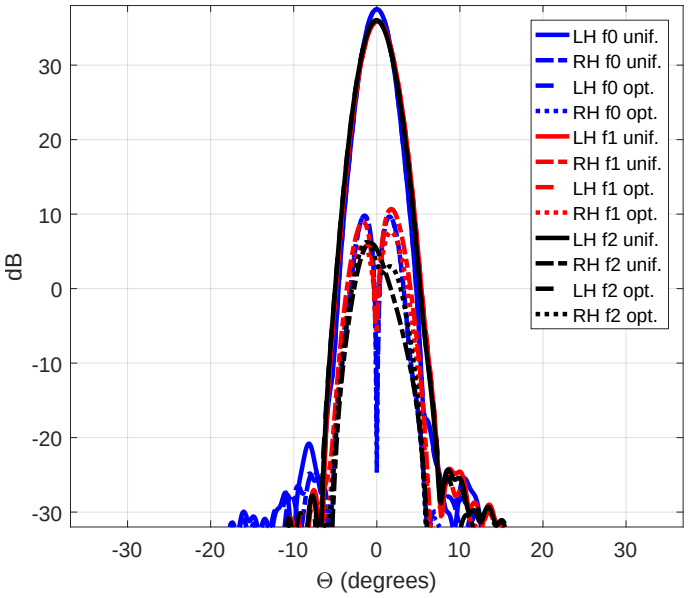

(a)

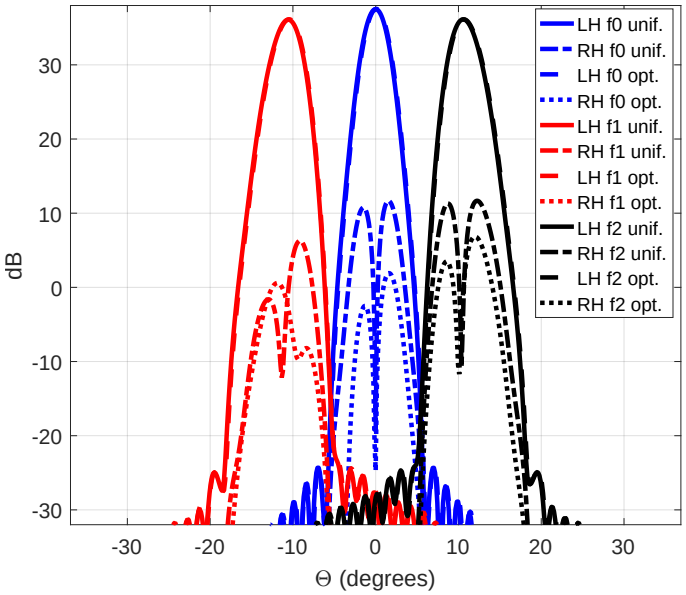

(b)

Figure 5.8: Far-field directivity (dB) at 14.5 GHz for (a) the vertical plane ($\Phi = 0°$) and (b) the horizontal plane ($\Phi = 90°$) for the three feeds (f0, f1 and f2) and the two polarising surfaces: array with uniform unit-cells and array with optimised unit-cells.

Improvements by simulation in the far-field horizontal plane between $8 - 10$ dB are achieved for feed 0, and between $5 - 6$ dB are achieved for feeds 1 and 2, as shown in Fig. 5.6b, Fig. 5.7b and Fig. 5.8b. Also, as it was discussed in Section 5.3, and shown in Fig. 5.6a, Fig. 5.7a and Fig. 5.8a, the element rotation has a small impact in the far-field vertical plane for the lateral feeds 1 and 2, while leaving

almost unaltered the vertical plane of the feed at the focus. Nevertheless, there is no appreciable deterioration for feeds 1 and 2. The cross-pol levels seem to be kept as the originals, or in any case decreased in a small amount (up to 3 dB).

5.5 Summary

This Chapter is a preliminary follow up of Chapter 4, where an optimisation procedure to reduce the cross-polarisation of single offset linear-to-circular polarisers for multiple primary feeds has been presented. The offset parabolic configuration fed by three ideal sources and the unit-cell that served as example have been presented in Section 5.2. Then an optimisation procedure based on unit-cell's element rotation has been explained in Section 5.3, where first an individual optimisation for each feed has been performed, and then a weighted average function from the three individual cases has been obtained. Section 5.4 has discussed the results by simulation, where improvements between $5-10$ can be obtained in the far-field horizontal plane. The procedure also shows a small impact in the far-field vertical plane, where small improvements up to 3 dB can be obtained.

The simulations presented in this chapter have been performed with the tool developed for the previous chapters for the analysis of reflector antennas where the reflector can be modelled as a PEC or as a FSS with the S-parameters computed by CST.

References

[1] S. T. Sharma, S. Rao, and L. Shafai, *Handbook of Reflector Antennas and Feed Systems, vol. III: Applications of Reflectors*. Artech House, 2013.

[2] S. K. Rao, "Parametric design and analysis of multiple-beam reflector antennas for satellite communications," *IEEE Antennas Propag. Mag.*, vol. 45, no. 4, p. 2634, Aug 2003.

[3] N. J. G. Fonseca and C. Mangenot, "Low-profile polarizing surface with dual-band operation in orthogonal polarizations for broadband satellite applications," *Proc. 8th Eur. Conf. Antennas Propag. (EuCAP'14)*, 2014.

[4] ——, "High-performance electrically thin dual-band polarizing reflective surface for broadband satellite applications," *IEEE Trans. Antennas Propag.*, vol. 64, no. 2, pp. 640–649, Feb 2015.

[5] M. Baunge, H. Ekstrom, P. Ingvarson, and M. Peterson, "A new concept for dual gridded reflectors," *Proc. 4th Eur. Conf. Antennas Propag. (EuCAP'10)*, 2010.

[6] E. K. Pfeiffer *et al.*, "Compact and stable earth deck multi-beam ka-band antenna structure and dual gridded reflector," *Proc. 5th Eur. Conf. Antennas Propag. (EuCAP'11)*, 2011.

[7] ESA TRP ITT AO/1-8608/16/NL/AF, *Dual-band polarising surfaces for single feed per beam broadband antennas*, May 2016.

[8] E. Doumanis, G. Goussetis, J. Gómez-Tornero, R. Cahill, and V. Fusco, "Anisotropic impedance surfaces for linear to circular polarization conversion," *IEEE Trans. Antennas Propag.*, vol. 60, no. 1, pp. 212–219, Jan 2012.

[9] CST Microwave Studio® [Online]. Available: https://www.cst.com/products/cstmws/.

[10] J. A. Nelder and R. Mead, "A simplex method for function minimization," *The Computer Journal*, vol. 7, no. 4, pp. 308–313, Jan 1965.

Chapter 6

Conclusions & future work

6.1 Conclusions

This thesis has covered the analysis and design of single linear-to-circular polarising reflector antennas in offset configurations exploiting periodic metallodielectric arrays. The main application of these devices is space communications, where high performances are expected. Therefore, the cross-polarisation performance of the antenna is one of the key parameters. To this end, the depolarisation properties of single reflector antennas has been the first scope of this thesis. This study is expected to give advanced insight into the origin of the cross-polarisation in reflector antennas before the periodic metallodielectric array is placed on the surface. This in turns is expected to help to develop techniques to reduce the cross-polarisation.

For the study of the depolarisation properties of single reflector antennas the software GRASP from TICRA [1] could be used. GRASP has become in the last years the preferred tool for the analysis and design of reflector antennas all over the world. However, even though there is a fairly complete free student version available, it only allows to compute the far-field using Physical Optics (PO), with the possibility to add diffraction. For the present thesis, it was proposed to start the study in the fields at the reflector aperture plane. For the far-field, it was proposed to compare PO with Geometrical Optics (GO) to understand why the former is the one most commonly used. Therefore, new tools were needed.

Furthermore, at the moment there is no software available in the market for the

analysis and design of periodic metallodielectric arrays (reflectarrays, FSS placed on top of reflectors, etc). Therefore this tool had to be developed from scratch.

The first challenge to develop such tool was to review the theory: quasi-optical approaches to model how the fields are reflected on the reflector surface, aperture antenna theory to obtain the far-field from the currents and Floquet's expansion of the fields and Method of Moments to obtain the reflection properties of periodic metallodielectric surfaces. All this theory can be found scattered through hundreds of papers and books going back in time more than one hundred years. Therefore, the first small contribution of this thesis is the presentation of all this theory on a self explanatory way (Chapter 2).

The tool developed for this thesis can be divided in two versions. The first version was focused on the analysis of single metallic reflectors fed by ideal feeds. Part of the theory reviewed in Chapter 2 was used to assume that the field propagating to the reflector can be viewed as rays. The aperture antenna theory applied to point sources was used in Chapter 3 to obtain general equations not found in any other source for the ideal feeds used to feed the reflector. Then these feeds were applied to the geometries of single and offset parabolic reflectors also reviewed in Chapter 3 to obtain the fields at the reflector aperture plane. The depolarisation properties of these two configurations were reviewed at the aperture plane for the different feeds, drawing the same conclusions as previous authors:

- The electric and magnetic dipoles (following Ludwig-II for the definition of linear polarisation) are not useful to feed offset configurations since they already give rise to cross-polarisation in the front-fed configuration.
- An offset configuration fed by a Huygens source (following Ludwig-III for the definition of linear polarisation) give rise to cross-polarisation. This cross-polarisation is maximum in the feed horizontal plane since it is the plane where the feed broadside direction does not match anymore with the main horizontal plane containing the vertex of the parabola. This cross-polarisation decreases as we move away from the horizontal plane, being zero at the vertical plane, where the feed broadside and the plane containing the vertex of the parabola match.

With respect to the far-field, it was found that GO was mainly used in old con-

tributions, probably due to the possibility to find closed equations for some feeds due to its simplicity. Other authors have used GO more recently since it can be easily implemented with the Fast Fourier Transform (FFT). However, as some authors pointed out, GO leads to false symmetries in the far-field vertical plane for offset configurations. This is an intrinsic limitation of the method since it performs a 2D Fourier Transform (FT) of the fields at the reflector aperture. On the other hand, PO performs a surface integral across the 3D reflector surface, leading to the expected asymmetries in the far-field vertical plane. For the front-fed configuration, it was found that GO predicts zero cross-polarisation in the far-field, while PO predicts small levels of cross-polarisation as we move away from the main planes to the oblique planes.

In the case of the offset configuration fed by a circularly polarised (CP) feed, a new (to the best of the author knowledge) explanation for the beam squint in the far-field horizontal plane was provided: the CP feed is formed by two orthogonal linearly polarised (LP) feeds with 90° phase difference. Therefore, the far-field of the reflector fed by the CP feed is equivalent to the combination of the far-fields of the same reflector fed by these two orthogonal LP feeds. As previously stated, these two cases will give rise to cross-polarisation. When they are combined, these individual cross-polarisations are the responsible of the beam squint. Therefore the cross-polarisation produced by the individual LP sources should be minimized in order to minimized the beam squint.

The far-field produced by the tool when using PO was in full agreement with GRASP, validating the tool for the analysis of single reflector antennas.

The second version of the tool was the addition of the modelling of practical sources and the change of the metallic reflector by a metallodielectric array. This was performed in Chapter 4. The near-field was extracted at the reflector surface by using CST Microwave Studio [2]. Then a novel way to extract the propagating modes from the total field was developed. The two main contributions of this modelling are the computation of the fundamental modes from the total near-field by using a Floquet's expansion of the field, and the computation of the angle of incidence of these fundamental modes seen by each unit-cell from the Poynting vector. Since only the fundamental modes are propagated to the far-field, the agreement of the far-fields for a flat reflector fed by a rectangular horn when using the total near-field

and when using only the fundamental modes validated the proposed procedure.

Due to time constraints, the S-parameters of each unit-cell on the metallodielectric array were computed with CST. Then these S-parameters were combined with the incident field to obtain the reflected field at each unit-cell, and from there, obtain the surface currents. Then the currents were integrated over the reflector surface (PO) to obtain the far-field. This tool, not available in the market, matched very well with the measurements of a FSS composed of uniform unit-cells performed in the anechoic chamber of Heriot-watt University.

A FSS composed of uniform unit-cells can have a poor cross-polarisation performance when used as a reflector. Its big size forces a wide range of angle of incidences across the reflector surface, which in turns deteriorates the FSS performance. Therefore, a novel optimisation procedure to decrease the cross-polarisation of such structures for a wide frequency band is also presented in Chapter 4. This two-step procedure is based on physical insight gained from the previous chapters and lead to cross-polarisation improvements up to 15 dB by simulation. This procedure could be combined with advanced optimisation techniques to achieve more efficient optimisation procedures.

Since one of the main technologies used in space communications is multi-beam antennas, Chapter 5 presents preliminary results where the far-fields of a reflector fed by three ideal feeds are optimised at the same time. The encouraging results obtained by the tool present the proposed optimisation procedure as a promising additional step in the complex optimisation of multi-beam reflector antennas comprising polarising surfaces.

6.2 Future work

Chapter 3 has covered the analysis of single reflector antennas. However, due to time limitations, there are several features that have been kept out but can (and will) be added:

- Dual configurations including the main reflector and a subreflector. Ray tracing techniques or the method described in Chapter 4 to obtain the feed near-field can be applied to obtain the reflected field from the subreflector. Then

a generalised aperture antenna theory without far-field approximation can be used to obtain the surface currents induced on the main reflector by the sub-reflector.

- The method to obtain the near-field of the feed explained in Chapter 4 rely on CST to obtain the complete near-field. However, a spherical wave expansion of the field can be used to directly obtain the near-field from the far-field [3]. An implementation of this tool was already attempted but time constraints made not possible to debug some errors in the code.
- Diffraction analysis could be also added to account for the diffraction at the reflector edges [4].

For simplicity purposes, a simple dipole geometry has been used for the unit-cells in Chapters 4 and 5. As it was mentioned in Chapter 2, entire domain basis functions are sufficient accurate to represent the surface currents on the dipoles. An implementation of these basis functions was developed, but since no effects of the copper conductivity were added, CST was used instead to obtain the S-parameters. For this reason, these basis functions have been left out of this thesis. More complex basis functions to account for the currents in more complex geometries can be implemented. The Rao-Wilton-Glisson (RWG) basis functions seem as one of the best candidates [5]. Other more complex basis functions (as the one used by TICRA [6]) could be implemented as well.

Other unit-cells could be used for more stringen applications. For example, unit-cells that convert the linearly polarised incident field into circularly polarised field with orthogonal rotations in two sub-bands are very useful for multi-beam antenna applications [7]. A unit-cell with such features was presented in [8]. Since the principle of operation is similar to the dipole element, the optimisation procedure from Chapter 4 could be applied to dual-band polarising reflectors comprising this unit-cell. Moreover, this unit-cell presents a better starting point to optimise the polarising reflector for several feeds due to its broader angular stability.

The optimisation procedure presented in Chapter 4 has been shown to provide a substantial improvement in the cross-polarisation performance of the linear-to-circular reflection polarisers compared to the original uniform unit-cell design. However, brute-force optimisation procedures as the ones used in reflectarrays [9] could be

used in a second iteration to get even further improvement. Furthermore, other far-field features such as beam steering or beam squint cancellation can be taken into account in the design process. It has been found in a series of theoretical studies carried out for an ongoing ESA project that it is not possible to produce beam squint cancellation and low cross-polarisation with doubly symmetric unit-cells (such as dipoles or the one from [8]). New asymmetric unit-cells would have to be introduced to provide these features. It has also been pointed out that it could be interesting to find out if the far-field phase could be used to obtain a more realisable target S-parameters during the synthesis process.

Finally, another possible future work could be the design of contoured beam or shaped reflector antennas [10]. These reflector antennas are used to produce contoured beams to cover more efficiently a specific area of the Earth. To analyse such structures it is common to express the deformation of the surface to produce such shaped beams as a series expansion function such as the Zernike polynomials [10]. TICRA's POS and GRASP software programs are extensively used in the reflector antenna community to design and analyse such reflectors. An in-house tool to analyse these structures could be very useful.

References

[1] TICRA staff, *GRASP Technical Description, TICRA, Copenhagen, 2005-2008.*

[2] CST Microwave Studio® [Online]. Available: https://www.cst.com/products/cstmws/.

[3] A. C. Ludwig, "Near-field far-field transformations using spherical-wave expansions," *IEEE Trans. Antennas Propag.*, vol. 19, no. 2, pp. 214–220, March 1971.

[4] G. B. Keller, "Geometrical theory of diffraction," *J. Opt. Soc. Amer.*, vol. 52, no. 2, pp. 116–130, Feb 1962.

[5] S. M. Rao, D. R. Wilton, and A. W. Glisson, "Electromagnetic scattering by surface of arbitrary shape," *IEEE Trans. Antennas Propag.*, vol. 30, no. 3, pp. 409–411, May 1982.

[6] E. Jorgensen, J. L. Volakis, P. Meincke, and O. Breinbjerg, "Higher order hierarchical legendre basis functions for electromagnetic modeling," *IEEE Trans. Antennas Propag.*, vol. 52, no. 11, pp. 2985–2995, Nov 2004.

[7] N. J. G. Fonseca and C. Mangenot, "High-performance electrically thin dual-band polarizing reflective surface for broadband satellite applications," *IEEE Trans. Antennas Propag.*, vol. 64, no. 2, pp. 640–649, Feb 2015.

[8] W. Tang, S. Mercader-Pellicer, G. Goussetis, H. Legay, and N. J. G. Fonseca, "Low-profile compact dual-band unit cell for polarising surfaces operating in orthogonal polarizations," *IEEE Trans. Antennas Propag.*, vol. 65, no. 3, pp. 1472–1477, March 2017.

[9] D. R. Prado, D. Arrebola, M. R. Pino, and F. Las-Heras, "Efficient crosspolar optimization of shaped-beam dual-polarized reflectarrays using full-wave anal-

ysis for the antenna element characterization," *IEEE Trans. Antennas Propag.*, vol. 65, no. 2, pp. 623–635, Feb 2017.

[10] S. T. Sharma, S. Rao, and L. Shafai, *Handbook of Reflector Antennas and Feed Systems, vol. III: Applications of Reflectors.* Artech House, 2013.

Appendix A

Vector calculus identities

$$\nabla \cdot (\nabla \times \vec{A}) = 0 \tag{A.0.1}$$

$$\nabla \times (\nabla \phi) = 0 \tag{A.0.2}$$

$$\nabla \times (\nabla \times \vec{A}) = \nabla(\nabla \cdot \vec{A}) - \nabla^2 \vec{A} \tag{A.0.3}$$

$$\nabla \times (\psi \vec{A}) = \psi(\nabla \times \vec{A}) + (\nabla \psi) \times \vec{A} \tag{A.0.4}$$

$$\nabla \cdot (\psi \vec{A}) = \psi(\nabla \cdot \vec{A}) + \vec{A} \cdot (\nabla \psi) \tag{A.0.5}$$

$$\vec{A} \times (\vec{B} \times \vec{C}) = (\vec{A} \cdot \vec{C}) \cdot \vec{B} - (\vec{A} \cdot \vec{B}) \cdot \vec{C} \tag{A.0.6}$$

$$\vec{A} \cdot (\vec{B} \times \vec{C}) = \vec{B} \cdot (\vec{C} \times \vec{A}) = \vec{C} \cdot (\vec{A} \times \vec{B}) \tag{A.0.7}$$

Appendix B

Gradient, divergence, curl and laplacian operations

For the following equations:

- V: a scalar.
- $\vec{A}$: a vector.
- ∇V: the gradient operator.
- $\nabla \cdot \vec{A}$: the divergence operator.
- $\nabla \times \vec{A}$: the curl operator.
- $\nabla^2 V$: the Laplacian operator.

B.1 Cartesian Coordinates

$$\nabla V = \hat{x}\frac{\partial V}{\partial x} + \hat{y}\frac{\partial V}{\partial y} + \hat{z}\frac{\partial V}{\partial z} \tag{B.1.1}$$

$$\nabla \cdot \vec{A} = \frac{\partial A_x}{\partial x} + \frac{\partial A_y}{\partial y} + \frac{\partial A_z}{\partial z} \tag{B.1.2}$$

$$\nabla \times \vec{A} = \begin{vmatrix} \hat{x} & \hat{y} & \hat{z} \\ \dfrac{\partial}{\partial x} & \dfrac{\partial}{\partial y} & \dfrac{\partial}{\partial z} \\ A_x & A_y & A_z \end{vmatrix} \tag{B.1.3}$$

$$\nabla^2 V = \frac{\partial^2 V}{\partial^2 x} + \frac{\partial^2 V}{\partial^2 y} + \frac{\partial^2 V}{\partial^2 z} \tag{B.1.4}$$

B.2 Spherical Coordinates

$$\nabla V = \hat{\rho}\frac{\partial V}{\partial \rho} + \hat{\theta}\frac{1}{\rho}\frac{\partial V}{\partial \theta} + \hat{\phi}\frac{1}{\rho \sin\theta}\frac{\partial V}{\partial \phi} \tag{B.2.1}$$

$$\nabla \cdot \vec{A} = \frac{1}{\rho^2}\frac{\partial(\rho^2 A_\rho)}{\partial \rho} + \frac{1}{\rho \sin\theta}\frac{\partial(A_\theta \sin\theta)}{\partial \theta} + \frac{1}{\rho \sin\theta}\frac{\partial A_\phi}{\partial \phi} \tag{B.2.2}$$

$$\begin{aligned} \nabla \times \vec{A} = {} & \hat{\rho}\frac{1}{\rho \sin\theta}\left(\frac{\partial(A_\phi \sin\theta)}{\partial \theta} - \frac{\partial A_\theta}{\partial \phi}\right) \\ & + \hat{\theta}\frac{1}{\rho}\left(\frac{1}{\sin\theta}\frac{\partial A_\rho}{\partial \phi} - \frac{\partial(\rho A_\phi)}{\partial \rho}\right) + \hat{\phi}\frac{1}{\rho}\left(\frac{\partial(\rho A_\theta)}{\partial \rho} - \frac{\partial A_\rho}{\partial \theta}\right) \end{aligned} \tag{B.2.3}$$

$$\nabla^2 V = \frac{1}{\rho^2}\frac{\partial}{\partial \rho}\left(\rho^2 \frac{\partial V}{\partial \rho}\right) + \frac{1}{\rho^2 \sin\theta}\frac{\partial}{\partial \theta}\left(\sin\theta \frac{\partial V}{\partial \theta}\right) + \frac{1}{\rho^2 \sin^2\theta}\frac{\partial^2 V}{\partial \phi^2} \tag{B.2.4}$$

Appendix C

Boundary conditions for a Perfect Electric Conductor

Finding and applying the boundary conditions between two different media is a very basic problem in electrodynamics, and it can be found extensively in the literature [1]. Nevertheless, it is very convenient to review it again.

At the boundary between two different media or at a surface with a specific charge and current densities, the electric and magnetic fields are not continuous. Fig.C.1 presents two different media with their associated electric and magnetic fields $\vec{E}_1$, $\vec{H}_1$ and $\vec{E}_2$, $\vec{H}_2$, and conductivities σ_1, σ_2. The boundary conditions are:

1) A discontinuity appears in the normal component of the electric flux density $\vec{D} = \vec{D}_2 - \vec{D}_1$ at the boundary due to the charge density across that boundary: $\hat{n} \cdot (\vec{D}_2 - \vec{D}_1) = \rho_e$. But since the surface is an infinite PEC, its conductivity is $\sigma_1 = \infty$[1]. Thus, $\vec{E}_1 = \vec{H}_1 = 0$ and the condition is reduced to

$$\hat{n} \cdot \vec{D}_2 = \hat{n} \cdot (\epsilon_2 \vec{E}_2) = \rho_e \tag{C.0.1}$$

2) Because of the absence of a magnetic charge, the normal to the magnetic flux density $\vec{B} = \vec{B}_2 - \vec{B}_1$ is: $\hat{n} \cdot (\vec{B}_2 - \vec{B}_1) = 0$. Since $\vec{H}_1 = 0$, the condition reduces to

[1] $\sigma_1 = \infty$ means that the field can not penetrate the medium, thus there is no electric or magnetic fields inside the volume

$$\hat{n} \cdot \vec{B}_2 = \hat{n} \cdot (\mu_2 \vec{H}_2) = 0 \tag{C.0.2}$$

3) Across the boundary, the tangential components of the electric fields are continuous: $\hat{n} \times (\vec{E}_2 - \vec{E}_1) = 0$. Thus, with $\vec{E}_1 = 0$, the condition reduces to:

$$\hat{n} \times \vec{E}_2 = 0 \tag{C.0.3}$$

4) There is a discontinuity between the tangential components of the magnetic fields: $\hat{n} \times (\vec{H}_2 - \vec{H}_1) = \vec{J}_s$. Applying $\vec{H}_1 = 0$, the condition reduces to:

$$\hat{n} \times \vec{H}_2 = \vec{J}_s \tag{C.0.4}$$

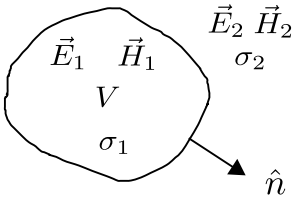

Figure C.1: Region of interest for the boundary conditions between two media.

The electric and magnetic fields $\vec{E}_2$ and $\vec{H}_2$ can be split into the incident and reflected fields in their medium: $\vec{E}_2 = \vec{E}_i + \vec{E}_r$. The current at the surface from condition 4) can be expressed as

$$\vec{J}_s = \hat{n} \times (\vec{H}_i + \vec{H}_r) = \hat{n} \times \vec{H}_i + \hat{n} \times \vec{H}_r \tag{C.0.5}$$

Since the surface is an infinite PEC, using the method of images [2], $\hat{n} \times \vec{H}_i = \hat{n} \times \vec{H}_r$. Thus,

$$\vec{J}_s = 2(\hat{n} \times \vec{H}_i) = 2(\hat{n} \times \vec{H}_r) \tag{C.0.6}$$

It is worth mentioning that $\vec{H}_i \neq \vec{H}_r$, but $|\vec{H}_i| = |\vec{H}_r|$ for a lossless surface. These two conditions can be derived from image theory [3], where the PEC is only affecting the direction, not the magnitude of the electric or magnetic fields. Both incident and reflected magnetic (or electric) fields can be decomposed into a pair of vectors,

one perpendicular to the surface, $\vec{H}_i^{\perp}$ or $\vec{H}_r^{\perp}$, and one parallel to the surface, $\vec{H}_i^{\parallel}$ or $\vec{H}_r^{\parallel}$, where the perpendicular vector is obtained as $(\vec{H}\cdot\hat{n})\hat{n}/|\hat{n}|^2$. Since the magnitudes of the incident and reflected fields are equal, then $\vec{H}_i^{\parallel} = \vec{H}_r^{\parallel}$. And since the perpendicular vector does not affect the operation $\hat{n}\times\vec{H}$, it can be asserted that Eq.C.0.6 holds.

From condition 3): $\hat{n}\times(\vec{E}_i+\vec{E}_r) = 0$. And by symmetry considerations: $\hat{n}\cdot\vec{E}_i = \hat{n}\cdot\vec{E}_r$. If another cross product is applied to both parts of the equality of condition 3), $\hat{n}\times(\hat{n}\times\vec{E}_r) = -\hat{n}\times(\hat{n}\times\vec{E}_i)$, and using Eq.A.0.6,

$$\vec{E}_r = 2\hat{n}(\hat{n}\cdot\vec{E}_i) - \vec{E}_i \tag{C.0.7}$$

Eq.C.0.7 gives the field reflected from the reflector surface, already obtained in Eq.2.3.37. And in the same way, using $\hat{n}\times\vec{H}_i = \hat{n}\times\vec{H}_r$ and relation 2): $\hat{n}\cdot\vec{H}_i = -\hat{n}\cdot\vec{H}_r$, Eq.2.3.38 can also be obtained,

$$\vec{H}_r = \vec{H}_i - 2\hat{n}(\hat{n}\cdot\vec{H}_i) \tag{C.0.8}$$

Appendix D

Local coordinate system

The definition of the local coordinate system (CS) (x_l, y_l, z_l) introduced in Section 3.2 depends on the geometry of the reflector. Since parabolic reflectors were the original target, a specific CS transformation was developed to perform transformations between the non-tilted CS and the local CS. The z-axis is already known, since it has to be equal to the normal to the surface. Therefore, from Eq.3.3.9

$$\hat{z}_l = \hat{n} = -\hat{x}' \sin\frac{\theta'}{2}\cos\phi' - \hat{y}' \sin\frac{\theta'}{2}\sin\phi' - \hat{z}'\cos\frac{\theta'}{2} \tag{D.0.1}$$

Then, assuming that for the vertical plane ($\phi' = 0°$) $\hat{x}_l$ is along the $x'z'$ plane and $\hat{y}_l = \hat{y}'$, and that for the horizontal plane ($\phi' = 90°$) $\hat{x}_l = \hat{x}'$ and $\hat{y}_l$ is along the $y'z'$ plane, it is possible to yield to the CS transformation matrix

$$\mathbf{M} = \begin{bmatrix} \sin\phi'^2 + \cos\phi'^2\cos\frac{\theta'}{2} & -(1-\cos\frac{\theta'}{2})\sin\phi'\cos\phi' & -\sin\frac{\theta'}{2}\cos\phi' \\ (1-\cos\frac{\theta'}{2})\sin\phi'\cos\phi' & -\cos\phi'^2 - \sin\phi'^2\cos\frac{\theta'}{2} & \sin\frac{\theta'}{2}\sin\phi' \\ -\sin\frac{\theta'}{2}\cos\phi' & -\sin\frac{\theta'}{2}\sin\phi' & -\cos\frac{\theta'}{2} \end{bmatrix} \tag{D.0.2}$$

However, it would be more suitable to describe the transformation independently of the reflector geometry. Daniele Bresciani from the Research and Technology Department of Thales Alenia Space has provided such transformation. The transformation is shown here under his approval.

A general transformation matrix can be defined as

$$\mathbf{M} = \begin{bmatrix} M_{11} & M_{12} & M_{13} \\ M_{21} & M_{22} & M_{23} \\ M_{31} & M_{32} & M_{33} \end{bmatrix} \tag{D.0.3}$$

The condition imposed to Eq.D.0.1, $\hat{z}_l = \hat{n}$, is again valid. Therefore, $M_{31} = n_x^l$, $M_{32} = n_y^l$ and $M_{33} = n_z^l$. Now, in order to reduce further the number of unknowns, we can assume that $\hat{x}_l$ has no component in $\hat{y}'$, i.e., $M_{12} = 0$. Then, like any rotation matrix (such as Eq.D.0.2), Eq.D.0.3 has to be an orthogonal matrix ($\mathbf{M}^{-1} = \mathbf{M}^T$). Therefore, the following two conditions are obtained

$$M_{11}M_{31} + M_{12}M_{32} + M_{13}M_{33} = 0 \tag{D.0.4a}$$

$$M_{11}^2 + M_{12}^2 + M_{13}^2 = 1 \tag{D.0.4b}$$

It is also possible to obtain $\hat{y}_l$ as $\hat{y}_l = \hat{z}_l \times \hat{x}_l$. With all these conditions it is possible to obtain all the components of Eq.D.0.3

$$\mathbf{M} = \begin{bmatrix} \pm\frac{n'_z}{\sqrt{n'^2_x + n'^2_z}} & 0 & \mp\frac{n'_x}{\sqrt{n'^2_x + n'^2_z}} \\ \mp\frac{n'_x n'_y}{\sqrt{n'^2_x + n'^2_z}} & \pm\sqrt{n'^2_x + n'^2_z} & \mp\frac{n'_y n'_z}{\sqrt{n'^2_x + n'^2_z}} \\ n'_x & n'_y & n'_z \end{bmatrix} \tag{D.0.5}$$

In the local CS defined in Section 3.2, $\hat{n}$ points inwards from the reflector. Therefore, the uppers signs in Eq.D.0.5 should be used.

It is also possible to impose that $\hat{y}_l$ is the unit vector that has no component in $\hat{x}'$, i.e., $M_{21} = 0$. Then knowing that the matrix has to be orthogonal, the following conditions are obtained

$$M_{21}M_{31} + M_{22}M_{32} + M_{23}M_{33} = 0 \tag{D.0.6a}$$

$$M_{21}^2 + M_{22}^2 + M_{23}^2 = 1 \tag{D.0.6b}$$

Finally, knowing $\hat{x}_l = \hat{y}_l \times \hat{z}_l$ yields

$$\mathbf{M} = \begin{bmatrix} \pm\sqrt{n_y'^2 + n_z'^2} & \mp\frac{n_x' n_y'}{\sqrt{n_y'^2+n_z'^2}} & \mp\frac{n_x' n_z'}{\sqrt{n_y'^2+n_z'^2}} \\ 0 & \pm\frac{n_z'}{\sqrt{n_y'^2+n_z'^2}} & \mp\frac{n_y'}{\sqrt{n_y'^2+n_z'^2}} \\ n_x' & n_y' & n_z' \end{bmatrix} \tag{D.0.7}$$

The three transformations are equally valid mathematically. However, the difference between them is translated into a different layout of the unit-cells. Therefore, it is expected that they show slightly different performances when used to lay a specific unit-cell on the reflector surface. To that end, Fig. D.1a and Fig. D.1b show the two principal planes of the far-field of a parabolic reflector antenna with a FSS on its surface, for the three transformations, using an offset configuration with $d = 600$ mm, $f = 400$ mm and $\theta_f = 50°$, and fed by an ideal Gaussian beam source (see Section 3.4.5). The unit-cell is the one used in Chapter 4.

Transformation 1 comes from Eq. D.0.2. Transformation 2 comes from Eq.D.0.5 And transformation 3 comes from Eq. D.0.7. As it can be observed in the two figures, the transformation that gives the lower cross-polarisation is transformation 2.

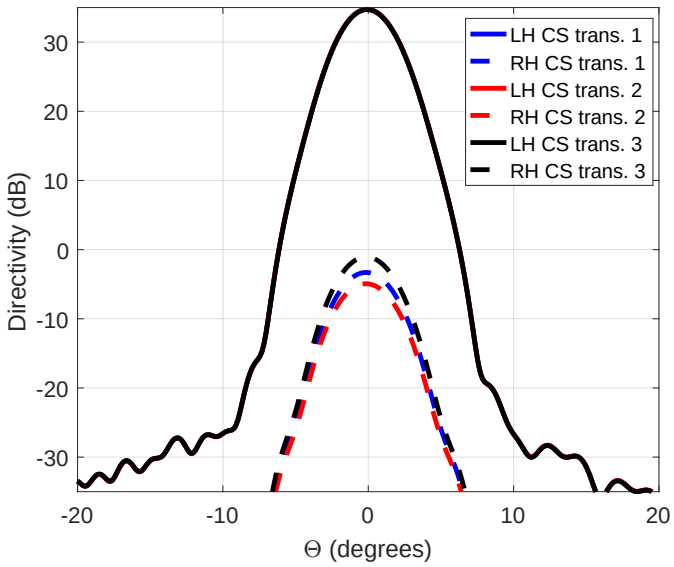

(a)

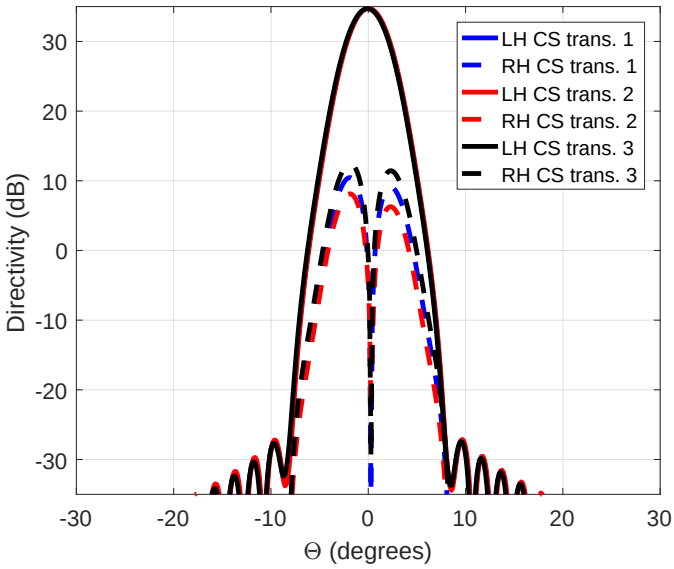

(b)

Figure D.1: Comparison of the local coordinate system transformations for the far-field (a) vertical plane ($\Phi = 0°$) and the (b) horizontal plane ($\Phi = 90°$).

Appendix E

Parabola definition

Fig. E.1 a) shows the geometry of a parabola, where D is a line called directrix, V is the point called vertex that gives the minimum of the parabola, and F is the focus. The distance from the focus to the vertex equals the distance from the vertex to the directrix. Following this assumption it is possible to stablish the next postulate:

- The distance from the focus to any point P_n on the parabola equals the distance from the same point on the parabola to a point on the directrix D_n, being the line formed by the points P_n and D_n perpendicular to the directrix.

As a derivation of this postulate it can be stated that:

- If a line L parallel to the directrix is traced at a specific distance (positive with respect to the y-axis) from the focus, as Fig. E.1 b) shows, all possible paths FP_nL_n have the same length.

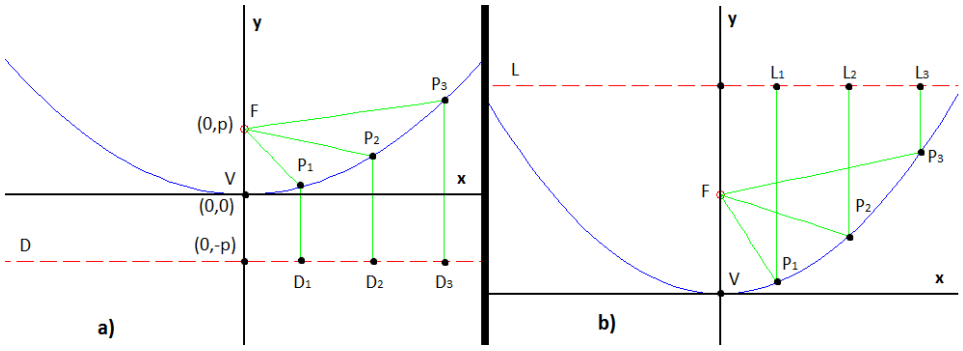

Figure E.1: Geometry of a parabola.

Using a 2-D Cartesian coordinates (x, y), the focus is placed at $(0, p)$, and the directrix at $y = -p$. Taking a point on the parabola, and following the postulate

stated above, for every point, both paths P_nD_n and FP_n are equal for the same n

$$y_n + p = \sqrt{(y_n - p)^2 + x_n^2} \tag{E.0.1}$$

what gives

$$4py_n = x_n^2 \tag{E.0.2}$$

Eq. E.0.2 can be generalized for a vertex V not only in the origin but at an arbitrary point (h, k)

$$4p(y_n - k) = (x_n - h)^2 \tag{E.0.3}$$

It is possible to rewrite Eq. E.0.3 as

$$y = ax^2 + bx + c \tag{E.0.4}$$

where $a = 1/(4p)$, $b = -h/(2p)$ and $c = (h^2 + k)/(4p)$. Equation E.0.4 is the so called *equation of the parabola*.

Appendix F

Change of coordinates

F.1 Cartesian to Spherical and vice-versa

Fig.F.1 shows a typical spherical coordinates system used in physics and engineering:

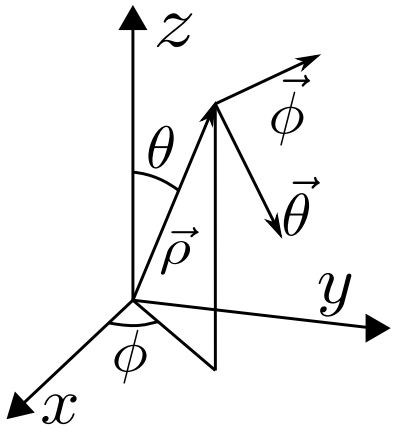

Figure F.1: Spherical coordinates system.

Cartesian coordinates to spherical coordinates

$$\rho = \sqrt{x^2 + y^2 + z^2} \tag{F.1.1}$$

$$\theta = \begin{cases} \arccos\left(\dfrac{z}{\sqrt{x^2+y^2+z^2}}\right) & z > 0 \\ \dfrac{\pi}{2} & z = 0 \\ \pi + \arccos\left(\dfrac{z}{\sqrt{x^2+y^2+z^2}}\right) & z < 0 \end{cases} \tag{F.1.2}$$

$$\phi = \begin{cases} \arctan\left(\dfrac{y}{x}\right) & x > 0 \ \& \ y > 0 \ (1^{\text{st}} \text{ Q}) \\ 2\pi + \arctan\left(\dfrac{y}{x}\right) & x > 0 \ \& \ y < 0 \ (4^{\text{th}} \text{ Q}) \\ \dfrac{\pi}{2}\text{sgn}(y) & x = 0 \\ \pi + \arctan\left(\dfrac{y}{x}\right) & x < 0 \ (2^{\text{nd}} \ \& \ 3^{\text{rd}} \text{ Q}) \end{cases} \tag{F.1.3}$$

At the z-axis, where $x^2 + y^2 = 0$, ϕ is not defined since it gives a singularity. For $x > 0$, $y > 0$ and $z > 0$, the transformation from spherical to Cartesian coordinates is

$$x = \rho \sin\theta \cos\phi \tag{F.1.4a}$$

$$y = \rho \sin\theta \sin\phi \tag{F.1.4b}$$

$$z = \rho \cos\theta \tag{F.1.4c}$$

Unit vector transformation from Cartesian to spherical coordinates

$$\begin{bmatrix} \hat{\rho} \\ \hat{\theta} \\ \hat{\phi} \end{bmatrix} = \begin{bmatrix} \sin\theta\cos\phi & \sin\theta\sin\phi & \cos\theta \\ \cos\theta\cos\phi & \cos\theta\sin\phi & -\sin\theta \\ -\sin\phi & \cos\phi & 0 \end{bmatrix} \begin{bmatrix} \hat{x} \\ \hat{y} \\ \hat{z} \end{bmatrix} \tag{F.1.5}$$

Unit vector transformation from spherical to Cartesian coordinates

$$\begin{bmatrix} \hat{x} \\ \hat{y} \\ \hat{z} \end{bmatrix} = \begin{bmatrix} \sin\theta\cos\phi & \cos\theta\cos\phi & -\sin\phi \\ \sin\theta\sin\phi & \cos\theta\sin\phi & \cos\phi \\ \cos\theta & -\sin\theta & 0 \end{bmatrix} \begin{bmatrix} \hat{\rho} \\ \hat{\theta} \\ \hat{\phi} \end{bmatrix} \tag{F.1.6}$$

F.2 Cartesian to Cylindrical and vice-versa

Cylindrical to Cartesian

$$x = r \cos\phi \tag{F.2.1a}$$

$$y = r \sin \phi \tag{F.2.1b}$$

$$z = z \tag{F.2.1c}$$

Cartesian to cylindrical

$$\rho = \sqrt{x^2 + y^2} \tag{F.2.2}$$

$$\phi = \begin{cases} 0 & x = 0 \ \& \ y = 0 \\ \arcsin\left(\frac{y}{r}\right) & x \geq 0 \\ -\arcsin\left(\frac{y}{r}\right) + \pi & x < 0 \end{cases} \tag{F.2.3}$$

$$z = z \tag{F.2.4}$$

Unit vector transformation from cylindrical to Cartesian coordinates

$$\begin{bmatrix} \hat{x} \\ \hat{y} \\ \hat{z} \end{bmatrix} = \begin{bmatrix} \cos\phi & -\sin\phi & 0 \\ \sin\phi & \cos\phi & 0 \\ 0 & 0 & 1 \end{bmatrix} \begin{bmatrix} \hat{r} \\ \hat{\phi} \\ \hat{z} \end{bmatrix} \tag{F.2.5}$$

Unit vector transformation from Cartesian to cylindrical coordinates

$$\begin{bmatrix} \hat{r} \\ \hat{\phi} \\ \hat{z} \end{bmatrix} = \begin{bmatrix} \cos\phi & \sin\phi & 0 \\ -\sin\phi & \cos\phi & 0 \\ 0 & 0 & 1 \end{bmatrix} \begin{bmatrix} \hat{x} \\ \hat{y} \\ \hat{z} \end{bmatrix} \tag{F.2.6}$$

F.3 Spherical to Cylindrical and vice-versa

From spherical to cylindrical

$$r = \rho \sin \theta \tag{F.3.1a}$$

$$\phi = \phi \tag{F.3.1b}$$

$$z = \rho \cos\theta \tag{F.3.1c}$$

From cylindrical to spherical

$$\rho = \sqrt{r^2 + z^2} \tag{F.3.2a}$$

$$\theta = \arctan\left(\frac{r}{z}\right) \tag{F.3.2b}$$

$$\phi = \phi \tag{F.3.2c}$$

References

[1] J. D. Jackson, *Classical Electrodynamics*, 3rd ed. Wiley & Sons, 1999.

[2] S. Silver, *Microwave Antenna Theory and Design*. McGraw-Hill, 1949.

[3] D. M. Pozar, *Microwave Engineering*, 4th ed. Wiley & Sons, 2012.